LA-UR-13-29094
Approved for public release; distribution is unlimited.

Title: “PHYSICAL PROCESSES IN THE MAGO/MTF SYSTEMS”

Author(s): Garanin, Sergey F
Reinovsky, Robert E.

Intended for: “PHYSICAL PROCESSES IN THE MAGO/MTF SYSTEMS”, RFNC-VNIIEF (in Russian) LANL (in English)

Issued: 2015-03-23 (rev.1)

Editor:
Reinovsky

$$S_{LB} = \frac{4\pi z^2 e^4}{m^2 v^4} \int \frac{dk}{k} \int dx \frac{\exp(-x^2/2)}{\sqrt{2\pi}\,|\varepsilon(k,x)|^2}$$

$$\frac{\partial B}{\partial x} = -\frac{4\pi}{c} j$$

Physical Processes in the MAGO/MTF Systems

$$m_j \frac{dv_y}{dt} = e\left(E_y - \frac{v_x}{c} B\right) - e\eta j$$

$$\frac{\partial f}{\partial t} + v\frac{\partial f}{\partial r} + \vec{F}\frac{\partial f}{\partial \vec{p}} = \mathrm{St}\, f$$

$$\rho\left[\frac{\partial v_\alpha}{\partial t} + (\vec{v}\nabla)v_\alpha\right] + \frac{\partial p}{\partial x_\alpha} - \frac{1}{c}[\vec{j}\,\vec{B}]_\alpha = -\frac{\partial \pi_{\alpha\beta}}{\partial x_\beta}$$

$$(U_{ee}/\varepsilon)^2 \sim N^{2/3}/Z^2$$

$$w_2 = \frac{B_1^2}{4\pi\rho_1}\left(1 - \frac{B_2}{B_1}\right)$$

Los Alamos
NATIONAL LABORATORY
EST. 1943

ВНИИ
VNIIEF

Physical Processes in the MAGO/MTF Systems

Sergey F. Garanin
All Russian Research Institute
of Experimental Physics
Sarov Russia

Editor
Robert E. Reinovsky, Los Alamos National Laboratory

ABSTRACT

The Monograph is devoted to theoretical discussion of the physical effects, which are most significant for the alternative approach to the problem of controlled thermonuclear fusion (CTF): the MAGO/MTF approach. The book includes the description of the approach, its difference from the major CTF systems—magnetic confinement and inertial confinement systems. General physical methods of the processes simulation in this approach are considered, including plasma transport phenomena and radiation, and the theory of transverse collisionless shock waves, the surface discharges theory, important for such kind of research. Different flows and magneto-hydrodynamic plasma instabilities occurring in the frames of this approach are also considered. In virtue of the general physical essence of the considered phenomena the presented results are applicable to a wide range of plasma physics and hydrodynamics processes.

The book is intended for the plasma physics and hydrodynamics specialists, post-graduate students, and senior students-physicists.

PREFACE

Controlled Thermonuclear Fusion (CTF) research has evolved into two mainline approaches—magnetic confinement and inertial confinement fusion. Over the last decades an alternative approach to controlled fusion has also been evolving known in the USA as Magnetized Target Fusion and in Russia as MAGO (MAGnitnoye Obzhatiye—magnetic compression). This approach is characterized by high energy densities, as in inertial fusion, and by the use of magnetic fields, as in magnetic confinement systems. The parameters of the MAGO/MTF plasma differ considerably from those in the conventional systems. Moreover, the computations for the MAGO/MTF systems should include physical processes that either have not been studied previously or exhibit new properties. In essence, a whole new plasma-physics field with abundant and diverse physics is being developed in this approach.

The aim of this book is theoretical discussion of the physical effects, which are most significant for the MAGO/MTF. The book includes the description of the approach, its difference from the major controlled thermonuclear fusion (CTF) systems—magnetic confinement and inertial confinement systems. General physical methods for the simulation of the processes in this approach are considered, including plasma transport phenomena and radiation, the theory of transverse collision less shock waves, the surface discharges theory— all important for such kind of research. Different flows and magnetohydrodynamic plasma instabilities occurring in the frames of this approach are also considered.

We hope that the monograph will help young scientists who are embarking on research in the MAGO/MTF field to get their bearings in the new field of physics. The monograph might be also useful for interdisciplinary specialists, since, given the significance of the phenomena discussed to general physics, the results presented can be applied to a broad range of plasma physics and hydrodynamics effects.

The references are distributed over the Chapters and are provided with the titles of the papers. The references include the papers that we needed for explanation and for obtaining the results presented in the book; thus, we have not attempted to show all the available papers relevant to the material discussed in each Chapter. A more detailed list of references can be built up basing on the given papers.

The author would like to thank the Los Alamos National Laboratory for its support of the writing of the book via the partner ISTC Project #3164p and Project Collaborator R.E. Reinovsky, Responsible Project Official V.V. Kirichenko, and Project Participants N.Yu. Belyakova, A.M. Buyko, E.M. Kravets, S.D. Kuznetsov, V.I. Mamyshev, V.N. Mokhov, and V.B. Yakubov for their enormous assistance in organizing the project and working on it. Special thanks are addressed to the translators—Yu.V. Panova and T.V. Zezyulina—for their terrific job in translating the book into English.

Table of Contents

1. INTRODUCTION

The rapid development of plasma physics in the second half of the twentieth century, and is still under way at present, came about because of the need for intensive research in a broad array of areas. Those areas involved a large range of technical and technological issues whose study began with gas-discharge research, which resulted in the development of effective and reliable light fixtures and plasma television sets. Also under intensive study are methods for the direct conversion of heat energy into electrical energy, plasma rocket engines, plasma-based tools for materials processing, etc. The study of plasma behavior is essential to astrophysical and geophysical research. The study of controlled thermonuclear fusion (CTF) has contributed greatly to the advancement of plasma physics, which has resulted in the development of fundamentally new plasma physics fields of research.

Worldwide, the efforts of most laboratories in the area of CTF are directed mainly at studying two types of physical systems: stationary systems, in which the thermal insulation of low-density, hot plasma, and its confinement are provided by magnetic fields (magnetic confinement fusion, or MCF) and inertial confinement systems, in which deuterium-tritium (DT) plasma is compressed quite rapidly to high densities (inertial confinement fusion, or ICF).

Although certain conditions (called the Lawson criterion [1.1]) must be fulfilled for plasma parameters in order to have thermonuclear ignition in each of these systems, namely,

1) the plasma must be heated to thermonuclear temperatures—about 10 keV;

2) the plasma must be confined long enough to allow the energy released during the fusion to be higher than that spent on plasma heating and confinement—the condition for the product of the final fuel density, n, and confinement time, τ, is $n\tau > 10^{14}$ s/cm^3;

the actual plasma parameters differ considerably. For example, the density of the thermonuclear plasma differs in these systems by 11 orders of magnitude. Moreover, in the magnetic confinement approach, the substantial effect of the magnetic fields and the stationary nature of the system lead to qualitative differences between this system and the inertial plasma confinement system (for example, the characteristic dimensions of the thermonuclear plasmas in the these systems differ by five orders of magnitude). As a result, the plasma physics fields of study referring to magnetic plasma confinement systems and inertial plasma confinement

systems have developed their own specific issues: in magnetic confinement systems, issues such as equilibrium and stability, transport problems in magnetic fields, etc.; and in inertial confinement systems, issues such as the interaction of intense radiation and matter, laser compression of thermonuclear targets, conversion of laser radiation into x-ray radiation, etc.

In 1976–1979, an alternative approach [1.2, 1.3] to the generally accepted ways of solving the CTF problem was proposed: the possibility of solving this problem on the basis of a nonstationary system with magnetic compression (MAGO [from the Russian, ***MAG****nitnoye* ***O****bzhatiye*]) was demonstrated. This approach consists of using a thermonuclear target and one or several cylindrical or spherical magnetic-field–driven liners to compress it. An important advantage of this approach is the possibility of conducting full-scale experiments for meeting the principal scientific challenge of CTF—achieving ignition of thermonuclear fusion without using expensive stationary energy sources such as powerful lasers, charged-particle accelerators, or large tokamaks (such facilities are required only at the stage of power-plant development). The MAGO system experiments can be conducted using relatively cheap explosive magnetic generators (EMG) [1.4, 1.5]. Subsequently, [1.6-1.9] such a system was labeled in the United States as Magnetized Target Fusion (MTF), in which preheated magnetized plasma was compressed. Unlike direct hydrodynamic compression of the initially cold fuel (as in ICF), the MAGO/MTF approach consists of two stages:

1. Initially magnetized plasma is created that is suitable for further compression (with a magnetic field of ~0.1 MG that has a closed configuration of the field lines, a density of ~10^{18} cm^{-3}, a temperature of ~300 eV, and a rather low content of impurities, since impurities may increase radiation losses).
2. Then, with powerful magnetic drivers (e.g., EMG), the plasma is quasi-adiabatically compressed by liners (with velocities on the order of 1 cm/μs) and the plasma parameters are brought to levels that meet the Lawson criterion.

The combination of two essential elements is needed to use this approach for preheated targets: a system for the generation of hot magnetized plasma, and a compression system with sufficiently high energy. In 1981, All-Russian Scientific Research Institute of Experimental Physics (VNIIEF) proposed a new method for generating thermonuclear magnetized plasma with a special MAGO plasma chamber, and that method was implemented experimentally in 1982. The results of that work were published in [1.6, 1.7]. Experiments with the MAGO chamber powered by megajoule-range EMG produced plasma with kiloelectron-volt

temperatures and a neutron yield of up to $4–5\cdot10^{13}$ per shot. It was computationally shown that ignition can be achieved with this system at energies of 100–500 MJ, energies which can be obtained using the disc EMGs already on hand at VNIIEF [1.10]. For this system, the degree of fuel compression need not be very high, and, accordingly, the implosion symmetry is truly achievable, which means that the principal ICF ignition difficulty—the stringent requirements for the implosion symmetry—is absent in MAGO. VNIIEF and Los Alamos National Laboratory (LANL) have collaborated extensively in the MAGO-MTF field [1.11, 1.12], studying liner systems and plasma obtained in the MAGO chamber.

In terms of its time and space scales, as well as the plasma density scales, MAGO system occupies an intermediate position between MCF and ICF (see Table 1.1).

Table 1.1. Approximate values of some plasma parameters for MCF, ICF, and MAGO thermonuclear plasmas

Plasma type	Temperature T, keV	Density n, cm^{-3}	Confinement time τ, s	Characteristic size R, cm	Magnetic field B, MG	Degree of stationarity $c\tau/R$	β	Electron magnetization $(\omega\tau)_e$
MCF	10	10^{14}	1	300	0.05	$3\cdot10^5$	0.03	$2\cdot10^8$
MAGO	10	10^{20}	10^{-6}	1	10	100	1	$5\cdot10^4$
ICF	10	10^{25}	10^{-11}	0.01	0	0.1	∝	0

When comparing MAGO with MCF and ICF, we should note that, although the presence of magnetic fields is common to MAGO and MCF, the vastly different characteristic plasma parameters result in the need to place emphasis on different physical effects. Only some of the instabilities that are dangerous in MCF are important in MAGO because of the relatively short characteristic times. Only the most rapidly growing instabilities, primarily magneto-hydrodynamic (MHD), need be taken into account in MAGO. The degree of the system's connectivity (stationarity) can be characterized by the quantity $\frac{c\tau}{R}$ (c is the characteristic speed of sound in the system, equal to $\sim10^8$ cm/s for T = 10 keV), which shows how many times the sound waves go around the system in its confinement time. The

force effect of the magnetic fields can be characterized by the quantity β given in the Table 1.1—the thermal-to-magnetic pressure ratio. For the characterization of the magnetization of the heat conductance, we can use the quantity $(\omega\tau)_e$.

When comparing MCF, ICF, and MAGO plasma parameters, we should, of course, bear in mind that it is not just the thermonuclear plasma with $T \sim 10$ KeV and $n\tau \sim 10^{14}$ cm^{-3}s that plays an important role in each system. For example, peripheral plasma and near-wall plasma are important for tokamaks (MCF), and the plasma corona plays an essential role for ICF, whereas the role of the cold plasma in the MAGO chamber (which includes plasmas heated by the shock waves during the chamber operation and plasmas remaining relatively cold or attaining moderate temperatures) is crucial in the MAGO system, as is the role of the any plasma associated with the liners compressing the hydrogen plasma. The parameters of these types of plasmas differ quite substantially, and consideration of the different physical effects is important for the different plasma-parameter ranges.

Thus, the parameters of the MAGO/MTF plasma differ considerably from those in the conventional systems. Moreover, the computations for the MAGO/MTF systems should include physical processes that either have not been studied previously or exhibit new properties. In essence, a whole new plasma-physics field with abundant and diverse physics is being developed in this approach.

The history of MAGO/MTF development extends back over more than 20 years, and a large number of experimental and theoretical papers have been published in that time. Among the publication are also reviews (see, for example, Kirkpatrick and Lindemuth [1.13], Garanin [1.14], Siemon *et al.* [1.15], and Garanin *et al.* [1.16]) that enunciate the concepts themselves and integral efforts, i.e., efforts devoted to relating the experiments in MAGO/MTF performance and their simulation. There are virtually no reviews devoted to specific effects characteristic of MAGO/MTF. Meanwhile, a good deal of work done in this area has developed theoretical approaches for describing the radiation properties of MAGO/MTF plasma, a theory of the collisionless shockwaves that are essential to those systems, a theory of surface discharges that is important for this research area since the plasma is confined with walls, etc.

In view of that, there is a need for a monograph that would present those effects. This book is devoted to the theoretical consideration of the most essential of them.

REFERENCES

1.1 J.D. Lawson. “Some Criteria for a Power Producing Thermonuclear Reactor,” *Proc. Phys. Soc. London,* Vol. B70, p. 6, 1957.

1.2 Yu.B. Khariton, V.N. Mokhov, V.K. Chernyshev, V.B.Yakubov. “On Operation of Magnetic Implosion Thermonuclear Targets,” *Sov. Phys. Usp.,* Vol. 19, p. 1032, 1976.

1.3 V.N. Mokhov, V.K. Chernyshev, V.B. Yakubov, M.S. Protasov, V.M. Danov, E.I. Zharinov. “On the Possibility of Solving the Problem of Controlled Thermonuclear Fusion on the Basis of Magneto-gasdynamic Cumulation of Energy,” *Sov. Phys. Dokl.* [Papers of the Academy of Sciences of the USSR], Vol. 24, p. 557, 1979.

1.4 V.K. Chernyshev. “Advances in High-Power Explosive Technology,” *Trudy RFYaTs-VNIIEF* [Proceedings of the RFNC-VNIIEF], No. 1, pp. 364–389, Sarov, 2001.

1.5 V.D. Selemir, V.A. Demidov. "Pulsed Power Explosive Generators for Physical Studies," *Proc. X Int. Conf. Megagauss Magnetic Field Generation and Related Topics.* Berlin. Ed M. von Ortenberg, Humboldt University, Berlin, Germany–VNIIEF, Sarov, Russia, pp 161–168, 2004.

1.6 A.M. Buyko, S.F. Garanin, Ye.V. Gubkov, V.M. Danov, O.Yu. Dementyeva, V.V. Zmushko, T.B. Lezhepekova, V.I. Mamyshev, V.N. Mokhov, E.S. Pavlovsky, V.B. Yakubov. “Magnetohydrodynamic Computations of the Heating of Magnetized Plasma by a Shock Wave with Supersonic Outflow from a Nozzle,” *VANT* [Aspects of Atomic Science and Technology] Methods and Programs for the Numerical Solution of Problems of Mathematical Physics Series, No. 3(14), pp. 30–32, 1983.

1.7 A.M. Buyko, V.K. Chernyshev, V.A. Demidov, Y.N. Dolin, S.F. Garanin, V.A. Ivanov, V.P. Korchagin, M.V. Lartsev, V.I. Mamyshev, A.P. Mochalov, V.N. Mokhov, I.V. Morozov, N.N. Moskvichev, S.V. Pak, E.S. Pavlovsky, S.V. Trusillo, G.I. Volkov, V.B. Yakubov, V.V. Zmushko. "Investigations of Thermonuclear Magnetized Plasma Generation in the Magnetic Implosion System MAGO," *Dig. Tech. Papers: Proc. IX IEEE Int. Pulsed Power Conf.* Eds. K. Prestwich and W. Baker, Institute of Electrical and Electronics Engineers, New York, Vol. 1, pp. 156–162, 1993.

1.8 I.R. Lindemuth, R.C. Kirkpatrick. "Parameter Space for Magnetized Fuel Targets in Inertial Confinement Fusion," *Nucl. Fusion,* Vol. 23, No. 3, pp. 263–284, 1983.

1.9 R.C. Kirkpatrick, I.R. Lindemuth, M.S. Ward. “Magnetized Target Fusion, an Overview,” *Fusion Technology,* Vol. 27, No. 3, pp. 201–214, 1995.

1.10 V.K. Chernyshev, B.E. Grinevich, V.V. Vahrushev, V.I. Mamyshev. "Scaling Image of 90 MJ Explosive Magnetic Generators," in *Megagauss Fields and Pulsed Power Systems (Megagauss-V).* Eds. V. Titov and G. Shvetsov, Nova Science Publishers, New York, pp. 347–350, 1990.

1.11 I.R. Lindemuth, C.A. Ekdahl, C.M. Fowler, R.E. Reinovsky, S.M. Younger, V.K. Chernyshev, V.N. Mokhov, A.I. Pavlovskii. "U.S./Russian Collaboration in High-Energy-Density Physics using High-Explosive Pulsed Power: Ultrahigh Current Experiments, Ultrahigh Magnetic Field Applications, and Progress Toward Controlled Thermonuclear Fusion," *IEEE Trans. Plasma Sci.,* Vol. 25, No. 6, pp. 1357–1372, 1997.

1.12 I.R. Lindemuth, R.E. Reinovsky, R.E. Chrien, J.M. Christian, C.A. Ekdahl, J.H. Goforth, R.C. Haight, G. Idzorek, N.S. King, R.C. Kirkpatrick, R.E. Larson, G.L. Morgan, B.W. Olinger, H. Oona, P.T. Sheehey, J.S. Shlachter, R.C. Smith, L.R. Veeser, B.J. Warthen, S.M. Younger, V.K. Chernyshev, V.N. Mokhov, A.N. Demin, Y.N. Dolin, S.F. Garanin, V.A. Ivanov, V.P. Korchagin, O.D. Mikhailov, I.V. Morozov, S.V. Pak, E.S. Pavlovsky, N.Y. Seleznev, A.N. Skobelev, G.I. Volkov, V.B. Yakubov. "Target Plasma Formation for Magnetic Compression/Magnetized Target Fusion (MAGO/MTF)," *Phys. Rev. Lett.,* Vol. 75, No. 10, pp. 1953–1956, 1995.

1.13 R.C. Kirkpatrick, I.R. Lindemuth. “Magnetized Target Fusion,” *Current Trends in International Fusion Research.* Ed. E. Panarella, Plenum Press, New York, p. 319–332, 1997.

1.14 S.F. Garanin. “The MAGO System,” *IEEE Trans. Plasma Sci.,* Vol. 26, No. 4, pp. 1230–1238, 1998.

1.15 I.R. Lindemuth, R.E. Siemon, "The Fundamental Parameter Space of Controlled Thermonuclear Fusion," *Am. J. Phys.*, Vol. 77, No. 5, pp. 407-416, 2009.

1.16 S.F. Garanin, V.I. Mamyshev, V.B. Yakubov. “The MAGO System: Current Status,” *IEEE Trans. Plasma Sci.,* Vol. 26, No. 4, pp. 2273–2278, 2006.

2. MAGO/MTF SYSTEMS

2.1. Plasma Formation Schemes

A number of ways have been proposed to generate a plasma that can be used for subsequent compression to achieve ignition or a large neutron yield. They differ considerably both in the plasma parameters (density, temperature, and magnetic-field configuration and intensity) and in the methods of plasma formation. Here we discuss three variants: cryogenic fiber z-pinch, MAGO plasma formation chamber, and field-reversed configuration (FRC).

2.1.1. Cryogenic Fiber Z-Pinch

In a cryogenic fiber z-pinch, a plasma is formed simply by passing a high current through a fiber (Fig. 2.1, [2.1]). In the past, such z-pinch was of interest when early experiments showed its "anomalous stability" [2.2]. With such anomalous stability, it appeared possible to directly heat a fiber-formed z-pinch to fusion temperatures through an electrical discharge using modest energy readily available from modern pulsed-power facilities of that time. Subsequent experiments and detailed two-dimensional computations [2.3], however, showed that $m = 0$ instabilities prevented such a z-pinch from reaching fusion conditions immediately. Nonetheless, later computations [2.4] showed that the $m = 0$ instabilities provide a mechanism for the pinch to fill an implosion vessel by forming a Kadomtsev-stable, wall-confined plasma. Since such plasma could be suitable for subsequent compression with liners, it was proposed to experimentally study it on the Colt facility (capacitor bank with a voltage of 100 kV, a current of 2 MA, and an energy of 200 kJ) at LANL. The proposed fiber was a thin polyethylene filament. Unfortunately, experiments [2.5, 2.6] showed that the plasma produced was strongly radiating and short-lived.

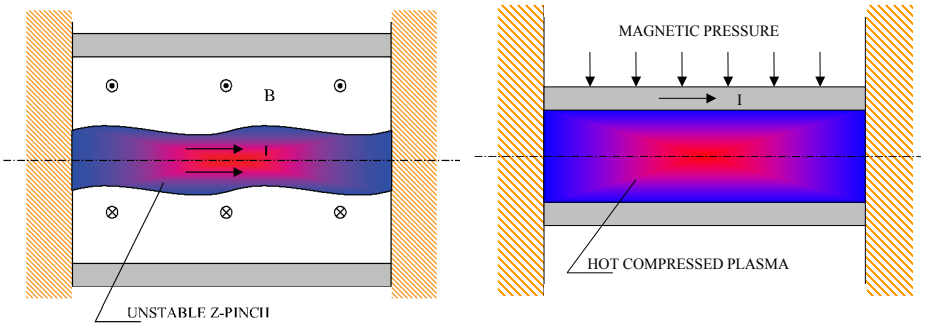

Fig. 2.1. Cryogenic fiber z-pinch. Left, plasma formation; right, implosion of a cylindrical liner.

2.1.2. MAGO Plasma Chamber

The MAGO chamber [2.7, 2.8] consists of two toroidal sections connected by a narrow annular nozzle (a design variant [2.9] is shown in Fig. 2.2). The chamber is filled with a low-density gas (deuterium or DT).

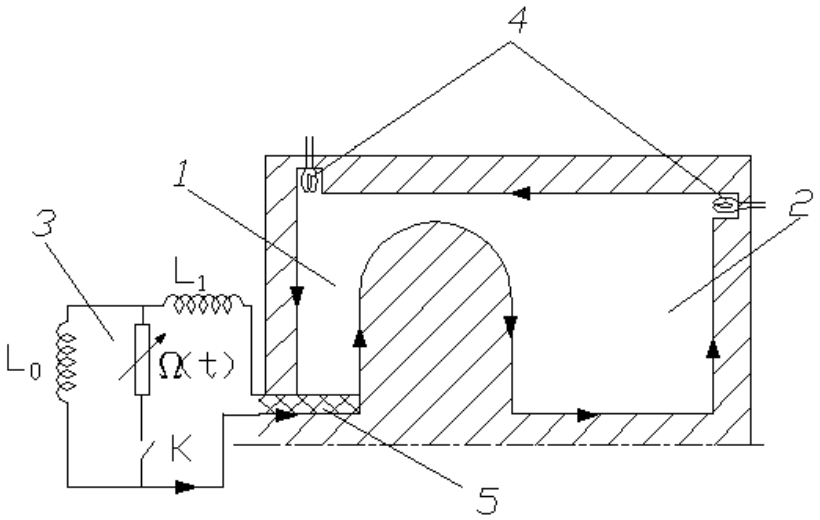

Fig. 2.2. Plasma chamber: 1) first section; 2) second section; 3) equivalent EMG scheme with the closing switch, K, and opening switch Ω(t); 4) inductive probes; 5) insulator.

It is assumed that at the start of chamber operation, an initial azimuthal, "bias" magnetic field has been generated by an initial current introduced into the walls of the chamber (the arrows show the direction of the current). This can be done using an additional source or the main source connected with the input of the first section—the left section in Fig. 2.2 (the switch K in Fig. 2.2 is open). The preliminary current should be introduced quite slowly to avoid a premature gas breakdown.*

When the main, relatively fast current-source is switched on (after the start of the operation of the opening switch Ω(*t*) in Fig. 2.2; the switch K is closed), a high electric field arising in the chamber initiates a gas discharge that results in the initial magnetic field being frozen into the generated cold plasma. (A conductance in the plasma capable of freezing the initial magnetic field into the plasma can also be generated using a special pulsed source of ionizing

*The results of research [2.10, 2.11] have shown that the MAGO chamber can also operate in a regime as described with no rod in the second section and, consequently, without preliminary powering.

radiation.) Driven by the rising magnetic field from the fast source, the plasma starts to move together with the magnetic field lines and to flow through the nozzle from the first chamber section to the second section.

If the Alfven velocity in plasma $c_A = \frac{B}{\sqrt{4\pi\rho}}$ is high enough that $c_A \tau >> L$, where τ is time of the source operation and L is the characteristic chamber size, and the nozzle is sufficiently narrow, then there is enough time for the total pressure to equalize in the most of the volume of each section; however, a pressure difference arises between the sections. In this case, a quasi-stationary plasma flow forms in the nozzle and in the adjacent chamber regions; the plasma velocity at the nozzle outlet becomes supersonic; and a shock wave in which plasma deceleration and heating take place is generated at the nozzle outlet.

Thus, in the device under consideration, the first section and the nozzle work as a plasma accelerator that is basically similar to a coaxial plasma accelerator [2.12]. The second section serves as a chamber for the deceleration and heating of the supersonic plasma jet.

It is easy to construct a picture of the quasi-stationary, one-dimensional, magneto-hydrodynamic (1D MHD) plasma flow. The plasma flow rate through the nozzle is limited to the maximum value [2.13]

$$Q = \frac{4}{3\sqrt{3}} d \sqrt{\frac{B_1^2}{8\pi}\rho_1} \quad , \qquad (2.1.1)$$

where d is the minimum cross section of the nozzle and B_1 and ρ_1 are the magnetic field and the plasma density at the nozzle inlet. In that flow, plasma is accelerated and rarefied while passing through the nozzle; then it is decelerated, compressed and heated in the shock wave; and then it is finally stopped by the pressure gradient and compressed to the total pressure in the second section.

It is remarkable, however, that it is possible to correlate the plasma states at the nozzle inlet in the first section and at the outlet in the second section after the complete stop if one does not care about the processes that take place in the plasma. Due to its generality, that should also be true when ideal hydrodynamics are not applicable in the nozzle region, such as, for example, when the flow is turbulent or if viscosity or some kinetic phenomena play an important role in the process. This relationship follows from the energy conservation law and is expressed as the condition of total enthalpy conservation (the Joule-Thomson process). Since the thermal

pressure in the first section (cold plasma with a temperature in the electron-volt range) is assumed to be small relative to the magnetic pressure, and the plasma's kinetic energy in each section is small relative to the magnetic energy (the nozzle is assumed to be sufficiently narrow), the condition of total enthalpy conservation of each plasma element in the flow has the form

$$\frac{B_1^2}{4\pi\rho_1} = w_2 + \frac{B_2^2}{4\pi\rho_2} \ ,$$

where B_2 and ρ_2 are magnetic field and plasma density in the second section (after complete stop) and w_2 is the plasma enthalpy in the second section. Given that the magnetic field is frozen into the plasma $\frac{B_1}{\rho_1} = \frac{B_2}{\rho_2}$, the enthalpy w_2 is determined with the formula

$$w_2 = \frac{B_1^2}{4\pi\rho_1}\left(1 - \frac{B_2}{B_1}\right) . \qquad (2.1.2)$$

For total pressure $P_2 << P_1$, B_2, will be much smaller than B_1, which means that $w_2 \approx \frac{B_1^2}{4\rho r_1}$, i.e., most of the magnetic energy can be converted to the thermal energy of the plasma.

From the formula (2.1.2) it follows that, for a given maximum magnetic field generated by the fast current-source, the temperature of the heated plasma is inversely proportional to its initial density. Thus, for the fast source and given chamber sizes, one can increase the plasma temperature by reducing its initial density. To preserve the consistency of the time of plasma outflow through the nozzle with the fast source operation time, according to (2.1.1), the nozzle width should be scaled (reduced) as a square root of the density.

To reach a temperature in the kiloelectron-volt range requires an outflow speed of ~ 10^8 cm/s and, similarly, an Alfven velocity of $c_A = \frac{B}{\sqrt{4\pi\rho}}$. To reach such velocities with, for example, a magnetic field of B ~ 0.5 MG (which corresponds to a current of ~5 MA at a radius 2 cm), a density of $\rho \sim 3 \cdot 10^{-6}$ g/cm^3 is needed. It should be noted that, because of the freezing-in, when the plasma is lifted from the smaller radius to a larger radius: from the insulator region at the chamber inlet to the nozzle region (Fig. 2.2), the velocity c_A is preserved.

The chamber will operate as described if the nozzle is sufficiently narrow. Otherwise, wave propagation processes will play a large role in the dynamics of the chamber operation, and the plasma flow may be unable to become quasi-stationary. In this case, however, if the nozzle is not very wide (if the chamber can still be regarded as consisting of two sections), the plasma can be heated as follows. If the insulator evaporation at the first section inlet is minor or completely absent (in the "*H*-thrown" discharge (see Section 6.5), then the plasma flowing out of the first section to the second is followed by a nearly pure magnetic field or a very-low-density residual plasma. During the plasma flow from the first section to the second, the pressure of that magnetic field, which is sustained by the current source, can become noticeably higher than the total average pressure in the second section (the total pressure in the second section may not be uniform, which is why one should speak of average pressure). After the plasma boundary (magnetic piston) has passed through the nozzle to the second section, the difference in the pressures on the magnetic piston and in the plasma in front of the piston generates a shock wave that will result in plasma heating. Since that shock wave propagates downstream, we refer to this chamber operating regime as a direct wave regime, in contrast to the quasi-stationary regime or the backward wave regime, where most of the heating takes place in the shock wave propagating upstream and, in the quasi-stationary case, slowly changing its position relative to the chamber.

The plasma heating can also occur, not only in shock waves, but also as a result of turbulent or near-wall processes associated with the plasma passing through the nozzle (see Section 5.3). This heating regime is similar to that of the backward wave regime in terms of its dynamic properties (with regard to the effect on the processes for establishing the total pressure), the location of the heating zone, and the fact that, in this case, it is the flowing plasma that is being heated (rather than plasma which has already entered the second section), which means that the common relation is applicable (2.1.2).

In most of the experiments conducted, the nozzle was not very narrow, and the experiments cannot be placed unequivocally in a given regime. However, the calculated and experimental data indicate that magnetized hot plasma can be generated using the MAGO chamber.

Calculations coupled with experimental data provide the following qualitative picture of the processes occurring in the chamber.

In the very beginning of the current rise, breakdowns take place in the first-section and the nozzle regions. The shock waves propagating from the breakdown locations and, maintained by the rising current at the chamber inlet, cause plasma ionization. Given that the characteristic rise times of the current are long by comparison with the times of magnetosonic wave propagation, those waves are relatively weak (though they manifest themselves conspicuously as the magnetic field oscillations in the chamber; see Fig. 2.3) and heat the plasma up to the electron-volt-range temperatures.

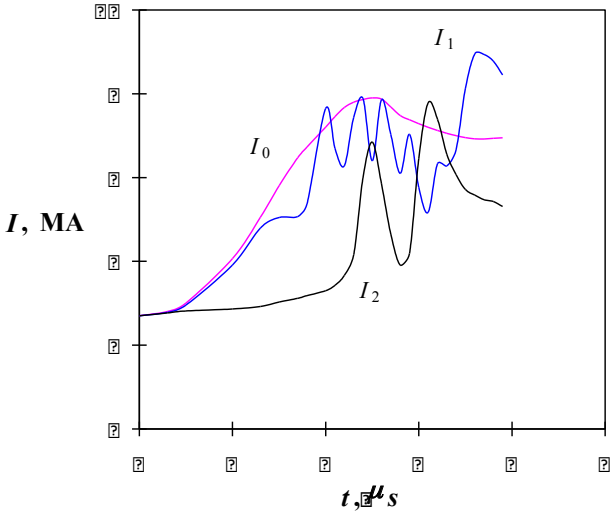

Fig. 2.3. Currents obtained using inductive probes: I_0 is the current at the chamber inlet; I_1 is the current in the first section; I_2 is the current in the second section.

Following the main plasma, driven by the growing magnetic field pressure, is a residual rarefied plasma perhaps made of ionized insulator vapors formed in the *H*-thrown discharge. Similarly, desorption of impurities from the chamber walls can also cause the appearance of an additional mass of plasma. The density of those vapors is higher than the density of the hydrogen plasma, and their motion maintains magnetic field oscillations in the chamber with a rather large period (on the order of a microsecond (see Fig. 2.3, curve $I_1(t)$ at the times $t \sim 3–4$ μs). The oscillation period is proportional to the square root of the density) and a high amplitude.

As the current rises, the difference between the magnetic pressures in the first and the second section increases, and if the nozzle is sufficiently narrow, a quasi-stationary plasma flow is formed with a shock wave at the second-section outlet. The Alfven-Mach number in the shock wave grows

initially, reaches 3–5, and then decreases. After the hydrogen plasma flows to the second section, the residual plasma or the insulator vapors start flowing through the nozzle. The Mach numbers continue to decrease, the shock wave disappears, and the flow becomes subsonic. If the nozzle is insufficiently narrow, the plasma is heated in the direct wave regime with a considerable effect on the heating caused by the anomalous friction of low-density plasma in the nozzle (see Section 5.3).

Plasma cooling due to classical electron and ion heat conduction during the times of interest to us is negligible as a result of the strong magnetization, and even the intensification of heat transport processes at the interfaces of the plasma and the insulator or at the exploding metal wall (see Sections 6.3 and 6.4) to values on the order of Bohm diffusion [2.14] is unable to cool the plasma. The influence of bremsstrahlung radiation losses is even weaker, provided there is no severe contamination of the hydrogen with impurities. But mixing of plasma with the denser insulator vapors drawn, following the main plasma, by convective instability development, can have a substantial effect on the cooling of the plasma. The development of such an instability is caused by the fact that the insulator vapors displacing plasma from large radii pass through a less intensive shock wave and cool down faster because of the radiation. As a result, they have a smaller β, and the situation becomes unstable. According to estimates (see Section 7.3.2), the convection processes that develop at the interface of the plasma and the cold chamber walls can also produce a noticeable effect on the cooling of the plasma.

The characteristic system parameters in the experiments varied within the following ranges, which corresponded to the chosen main regime of chamber operation: the preliminary powering current was 1–3 MA; the final current at the chamber inlet was 3–9 MA; the current rise time was 1–3 μs; the deuterium, or DT, density corresponded to pressures of 1–20 Torr; the chamber radius was 6–10 cm; the first section width was 1.5–3 cm; the second chamber width was 4–10 cm; and the nozzle width was 0.5–2 cm.

According to the calculations for these initial parameters, the maximum plasma velocity at the nozzle outlet is $(0.5–3)\cdot10^8$ cm/s, the maximum plasma ion temperature is 2–30 keV, the maximum electron temperature is 0.6–2 keV, the yield of thermonuclear DT-neutrons is 10^{11}–10^{13}, and the neutron pulse duration is 0.5–2 μs.

The measured currents obtained in the MAGO-2 experiment [2.9] are shown in Fig. 2.3. The peak current flowing in the chamber was $I_{0\max}$ = 7.7 MA at its maximum derivative $\dot{I}_{0\max}$ = 3.8 MA/μs. If we compare

the current oscillations observed in the chamber, I_1 and I_2, with the MHD computation results, we can relate these oscillations to the excited magneto-sonic waves, as well as their start with the arrival of the first MHD compression waves at the probe locations. The arrival time of the first MHD waves and the period of magneto-sonic oscillations agree with the MHD computation results [2.9].

An idea of the processes that take place in the MAGO chamber is provided by the pictures in Fig. 2.4 of the distribution of density, temperature and neutron yield in the chamber volume obtained for different moments in time in one of the two-dimensional simulations of plasma generation (initial pressure of 10 Torr, preliminary powering current of 1.6 MA, final current at the chamber inlet of 5.5 MA, current rise time of 2 μs, neutron yield of $4 \cdot 10^{12}$, and average plasma temperature of 0.55 keV).

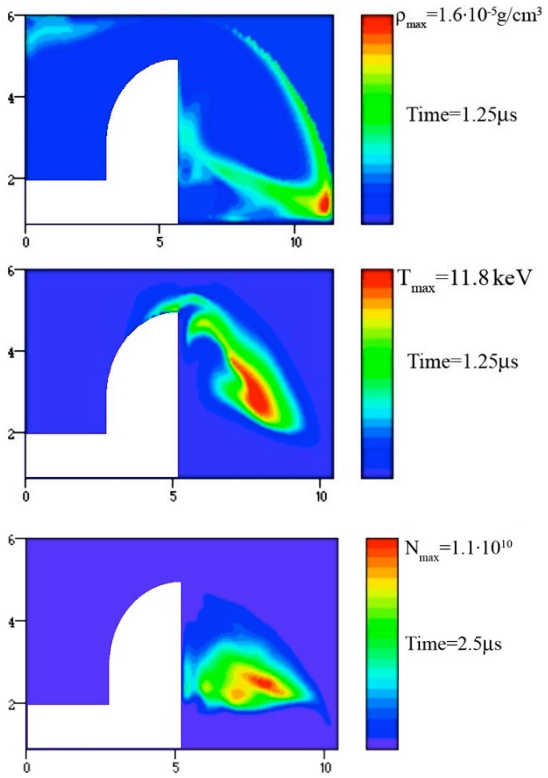

Fig. 2.4. Distributions of density ρ, ion temperature T, and neutron yield N in the MAGO chamber space, obtained in 2D simulation.

Figure 2.4 shows that the shock waves propagating from the locations of the initial gas breakdown (from the insulator at the chamber inlet and the nozzle region), push the plasma into the second section. The low-density residual plasma behind the magnetic piston in the first section is accelerated, when passing through the nozzle, to high velocities $(0.5–2)\cdot10^8$ cm/s) and is heated during its deceleration, to ion temperatures of 5–20 keV. This hot, low-density plasma is the major source of neutrons and, according to Fig. 2.4, occupies a considerable proportion of the chamber space. Note, that although the mechanisms shown in Fig. 2.4 for heating plasma to the high temperatures are mainly collisionless (such as collisionless shock waves, see Chapter 4), they can be modeled with simulations using numerical viscosity. That is because the Hugoniot and other general energy relations (see above) do not depend on the real physical mechanisms of dissipation, which determine only the widths of the shock wave fronts and transient layers.

The extent to which the results of the two-dimensional simulations match the experimental results can be illustrated by comparing, as in Fig. 2.5, the experimentally measured and the calculated time dependences of the current derivative *dI/dt* in the MAGO chamber and the neutron yield from the chamber obtained for one of the experiments [2.9]. On the *dI/dt* plot, modeled times for current features agree with the experimental times, but their amplitudes differ considerably after current sheath penetration into the second section (for $t > 2.5$ μs). That could be because certain physical processes were not taken into account in the model: the Hall effect, which can result in a more profound negative spike of *dI/dt,* and the evolution of gas from the electrode material or insulator evaporation, which could shield current probe readings from the processes in the second section and result in subsequent smoother behavior of *dI/dt*.

The experimental pinhole images of the neutron generation region (Fig. 2.6) also demonstrate the qualitative agreement of the calculation results for neutron spatial distribution (see Fig. 2.4) with the experiment.

Interferometric measurements [2.9] have shown that, in the first section, plasma density turns out to be lower than the initial particle density in the chamber. This agrees with the MHD computation results in which low plasma density at the beginning of the process indicates incomplete ionization and then plasma “floating up” from the smaller radii to the larger with decreasing density (see above). The appearance of the plasma in the second section also agrees with the MHD computations, demonstrating the arrival of the ionizing shock wave.

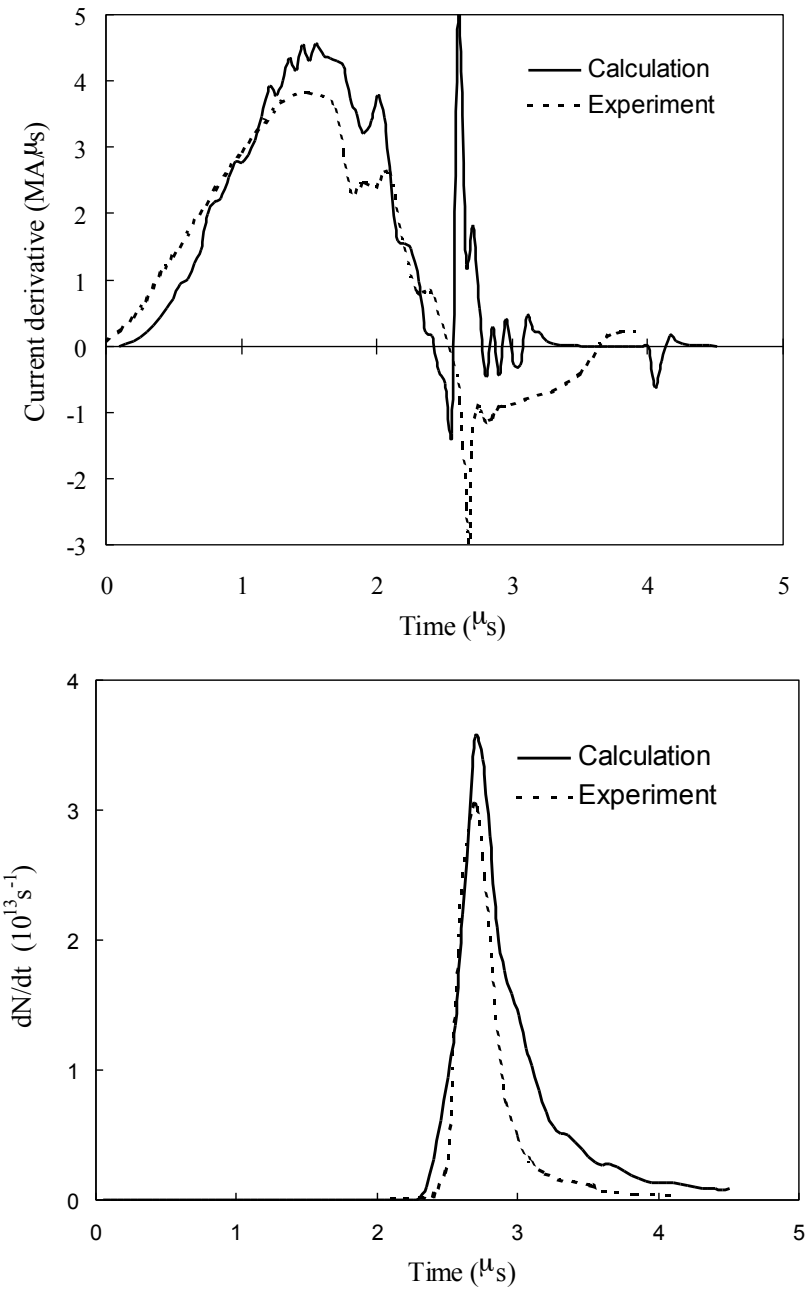

Fig. 2.5. Calculated and experimental time dependences of the current derivatives in the MAGO chamber and the neutron yield from the chamber.

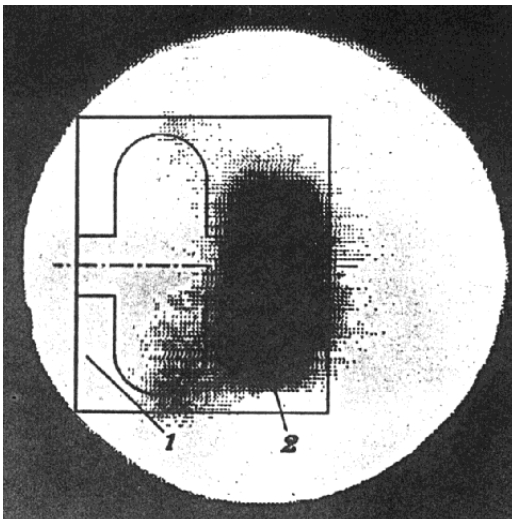

Fig. 2.6. Pinhole image of the neutron generation region. The chamber contours are shown: 1) the first section; 2) the second section.

The two-dimensional computations have shown that at any moment in time in the nozzle region, there is a considerable non-uniformity of plasma velocity and density across the flow, as a result of which the temperature of the heated plasma decreases from the internal electrode to the external electrode by more than an order of magnitude. This non-uniformity is related to the fact that the density of the plasma "floating up" from smaller radii decreases ~1 / r^2, and the plasma path to the nozzle from smaller radii (that is, from the insulator in the first section) along the internal electrode is considerably shorter than that along the external electrode, and the less-dense plasma arrives at the nozzle earlier along the internal electrode.

Note that when the chamber is filled with the DT-mixture, a number of additional effects may appear during the operation of the device, in contrast with the case of pure deuterium:

1. The tritium beta-decay electrons produce the initial volume ionization. Therefore during preliminary powering, free charges will be distributed throughout the chamber volume, and all that can affect the discharge development after the fast source is switched on.

2. The presence of two ion species can affect the structure of the collisionless shock wave front (see Section 4.4) and, thus, the ion temperature (in the plasma containing two ion species, the ion temperature should be higher).

2.1.3. Field-Reversed Configuration (FRC)

The FRC has closed poloidal magnetic field lines in a cylindrically symmetric plasma and open magnetic field lines between the plasma and its confinement/compression wall (Fig. 2.7). Such a configuration can be formed with a suitable theta-pinch discharge in the following way. An axial bias magnetic field is first created in a gas, and the gas is ionized. Then the main theta discharge injects a field opposite in polarity to the bias field, causing the original bias field lines to connect to the injected field lines to form closed flux surfaces. Further flux injection compresses the field-plasma ensemble and introduces open vacuum field lines into the region between the wall and the plasma. Such magnetized-plasma configurations have a number of advantages. One is that the plasma β is relatively high and the lifetime can be equal to many Alfven times, although the reasons for that are not entirely clear. Another is that, under radial compression, the effective magnetic field line tension causes the plasma to contract axially as well, leading to volume compression that is roughly proportional to the radius to the 2.4 power. Finally, the vacuum magnetic field between the plasma separatrix and the wall creates a natural divertor for escaping plasma, and helps buffer the plasma core from impurities introduced from the wall.

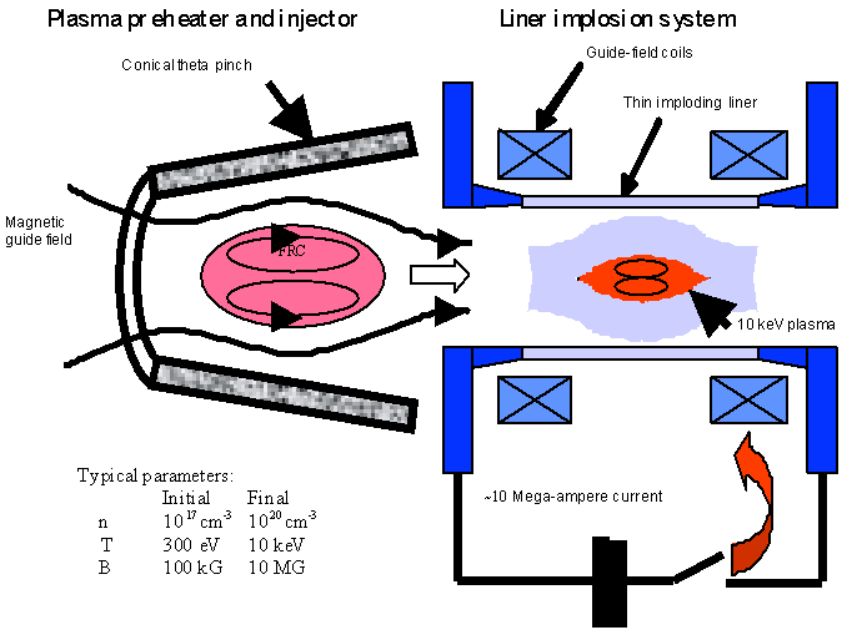

Fig. 2.7. Formation and compression of FRC as an MTF target.

The FRC plasma densities and temperatures of ~10^{17} cm^{-3} and 100–300 eV, respectively, [2.15–2.17] are necessary, according to computational results, to reach fusion-relevant conditions ($n \sim 10^{19}$ cm^{-3}, $T \sim$ several keV) after liner compression. At present, the studies of FRC formation and their compression by liners are being conducted in the United States jointly by several laboratories, including the Air Force Research Laboratory (AFRL), in Kirtland, N.M.; Los Alamos National Laboratory (LANL), in Los Alamos, N.M.; and the University of Nevada, Reno, in Reno, N.V. FRC stability, transportation and compression are being studied with the use of various MHD codes. At LANL and AFRL, experimental studies of FRC formation and its translation into the interior of a liner are under way. At AFRL, the implosion of compressing liners is being studied experimentally, and FRC compression experiments are expected to be performed after the plasma formation work is completed.

2.2. Liner Implosion Drivers

Although a large variety of drivers, such as lasers and particle beams can be used for the implosion of liners in the second stage of operation of the MAGO/MTF system, the fundamental attractiveness of the system consists in the fact that it can employ comparatively lower-velocity liners and, accordingly, drivers with relatively long characteristic times. To achieve ignition in MAGO-MTF, the drivers must have a rather high energy of 100–500 MJ. Such energy levels can be provided by using the disc explosive magnetic generator (EMG) already available at VNIIEF [2.18].

The magnetic implosion of liners, however, including "laser–plasma" experiments, can be studied on smaller stationary facilities. An example of such a facility is the Shiva-Star facility at AFRL, with a characteristic energy of about 9 MJ and a current level on the order of 15 MA. The magnetic implosion of condensed quasi-spherical [2.19] and cylindrical [2.16, 2.20, 2.21] liners, which may be of interest to MTF, is being studied on that facility.

Higher energy (20 MJ, 20 MA) is provided by LANL's Atlas facility. That facility has been used for a large number of liner-implosion studies in which the stability of condensed liners played an important role [2.20, 2.21]. At present, that facility is mothballed.

A considerable contribution to the study of liner physics has been made by smaller-scale facilities. Thus, the Pegasus capacitor bank (4 MJ, 12 MA) at LANL [2.22–2.23] has been used for liner-implosion experiments and for the investigation of condensed-liner stability. A typical cylindrical aluminum liner for experiments on Pegasus had a diameter of 4.8 cm, a length of 2 cm, and a thickness of 0.4 mm.

Even smaller facilities—such as Zebra at the University of Nevada, Reno, with a characteristic current of 1 MA, but with a short rise time of ~100 ns—are being used efficiently for the study of the interaction of megagauss magnetic fields with metal surfaces and of the plasma formation resulting from such interactions [2.24–2.27], i.e., for problems that are important for MAGO/MTF systems.

It would be rather interesting to use the ZR facility (26 MA, 100 TW, 100–300 ns) at Sandia National Laboratories [2.28] for MAGO-MTF and for the study of liner-implosion physics.

EMGs represent a potential type of driver that can be used both for research purposes and for full-scale experiments involving plasma compression. The Los Alamos Procyon system couples a helical EMG with an explosively operated opening switch to develop approximately 20 MJ of inductively stored energy [2.29]. Procyon has been used in liner experiments to deliver a 16 MA, 3-μs-rise pulse to a 2-cm-long, 8-cm-diameter, 1-mm-thick cylindrical aluminum liner, which reached a velocity greater than 1 cm/μs.

VNIIEF has developed a broad spectrum of various EMGs (see, for example, [2.30 and 2.31]), both helical and disc, that are capable of delivering currents from 1 MA to hundreds of MAs over times ranging from several microseconds to hundreds of microseconds and are outfitted with various types of opening switches that can be used to shorten current pulses to the times of less than 1 μs. VNIIEF-developed EMGs provide a means for driving target implosions at energy levels more than an order of magnitude higher than any other existing target drivers and appear to provide sufficient energy for testing the MAGO/MTF concept on the scale required for the thermonuclear ignition. Generators delivering more than 200 MJ of magnetic energy [2.32] have been demonstrated. A joint VNIIEF/LANL experiment, HEL-1 [2.33], used a VNIIEF five-module, 1-m-diameter disc EMG to drive a massive cylindrical aluminum liner that had an initial radius of 24 cm, a thickness of 4 mm, and an initial length 10 cm. Because the z-pinch electrodes, delivering current to the liner during implosion converged with a 6° slope, the length of the liner was less than 6 cm when the liner reached the measuring unit (diagnostic package) at a radius of 5.5 cm. The EMG delivered a current pulse in excess of 100 MA to the liner. The experimental results showed that the liner had a velocity of 0.8 cm/μs and a kinetic energy about 25 MJ when it contacted the measuring unit. The results of such experiments will provide the basis for projecting the utility of ultrahigh-energy liners in a MAGO/MTF context.

REFERENCES

2.1 I.R. Lindemuth, C.A. Ekdahl, R.C. Kirkpatrick, R.E. Reinovsky, P.T. Sheehey, R.E. Siemon, F.J. Wysocki, V.K. Chernyshev, V.N. Mokhov, A.N. Demin, S.F. Garanin, V.P. Korchagin, I.V. Morozov, V.B. Yakubov, J.L. Eddleman, J.H. Hammer, D.D. Ryutov, A.Toor, D.H. McDaniel, C. Deeney, J.H. Degnan, G.F. Kiuttu, R.E. Peterkin, Jr., "Magnetic-Compression/Magnetized-Target Fusion (MAGO/MTF): A Marriage of Inertial and Magnetic Confinement," Fusion Energy 1996. Proc. Sixteenth Int. Conf. Fusion Energy. Organized by the IAEA and held in Montreal, 7-11 October 1996. IAEA Vienna, 1997. Vol. 2, pp. 723–734, 1997.

2.2 J.D. Sethian, A.E. Robson, K.A. Gerber, A.W. DeSilva. "Enhanced Stability and Neutron Production in a Dense Z-Pinch Plasma Formed from a Frozen Deuterium Fiber," *Phys. Rev. Lett.,* Vol. 59, pp. 892–895, 1987; J. Sethian, *et al. Phys. Rev. Lett.,* Vol. 59, p. 1790, 1987 (E).

2.3 P. Sheehey, J.E. Hammer, I.R. Lindemuth, D.W. Scudder, J.S. Shlachter, H. Ralph, R.H. Lovberg, R.A. Riley, Jr. "Two-Dimensional Direct Simulation of Deuterium-Fiber-Initiated Z Pinches with Detailed Comparison to Experiment," *Phys. Fluids,* Vol. B4, No. 11, pp. 3698–3706, 1992.

2.4 P. Sheehey, R.J. Faehl, R.C. Kirkpatrick, I.R. Lindemuth. "Computational Modeling of Magnetically Driven Liner-on-Plasma Fusion Experiments," *Proc. VII Int. Conf. Megagauss Magnetic Field Generation and Related Topics.* Eds. V. K. Chernyshev, V.D. Selemir, and L.N. Plyashkevich. Sarov: VNIIEF, Part I, pp. 425–430, 1997.

2.5 J.M. Taccetti, F.J. Wysocki, G. Idzorek, H. Oona, R.C. Kirkpatrick, I.R. Lindemuth, P.T. Sheehey. "Measurement of MTF Target Plasma Temperature using Filtered Photodiodes," *Dig. Tech. Papers, 12th IEEE Int. Pulsed Power Conf.* Eds. C. Stallings and H. Kirbie in cooperation with IEEE Nuclear and Plasma Sciences Society, Vol. 2, pp. 696–699, Monterey, California, USA, 1999.

2.6 F.J. Wysocki, J.M. Taccetti, J.F. Gerwin, J.F. Benage, G. Idzorek, H. Oona, R.C. Kirkpatrick, I.R. Lindemuth, P.T. Sheehey. "Analysis of Data from MTF Target Plasma Experiments," *Dig. Tech. Papers, 12th IEEE Int. Pulsed Power Conf.* Eds. C. Stallings and H. Kirbie in cooperation with IEEE Nuclear and Plasma Sciences Society, Vol. 2, pp. 700–703, Monterey, California, USA, 1999.

2.7 A.M. Buyko, S.F. Garanin, E.V. Gubkov, V.M. Danov, O.Yu. Dementyeva, V.V. Zmushko, T.B. Lezhepekova, V.I. Mamyshev, V.N. Mokhov, E.S. Pavlovsky, V.B. Yakubov. "Magnetohydrodynamic Computations of Magnetized-Plasma Heating by a Shock Wave in a Supersonic Outflow from a Nozzle"). *VANT* [Aspects of Atomic Science and Technology]. Methods and Programs for the Numerical Solution of Problems of Mathematical Physics Series, No. 3(14), pp. 30–32, 1983.

2.8 A.M. Buyko, V.K. Chernyshev, V.A. Demidov, Y.N. Dolin, S.F. Garanin, V.A. Ivanov, V.P. Korchagin, M.V. Lartsev, V.I. Mamyshev, A.P. Mochalov, V.N. Mokhov, I.V. Morozov, N.N. Moskvichev, S.V. Pak, E.S. Pavlovsky, S.V. Trusillo, G.I. Volkov, V.B. Yakubov, V.V. Zmushko. "Investigations of Thermonuclear Magnetized Plasma Generation in the Magnetic Implosion System MAGO," *Third Zababakhin Scientific Talks*, Kyshtym, Russia, January 1992. *Dig. Tech. Papers: Proc. IX IEEE Int. Pulsed Power Conf.* Eds. K. Prestwich and W. Baker, Institute of Electrical and Electronics Engineers, New York, Vol. 1, pp. 156–162, 1993; *Sov. Phys. Dokl.* [Papers of the Academy of Sciences][sic], Vol. 344, No. 3, pp. 323–327, 1995.

2.9 I.R. Lindemuth, R.E. Reinovsky, R.E. Chrien, J.M. Christian, C.A. Ekdahl, J.H. Goforth, R.C. Haight, G. Idzorek, N.S. King, R.C. Kirkpatrick, R.E. Larson, G.L. Morgan, B.W. Olinger, H. Oona, P.T. Sheehey, J.S. Shlachter, R.C. Smith, L.R. Veeser, B.J. Warthen, S.M. Younger, V.K. Chernyshev, V.N. Mokhov, A.N. Demin, Y.N. Dolin, S.F. Garanin, V.A. Ivanov, V.P. Korchagin, O.D. Mikhailov, I.V. Morozov, S.V. Pak, E.S. Pavlovskii, N.Y. Seleznev, A.N. Skobelev, G.I. Volkov, V.B. Yakubov. "Target Plasma Formation for Magnetic Compression/Magnetized Target Fusion (MAGO/MTF)," *Phys. Rev. Lett.,* Vol. 75, No. 10, pp. 1953–1956, 1995.

2.10 A.A. Bazanov, S.F. Garanin, S.D. Kuznetsov, V.I. Mamyshev, V.N. Mokhov, A.N. Subbotin, V. B. Yakubov. "Numerical Simulation of MAGO/MTF Chamber Operation and Comparison of Computed Data with Some Experiments," *Proc. VIII Int. Conf. on Megagauss Magnetic Field Generation and Related Topics.* Tallahassee, Florida, USA, October 18–23, 1998. Ed. H. J. Schneider-Muntau, World Scientific, Singapore, pp. 298-301, 2004.

2.11 A.A. Bazanov, N.I. Pozdov. "Initial Experiments with the Plasma Chambers MAGO, Having no Central Current-Carrying Post in the Plasma Heating Compartment," *Proc. VIII Int. Conf. on Megagauss Magnetic Field Generation and Related Topics*. Tallahassee, Florida, USA, October 18–23, 1998. Ed. H. J. Schneider-Muntau, World Scientific, Singapore, pp. 294-297, 2004.

2.12 A.I. Morozov, L.S. Solovyev. "Stationary Plasma Flows in Magnetic Field," *Voprosy Teorii Plazmy: Sb. Statey* (Reviews of Plasma Physics: Collection of Papers). Ed. M. A. Leontovich. Moscow: Atomizdat [Publishing House], No. 8, pp. 3–87, 1974.

2.13 L.D. Landau, E.M. Lifshits. Fluid Mechanics, 2nd ed. Addison-Wesley Publishing Co., Reading, MA, 1987.

2.14 L.A. Artsimovich. *Upravlyayemyye Termoyadernyye Reaktsii* (Controlled thermonuclear reactions). Moscow, Fizmatgiz [Publishing House], 1961.

2.15 M.H. Frese, S. Frese, G. Marklin, G.F. Kiuttu, J.H. Degnan, R E. Peterkin, E.L. Ruden, P.J. Turchi, C. Grabovski, T. Cavazos, D. Gale, W. Sommars, T.P. Intrator, R. Kirkpatrick, R.E. Siemon, J.M. Taccetti, G.A. Wurden. "FRC Plasma Formation for Magnetized Target Fusion," *Proc. IX Int. Conf. Megagauss Magnetic Field Generation and Related Topics, Moscow–St. Petersburg, 2002.* Eds. V.D. Selemir and L.N. Plyashkevich. Sarov: VNIIEF, pp. 672–677, 2004.

2.16 J.H. Degnan, T. Cavazos, D. Clark, S.K. Coffey, R.J. Faehl, M.H. Frese, D. Fulton, J.C. Gueits, D. Gale, T.W. Hussey, T.P. Intrator, R. Kirkpatrick, G.F. Kiuttu, F.M. Lehr, J.D. Letterio, I.R. Lindemuth, W. McCullough, R. Moses, R.E. Peterkin, R. E. Reinovsky, N.F. Roderick, E.L. Ruden, J.S. Shlachter, K.F. Schoenberg, R.E. Siemon, W. Sommars, J.M. Taccetti, P.J. Turchi, G.A. Wurden, F.J. Wysocki. "On Research on Magnetic Pressure Implosion of Long Cylindrical Liners, Suitable for Subsequent Compression of the Field Reversed Configuration Type of Compact Toroids," *Proc. IX Int. Conf. Megagauss Magnetic Field Generation and Related Topics, Moscow–St. Petersburg, 2002.* Eds. V.D. Selemir and L.N. Plyashkevich. Sarov: VNIIEF, pp. 730–737, 2004.

2.17 C. Grabovski, J. Degnan, M. Babineau, F. Camacho, S. Coffey, G. Coulter, M. Domonkos, D. Gale, B. Martinez, J. Parker, D. Ralph, E. Ruden, W. Sommars, S. Hsu, T. Intrator, R. Renneke, P. Sieck, B. Waganaar, G. Wurden. "FRC compression heating experiment (FRCHX) at AFRL," *Dig. Tech. Papers, Pulsed Power & Plasma*

Science 2007 Conference. Eds. E. Schamiloglu and F. Peterkin in cooperation with IEEE Nuclear and Plasma Sciences Society, Vol. 2, pp. 1728–1731, Albuquerque, New Mexico, United States, 2007.

2.18 V.K. Chernyshev, B.E. Grinevich, V.V. Vahrushev, V.I. Mamyshev. "Scaling image of 90 MJ Explosive Magnetic Generators," in *Megagauss Fields and Pulsed Power Systems (Megagauss-V).* Eds. V. Titov and G. Shvetsov. New York: Nova Science Publishers, pp. 347–350, 1990.

2.19 J.H. Degnan, F.M. Lehr, J.D. Beason, G.P. Baca, D.E. Bell, A.L. Chesley, S.K. Coffey, D. Dietz, D.B. Dunlap, S.E. Englert, D.G. Gale, J.D. Graham, J.J. Havranek, C.D. Holmberg, T.W. Hussey, R.A. Lewis, C.A. Outten, R.E. Peterkin, Jr., D.W. Price, N.F. Roderick, E.L. Ruden, U. Shumlak, G.A. Smith, P.J. Turchi. "Electromagnetic Implosion of Spherical Liner," *Phys. Rev. Lett.,* Vol. 74, No. 1, pp. 98–101, 1995.

2.20 R.E. Reinovsky, W.E. Anderson, W.L. Atchison, R.J. Faehl, R.K. Keinigs, I.R. Lindemuth, D.W. Scudder, J.S. Shlachter, A.J. Taylor. "Pulsed Power Hydrodynamics: a New Application of High Magnetic Field," *Proc. IX Int. Conf. Megagauss Magnetic Field Generation Related Topics, Moscow–St. Petersburg, 2002.* Eds. V.D. Selemir and L.N. Plyashkevich. Sarov, Russia: VNIIEF, pp. 696–705, 2004.

2.21 W.L. Atchison, R.J. Faehl, I.R. Lindemuth, R.E. Reinovsky, R.M. Stringfield. "Dependence of Solid Liner Stability on Drive Conditions During Magnetic Implosion," *Proc. IX Int. Conf. Megagauss Magnetic Field Generation Related Topics. Moscow–St. Petersburg, 2002.* Eds. V.D. Selemir and L.N. Plyashkevich. Sarov, Russia: VNIIEF, pp. 710–717, 2004.

2.22 R. Reinovsky, W. Anderson, W. Atchison, R. Bartsch, D. Clark, C. Ekdahl, R. Faehl, J. Goforth, R. Keinigs, I. Lindemuth, D. Morgan, G. Rodrigues, J. S. Shlachter, D. Tasker. "Stability of Magnetically Imploded Liners for High Energy Density Experiments," *Megagauss Magnetic Field Generation, its Application to Science and Pulsed Power Technology. Proc. VIII Int. Conf. Megagauss Magnetic Field Generation and Related Topics.* Ed. H. J. Schneider-Muntau. Singapore: World Scientific, pp. 473–478, 2004.

2.23 A.M. Buyko, O.M. Burenkov, S.F. Garanin, Yu.N. Gorbachev, B.E. Grinevich, V.V. Zmushko, G.G. Ivanova, A.I. Kuzyaev, V.N. Mokhov, P.N. Nizovtsev, A.A. Petrukhin, A.I. Pishchurov, V.P. Soloviev, V.N. Sofronov, V.K. Chernyshev, V.B. Yakubov, B.G. Anderson, W.E. Anderson, W.L. Atchison, R.R. Bartsch, W. Brostie, J. Cochrane, C.A. Ekdahl, R.J. Faehl, I.R. Lindemuth, D.V. Morgan, H. Oona, R.E. Reinovsky, J. Stokes, L.C. Tabaka, S.M. Younger. "Instability Growth of Magnetically Imploded Cylindrical Aluminum and High-Strength Aluminum Alloy Liners," *Megagauss Magnetic Field Generation, its Application to Science and Pulsed Power Technology. Proc. VIII Int. Conf. Megagauss Magnetic Field Generation and Related Topics.* Ed. H. J. Schneider-Muntau. Singapore: World Scientific, pp. 479–481, 2004.

2.24 R.E. Siemon, B.S. Bauer, T.J. Awe, M.A. Angelova, S. Fuelling, T. Goodrich, I.R. Lindemuth, V. Makhin, W.L. Atchison, R.J. Faehl, R.E. Reinovsky, P.J. Turchi, J.H. Degnan, E.L. Ruden, M.H. Frese, S.F. Garanin, V.N. Mokhov. "The Challenge of Wall-Plasma Interaction with Pulsed Megagauss Magnetic Fields," *J. Fusion Energ.* Springer Science+Business Media, LLC, 2008.

2.25 S. Fuelling, T.J. Awe, B.S. Bauer, T. Goodrich, A. Haboub, V.V. Ivanov, V. Makhin, A. Oxner, R. Presura, R.E. Siemon. "A Zebra Experiment to Study Plasma Formation by Megagauss Fields," *IEEE Trans. Plasma Sci.,* Vol. 36, No. 1, Part I, pp. 62–69, 2008.

2.26 T.J. Awe, B.S. Bauer, S. Fuelling, and R.E. Siemon. "Threshold for Thermal Ionization of an Aluminum Surface by Pulsed Megagauss Magnetic Field," *Phys. Rev. Lett.*, Vol. 104, No. 3, p. 035001, 2010.

2.27 S.F. Garanin, S.D. Kuznetsov, W.L. Atchison, R.E. Reinovsky, T.J. Awe. B.S. Bauer, S. Fuelling, I.R. Lindemuth, R.E. Siemon. "Numerical Simulations of Thick-Aluminum-Wire Behavior Under Megaampere-Current Drive," *IEEE Trans. Plasma Sci.,* Vol. 38, No. 8, pp. 1815-1821, 2010.

2.28 M.K. Matzen. "Pulsed power sciences at Sandia National Laboratory—The Next Generation," *Dig. Tech. Papers, Pulsed Power & Plasma Science 2007 Conf.* Eds. E. Schamiloglu and F. Peterkin in cooperation with IEEE Nuclear and Plasma Sciences Society, Vol. 2, pp. 1–15, Albuquerque, New Mexico, USA, 2007.

2.29 J.H. Goforth, H. Oona, B.G. Anderson, W.E. Anderson, W.L. Atchison, E. Bartram, J.F. Benage, R.L. Bowers, J.H. Brownell, C.E. Findley, C.M. Fowler, O.F. Garcia, D.H. Herrera, T.J. Herrera, G. Idzorek, J.C. King, I.R. Lindemuth, H. Lee, E.A. Lopez, S.P. Marsh, E.C. Martinez, W. Matuska, G.T. Nakafuji, M.C. Thompson, D.L. Peterson, R.E. Reinovsky, M. Rich, J.S. Shlachter, J.L. Stokes, L.J. Tabaka, D.T. Torres, M.L. Yapuncich, W.D. Zerwekh, N.F. Roderick, P.J. Turchi. "Procyon High Explosive Pulsed Power Experiments," *Proc. VII Int. Conf. Megagauss Magnetic Field Generation and Related Topics.* Eds. V.K. Chernyshev, V.D. Selemir, and L.N. Plyashkevich. Sarov: VNIIEF, Part I, pp. 248–253, 1997.

2.30 V.K. Chernyshev. "Superpower Explosive Magnetic Energy Sources (XX century results. Tasks in the beginning of XXI century," *Proc. X Int. Conf. Megagauss Magnetic Field Generation and Related Topics.* Ed. M. von Ortenberg. Berlin, Germany, Humboldt University–Sarov, Russia, VNIIEF, pp. 17–28, 2004.

2.31 V.D. Selemir, V.A. Demidov. "Pulsed Power Explosive Generators for Physical Studies," in *Proc. X Int. Conf. Megagauss Magnetic Field Generation and Related Topics.* Ed. M. von Ortenberg. Berlin, Germany, Humboldt University–Sarov, Russia, VNIIEF, 2004.

2.32 V.A. Shevtsov, V.S. Andreev, V.A. Demidov, A.I. Krayev, V.B. Kudelkin, Ye.V. Panturov, A.A. Petrukhin, V.P. Pogorelov, V.K. Chernyshev, V.I. Shpagin. "Results of a Powerful Disk EMG Experimental Investigation," *Proc. VII Int. Conf. Megagauss Magnetic Field Generation and Related Topics.* Eds. V.K. Chernyshev, V.D. Selemir, and L.N. Plyashkevich. Sarov: VNIIEF, Part I, pp. 274–275, 1997.

2.33 V.K. Chernyshev, V.N. Mokhov, V.N. Buzin, O.M. Burenkov, A.M. Bujko, V.V. Vakhrushev, S.F. Garanin, B.E. Grinevich, Yu.N. Gorbachev, V.A. Demidov, V.I. Dudoladov, V.V. Zmushko, A.I. Kuzyaev, A.I. Kucherov, B.M. Lovyagin, Y.I. Matsev, P.N. Nizovtsev, A.A. Petrukhin, A.I. Pishchurov, S.S. Sokolov, V.P. Solovjov, A.I. Startsev, V.B. Yakubov, B.G. Anderson, C.A. Ekdahl, J.H. Goforth, D. Clark, I.R. Lindemuth, R.E. Reinovsky, R.J. Faehl, S.M. Younger. "Study of High Energy Liner Compression in HEL-1 Experiment," *Dig. Tech. Papers, Proc. XI IEEE International Pulsed Power Conf.* Eds. G. Cooperstein and I. Vitkovitsky in cooperation with IEEE Nuclear and Plasma Sciences Society, pp. 566–572, 1997.

3. PHYSICAL PROCESSES AND SIMULATION TECHNIQUES

3.1. Basic Physical Processes

As mentioned in the introduction, plasma parameters in MAGO-MTF systems differ significantly from those in conventional systems. This difference applies to space and time scales and plasma densities. MAGO-MTF occupies an intermediate position between magnetic confinement and inertial confinement fusion systems separated by about ten orders of magnitude in density and time, and about five orders of magnitude in characteristic space sizes. Correspondingly, simulations of MAGO-MTF systems require including the physical effects, which either have not been studied before, or display new properties.

One of the basic plasma heating mechanisms in MAGO-MTF systems is heating in transverse shock waves, which are most often collisionless under low-density and strongly magnetized plasma conditions. For the MAGO plasma, transverse collisionless shock waves (CSW) with moderate Mach numbers need to be considered; including the effects of plasma resistance and Joule heating, and 2D effects resulting from the growth of instabilities. Also of importance is the issue of plasma conditions downstream from the CSW front (i.e., the relation between electronic and ion heating and the ion spectrum downstream from the front), and the consideration of CSW in plasma with several ion components (i.e.,, CSW in DT plasma).

In the plasma of a MAGO system, essential processes include the Hall effect and other collisionless transport processes. For these processes, one can distinguish several major effects. First, the Hall effect results in a considerable increase of magnetized plasma resistance. In order to quantify magnetic field penetration into plasma, one needs to consider the Hall effect and associated voltage. Second, accounting for the Hall effect leads to a difference between the anode and the cathode, whereas conventional magnetic hydrodynamics is invariant with respect to electrode polarity. Experiments demonstrate that MAGO chamber performance is essentially dependent on the polarity of electrodes. For example, neutron yield generated in the chamber varies several orders of magnitude with the alteration in electrode polarity. In order to understand the physics of the processes that take place there, one has to analyze the flows, primarily those that occur near electrodes, subject to the Hall effect. An important challenge here is the essentially two-dimensional character of the Hall effect, so the possibility of reduction of some flows to the one-dimensional case might considerably simplify their analysis. Third, the Hall effect and other collisionless transport processes may affect plasma cooling. In the MAGO system, plasma cooling

due to classic electron and ion heat conduction is insignificant because plasma is strongly magnetized. A more important role is played by drift-related heat and particle flows. They need to be evaluated both at the stage of pre-heating, and at the stage of further compression and ignition.

Numerical simulations of the MAGO system require using plasma transport coefficients and quantities that determine radiation/matter interaction. Braginskii coefficients [3.1] are often used as transport coefficients, and standard formulas or Post-Jensen tables [3.2] are typically used as radiation/matter interaction coefficients. However, MAGO plasma is often rather dense and non-ideal, and electron occupancy of levels can be closer to the thermodynamic one (or Fermi one for multiply charged ions), rather than to the coronal. For low dense coronal MAGO plasma apart from radiation losses, one should also take into account, and estimate for arbitrary heavy impurities, the spectra that are important for plasma diagnostics by emitting radiation flux measurements. Therefore, one has to deal with the non-ideal case for transport coefficients (first of all, for conductivity), and with approximate calculations of radiation properties of hydrogen and multiply charged plasma in local thermodynamic or coronal equilibrium.

Of importance for MAGO-MTF systems is the matter of surface discharges that occur when the magnetic flux enters plasma or an insulator (*H*-pressed discharges) or escapes through the insulator surface (*H*-thrown discharge), and of magnetized plasma cooling at the plasma/condensed matter interface. These discharges result in magnetic flux and energy losses (in *H*-pressed discharges), or constrain energy fluxes delivered to the system, and can lead to penetration of the insulator material into hydrogen plasma (in the *H*-thrown discharge).

When considering and accounting for various plasma instabilities and their effects on plasma flows and plasma cooling processes in MAGO-MTF, as their characteristic times are relatively short, it is important to take into account only the most rapidly growing instabilities, such as MHD instabilities.

2D plasma flows are often characterized by high velocity contrast across the flow (cases close to tangential discontinuities or tangential discontinuities themselves). In the supersonic case, these discontinuities can be stable with respect to the perturbations in the plane velocity/normal to the discontinuity surface, i.e, in 2D simulations in this plane. However, a question of stability of respective flows for arbitrary perturbations arises.

Plasma flows at the plasma preheating stage and at the liner acceleration can produce conditions for the development of Rayleigh-Taylor and sausage instabilities that can be treated as manifestations of the general

MHD interchange instability. It is important to ascertain conditions for its development and calculate its increment. Nonlinear development of this instability results in the growth of characteristic wavelengths and formation of some self-similar solutions that – in spite of their being unstable – under experimental conditions can persist for a relatively long time. Considering these solutions might make it possible to explore not only MHD flows that occur under certain conditions, but also some properties of turbulence that evolve in such unstable cases and turbulent plasma cooling mechanisms.

For the MHD plasma flows in the magnetic field present in the MAGO-MTF systems, turbulence may have a two-dimensional character, because the magnetic field precludes bending of magnetic field lines. Turbulence, per se, is important in considering material wash-out from the walls and plasma contamination with impurities. Therefore, one has to address the matters of two-dimensional turbulence, its relaxation and effects on the wash-out processes.

3.2. Kinetic Approach

The most detailed description of plasma is provided by the kinetic approach, which relies upon the use of a particle distribution functions in "phase space" (spatia and momentum coordinates) $f(t,\vec{r},\vec{p})$. In thermodynamic equilibrium, this function takes the form of a Maxwell distribution (or Fermi distribution for electrons accounting for degeneracy), and in a general case its variation is described by a set of kinetic equations (Boltzmann equations) for each species of particles (electrons, ions, atoms or molecules) written as:

$$\frac{\partial f}{\partial t} + v\frac{\partial f}{\partial r} + \vec{F}\frac{\partial f}{\partial \vec{p}} = \mathrm{St}\, f \ , \qquad (3.2.1)$$

where F is the force acting on a particle, which is equal to

$$F = ze\left(\vec{E} + \frac{1}{c}[\vec{v}\,\vec{B}]\right),$$

for charged particles with a charge ze in the electric field $\vec{E}$ and magnetic field $\vec{B}$, and St f is the integral of collisions of a given species of particles with particles of all species. The integral of charged particles collisions of logarithmic accuracy (accuracy on the order of $1/\ln(1/\lambda)$, where λ is the so called plasma parameter, see Section 3.3.3), was derived by L.D. Landau, and a more accurate expression for the integral of collisions that enables

calculations of many processes with an accuracy on the order of λ was obtained by B. Balescu and A. Lenard.

To describe plasma flows with large space and time scales, one can obtain from the kinetic approach, a less detailed hydrodynamic description, or—if electric and magnetic fields are taken into account—a magneto-hydrodynamic description. Then, the kinetic description will allow calculating the so-called transport coefficients, such as electrical conductivity, viscosity, thermal conductivity, etc, that need to be included in MHD equations, when these should account for the effect of corrections due to the contribution of collisional paths and other transport lengths.

In some cases, for plasma flow description, it is convenient to use the so-called hybrid approach, when one of the species of particles is described by the hydrodynamic equations, and the other by using the kinetic equations. Such an approach typically suggests a hydrodynamic description of the electronic component, because electrons have small characteristic times of collisions and small kinetic scales in space and time determined by Larmor gyration in the magnetic field. Ions, however, should be treated within the kinetic approach to describe processes on scales of the ion Larmor radius and the period of ion Larmor gyration. Such an approach will be used in this work to model collisionless shock waves (Chapter 4).

3.3. Magnetohydrodynamic (MHD) Approach

3.3.1. Equations and Validity Conditions of Magnetohydrodynamics

If characteristic space lengths of the problem and time scales in question are large enough (specific criteria for MAGO system simulations are discussed below), such plasma flows can be described using a set of MHD equations. In this case, plasma is treated as a continuum characterized by macroscopic parameters: density, velocity, pressure and temperature. Due to the large difference in masses of electrons and ions, energy exchange as a result of their collisions proves to be relatively slow, and in a number of cases temperatures of electrons and ions can be considered different. A set of MHD equations for a two-component system of electrons and ions can be derived from the set of kinetic equations (3.2.1) and written as follows:

continuity equation for mass density ρ

$$\frac{\partial \rho}{\partial t} + \mathrm{div}\rho\vec{v} = 0 \ , \qquad (3.3.1)$$

equation of motion

$$\rho\left[\frac{\partial v_\alpha}{\partial t}+(\vec{v}\nabla)v_\alpha\right]+\frac{\partial p}{\partial x_\alpha}-\frac{1}{c}[\vec{j}\,\vec{B}]_\alpha=-\frac{\partial \pi_{\alpha\beta}}{\partial x_\beta}, \qquad (3.3.2)$$

equations of heat balance for electrons and ions

$$\frac{3}{2}n_e\left[\frac{\partial}{\partial t}+(\vec{v}_e\nabla)\right]T_e+p_e\,\mathrm{div}\,\vec{v}_e=-div\,\vec{q}_e+Q_e$$

$$\frac{3}{2}n_i\frac{dT_i}{dt}+p_i\,\mathrm{div}\,\vec{v}=-div\,\vec{q}_i-\pi_{\alpha\beta}\frac{\partial v_\alpha}{\partial x_\beta}+Q_i\ , \qquad (3.3.3)$$

where $\pi_{\alpha\beta}$ is viscous stress tensor, $p_e = n_eT_e$, $p_i = n_iT_i$, $p = p_e + p_i$, $\vec{v}_e = \vec{v} - \vec{j}/en_e$, q_e, q_i are heat fluxes transferred by electrons and ions, Q_e, Q_i is heat gained by the electrons and ions as a result of their collisions with other particles (including interaction with radiation or radiation losses for electrons).

Equations (3.3.1–3) need to be supplemented with Maxwell equations for a quasi-stationary electromagnetic field

$$\mathrm{rot}\,\vec{E}=-\frac{1}{c}\frac{\partial \vec{B}}{\partial t}\ ,$$

$$\mathrm{div}\,\vec{B}=0\ , \qquad (3.3.4)$$

$$\mathrm{rot}\,\vec{B}=\frac{4\pi}{c}\vec{j}$$

and joined with an equation that expresses the "generalized Ohm law" of the form

$$\vec{E}+\frac{1}{c}[\vec{v}\,\vec{B}]=\vec{F}\ , \qquad (3.3.5)$$

where $\vec{F}$ is linear combination of current $\vec{j}$ and gradients of thermodynamic quantities. The quantities $\pi_{\alpha\beta}$, q_e, q_i, Q_e, Q_i should be expressed through the factors that create departure from equilibrium, and in this case they define transport processes, and respective coefficients, called transport coefficients or kinetic coefficients. All transport effects provide for corrections due to the finite lengths of kinetic processes (for example, due to the corrections related to the finite path length of particles in plasma). So-called ideal magnetohydrodynamics ignores such corrections, and e.g., the quantities $\pi_{\alpha\beta}$, q_e, q_i are not taken into account. Note that the difference in

velocities of electrons and ions, which is included in the MHD equations (3.3.3) and should therefore be incorporated in the generalized Ohm law (3.3.5) in this case, is also one of transport effects and it should not be taken into account in ideal magnetohydrodynamics.

The MHD equations underlie techniques and codes that enable simulations of different processes in MAGO-MTF systems. In particular, 1D and 2D (typically, in the *r, z* coordinates due to the axial symmetry of initial geometries, see Fig. 2.2) MHD techniques are widely used to simulate the performance of the MAGO chamber [3.3-3.6].

The criteria for the validity of the MHD approach [3.1] for description of plasma flows in the MAGO chamber at temperatures below one kilo-electron-volt are satisfied, except regions with high gradients (shock waves or near-anode zones). As for plasma heated to kilo-electron-volt temperatures, the condition of smallness of spatial gradients $r_i l / R^2 << 1$ (r_i is ion Larmor radius, l is particle path length, R is chamber radius) holds here, but the condition of slowness of values variation in time $\frac{d}{dt} << \frac{1}{\tau_{aa}}$ (τ_{aa} is a collisional time) is satisfied for the electron component and is not for ions. Since this MHD description is not quite correct, we ask, what physical consequences may result.

First, the MHD calculations assume an isotropic distribution of ion velocities along the directions along and across the magnetic field. This distribution does not have time to be established due to infrequentcollisions, and in our geometry ions attaining “thermal” velocities across the field in heating (in the shock wave, see Chapter 4) should have had almost no velocities along the field, and the effective adiabatic index of the hot ion component might have been close to two rather than equal to 5/3. However, this change does not seem to severely affect the flow dynamics and, that is more essential, this ion distribution is unstable (see Section 4.2). Instability evolution should lead to effective “isotropization” of the distribution during the characteristic times $\sim \omega_i^{-1}$ small under our conditions. Second, as by virtue of rare collisions, the Maxwellian distribution of ions cannot have time to be settled, the real ion spectrum should be used to evaluate the thermonuclear fusion rates and neutron yield. Clearly, it is important to specify the ion spectrum, mainly for diagnostics of plasma by its neutron emission [3.7]. As for the effect of the real ion spectrum on the neutron yield value, in the kiloelectrovolt region, the ion spectrum specification changes the neutron yield not very considerably, by several times (see Section 5.3).

Thus, 1D and 2D calculations in the MHD approximation can be considered as quite a good approach to describe plasma in the MAGO chamber on the whole [3.8].

The approximations used in the MHD calculations do not take into account some effects, which, however, can play an important role in the chamber operation. Among them the following can be mentioned.

1) As initially the chamber is filled with cold DT-gas, its conversion to plasma occurs due to gas breakdown in the magnetic field. It is difficult to describe the breakdown phenomena evolution with the MHD approximation because an important role can be played by plasma non-quasi-neutrality and quite a complex combination of atom kinetic ionization and excitation processes, as well as the differences in motion between the plasma (electron-ion) component and neutrals (plasma slipping relative to the neutrals) at low ionization degrees. The problem complexity increases due to the important role played by radiation transport and the influence of impurities on the discharge formation. When the breakdown evolves, the azimuthal asymmetry and the discharge filamentation may develop, processes that are significant for Z-pinch [3.9]. To describe breakdown processes, in the MHD calculations one can use phenomenological models, such as the electron cost model [3.9]. This model can be modernized to take into account the conductivity magnetizing at low degrees of ionization. When describing the breakdown development using this model, we can assume that for low degrees of ionization, apart from usual energy expenditure in creating ionization, which are taken into account by the Saha equation, additional energy losses due to radiation and energy exchange between electrons and neutral atoms, require an additional expenditure of ~100 eV for the generation of each electron (also including the expenditure related to inelastic molecular processes, dissociation, etc.). However, this model, being phenomenological, hardly can work in a wide range of conditions without a change in the phenomenological parameters.
2) Plasma contamination with impurities from the walls and the insulator, wall evaporation: The conditions of contamination have much in common with the conditions existing in the plasma accelerators, plasma focus and other dynamical plasma devices; however, in our case the issue of contamination is more acute because of the need for subsequent compression. In modern codes it is possible to introduce models of material evolution from electrodes

into plasma; at present such models are successfully employed (see Section 7.3.3).

3) Development of MHD-instabilities: The set of the available experimental data shows that the azimuthally asymmetric instabilities do not noticeably affect the chamber operation. The situation here is similar to that in the Z-pinch where the main instability is the convective one, $m = 0$ [3.9, 3.10]; however, here we have an additional favorable circumstance: presence of the preliminary magnetic field. The $m = 0$ instability in 2D calculations is taken into account automatically; in 1D calculations, which are usually conducted in the channel approximation (i. e., along some centerline in the chamber, with the dependences of the channel mean radius and its cross-section width on the total path along the channel, corresponding to the chamber geometry) it can be simulated using exponential factors ch($\int\gamma dt$) in the coefficients of magnetic diffusion and heat conductivity (γ is the instability increment). The instability development conditions and the increment, γ, calculation in the presence of acceleration (that is in the conditions of both the Rayleigh-Taylor and sausage instabilities) is considered in Section 7.1.2. As for the development of azimuthally asymmetric perturbations, they may occur yet in the zones of tangential discontinuities or high velocity gradients (in the nozzle region), though their growth increments are small compared with the hydrodynamic ones (see Section 7.1.1). Apart from this, the azimuthally asymmetric instabilities in longer times can cause forceless configurations of the magnetic field [3.11] and lead to fast plasma cooling in them.

4) Kinetic phenomena arising in plasma flow along electrodes (Chapter 5): When plasma flows along electrodes, plasma can be heated due to its friction on an electrode. This heating is most significant for the nozzle region, where the velocity of plasma is ~10^8 cm/s. Here the processes can take place at the scales of the ion Larmor radius. Analysis of the situation analysis is complicated by the Hall effect, which carries magnetic flux to the anode, rarefying the plasma and, on the contrary, the magnetic flux is removed from the cathode increasing the plasma density. Near the anode, the hydrodynamic approach may be invalid due to the appearance of vacuum regions. Near the cathode, the situation remains controlled by hydrodynamics; however, it seems difficult to describe such dense layers of the near-cathode plasma in the direct computations

of the chamber operation. These kinetic phenomena lead to asymmetry relative to the electrodes' polarity.

5) Collisionless shock waves (CSW) (Chapter 4): Since downstream from the shock wave front the plasma is strongly magnetized ($\omega\tau$) >> 1, such a shock wave is collisionless, i. e. the effective heating takes place, not due to particle collisions, but due to randomization and ionization and the development of instabilities. At these conditions for one-component plasma, the fraction of the electron heating is the main up to the Alfven-Mach numbers $M_A \sim 8$, but for the two-component plasma (DT), the fraction of the ion heating considerably increases and becomes equal to the electron one at $M_A \sim 4$. CSW are a widespread phenomenon in space and laboratory plasmas. The MAGO chamber plasma is a new venue for their manifestation where unique conditions are provided.

3.3.2. Equations of State

In the equations of heat balance of electrons and ions (3.3.3–4), for each of these components, it is assumed that $p_a = n_a T_a$ ($a = e$ or i), and the number of charged particles for the given plasma component is considered to be constant (degree of ionization does not change). The gas of particles described by such an equation of state is called an ideal gas. In a general case, however, the equation of state has a more complex form: $p_a = p_a(\rho, T_a)$, $\varepsilon_a = \varepsilon_a(\rho, T_a)$, and the equations of heat balance will have some changes. Let us write the equation of heat balance for the case when electron and ion temperatures can be considered equal and hence one can use a general equation of state, $p = p(\rho,T)$, $\varepsilon = \varepsilon(\rho,T)$, for the whole set of particles constituting each plasma component: electrons, ions of all possible kinds, and neutrals

$$\rho \frac{d\varepsilon}{dt} + p \operatorname{div} \vec{v} = -div\,\vec{q} + Q \ .$$

As to the equations of state needed for MAGO-MTF system simulations, for low-density hydrogen (DT) plasma with temperatures that are not too low, one can use the Saha equation [3.12-3.13], and, if necessary, add dissociation losses into the energy equation. As a result, this equation can at low ionization transform into the electron cost model [3.9].

A more complicated issue is that related to the equations of state of liners that compress plasma, metal walls that confine plasma, and other involved materials that are originally condensed and then—as they get heated—transform to plasma, as they get compressed and as they expand in MHD

flows. The plasma state of the materials in the region of multiple ionization can be described rather efficiently and accurately using the approximate Raizer method [3.13].

However, MHD simulations often require that wide-range equations of state be used to describe the behavior of materials starting from low temperatures (around room temperature) and condensed state up to high temperatures (dozens or even hundreds of electron-volts) and plasma state. In this case, quite a straightforward way to describe the equation of state will be to represent pressure p and specific internal energy ε as a sum of three temperature and pressure dependent terms: cold, or elastic, term, hot term coinciding with the equation of state of multiply ionized plasma, and the lattice term describing the contribution of the condensed material to the thermal capacity and getting relatively smaller at higher temperatures in the plasma region. This way is in general the same as the three-term equation of state [3.13], with the only essential difference in the forms of the plasma term. Perhaps, such a description of the equation of state can prove to be less accurate, but it is wide-range, and it can be helpful as applied to the cases where no accurate description of intermediate states (between condensed state and plasma) is required. Since such equations of state are semi-empirical and contain phenomenological parameters, they can be set up using other, more accurate, equations of state for narrower ranges. Examples of equations of state set up for aluminum and copper include [3.14–3.15], where the equation of state for copper [3.15] was generated using the data of [3.16], resting on experimental results obtained for electrically exploding wires.

At present, equations of state are explored actively – both experimentally and theoretically – especially in high energy density regions (see e.g., [3.17]). Quantum Molecular Dynamics (QMD) [3.17–3.18], in which electrons are treated in the quantum mechanics framework (using the density functional theory) and nuclei are treated in a classical way, proved to be a fruitful approach to designing equations of state in this region.

Since experimental data and theoretical and computational results obtained using various models build up with time, it is convenient to use tables for data representation. The SESAME database [3.20] is an example of such tables.

Note that considerations of equations of state often produce additional information that can be used for calculations of electrical conductivity or other transport coefficients. For example, ionization degree obtained in calculations of the plasma term of the wide-range equation of state [3.14–3.15] can be used to calculate electrical conductivity in the plasma region, and in QMD simulations of equations of state one can use the Kubo-Greenwood formula to

calculate electrical conductivity and opacity in the low-frequency region. In addition, phenomenological parameters for equations of state that are used to describe experimental data are also often chosen in conjunction with conductivity, as was the case in choosing phenomenological parameters of the equations of state [3.14–3.16], where the equation of state–conductivity system was used to describe the results of electrical explosions of wires. Thus, it is often more reasonable to address the issue associated with equations of state in a more comprehensive manner, together with conductivity and other transport coefficients and properties of materials.

3.3.3. Plasma Transport Coefficients. Electrical Conductivity of Multiply Ionized Non-Ideal Plasma

As mentioned above, within the hydrodynamic plasma description, one should take into account different transport processes and respective transport coefficients. As plasma is magnetized, along with plasma properties, such as electrical and thermal conductivity, viscosity, and electron and ion temperature balancing, one should also take into account Hall, Nernst, Leduc-Righi effects etc. In addition, transport coefficients in a magnetic field turn out to be anisotropic and dependent on the direction of the magnetic field. Detailed calculations of transport coefficients for plasma based on the Landau kinetic equation were performed by S.I. Braginsky [3.1], and these constitute the most widely used results in the classical theory of transport in plasma. For the case of highly magnetized plasma, transport coefficients are derived in [3.21], which complements [3.1], because [3.21] provides coefficients calculated analytically for arbitrary ion charge z.

Note, however, that the presence of strong fields or currents and high gradients of quantities in plasma in many cases can disturb thermodynamic equilibrium and result in so-called plasma turbulence. In such cases, effective transport coefficients may grow considerably and result in anomalous transport coefficients. An example of such an anomalous transport coefficient is anomalous resistance, which plays an essential role in many plasma systems. For example, in plasma focus devices, it is important as an acceleration mechanism for neutron generation [3.22].

As already mentioned, the Landau collision integral has a logarithmic accuracy (on the order of $1 / \ln(1 / \lambda)$, where λ is the plasma parameter), which is inherited by the transport coefficients calculated on its basis. Low-density hydrogen plasma in MAGO-MTF systems is ideal enough, i.e., its plasma parameter is very small; so the logarithmic accuracy in determining its transport coefficients may prove to be quite sufficient. However, as for the relatively dense plasma of liners or walls, the logarithmic accuracy may turn out to be not enough. The key transport coefficient of such plasma might be electrical conductivity, because the role of other coefficients can

be small due to the effects of radiation transport, in contrast with which electron and ion heat conductivities may prove to be inessential. Radiation transport brings down the temperature of plasma making it less magnetized and, consequently, suppressing the role of other transport coefficients.

Therefore, it is required to calculate electrical conductivity with an accuracy better than the logarithmic one. Let us perform higher-accuracy calculations of electrical conductivity for the case of Lorentz plasma, i.e., plasma with $z >> 1$.

Thus, let us consider a multiply ionized plasma with the plasma parameter

$$\lambda = \frac{ze^2}{DT} \tag{3.3.6}$$

($D = \sqrt{\frac{T}{4\pi n z^2 e^2}}$ is Debye radius; n is ion density, T is temperature), which can be not very small. Plasma with $\lambda<1$ is called non-ideal. Corrections related to this non-ideal property influence many quantities, including thermodynamic ones; but as distinct from thermodynamics quantities, when these corrections prove to be on the order of λ [3.12], corrections for plasma being non-ideal are expected to have a particularly strong impact on transport coefficients calculated with an accuracy $\sim \frac{1}{\ln\frac{1}{\lambda}}$. It is therefore worth doing to calculate electrical conductivity with a higher accuracy, $\sim \frac{\lambda}{\ln\frac{1}{\lambda}}$.

In [3.23], such calculations were performed using the Sonin polynomial expansion of the solution to the transport equations within the Chapman-Enskog approach; but the resulting expression for conductivity becomes infinite for the non-ideal plasma parameter $\lambda \cong 0.8$. Thus, the range of validity of calculations [3.23] is in fact rather narrow (for comparison let us note that, e.g., corrections to thermodynamic quantities are small for $\lambda >> 6$). Therefore, when considering the case of Lorentz plasma $z >> 1$ and ignoring electron-electron collisions in this section, we will be able to do without Sonin polynomial expansion of the transport equation and expand the validity range of the approximation. For $z \sim 1$, the accuracy of the "Coulomb logarithm" obtained below will be $\sim \frac{1}{\ln\frac{1}{\lambda}}$; thus, if we use the

below Coulomb logarithm in expressions for electrical conductivity [3.1, 3.21] taken into account electron-electron collisions but calculated with accuracy $\sim \frac{1}{\ln\frac{1}{\lambda}}$, the accuracy of such electrical conductivity calculations can be estimated as $\frac{1}{z\ln\frac{1}{\lambda}} + \frac{\lambda}{\ln\frac{1}{\lambda}}$.

It is known [3.21] that electrical conductivity of the Lorentz gas is

$$\sigma = \frac{ze^2}{3T}\frac{\overline{v}}{S_{tr}}, \tag{3.3.7}$$

where v is the velocity of electrons, S_{tr} is the transport cross section of electron scattering on ions, and the bar means averaging over the electron distribution function. The problem thus reduces to calculating the transport cross section. In order to ensure the improved logarithmic accuracy of such calculations, we can use the Lenard-Balescu integral for the cross section*

$$S_{LB} = \frac{4\pi z^2 e^4}{m^2 v^4}\int\frac{dk}{k}\int dx\frac{\exp(-x^2/2)}{\sqrt{2\pi}\,|\varepsilon(k,x)|^2} \tag{3.3.8}$$

m is electron mass,

$$\varepsilon(k,x) = 1 + \frac{1}{k^2}\left(1 + \frac{x}{\sqrt{\pi}}\right)\int_{-\infty}^{\infty} dz\frac{\exp(-z^2)}{z - x - i0}$$

is dielectric permittivity, where electron screening is neglected because z >> 1. The integral (3.3.8), however, diverges at a large transfer of momentum k, because it has been derived assuming that k's are small (small scattering angles). In order to eliminate this divergence, one can subtract from the integral (3.3.8) the cross section of scattering on any static potential with Coulomb center obtained within the same assumption of small k's (Fokker-Planck cross section S_{FP}). If one then adds the cross section on this potential without the assumption about small k's that correctly accounts for close collisions, one can obtain a solution with a

*Here we will consider a quasi-classical cross section. For incomplete ionization, e.g., when $T < I < \frac{z^2e^4m}{\hbar^2}$ (I is ionization potential), the quasi-classical approximation is appropriate.

relevant accuracy. There is a known classical transport cross section for scattering on the Debye potential $\frac{ze^2}{r}\exp(-r/D)$ [3.24]

$$S = \frac{4\pi z^2 e^4}{m^2 v^4}\left(\ln\frac{mv^2}{T\lambda}\frac{2}{\gamma} - \frac{1}{2}\right) \tag{3.3.9}$$

($\lambda = 1.78\ldots$). Subtracting the Fokker-Plank integral for the Debye potential S_{FP} from (3.3.8) and integrating over x as in [3.25], one obtains

$$S_{LB} - S_{FP} = \frac{1}{2}\frac{4\pi z^2 e^4}{m^2 v^4} \ . \tag{3.3.10}$$

The transport cross section S_{tr} is a sum of (3.3.9) and (3.3.10)

$$S_{tr} = \frac{4\pi z^2 e^4}{m^2 v^4}\ln\frac{mv^2}{T\lambda}\frac{2}{\gamma} \ , \tag{3.3.11}$$

and, hence, electrical conductivity

$$\sigma = \frac{4}{\pi}\sqrt{\frac{2}{\pi}}\frac{T}{ze^2}\sqrt{\frac{T}{m}}\overline{\ln^{-1}} \ , \tag{3.3.12}$$

where

$$\overline{\ln^{-1}} = \frac{1}{6}\int_0^\infty \frac{dy\, y^3\exp(-y)}{\ln\frac{4}{\gamma}\frac{y}{\lambda}} \ . \tag{3.3.13}$$

The accuracy of expression (3.3.13) is $\sim \frac{\lambda}{\ln\frac{1}{\lambda}} + \frac{1}{z\ln\frac{1}{\lambda}}$. If we restrict ourselves to the accuracy of $\sim \frac{1}{(\ln\frac{1}{\lambda})^2} + \frac{1}{z\ln\frac{1}{\lambda}}$, expression (3.3.13) can be written in the form of a logarithm with a corrected coefficient under the logarithm sign

$$\overline{\ln^{-1}} \cong \frac{1}{\ln\frac{4\exp(11/6)}{\gamma^2\lambda}} \cong \frac{1}{\ln\frac{7{,}89}{\lambda}} \ . \tag{3.3.14}$$

Integral (3.3.13) is improper, but it is easy to understand that the way of divergence elimination with $y = \frac{\gamma\lambda}{4}$ is not important, because the region $y \sim \lambda$ contributes $\sim \lambda^4$. Therefore, one can consider this integral, for example, as a principal value. The results of integral calculations are given in Table 3.1. For comparison, this table also gives the values of logarithm (3.3.14).

Table 3.1. Comparison of two Logarithmitic Approximations.

λ	0.1	0.2	0.5	1	2	3	4	5	6
$1/\overline{\ln^{-1}}$	4.30	3.58	2.62	1.86	1.13	0.815	0.692	0.678	0.762
$\ln\frac{7.89}{\lambda}$	4.37	3.68	2.76	2.07	1.37	0.967	0.679	0.456	0.274

Table 3.1 shows that the integral (3.3.13) starts to drop at $\lambda \geq 5$, so expression (3.3.13) cannot be used in this range. Comparing (3.3.13) and (3.3.14) indicates that (3.3.14) is quite accurate.

For $z >> 1$ and not very small λ, it may turn out that ion locations strongly correlate, because the ion parameter of non-ideality equals to $z\lambda$. Since the screening radius in this case will be on the order of the distance between ions, in order to provide higher generality, one should supplement formulas (3.3.13-14) with a plasma parameter reading as

$$D = \max\left\{\sqrt{\frac{T}{4\pi n z^2 e^2}}, \frac{1}{4}\left(\frac{3}{4\pi n}\right)^{1/3}\right\} .$$

3.4. Plasma Radiation

Radiation transport and emissive processes play an important role in MAGO-MTF systems. One should account for both radiation losses in hydrogen plasma with impurities, and radiation transport in dense plasma of liners and walls. Therefore, approximate methods are required for calculations of radiation properties of hydrogen and multiply charged plasma in local thermodynamic or coronal equilibrium.

3.4.1. The Rate of Energy Exchange Between Planck Radiation and Hydrogen-Like Thermodynamic Equilibrium (LTE) Plasma

In simulations of radiation/plasma interaction, one often encounters the case, when plasma is situated in a Planck radiation field, where Planck temperature is different from that of plasma electrons. In this case, an important characteristic is the rate of energy exchange between radiation and matter. Formulas to describe energy transfer due to the Compton effect and free-free transitions in the field of nuclei are given in [3.26, 3.27].

In this section, along with free-free transitions, we will also include free- In In this section, along with free-free transitions, we will also include free-bound and discrete transitions for hydrogen-like plasma and obtain simple approximate formulas for the energy exchange rate to extend the range of applicability of the energy exchange rate formulas to the low temperature region, on the order of ionization potential or lower. In doing so, we consider plasma to be in local thermodynamic equilibrium* (LTE).

Let us consider optically thin plasma with electron temperature T; plasma interacts with black body radiation of temperature θ. Then, the rate of energy transfer from the matter to the radiation in unit volume $S(T,\theta)$ will be defined by the formulas from [3.13]

$$S(T,\theta) = \int_0^\infty d\omega\, S(\omega) \ , \tag{3.4.1}$$

$$S(\omega) = \frac{\hbar\omega^3}{\pi^2 c^2} \frac{\exp\left(-\frac{\hbar\omega}{T}\right) - \exp\left(-\frac{\hbar\omega}{\theta}\right)}{1 - \exp\left(-\frac{\hbar\omega}{\theta}\right)} \kappa_\omega(T) \ , \tag{3.4.2}$$

where $\kappa_\omega(T)$ is spectral absorption coefficient, ω is frequency.

Let us first address the bremsstrahlung mechanism of energy transfer.

---

* The formal criterion of thermodynamic equilibrium [3.28] $n_e >> \frac{m^3 e^6}{\hbar^6} \frac{e^6}{\hbar^3 c^3} Z^7$ for hydrogen plasma corresponds to $n_e >> 3 \cdot 10^{18}$ cm^{-3} , but this criterion applies only to the equilibrium of levels n = 1, 2. If the whole spectrum of levels will be taken into account, the actual range of applicability of the formulas below will be wider.

In the quasi-classical approximation, when T, $\theta << I$ ($I = 13.6\ Z^2$ eV is ionization potential of the hydrogen-like ion with charge Z), the bremsstrahlung absorption coefficient reads as (Kramers formula)

$$\kappa_\omega^K = \frac{16\pi^2}{3}\left(\frac{2\pi}{3mT}\right)^{1/2}\frac{Z^2e^6}{\hbar cm\omega^3}n_Z n_e \qquad (3.4.3)$$

(n_Z is density of ions with charge Z, n_e is electron density, m is electron mass). By substituting (3.4.3) into (3.4.1–2), we obtain

$$S_K = J_K(T)\phi_K\left(\frac{\theta}{T}\right), \qquad (3.4.4)$$

where J_K (T) is intensity of classical bremsstrahlung

$$J_K(T) = \frac{16}{3}\left(\frac{2\pi T}{3m}\right)^{1/2}\frac{Z^2e^6}{mc^3\hbar}n_Z n_e, \qquad (3.4.5)$$

$$\phi_K(x) = x\int_0^\infty dt\,\frac{\exp(-xt)-\exp(-t)}{1-\exp(-t)} = -x[\ln\gamma + \psi(x)], \qquad (3.4.6)$$

($\ln\lambda = 0.577\ldots$, and $\psi(x)$ is logarithmic derivative of the Γ-function, $\psi(x) = \Gamma'(x)/\Gamma(x)$). An interpolation formula for $\varphi_K(x)$ with correct behavior at 0, 1 and ∞ can be written as

$$\phi_K = 1 - x\ln\left(x + \frac{12-\pi^2}{\pi^2-6}\right) + x\left(\ln\frac{6}{\pi^2-6} - 1\right). \qquad (3.4.7)$$

In the Born approximation, when T or $\theta >> I$, the absorption factor becomes accompanied with the Gaunt factor

$$g\left(\frac{\hbar\omega}{T}\right) = \frac{\sqrt{3}}{\pi}\exp\left(\frac{\hbar\omega}{2T}\right)K_0\left(\frac{\hbar\omega}{2T}\right)$$

($K_0(x)$ is Macdonald function), and then, in accordance with [3.26] we obtain for bremsstrahlung energy transfer

$$S_B = J_K(T)\phi_B\left(\frac{\theta}{T}\right), \qquad (3.4.8)$$

$$\phi_B(x) = \int_0^\infty dt\, g(t) \frac{\exp(-t) - \exp(-t/x)}{1 - \exp(-t/x)} \ . \qquad (3.4.9)$$

The interpolation formula to describe $\varphi_B(x)$ to within better than 0.5 % can be expressed as follows:

$$\varphi_B(x) = \frac{2\sqrt{3}}{\pi}\left(1 - \frac{4.52x^2}{1 + 1.69\sqrt{x} + 1.83x}\right). \qquad (3.4.10)$$

Let us note that functions $\varphi_K(x)$ and $\varphi_B(x)$ in a wide range of x are close to each other and differ significantly only when $x >> 1$.

Let us now proceed to considering recombination radiation and lines.

As we assume plasma to be in thermodynamic equilibrium, concentrations of ions and electrons will meet the Saha equation

$$n_{Z-1} = n_Z n_e \left(\frac{2\pi\hbar^2}{mT}\right)^{3/2} \exp\left(\frac{I}{T}\right) \ . \qquad (3.4.11)$$

For $Z \neq 1$, let us assume $n_{Z-1} << n_Z$ to be able to include only hydrogen-like energy levels and ignore radiation absorption on ions with a charge less than Z-1. For Z=1 (hydrogen plasma), the degree of ionization can be arbitrary.

For approximate radiation/matter interaction description, the discrete spectrum of levels starting from some negative energy E_0 can be replaced by a continuous one, and other levels can be accounted for explicitly. We will include explicitly two lower levels n = 1, 2, and all the spectrum from $E_0 = -\frac{I}{2.5^2} = -0.16\,I$ will be considered continuous. This will allow us to obtain an approximate expression for $S(T,\theta)$ for any ratios between T, θ, I using semi-classical Kramers formulas.

As a result of such lowering of the "continuous" spectrum bound, the density of free electrons near the nucleus and, consequently, the intensity of free-free transitions will grow a factor of $\exp(-E_0 / T)$. As we use a semi-classical description, the contribution of free-free transitions to the rate of radiation/matter energy exchange will be given by

$$S_{ff} = J_K(T)\phi_K\left(\frac{\theta}{T}\right)\exp(-E_0/T) \ . \qquad (3.4.12)$$

Similarly to (3.4.12), using the Saha equation (3.4.11), we obtain the intensity of "bound-free" transitions from levels $n = 1, 2$

$$S_{fb} = J_K(T)\frac{2I\theta}{T^2}\left[\exp\left(\frac{I}{T}\right)\int\limits_{\frac{I+E_0}{\theta}}^{\infty} dt\,\frac{\exp\left(-\frac{\theta t}{T}\right)-\exp(-t)}{1-\exp(-t)}+\right.$$

$$\left.+\frac{1}{8}\exp\left(\frac{I}{4T}\right)\int\limits_{\frac{I/4+E_0}{\theta}}^{\infty} dt\,\frac{\exp\left(-\frac{\theta t}{T}\right)-\exp(-t)}{1-\exp(-t)}\right]. \qquad (3.4.13)$$

Finally, the contribution of discrete transitions that will be represented here only by the line L_a can be written as

$$S_{bb} = J_K(T)\frac{1}{2}\left(\frac{I}{T}\right)^2\exp\left(\frac{I}{T}\right)\frac{\exp\left(-\frac{3I}{4T}\right)-\exp\left(-\frac{3I}{4\theta}\right)}{1-\exp\left(-\frac{3I}{4\theta}\right)}\,. \qquad (3.4.14)$$

One can obtain an approximate formula for integrals (3.4.13) that describes the range of $T \sim \theta \geq I$ to within about 20 % and yields correct asymptotic forms in other ranges

$$S_{fb} = J_K(T)\frac{2I\theta}{T^2}\left[\frac{9}{8}\exp\left(-\frac{E_0}{T}\right)\left(\frac{T}{\theta}-1\right)+\exp\left(\frac{I}{T}\right)\ln\frac{1-\exp\left(-\frac{I+E_0}{\theta}\right)}{1-\exp\left(-\frac{I+E_0}{T}\right)}+\right.$$

$$\left.+\frac{1}{8}\exp\left(\frac{I}{4T}\right)\ln\frac{1-\exp\left(-\frac{0.25I+E_0}{\theta}\right)}{1-\exp\left(-\frac{0.25I+E_0}{T}\right)}\right]. \qquad (3.4.15)$$

To improve the accuracy of the contribution of discrete transitions, one can use an exact value of oscillator strength; the factor of 0.5 in expression (3.4.14) will then be replaced by 0.358.

Note that free-free transitions have a considerable contribution into S only when $T \geq I$. Consequently to increase the accuracy, for φ in (3.4.12) one can use formula (3.4.10) instead of (3.4.7).

Finally, summing (3.4.12), (3.4.14) and (3.4.15) with the above changes, we obtain

$$S = J_K(T)\left\{ \phi_B\left(\frac{\theta}{T}\right)\exp(-E_0/T) + \right.$$

$$+\frac{2I\theta}{T^2}\left[\frac{9}{8}\exp\left(-\frac{E_0}{T}\right)\left(\frac{T}{\theta}-1\right)+\exp\left(\frac{I}{T}\right)\ln\frac{1-\exp\left(-\frac{I+E_0}{\theta}\right)}{1-\exp\left(-\frac{I+E_0}{T}\right)}+\right.$$

$$\left.+\frac{1}{8}\exp\left(\frac{I}{4T}\right)\ln\frac{1-\exp\left(-\frac{0.25I+E_0}{\theta}\right)}{1-\exp\left(\frac{0.25I+E_0}{T}\right)}\right]+$$

$$\left.+0.358\left(\frac{I}{T}\right)^2\exp\left(\frac{I}{T}\right)\frac{\exp\left(-\frac{3I}{4T}\right)-\exp\left(-\frac{3I}{4\theta}\right)}{1-\exp\left(-\frac{3I}{4\theta}\right)}\right\}. \qquad (3.4.16)$$

For $\theta = 0$, formula (3.4.16) reduces to a formula for radiation intensity of optically thin plasma,

$$S = J_K(T)\left[\left(1.10+\frac{9I}{4T}\right)\exp\left(\frac{0.16I}{T}\right)+0.358\left(\frac{I}{T}\right)^2\exp\left(\frac{I}{4T}\right)\right]. \qquad (3.4.17)$$

In order to evaluate the accuracy of the formulas, radiation intensity calculated using formula (3.4.17) with interpolations was compared with calculations without such interpolations. The maximum difference of 15% was observed at $T \approx 8I$. The maximum error of formula (3.4.16) can be expected to be approximately the same.

For T >> *I*, the primary role in formula (3.4.16) is played by the first term, and the formula reduces to (3.4.8)*. The terms in formula (3.4.16) that do not appear in (3.4.8) are particularly important in the range of $T \le I$. Fig. 3.1 shows an illustrative dependence of the expression in braces in (3.4.16) (and isolated summands "*ff*", "*fb*", "*bb*") on radiation temperature θ for $T = 0.5I$. Fig. 3.1 shows that throughout the range of temperatures θ, the primary role in this case is played by summand (3.4.15) ("*fb*"). At small θ it follows from (3.4.17) that the role of summand "*bb*" grows as temperature T decreases, whereas the major contribution to $S(T,\theta)$ at $\theta >> I >> T$ will still be made by summand (3.4.15), which yields in this limiting case

$$S(T,\theta) = -J_K(T)\frac{2I\theta}{T^2}\exp\left(\frac{I}{T}\right)\ln\frac{\theta}{I+E_0} \quad . \qquad (3.4.18)$$

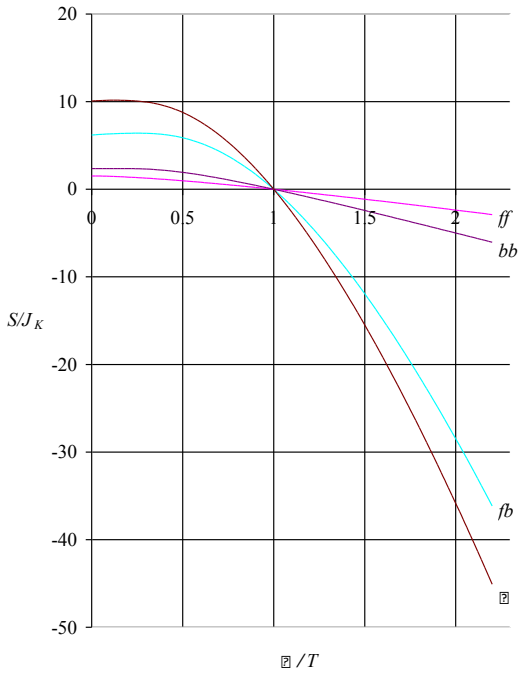

Fig. 3.1. Radiation/matter energy exchange rate (including free-free "ff", free-bound "fb" and bound-bound "bb" transitions) as a function of radiation temperature θ for T = 0.5I.

* Note that formula (3.4.16) cannot be used to determine corrections to the Bremsstrahlung formula (3.4.8) at $T >> I$ because of the introduced interpolations.

3.4.2. Recombination Radiation and Bremsstrahlung of Multiply Ionized Plasma

For multiply charged ions in plasma, along with free-free transitions (bremsstrahlung), one should also take into account free-bound (recombination radiation) and bound-bound (line radiation) transitions. As for recombination radiation and bremsstrahlung, when for ions with charge z in plasma the number of electrons of the ion is large enough $N >> 1$, but is small compared to the charge of the nucleus Z, i.e., $1 << N = Z - z << Z$, it is possible to obtain rather simple formulas to describe this radiation. In this case, one can consider the potential, where bound electrons are moving, to be Coulomb potential, and use formulas obtained for the Coulomb problem.

Let us find the intensity of recombination radiation: radiation generated in plasma when a free electron is captured by an ion with photon emission. If the initial velocity of the electron is $v = p$, and it is captured to the level with the principal quantum number n, energy of the photon emitted in this case will be given by (here and in Section 3.4 below we will use atomic units $e = m = \hbar = 1$)

$$\omega = E + \left|E_n\right| = \frac{p^2}{2} + \frac{Z^2}{2n^2} \ .$$

In the quasi-classical approximation, when $n \sim N^{1/3} >> 1$, it follows from this formula that emission of photons in a small range of frequencies $d\omega$ corresponds to electron capture to a small range of levels

$$dn = -\frac{n^3}{Z^2} d\omega \ .$$

Energy emitted per unit volume of plasma per unit time in the small range of frequencies (energies) $d\omega$ is equal to

$$dI_\omega^{(R)} = -n_e n_Z \omega \, dn \int v \sigma_n f\left(E\right) d\vec{v} = n_e n_Z \omega \frac{n^3}{Z^2} d\omega \int v^2 \sigma_n f\left(E\right) dE \, d\Omega_{\vec{v}} \ , \quad (3.4.19)$$

where n_e and n_z are concentrations of free electrons and positive ions with nuclear charge Z, σ_n is an effective cross-section of free electron capture to the level n equal to [3.13]

$$\sigma_n = \frac{16\pi}{3\sqrt{3}} \frac{Z^4}{c^3 v^2 \omega} \frac{1}{n^3} \ ,$$

$f(E)$is the distribution function of free electrons in plasma with temperature T of the form

$$f\left(E\right)=\left(2\pi T\right)^{-\frac{3}{2}}e^{-\frac{E}{T}}, \tag{3.4.20}$$

and $d\Omega_{\vec{\nu}}$ is the elementary solid angle of the emitted photon. The maximum electron energy that can contribute to recombination radiation of frequency ω is equal to the photon energy of this frequency $E_{\max} = \omega$, and the minimum energy is

$$E_{\min}=\begin{cases}0 & for\ \omega<I,\\ \omega-I & for\ \omega>I.\end{cases}$$

Integration of expression (3.4.19) in the given range accounting for the isotropic character of electron distribution yields

$$dI_{\omega}^{(R)}=n_e n_Z\frac{16Z^2}{3c^3}\sqrt{\frac{2\pi}{3T}}\left(e^{-\frac{\max\left(0,\omega-I\right)}{T}}-e^{-\frac{\omega}{T}}\right)d\omega\,. \tag{3.4.21}$$

The intensity of bremsstrahlung is found using the formula [3.13]

$$dI_{\omega}^{(B)}=n_e n_Z\frac{16Z^2}{3c^3}\sqrt{\frac{2\pi}{3T}}e^{-\frac{\omega}{T}}d\omega\,. \tag{3.4.22}$$

Summing expressions (3.4.21) and (3.4.22) we obtain the total intensity of recombination radiation and bremsstrahlung:

$$dI_{\omega}^{(BR)}=n_e n_Z\frac{16Z^2}{3c^3}\sqrt{\frac{2\pi}{3T}}e^{-\frac{\max\left(0,\omega-I\right)}{T}}d\omega\,.$$

For $\omega < I$, $\dfrac{dI_{\omega}^{(BR)}}{d\omega}$ is constant, and for $\omega > I$ it exponentially decays with frequency. The total intensity of continuous (bremsstrahlung plus recombination radiation) equals

$$I^{(BR)}=\frac{16\sqrt{2\pi}}{3\sqrt{3}c^3}Z^2\sqrt{T}\left(1+I/T\right). \tag{3.4.23}$$

3.4.3. Line Radiation of Multiply Ionized LTE Plasma

Bound-bound transitions (line radiation) often play a decisive role in transport problems. In particular, they have the major contribution to radiation losses of low temperature plasma ($T < Z^2$).

It is particularly difficult to account for bound-bound transitions, because this requires incorporating ion distribution by ionization degree and numerous transitions between complex quantum states of ions with a large number of electrons. Such a program is conducted in quantum-statistics models [3.29]. Simulations of radiation properties of materials using such programs are rather complicated and are not easily accessible. It would be desirable to have simple formulas providing a correct description of physics in some ranges of plasma parameters and giving satisfactory results in these ranges. In particular, such a necessity exists in calculations of radiation of dense multiply charged plasma, which is typical of compressed MAGO-MTF target shells, where plasma can be in the state of local thermodynamic equilibrium LTE.

A noticeable simplification of the problem can be attributed to the fact that characteristic electron energy levels for multiply charged ions have large quantum numbers. The motion of electrons occupying these levels is quasi-classical. Therefore, radiation of the ions can be calculated in the quasi-classical limit. In addition to this simplification we consider the case of high temperatures, when the potential, in which electrons are moving, can be considered Coulomb potential. This problem was solved in [3.30].

For the potential, in which electrons are moving, to be treated as Coulomb potential, should either the number of electrons in the ion N be small compared to the nuclear charge $N << Z$, or $T >> Z$, because – as one can show – the major contribution in this case will be made by electrons flying near the nucleus, which are deflected by the field that can be considered Coulomb field. Since the frequency of electron orbiting in the Coulomb field is $\omega_n = \frac{Z^2}{n^3}$ [3.31, 3.32], where n is the principal quantum number, and $N \sim n^3$, both conditions can be written as $\max(T, \omega_n) >> Z$. As discussed, we consider the range of validity of the quasi-classical approach $\max(T, \omega_n) << Z^2$, in which the role of line spectrum in radiation is particularly important.

The intensity of radiation of the k-th harmonic of electrons moving in the Coulomb field with a negative energy E, is [3.31]

$$I_k = \frac{64k^2E^4}{3c^3Z^2}\left[J_k'^2(k\varepsilon) + \frac{1-\varepsilon^2}{\varepsilon^2}J_k^2(k\varepsilon)\right], \qquad (3.4.24)$$

where ε is eccentricity of the elliptical motion of an electron.

To obtain the average intensity of radiation $\bar{I}_k$ of electrons in the electron shell with the energy E, the expression (3.4.24) should be averaged over the values of electron orbital momenta keeping in mind that the number of electrons with given angular momentum l is proportional to l, i.e., (3.4.24) should be integrated over $d\varepsilon^2$ (within the limits from zero to unity). Taking the integral as indicated in [3.31], we obtain

$$\bar{I}_k = \frac{128kE^4}{3c^3Z^2} J_k(k) J_k'(k) \ . \qquad (3.4.25)$$

The quantity

$$\xi_k \equiv \pi\sqrt{3}kJ_k(k)J_k'(k) \qquad (3.4.26)$$

for large k has an asymptotic form of

$$\xi_k \cong 1 - \frac{\Gamma(1/3)}{5\cdot 6^{1/3}\Gamma(2/3)} \frac{1}{k^{2/3}} \approx 1 - \frac{0{,}21775}{k^{2/3}} \ ,$$

which also provides a good description of these quantity values for moderate values of k.

Since the major contribution into emission of ions is made by electron shells with energies close to the ionization potential, one can ignore the dependence of the frequency ω_n on n, taking its frequency $\omega_n = \omega_I$ at the energy level equal to the ionization potential I determined by the Saha equation for multiple ionization [3.13]

$$I = T \ln \frac{2}{n_e} \left(\frac{T}{2\pi} \right)^{3/2} , \qquad (3.4.27)$$

where n_e is electron density. Then, intensity of radiation of the k-th harmonic from all electron shells will be equal to

$$J_k = \sum_n 2n^2 \bar{I}_k f(E_n)[1 - f(E_n - k\omega_I)] \ . \qquad (3.4.28)$$

Here, $2n^2$ is the number of electrons on the n-th shell,

$$f(E_n) = \frac{1}{\exp\left(\frac{E_n - \mu}{T} \right) + 1}$$

is Fermi-Dirac electron distribution function corresponding to the occupancy of the n-th level, and the factor $1 - f(E_n - k\omega_I)$ accounts for the occupied energy levels.

As we assume that $T << Z^2$, the factor $2n^2 I_k$ in formula (3.4.28), weakly depends on n compared to the product $f(E_n)[1 - f(E_n - k\omega_I)]$, and we can withdraw it from under the sum sign, taking its value at the energy level equal to the ionization potential (3.4.27).

The sum

$$S_k = \sum_n f(E_n)[1 - f(E_n - k\omega_I)] \qquad (3.4.29)$$

is calculated as follows. Let us designate $\eta = \exp\left(\frac{E_0 - \mu}{T}\right)$, where E_0 is some energy level close to the ionization potential. Then, $E_n = E_0 + n\omega_I$ and

$$S_k = \sum_n \frac{\eta \exp[\omega_I (n-k)/T]}{[\eta \exp(\omega_I n/T)+1]\{\eta \exp[\omega_I (n-k)/T]+1\}} .$$

Note that

$$S_k = \exp(-\omega_I k/T) \sum_n [1 - f(E_n)] f(E_n - k\omega_I) . \qquad (3.4.30)$$

Then, multiplying (3.4.30) by $\exp(kw_I / T)$ and subtracting (3.4.29) from it, we obtain

$$[\exp(k\omega_I / T) - 1] S_k = \sum_n [f(E_n - k\omega_I) - f(E_n)] =$$

$$= \sum_{n=-\infty}^{\infty} \left[\frac{1}{\eta \exp[\omega_I (n-k)/T]+1} - \frac{1}{\eta \exp(\omega_I n/T)+1} \right] . \qquad (3.4.31)$$

The right-hand sum of (3.4.31) is easy to calculate, if we notice that the contributions to it from the first and the second term are canceled out in the n-th and $(n-k)$-th sum elements. The sum becomes finite and equal to

$$\lim_{n \to -\infty} \sum_{l=n}^{n+k-1} \frac{1}{\eta \exp(\omega_I l/T)+1} = k .$$

As a result,

$$S_k = \frac{k}{\exp(k\hbar\omega_I / T) - 1}. \qquad (3.4.32)$$

Substitution of (3.4.32) into intensity (3.4.28) gives spectral radiation intensity per ion

$$J_k = \frac{16}{3\sqrt{3}\pi}\frac{Z^2}{c^3}\omega_I^2\xi_k\frac{k}{\exp\left(\frac{k\omega_I}{T}\right) - 1}. \qquad (3.4.33)$$

For $\omega_I << T$, the discrete spectrum in the formula (3.4.33) can be replaced with the continuous spectrum $\omega = k\omega_I$ and (3.4.33) converts to the formula of Ref. [3.33]

$$J_\omega = \frac{16}{3\sqrt{3}\pi}\frac{Z^2}{c^3}\frac{\omega}{\exp\left(\frac{\omega}{T}\right) - 1},$$

derived assuming that intervals between levels ω_n are small compared to the temperature T, which is valid for very dense plasma.

The total radiation intensity is equal to

$$J = \sum_k J_k = \frac{8\pi}{9\sqrt{3}}\frac{Z^2}{c^3}T^2F(\omega_I / T), \qquad (3.4.34)$$

where

$$F(x) = \frac{6x^2}{\pi^2}\sum_{k=1}^{\infty}\frac{k\xi_k}{\exp(kx) - 1}, \qquad (3.4.35)$$

and ξ_k is defined as (3.4.26). The plot of $F(x)$ is shown in Fig. 3.2. At $x = 0$, we have $F = 1$ and formula (3.4.34) transforms into the formula of Ref. [3.33] in the limit of high densities, when radiation intensity per ion does not depend on the density and is proportional to the square of temperature; i.e., in the limit of high densities, the plasma radiation is the radiation of a population of ions, each of which is heated to temperature T. For large values of x (low densities), radiation intensity is determined only by one harmonic (3.4.33).

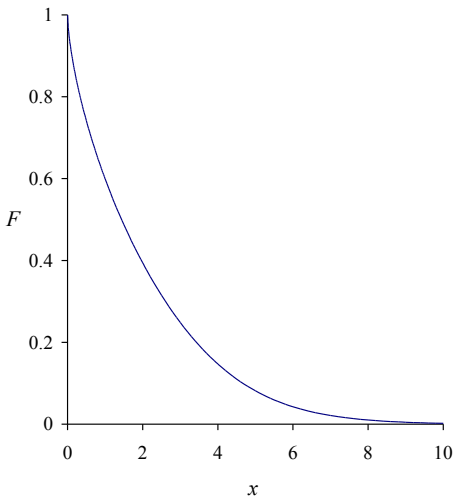

Fig. 3.2. Function F(x) defined by formulas (3.4.35), (3.4.26).

The accuracy of formulas (3.4.33–34) for the case $T < \omega_I$ can be estimated as $\mathrm{O}\left(\frac{N}{Z}+\frac{1}{N^{2/3}}\right)$, where the first term is associated with the assumption of the potential being close to the Coulomb potential, and the second term is related to the quasi-classical approximation. Such accuracy is not very high, and because of real numerical factors, formulas (3.4.33-34) can be expected to describe ion radiation with an error of several times. Nevertheless, it makes sense to use these formulas in problems where this accuracy is sufficient and it is not necessary to use complex calculations [3.29] providing accuracy on the order of $\mathrm{O}\left(\frac{N}{Z}\right)$ (the error is attributed to the fact that the approach of Ref. [3.29] does not include polarization effects* [3.34–3.35]).

Let us compare results of plasma radiation calculations using formulas (3.4.33–34) with an example of calculations for gold given in Ref. [3.29]. In accordance with [3.29], Planck-averaged absorption coefficients κ_P that are related to radiation intensity J as

$$\kappa_P = \frac{n_Z}{4\sigma T^4 \rho} J \ \ (\mathrm{cm}^2/\mathrm{g}) \qquad (3.4.36)$$

*Indeed, since electron density in an atom is on the order of Z^3 / N, the square of the plasma frequency for the electron gas within the atom will be on the order of $\omega_{pe}^2 \sim Z^3 / N$. One can expect that the neglect of polarization effects leads to an error estimated as the ratio of the square of the plasma frequency to the square of the characteristic frequency $\omega \sim Z^2 N$, i.e. on the order of N / Z.

(σ is the Stefan-Boltzmann constant, ρ is the density of matter in g/cm^3, and n_z is the ion density), are κ_P = 150 cm^2/g and κ_P = 440 cm^2/g for T = 1 keV and densities ρ = 0.1 and 1 g/cm^3, respectively. Judging from the spectra presented in the graphs, most of emitted energy is contained in lines of energy 3, 11, and 12 keV. Calculations by formula (3.4.27) using the ionization potentials of Ref. [3.36] yield I = 9.12 keV and average degree of ionization z = 69.6 for ρ = 0.1 g/cm^3. If we define the principal quantum number n at an energy level corresponding to the ionization potential from relationship

$$I = \frac{z^2}{2n^2} \ ,$$

then energy ω_I can be considered equal to $\omega_I = 2I / n$, which for ρ = 0.1 g/cm^3 gives n = 2.69, and ω_I = 6.8 keV. In this case, F = 0.0248 and calculations using formulas (3.4.34–3.4.36) give κ_P = 180 cm^2/g (somewhat better agreement with the results of [3.29] will be obtained if Z in formula (3.4.34) is replaced with z yielding κ_P = 140 cm^2/g). According to (3.4.33), 99.7% of all emitted energy is contained in line ω_I= 6.8 keV. Similarly, for ρ = 1 g/cm^3, we obtain n = 2.9, ω_I = 4.8 keV, F = 0.0949 and κ_P = 670 cm^2/g (subject to z being used instead of Z in formula (3.4.34) κ_P = 440 cm^2/g). Line ω_I = 4.8 keV contains 98 % of all emitted energy. Thus, for the given plasma parameters, Planck absorption coefficients differ from calculations [3.29] by not more than the factor of 1.5 and provide reasonable information on the spectrum (emitted lines are some average representatives of the lines emitted in calculations [3.29]), which is quite acceptable for such an approximate approach.

For rather low plasma densities and small optical thicknesses, when radiation is not in equilibrium with matter, the plasma radiation is described by the coronal approximation (see below). A question arises, for what densities should we use formulas (3.4.33–34), and when should we use formulas and tables of the coronal approximation? A rough approach to answering this question can be formulated as follows: one should use the approximation that gives the smallest radiation intensity. For example, as shown by the above Planck absorption coefficients for gold plasma at T=1 keV, radiation intensity in the region of ρ = 0.1 g/cm^3 turns out approximately 500 times smaller than the value in coronal radiation tables [3.37]. Thus, formulas (3.4.33–34) should provide reasonable results for these plasma parameters.

3.4.4. Coronal Model Line Radiations of Multiply Charged Impurities in Plasma. Statistic Approach

Line radiation of impurities of heavy elements can result in considerable cooling of hydrogen plasma in MAGO/MTF systems; it is therefore essential to know the intensity of their radiation. In addition, one should be able to calculate the emitted spectra predict plasma properties based on the measurements of such spectra. Low-density plasma, which does not stay in the outer radiation fluxes and which is transparent to intrinsic radiation, is typically in the state of "coronal equilibrium," when the rate of electron collisional ionization is counterbalanced by the rate of recombination, which for partly ionized ions is mostly dielectronic. An absence of equilibrium radiation and transitions induced by it leads to the deviation of a level population distribution from thermodynamic one. In the coronal limit we can assume that ions in the exited states are not present, since in a low-density plasma with low collisions frequency, radiation transitions (or Auger processes) are much more probable for the exited states than collisions with free electrons, the ions finally decay to the ground state due to these transitions.

In order to describe radiation properties of coronal plasma, one should consider kinetics of interactions between free electrons and ions with different charges and different configurations, accounting for different transitions between levels and changes in the occupancy of states during such transitions. This problem is rather complicated, and requires that a large number of ion states and transitions between them be taken into account for multiply charged plasma (Z, $N >> 1$, Z is nuclear charge, N is number of electrons in the ion) (see e.g. [3.37-3.40]). However, one can apply the statistical model of the atom for many-electron ions, and use a small parameter present there – the inverse value of the quantum number - for description of kinetics and the model of electron gas based on this parameter using—for description of electrons in the ion. This approach was proposed in Ref. [3.40], where it yielded ionization and recombination rates and ionization balance in plasma with any many-electron ions given that $Z >> N >> 1$.

In the statistical model of the atom, electrons move in a self-consistent field determined by the Coulomb field of the nucleus and the bulk charge of the whole set of electrons. The relative quantity of pair (correlation) interactions compared to the self-consistent field is estimates as [3.40]

$$(U_{ee} / \varepsilon)^2 \sim N^{2/3} / Z^2 .$$

For heavy ions, $Z >> 1$, this parameter is rather small, and one can therefore consider individual movements of electrons or holes (states unoccupied by electrons). Thus, one can ask a question about the number of electrons and holes formed per unit time as a result of collisions of free electrons in plasma with bound ones, and about the probability of radiation relaxation of excited electrons and lifetime of holes with respect to their filling with electrons from higher shells. These holes can be filled as a result of radiation transitions of electrons from higher levels (making a contribution to line radiation, which in this case is usually called characteristic radiation) and as a result of released energy transfer to the electron from a higher shell and transition of this electron to the continuous spectrum (the process that determines the Auger widths of X-ray terms [3.32]).

When considering characteristic radiation, one should take into account that for a deep hole the probability of the Auger effect that does not result in photon emission is dominating. If we consider complex ions with a large number of electrons $N >> 1$, motion of electrons can be described in the quasi-classical framework, because characteristic quantum numbers $n \sim N^{1/3}$ are large in this case. In this approximation, hole formation and the Auger effect can be represented as the outcome of pair collisions of electrons, and electrons in the atom can be represented as electron gas. Considering these processes, we will address separately the high-frequency part of characteristic radiation $h\omega > I$, where I is ionization potential, because only characteristic radiation contributes to this part of the line spectrum.

Collisions of electrons should be treated in the Born approximation [3.32], because in the range of temperatures and bound electron energies of interest $T, \varepsilon >> 1$, $1 / v << 1$ (v is relative velocity of electrons). For collisions of identical particles (electrons), scattering cross section is given as [3.32]

$$d\sigma = \frac{1}{v^4}\left(\frac{1}{\sin^4\frac{\chi}{2}} - \frac{1}{2\sin^2\frac{\chi}{2}\cos^2\frac{\chi}{2}}\right)do, \qquad (3.4.37)$$

where χ is scattering angle, o is solid angle.

In this case, relative accuracy of the approach in question can be estimated as accuracy of the quasi-classical approach, in which the spectrum of levels is considered continuous and the distance between levels Z^2 / n^3 is ignored compared to energy levels Z^2 / n^2, i.e. $\sim 1 / n \sim N^{-1/3}$. Note that radiation spectra obtained within the proposed approach prove to be continuous due to the quasi-classical approximation we use, i.e., it is suggested that the

number of emitted lines is large enough, and the spectrum yields a pattern averaged over a large number of lines.

In addition to the high-frequency part of characteristic radiation, we will also consider collision of free electrons with a multiply charged ion, which results in ion excitation and subsequent radiation relaxation contributing to the low-frequency part of the line spectrum ($\omega < I$). The channel considered should make the major contribution to the total radiation intensity and agree in the order of magnitude with radiation intensity calculations using the multi-level coronal model. One can expect that the calculated line radiation spectra in this case will correctly reproduce dependencies on the problem's basic parameters (they depend on the quasi-classical parameter of the problem determined by the principal quantum number n of electrons at the level of ionization potential of ions being considered and ratio I / T).

The resulting spectra of coronal plasma will be used in our analysis of data obtained in one of the MAGO experiments.

Now, let us start by finding the intensity of high-frequency radiation produced when a free electron kicks out a bound one from a deep level of the atom. The resulting hole in the deep level is occupied by an electron either as a result of the Auger effect, or as a result of photon emission by an electron from the higher level and transition of this electron to the hole location; thus, the intensity of characteristic radiation will be determined by the competition of two processes: Auger effect and radiation hole filling. Therefore, before we consider characteristic radiation intensity, we should find the probability of the Auger effect.

To find this probability, let us consider a potential well of depth U occupied by electrons up to the level—I (ionization potential). Let there be a hole formed in the level—ε as a result of collisional ionization. After the collision of two electrons from the potential well with energies ε_1 and ε_2, as a result of the Auger effect, the hole is occupied by one electron, whereas the other transits into the continuous spectrum (Fig. 3.3). Fig. 3.3 shows that the Auger effect is possible only if the hole energy is $\varepsilon > 2I$.

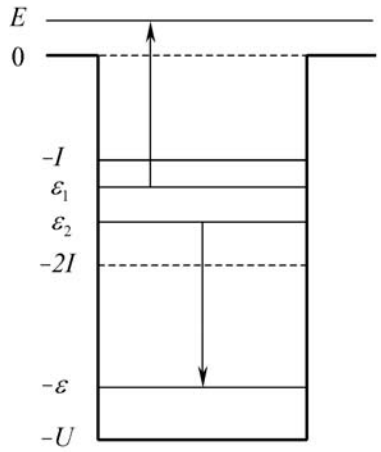

Fig. 3.3. Transitions between levels for the Auger effect.

The rate of hole filling (Auger width) is obtained from the kinetic equation [3.21]:

$$\dot{w} = \frac{1}{2}(2\pi)^3 \frac{df_2}{dt} = \frac{1}{2}(2\pi)^3 \int v\, d\sigma\, f_2 f_1\, d^3 p_1' . \qquad (3.4.38)$$

Here, p_1' is the momentum of the outgoing electron, f_1 and f_2 are equilibrium functions of electron distribution in the well, accounting that there may be two electrons in each cell of the phase space:

$$f_1 = f_2 = \frac{1}{4\pi^3} . \qquad (3.4.39)$$

For the ion, the role of potential well depth at this radius is played by potential energy $U(r)$, which in the case of interest, $N << Z$ can be treated as Coulomb energy. To find the Auger width in this case, one should take the integrals in expression (3.4.38) and average it over the trajectory of hole motion. The calculations yield:

$$\langle \dot{w} \rangle = \frac{2}{\pi}\left(\frac{(q-2)(q-3)(2q-1)}{3(q-1)^2} + \left(1 + \ln\frac{q}{q-1}\right)\ln(q-1) - \frac{\pi^2}{12} - \mathrm{dilog}\left(\frac{q}{q-1}\right)\right), \qquad (3.4.40)$$

where $q = \varepsilon / I$,

$$\mathrm{dilog}(x) = \int_1^x \frac{\ln(t)}{1-t} dt .$$

Close to the Auger effect threshold, the Auger width grows with q quadratically, and for $q >> 1$, it grows linearly.

Let us now find the intensity of high-frequency radiation produced after the kick-out of a bound deep-level electron by a free electron. When a hole forms at the deep level, e > 2I, with dominating probability, it will be occupied as a result of the Auger effect, rather than due to photon emission by the electron from the higher level and transition of this electron to the hole location. Therefore, the total rate of hole filling can be considered equal to $\langle \dot{w} \rangle$, and spectral intensity of radiation from unit volume will be

$$dI_\omega^{(Ch)} = n_Z \omega \int \frac{dW_\omega}{\langle \dot{w} \rangle} \frac{d\dot{N}_h}{dM\, d\varepsilon} dM\, d\varepsilon , \qquad (3.4.41)$$

where dW_ω is the probability of photon emission of energy ω in the range $d\omega$, $\frac{d\dot{N}_h}{dM\, d\varepsilon}$ is the number of holes of energy $-\varepsilon$ and angular momentum M that form in the ion per unit time.

Since high-frequency photons $\omega \sim \varepsilon$ correspond to high harmonics and are emitted by holes with small angular momenta [3.31], probability dW_ω can be found using an asymptotic formula of Ref. [3.31] for the intensity of very high harmonics for moving along a nearly parabolic orbit.

The number of holes with energy module ε and the small angular momentum M, locating at the radius r_2, that form in the ion per unit time will be determined by the number of collisions of free electrons with bound ones [3.21]

$$\frac{d\dot{N}_h}{dM d\varepsilon dr_2} = n_e \frac{M}{p_2^2 r_2^2} \int v\, d\sigma\, f_1 f_2 p_2 r_2^2 d^3 p_1 d\Omega_{\vec{p}_2} d\Omega_{\vec{r}_2} ,$$

where f_1 is the free electron distribution function (3.4.20), f_2 is the distribution function of electrons in the ion (3.4.39), p_1 and p_2 are free and bound electron momenta.

Radiation intensity is found after substituting expressions for the hole generation rate, photon emission probability dW_ω, and the Auger effect probability (3.4.40) into the general formula (3.4.41). Integration over angular momenta and hole energies gives

$$dI_\omega^{(Ch)} = d\omega \frac{8\sqrt{2\pi}}{9\sqrt{3}} \frac{n_e n_Z Z^2}{c^3\sqrt{T}} \times$$

$$\times \int_{\xi+s}^{\infty} \frac{e^s \left(4y \left(\frac{e^{s-y}}{(y-s)^2} - \frac{e^{s-y}}{y-s} - Ei(s-y) \right) + 6\left(\frac{e^{s-y}}{y-s} + Ei(s-y) \right) \right) - 3e^y \left(Ei(s-y) \right)^2}{\frac{(y-2s)(y-3s)(2y-s)}{3s(y-s)^2} + \left(1 + \ln\frac{y}{y-s}\right) \ln\left(\frac{y}{s} - 1\right) - \frac{\pi^2}{12} - \mathrm{dilog}\left(\frac{y}{y-s}\right)} dy. \qquad (3.4.42)$$

Here, we introduce designations $y = \varepsilon / T$, $s = I / T$, $\xi = \omega / T$.

On approach to the Auger effect threshold $\varepsilon = 2I$, intensity (3.4.42) is proportional to $(\omega - I)^{-1}$. Thus, (3.4.42) defines $dI_\omega^{(Ch)}$ for frequencies $\omega > I$, at which the probability of the Auger effect exceeds the probability of radiative relaxation. At higher frequencies $\omega >> T$, $dI_\omega^{(Ch)}$ decreases in accordance with

$$\frac{dI_\omega^{(Ch)}}{d\omega} = \frac{44\sqrt{2\pi}}{3\sqrt{3}} \frac{n_e n_Z Z^2}{c^3\sqrt{T}} \frac{s}{\xi^3} e^{s-\xi}.$$

As a result of the presence of the power factor that decreases with frequency, for very high frequencies the contribution of the characteristic spectrum proves to be smaller than that of bremsstrahlung and recombination radiation.

Total intensity of high-frequency radiation diverges logarithmically as ω approaches I. This divergence is attributed to the fact that we consider the probability of hole filling to be determined only by the Auger effect; the probability vanishes as the hole energy approaches I. Including the probability of radiative hole filling will suppress this divergence. To calculate total intensity with logarithmic accuracy, one can cut off the divergence at $\omega - I = \delta_I I$, where the small value of δ_I is taken such as to meet the condition

$\frac{dI_{\omega}^{(Ch)}}{d\omega}(\omega_{\delta}) \sim \frac{I^{(L)}}{\omega_{\delta}}$ in the order of magnitude, where $I^{(L)}$ is the characteristic intensity of line radiation, $\omega_{\delta} = (1 + \delta_I)I$. Thus, the value of δ_I turns out to be on the order of 0.001. The value of intensity of high-frequency characteristic radiation with respect to the sum of bremsstrahlung and recombination radiation (3.4.23) for several values of I/T is given in Table 3.2.

Table 3.2. Relative value of $I^{(Ch)}$ and $I^{(BR)}$.

I / T	0.5	1	1.5	2	2.5	3
$I^{(Ch)} / I^{(BR)}$	1.90	2.03	1.92	1.77	1.62	1.48

Let us now consider line radiation of the range $\omega < I$, where the contribution to total radiation is dominant. For the copper plasma under consideration, this contribution exceeds 97%. It is particularly difficult to account for it, because within our approach it requires considering all possible distributions of excited ions, complex competition of radiation and Auger processes, including those with triple collisions (see [3.40]).

When a bound electron is kicked out from the ion by a free electron, a hole forms at the bound electron site, and electrons—depending on the energy redistribution as a result of their collision—transit into the continuous spectrum or to vacant ion levels. This is accompanied by ionization, recombination (dielectronic) or ion excitation, while excited electrons emit energy as they move and descend to lower energy levels until they reach ionization potential. Emitting holes will in a similar way ascend in energy. The process of hole radiation emission can be described using the same formulas that are used for electrons, because their trajectories are the former trajectories of kicked-out bound electrons.

Let us use numeral 1 to denote the range of positive electron energies, and numerals 2, 3, 4 for energy ranges $(-I, 0)$, $(-2I, -I)$, $(-\infty, -2I)$, respectively (see Fig. 3.4).

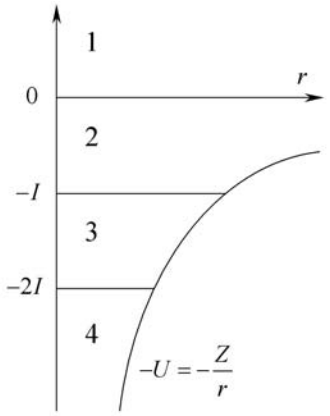

Fig. 3.4. Denotation of energy ranges.

Numerous channels contribute to line radiation (transition of electrons and holes into different energy ranges), and calculations of line radiation in these is rather a complicated task, especially given the competition between the Auger and radiation processes and the necessity to take into account triple collisions for a number of channels. The simplest way is to calculate the contribution to line radiation in the channel 1+3→1+2, in which, following the collision of a free electron with an electron from range 3, one of them moves to the continuous spectrum, and the other gets excited, i.e. moves to range 2. A hole forms instead of the electron from range 3. The same channel makes the major contribution to the intensity of line radiation, because it allows for the possibility of small energy transfer (the free electron remains free), and, consequently, will lead to logarithmically large integrals, and because at small energy transfer the excited state of the atom will have no Auger decay possibility (i.e., the Auger channel will not compete with the radiation channel). We restrict ourselves to calculating the intensity of plasma line radiation produced by this channel alone.

Let us denote energy of the hole in range 3 as $-\varepsilon_h$, and energy of the excited electron in range 2 as $-\varepsilon_e$. If the energy difference between the electron from range 2 and the hole is smaller than I (here we consider only such transitions in order to ignore the competition of the Auger effect), the resulting excited state will only have the possibility of radiative relaxation; hence, in this case, inelastic electron-ion collision will take place without change in the charge state of the ion. In the course of relaxation, the electron will move down to the level—I losing its energy for emission. The hole, on the opposite, will rise to the level—I and also emit energy. The emitted energy will concentrate in the frequency range $\omega < I$.

Total intensity of emitted energy is found using formula

$$I_0 = \int \left(\varepsilon_h - \varepsilon_e\right) \frac{d\dot{N}}{d\varepsilon_e d\varepsilon_h} d\varepsilon_e d\varepsilon_h . \qquad (3.4.43)$$

Distribution of forming holes and excited electrons in energies and angular momenta is found by analogy with characteristic radiation. The integrals obtained in the calculations of these quantities diverge as hole energy tends to I. This divergence is attributed to the fact that a large contribution to the scattering cross-section is made by far Coulomb collisions that take place at small energies of free electrons E and values of ε_h close to I. In reality, the divergence will be cut off, because energy transferred to the bound electron

cannot be smaller than the distance between neighbor levels in the ion. To get rid of this divergence (and perform calculations with logarithmic accuracy), we assume that excited electron and hole energies cannot differ from I less than by

$$\Delta I = \frac{I}{2n},$$

which has the same order of magnitude as the distance between neighbor energy levels near I. Here, n is the principal quantum number at the energy level I.

In the calculations to obtain more accurate data, one should use some effective charge Z_{eff} instead of nuclear charge Z. For this quantity, one can suggest the following interpolation formula [3.40] that provides a reasonable description of limiting cases $z << Z$ and $z \approx Z$:

$$Z_{eff} = \sqrt[3]{(z+1)^2 Z}.$$

Fig. 3.5 shows the value of (3.4.43) and radiation intensity from [3.2] for a number of temperatures for copper plasma. Fig. 3.5 shows that the calculated radiation intensity agrees with [3.2], and differences do not exceed a factor of 2.5.

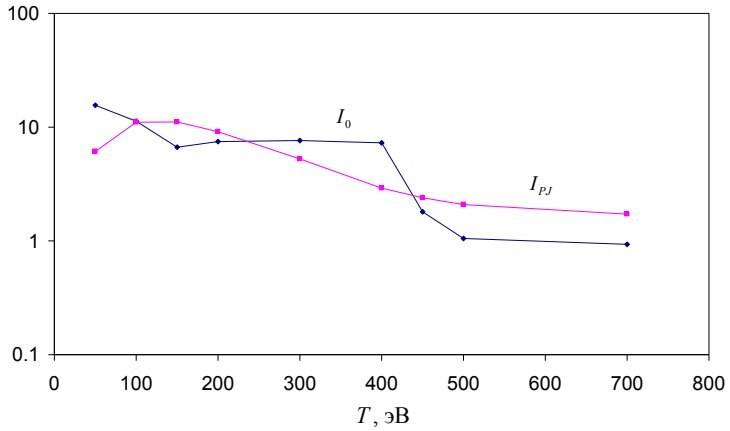

Fig. 3.5. Values of I_0 and radiation intensity from [3.2] (I_{PJ}) for copper plasma.

During the finite motion in the field of charge Z, the electron or the hole with energy module $\tilde{E}$ emits a set of frequencies [3.31]

$$\omega_k = \frac{k}{Z}\left(2\tilde{E}\right)^{\frac{3}{2}},$$

where k is a harmonic number.

The spectrum of radiation emitted by the particle is obtained using the formula for spectral intensity and the relationship between momentum and energy of particles during radiation descend or ascend from [3.31]. The sought spectrum of line radiation is found by integrating the spectra of all forming particle pairs.

The resulting radiation spectrum depends on two quantities, $s = I / T$ and ω / ω_0, and consists of weak peaks near the harmonics, being multiples of the main radiation frequency at the energy level I

$$\omega_0 = \frac{1}{Z}\left(2I\right)^{3/2}.$$

Fig. 3.6 shows a spectrum of plasma line radiation per one ion and one free electron for the case of $s = 1.93$, $n = 3.16$. (Such parameters present, e.g., copper plasma at a temperature of $T = 0.3$ keV, with $Z_{eff} = 20.6$, $\omega_0 = 366$ eV, $I = 578$ eV.) Fig. 3.6 shows that spectral intensity of radiation decreases with frequency growth rather slowly (theoretical analysis suggests that it decreases according to the law $\omega^{-5/3}$). Integration over the range $\omega < I$ for real ions with a not very large number of electrons gives only a small part of total emitted energy, therefore the question as to how to distribute the remaining energy over the spectrum remains open.

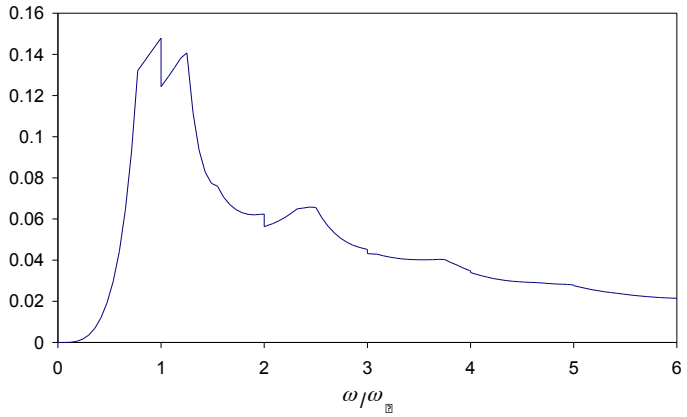

Fig. 3.6. Spectrum of plasma line radiation for s = 1.93 and n = 3.16.

To describe the MAGO experiments, we have considered hydrogen plasma with copper impurities and impurities of light elements (C, N, O) with temperatures around hundreds of electronvolts. The total radiation spectrum of such plasma was built as follows.

For copper plasma, the difference between the total intensity of emitted energy (3.4.43) and integral over the calculated spectrum in the range $\omega < I$ was located at two lines emitted during radiative relaxation after collisional electron transitions $n \rightarrow n+1$ and $n-1 \rightarrow$ n. The line spectrum in the range $\omega > I$ was calculated using formulas for characteristic radiation. The resulting total line spectrum was summed up with the continuous spectrum, the formulas for which are given in Section 3.4.2.

The spectrum of copper impurities for $T = 0.3$ keV is shown in Fig. 3.7.

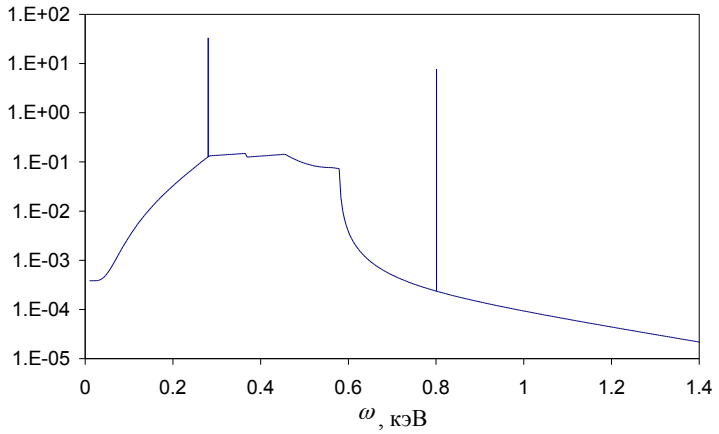

Fig.3.7. Radiation spectrum of copper plasma at T = 0.3 keV.

Ionization potential of hydrogen plasma at the temperatures of interest is $I_H << T$, so the spectrum of its radiation reduces to the bremsstrahlung spectrum.

The number of bound electrons in the light elements in question for considered temperatures does not exceed 2. Therefore, to describe the continuous part of the light elements' spectrum, we have used more accurate – compared to Section 3.4.2 – formulas from Ref. [3.13]. The difference between the value from [3.2] and the integral over the continuous spectrum (line spectrum intensity) was placed into the line $2p \rightarrow 1s$.

In the МАГО-IX experiment, time-resolved spectrometry of soft x-rays was performed in one of the chamber compartments using the DANTE spectrometer in the range of 0.2–1.5 keV using vacuum x-ray diodes.

To simulate values of signals, 2D MHD simulations of plasma motion in this experiment were performed in two different setups: one under the assumption of purely hydrogen plasma without impurities, and the other with washing out of copper and light elements (CO) from walls by plasma, with hydrogen plasma containing 3% of nitrogen impurities (by weight). The calculated radiation intensity was obtained by integrating radiation intensity per unit volume of plasma over the chord, along which the detectors were directed in the experiment.

Experimental and simulated signals of the x-ray diodes are given in Table 3.3. Table 3.3 shows that the agreement between simulated and experimental signals improves, if the simulations suggest plasma contamination with copper from the walls. In addition, whereas the duration of simulated signals with copper wash-out is fractions of a microsecond as in the experiment, simulated signals for pure hydrogen plasma last many microseconds at an approximately constant level.

Table 3.3. Simulated and experimental x-ray diode signals in the MAGO-IX experiment. All quantities are given relative to their values in the 0.2 keV channel.

Channel	Experimental signal J_{exp}	Simulated signal for plasma with impurities J	J / J exp	Ratio of simulated signal for pure plasma to J_{exp}
0.2 keV	1	1	1	1
0.4 keV	0.052	0.027	0.51	1.6
1.25 keV	0.086	0.030	0.34	5.8

Thus, we can state that the radiation spectrum of multiply charged plasma found for the coronal equilibrium helps analyze experimental data and obtain information on impurities in plasma.

REFERENCES

3.1 S.I. Braginskii. "Transport Processes in a Plasma," *Voprosy Teorii Plazmy: Sb. Statey.* Ed. M.A. Leontovich. Moscow: Atomizdat [Publishing House], No. 1, pp. 183–272, 1963; Reviews of Plasma Physics. Consultants Bureau, New York, Vol. 1, p. 205, 1965.

3.2 D.E. Post, R.V. Jensen, C.B. Tarter, W.H. Grassberger, W.A. Lokke. "Steady-State Radiative Cooling Rates for Low-Density, High-Temperature Plasmas," *Atom. Data and Nucl. Data Tables,* Vol. 20, No. 5, pp. 397–439, 1977.

3.3 J.L. Eddleman, C.W. Hartman. "Computational MHD Modeling of the MAGO Experiment," Preprint UCRL-JC-114685, 1993.

3.4 P.T. Sheehey, R.J. Faehl, R.C. Kirkpatrick, I.R. Lindemuth. "Computational Modeling of Magnetically Driven Liner-on-Plasma Fusion Experiments," *Proc. VII Int. Conf. on Megagauss Magnetic Field Generation and Related Topics,* Eds. V.K. Chernyshev, V.D. Selemir, and L.N. Plyashkevich. Sarov: VNIIEF, Part I, pp. 425–430, 1997.

3.5 O.M. Burenkov, S.F. Garanin, V.P. Korchagin, V.I. Mamyshev, I.V. Morozov, V.N. Mokhov, V.K. Chernyshev, V.B. Yakubov, I.R. Lindemuth, G. Idzorek. "Results of Numerical Simulations for Some Joint VNIIEF/LANL Experiments with MAGO Chamber," *Proc. IX Int. Conf. on Megagauss Magnetic Field Generation and Related Topics, Moscow–St. Petersburg, 2002.* Eds. V.D. Selemir and L.N. Plyashkevich. Sarov: VNIIEF, pp. 545–550, 2004.

3.6 S.F. Garanin, V.I. Mamyshev, V.B. Yakubov. "The MAGO System: Current Status," *IEEE Trans. Plasma Sci.,* Vol. 34, No. 5, pp. 2273–2278, 2006.

3.7 O.M. Burenkov, V.B. Yakubov, S.F. Garanin, A.N. Demin, V.I. Dudin, V.P. Korchagin, I.V. Morozov, V.N. Mokhov, E.S. Pavlovskii, V.K. Chernyshev. "Study of Plasma in MAGO Chamber by Own Neutron Radiation," *Fizika plazmy* (Plasma Physics), Vol. 23, No. 3, pp. 203–209, March 1997.

3.8 S.F. Garanin. "The MAGO system," *IEEE Trans. Plasma Sci.,* Vol. 26, No. 4, pp. 1230–1238, 1998.

3.9 V.V. Vikhrev, S.I. Braginskii. "Z-pinch Dynamics," *Voprosy teorii plazmy: Sb. Statey* (Reviews of Plasma Physics: Collection of Papers). Ed. M.A. Leontovich. Moscow: Atomizdat [Publishing House], Vol. 10, pp. 243–318, 1980.

3.10 V.F. Dyachenko, V.S. Imshennik. “Two-Dimensional Magnetohydrodynamic Model of Z-Pinch Plasma Focus,” *Voprosy teorii Plazmy: Sb. Statey* (Reviews of Plasma Physics: Collection of Papers). Ed. M.A. Leontovich. Moscow: Atomizdat [Publishing House], Vol. 8, pp. 164–245, 1974

3.11 B.B. Kadomtsev. *Kollektivnyye Yavleniya v Plasme* [Collective Phenomena in Plasma]. Moscow: Nauka [Publishing House], 1988.

3.12 L.D. Landau, E.M. Livshits. *Statisticheskaya Fizika. Chast 1* [Statistical Physics. Part 1]. Moscow: Fizmatlit [Publishing House], 2001.

3.13 Ya.B. Zeldovich, Yu.P. Raizer. *Fizika Udarnykh Voln Vysokotemperaturnykh Gidrodinamicheskikh Yavleniy* [Physics of Shock Waves and High-Temperature Hydrodynamic Phenomena]. Moscow: Nauka [Publishing House], 1966; Vol. 1. Academic Press, New York, 1966.

3.14 A.M. Buyko, S.F. Garanin, V.A. Demidov, V.N. Kostyukov, A.I. Kuzjaev, A A. Kulagin, V.I. Mamyshev, V.N. Mokhov, A.A. Petrukhin, P.N. Piskarev, M.S. Protasov, V.K. Chernyshev, V.A. Shvetsov, V.B. Yakubov. “Investigation of the Dynamics of a Cylindrical Exploding Liner Accelerated by a Magnetic Field in the Megagauss Range,” in *Megagauss Fields and Pulsed Power Systems*. Eds. V.M. Titov and G.A. Shvetsov, New York: Nova Science Publishers, pp. 743–748, 1990.

3.15 S.F. Garanin, V.I. Mamyshev. "Magnetized Plasma Cooling at the Interface with Exploding Metal Wall," PMTF [Journal of Applied Mechanics and Technical Physics], No. 1, pp. 30–37, Jan.–Feb. 1990.

3.16 Yu.D. Bakulin, V.F. Kuropatenko, A.V. Luchinskiy. “Magnetohydrodynamic Simulations of Exploding Wires,” *ZhTF* [Journal of Technical Physics], Vol. 46, No. 9, pp. 1963–1969, 1976.

3.17 V.E. Fortov. “Strong Shock Waves and Extreme States of Matter,” *UFN* [Advances in the Physical Sciences], Vol. 177, No. 4, pp. 347–368, 2007.

3.18 M.P. Desjarlais, J.D. Kress, L.A. Collins. “Electrical Conductivity for Warm, Dense Aluminum Plasmas and Liquids,” *Phys. Rev. E, Stat. Phys. Plasmas Fluids Relat. Interdiscip. Top.,* Vol. 66, p. 025401, 2002.

3.19 M.P. Desjarlais. “Density-Functional Calculations of the Liquid Deuterium Hugoniot, Reshock, and Reverberation Timing,” *Phys. Rev. B, Condens. Matter,* Vol. 68, p. 064204, 2003.

3.20 S.P. Lyon, J.D. Johnson. “T-1 Handbook of the SESAME Equation of State Library,” LANL Report No. LA-CP-98-100.

3.21 E.M. Lifshits, L.P. Pitaevsky. *Fizicheskaya Kinetika* [Physical Kinetics]. Moscow: Nauka [Publishing House] 1979; Pergamon, Oxford, 1980.

3.22 S.F. Garanin, V.I. Mamyshev. “Two-Dimensional MHD Simulations of a Plasma Focus with Allowance for the Acceleration Mechanism for Neutron Generation," *Plasma Phys. Reports* (Translated from Fizika Plazmy), Vol. 34, No. 8, pp. 639–649, 2008.

3.23 R.H. Williams, H.E. De Witt. “Quantum-Mechanical Plasma Transport Theory,” *Phys. Fluids,* Vol. 12. p. 2326, 1969.

3.24 R.L. Liboff. “Transport Coefficients Determined using the Shielded Coulomb Potential,” *Phys. Fluids,* Vol. 2. p. 40, 1959.

3.25 H.A. Gould, H.E. De Witt. “Convergent Kinetic Equation for a Classical Plasma,” *Phys. Rev.,* Vol. 155, p. 68, 1967.

3.26 G.S. Fraley, E.I. Linnebur, R.G. Mason, R.L. Morse. “Thermonuclear Burn Characteristics of Compressed Deuterium-Tritium Microspheres,” *Phys. Fluids,* Vol. 17, p. 474, 1974.

3.27 Ya.B. Zeldovich, I.D. Novikov. *Stroyeniye i evolyutsiya Vselennoy* [Structure and evolution of the Universe]. Moscow: Nauka [Publishing House], 1975.

3.28 L.A. Vaynshteyn, I.I. Sobelman, E.A. Yukov. *Vozbuzhdeniye Atomov I Ushireniye Spektralnoy Linii* [Excitation of Atoms and Broadening of Spectral lines]. Moscow: Nauka [Publishing House], 1979.

3.29 A.F. Nikiforov, V.G. Novikov, V.B. Uvarov. *Kvantovo-Statisticheskiye Modeli Vysokotemperaturnoy Plazmy* [Quantum-Statistical Models of High-Temperature Plasma]. Moscow: Fiziko-matematicheskaya literatura [Physical and Mathematical Literature], 2000.

3.30 S.F. Garanin. “Line Radiation of Multiply Charged Ions with a Fermi-Dirac Level Distribution of Electrons at High Temperatures,” *High Temperature* (Translated from Teplofizika Vysokikh Temperatur), Vol. 41, No. 4, pp. 421–424, 2003.

3.31 L.D. Landau, E.M. Livshits. *Teoriya Polya* [Field Theory]. Moscow: Nauka [Publishing House], 1967; *The Classical Theory of Fields,* Pergamon, London, 1971.

3.32 L.D. Landau, E.M. Lifshits. *Kvantovaya Mekhanika* [Quantum Mechanics]. Moscow: Fizmatgiz [Publishing House], 1963.

3.33 S.F. Garanin. "Radiation of High-Z Ions at Thermodynamic Electron Shell Filling," in 1st Int. Congress on Radiation Physics, High Current Electronics and Modification of Materials. Tomsk, Russia, September 24–29, 2000. Proc., Vol. 2, pp. 191–192, 2000.

3.34 J.A. Ball, J.A. Wheeler, E.L. Firemen. "Photoabsorption and Charge Oscillation of the Thomas-Fermi Atom," *Rev. Mod. Phys.,* Vol. 45, pp. 333–352, 1973.

3.35 S.F. Garanin, E.M. Palagina. "Photoabsorption in the Statistical Model of an Atom: Noninteracting Electron Model and Effect of Polarization," *J. Exp. Theor. Phys.* (Translated from Zh. Eksp. Teor. Fiz.), Vol. 104, No. 4, pp. 527–534, 2007.

3.36 T.A. Carlson, C.W. Nestor, Jr., N. Wasserman, J.D. McDowell. "Calculated Ionization Potentials for Multiply Charged Ions," *Atom. Data,* Vol. 2, pp. 63–99, 1970.

3.37 G.A. Vergunova, E.M. Ivanov, V.B. Rozanov. "Computation of Optical Parameters of Nonequilibrium Al and Cu Plasma," Preprint No. 74, Institute of General Physics, Russ. Acad. Sci., Moscow, 1999.

3.38 G.A. Vergunova, S.F. Garanin, E.M. Ivanov, S.D. Kuznetsov, V.B. Rozanov. "X-radiation of Light Element Impurities in MAGO/MTF Plasma," Preprint No. 43. Institute of General Physics, Russ. Acad. Sci., Moscow, 2001.

3.39 P.D. Gasparyan, A.A. Gorshikhin. "Linear Noise Approximation for Simulations of Non-Equilibrium Fluctuations of Occupancy Numbers in Radiative-Collisional Averaged Ion Models," *Fizika Plazmy* [Plasma Physics], Vol. 29, No. 4, p. 425, 2003.

3.40 S.F. Garanin, E.M. Palagina. "Analysis of Ionization and Recombination Processes Under the Coronal Equilibrium Conditions by using Statistical Atomic Model," *Plasma Phys. Rep.* (Translated from Fiz. Plasmy), Vol. 33, No. 8, pp. 684–695, 2007.

4. TRANSVERSE COLLISIONLESS SHOCK WAVES AND PLASMA HEATING IN THEM

In many cases, magnetohydrodynamic flows, like hydrodynamic flows, because of the nonlinearity of their governing equations, result in discontinuities—shock waves. In low-density plasma, the free paths of ions and electrons behind the shock front, which, in collisional plasma, determine the width of the shock front, may prove to be very large and, in any case, markedly exceeding the Larmor radii of the respective particles. In this case, the width of the shock waves is determined by the Larmor radii of the particles, rather than by their free paths; and energy dissipation mechanisms in the shock wave become collisionless and are governed by the development of various instabilities at the front and by the reflection of particles from the front region.

Collisionless shock waves (CSW) occur in such astrophysical events as the encounter between solar wind and the earth's magnetic field and the interaction between flows of matter ejected by galaxies and exploding supernovae and the interstellar medium. In the laboratory, CSWs occur in the low-density plasma of *Z*- and Θ - pinches, and they also play an important role in plasma heating in an approach to controlled thermonuclear fusion like MAGO/MTF.

One can point to several aspects that promote interest in CSWs. First, they are of fundamental interest as an example of a phenomenon in which we see the dissipation of energy and the efficient growth of entropy in the absence of particle collisions. Second, unlike with collisional shock waves, plasma conditions downstream of the CSW front are not determined merely by the conservation laws (Hugoniot) and remain non-equilibrium. That raises the question, In what state is plasma downstream of the CSW front, and what is the hierarchy of scales for the further relaxation of the plasma to equilibrium? Finally, there is practical interest in CSWs because, in various cases, different plasma components (electrons, ions, or, in multi-component plasma, different ion species) may be heated in CSW. In controlled fusion systems, heating of the ion component is of primary importance, which means the CSW can be used to accomplish that task.

We shall consider the simplest, though, perhaps, the most frequent and instructive, configuration of a perpendicular CSW, i.e., a configuration where the direction of the shock wave movement x is perpendicular to the magnetic field directed initially along z. In addition, for simplicity, the CSW will be assumed to propagate in cold plasma with zero temperature and zero thermal pressure. In that case, shock waves can be regarded as collisionless, if the ion

component (and even more so, the electron component) of the plasma downstream of the front is magnetized $(\omega\tau)_i >> 1$ (ω_i is the Larmor frequency of ions, and τ_i is ion–ion collision time). Although particle distribution downstream of the CSW front for collisionless plasma must differ from the Maxwell distribution, one can use, instead of temperature, the average energy of random motion of particles obtained using the Hugoniot to assess the degree of magnetization $(\omega\tau)_i$ downstream of the front.

The largest length that will determine the structure of the CSW front for collisionless plasma will be the ion Larmor radius, which, for a shock wave with a Mach number of $M_A \sim 1$ (since we are working with cold plasma, we will use the Alfven-Mach number M_A, which is equal to the ratio of the shock wave velocity to the Alfven velocity upstream of the front, as the measure of shock wave strength) is, in terms of order of magnitude, equal to c/ω_{pi} (ω_{pi} is plasma ion frequency). For cold plasma with a small M_A, however, ions are not reflected off the CSW front, and for a single-component plasma, we have a single-stream flow with cold ions (having almost no velocity relative to one another) downstream of the front. Here, the CSW structure forms on smaller scales that are determined by the current velocity of electrons. According to the first CSW model [4.1], that scale can be determined by electron inertia and can be equal to $\sim c / \omega_{pe}$, and the front will have an oscillatory structure (a wave determined by electron dispersion). But in fact, current instabilities—primarily, the ion-acoustic instability—should develop at the CSW front, resulting in anomalous plasma resistivity and a resistive front width larger than the width due to electron dispersion, although much smaller that the ion Larmor radius c / ω_{pi}. Anomalous Joule heating goes mainly to the electron component of the plasma.

Thus, one can use, as the basic model for describing the CSW, the so-called hybrid model, in which ions are described kinetically, and electrons, hydrodynamically as a gas with temperature and pressure. Friction between electrons and ions results in electric resistance, which, at the leading edge of the CSW front, can create a resistive jump (with the influence of some effective electron thermal conductivity), with scales that are small by comparison with those of the ion Larmor gyration.

The CSW can be studied with this model in the following sequence: we first consider a one-dimensional (1-D) case, assuming that the distribution of all quantities in the CSW depends on only one coordinate perpendicular to the front, and look at the results obtained in that case; then we evaluate stability of the solution obtained, and if the solution is unstable, we attempt to obtain turbulent state of the CSW, taking the growing instabilities into account in a 2D formulation.

Note that there are many papers devoted to the study of CSWs (see, for example, [4.2–4.5]). In this section, for consistency and convenience of description, we will focus on our results [4.6–4.9].

The CSW modeling problems that we examined were solved for non-stationary conditions, with the assumption that, for $x = 0$, there is an ideally conducting, rigid piston toward which an initially uniform semi-infinite plasma is flowing at a given velocity –μ. The initial plasma density is n_0, and the initial magnetic field is B_0. The following units of measurement were used: n_0 for density, B_0 for magnetic field, initial Alfven velocity for velocity, inverse initial ion Larmor frequency ω_{i0}^{-1} for time, and c / ω_{pi} for the coordinate, where ω_{pi} is the initial ion plasma frequency.

4.1. One-Dimensional Hybrid Simulations

Biskamp, Berezin and Vshivkov, Leroy *et al.,* Bashurin *et al.,* and Garanin and Golubev [4.2–4.4, 4.10, and 4.11] studied CSWs with 1D hybrid numerical modeling (with a coordinate perpendicular to the wave front) and took into account various physical processes. Since classical plasma resistivity due to Coulomb collisions is negligible under CSW conditions, it was generally ignored in the simulations. Bashurin *et al.* [4.10] performed CSW modeling that took into account ion gyration for the infinite Alfven-Mach number M_A, and Garanin and Golubev's modeling [4.11] took ion gyration into account for finite supercritical numbers M_A, with additional accounting for electron dispersion. However, as already mentioned, under most experimental conditions, current-driven instabilities should develop at the CSW front, leading to anomalous resistivity, which results in a resistive shock-front width that is larger than the scale c / ω_{pe} attributed to electron dispersion. CSW modeling with account taken of anomalous resistivity was performed by Leroy *et al.* [4.3]. Note that the ion distribution obtained in the 1D simulations downstream of the CSW front proved to be unstable [4.12] (see Section 4.2), which means that the shock wave itself is also unstable and is distorted on a scale length on the order of $\sim c / \omega_{pi}$, which was demonstrated by Thomas [4.5] for CSWs with large Mach numbers. Plasma resistivity was not taken into account in that paper, on the strength that it should be insignificant at large Mach numbers, and relatively small spatial scales need to be resolved in order to take it into account.

Electron heating and ion heating are important shock-wave characteristics, as is the ion distribution downstream of the wave front. The ion distribution in an MHD flow can be seen as preserving its shape and adiabatically changing with density for times that are short by comparison with ion–ion collision time (after the relaxation due to the onset of the instability

associated with anisotropy of the distribution function), whereas the ratio of electron heating to ion heating can be regarded as constant for times that are short by comparison with the time for equalization of the electron and ion temperatures; the electron and ion energies themselves change adiabatically with density. The issue of the ratio of electron heating to ion heating and the ion distribution function (IDF) are also of practical importance to plasma facilities in which plasma is heated by means of CSWs, particularly in the MAGO facility. The plasma diagnostics used in such facilities, which is based on the measurement of the spectrum of thermonuclear neutrons [4.13], are directly related to the ion spectrum, especially to its high-energy range. Unfortunately, those characteristics have not always been considered in CSW studies, and there are no reliable direct data for perpendicular waves with intermediate Mach numbers in cold plasma.

We will consider CSWs with an initially zero electron β and a low ion β, with account taken of anomalous resistivity in a 1D model for different Alfven-Mach numbers [4.6], focusing primarily on the relative roles of electron and ion heating and IDF, as well as on the mechanism of ion heating. Since, for the CSWs of interest, it is impossible to determine the plasma state downstream of the front by using merely the conservation laws (Hugoniot), our approach of direct modeling of the CSW and analysis of the effective heating of the different plasma components makes it possible to obtain the missing information. The results obtained in this study allow us to proceed to a hydrodynamic description of the behavior of plasma with CSWs, with a substantiated redistribution of energy among the various plasma components.

4.1.1. Physical model

In the 1D model in question, the magnetic field preserves its original direction along the z-axis. We will describe the electrons using hydrodynamic variables—density n, velocity $\vec{v}_e$, temperature T_e, and pressure p_e — and will assume that $p_e = nT_e$ and that the adiabatic index is $\gamma = 5/3$. Ions, however, are described kinetically, particle velocities are designated as $\vec{v}$, and ion density and velocity averaged over the distribution function are n_i and $\vec{U}$. Plasma is assumed to be quasi-neutral ($n = n_i$, and from the continuity equation in the 1D formulation, $v_{ex} = U_x$).

Equations of ion motion have the following form:

$$m_i \frac{dv_x}{dt} = e\left(E_x + \frac{v_y}{c}B\right), \qquad (4.1.1)$$

$$m_i \frac{dv_y}{dt} = e\left(E_y - \frac{v_x}{c}B\right) - e\eta j \ , \qquad (4.1.2)$$

where m_i is the ion mass, $j = en(U_y - v_{ey})$ is the current density, and η is the plasma resistivity. We will ignore electron dispersion compared to resistivity and write the equations of electron motion as follows (in the form of the generalized Ohm's law that relates the electric field and the current density)

$$-en\left(E_x + \frac{v_{ey}}{c}B\right) - \frac{\partial p_e}{\partial x} = 0 \ , \qquad (4.1.3)$$

$$-en\left(E_y - \frac{v_{ex}}{c}B\right) + en\eta j = 0 \ . \qquad (4.1.4)$$

The equation for electron energy is

$$\frac{\partial\left(\frac{3}{2}p_e\right)}{\partial t} = \frac{\partial}{\partial x}\left(-\frac{3}{2}v_{ex}p_e + \chi\frac{\partial T_e}{\partial x}\right) - p_e\frac{\partial v_{ex}}{\partial x} + (1-\alpha)\eta j^2 \ , \qquad (4.1.5)$$

where χ is the electron thermal conductivity. Joule heating of electrons in (4.1.5) is reduced because, under the assumption of an anomalous ion–acoustic resistivity, a fraction of the Joule heating is spent on ion heating; here we assume that fraction to be equal to α. At present, the existing theory of ion–acoustic resistivity contains no detailed description of ion heating and the corresponding change in the IDF under conditions when the ion-acoustic turbulence causes anomalous plasma resistivity. To provide a qualitative description of ion heating, we assume that the IDF changes in a self-similar fashion, i.e., the change of local velocities of ions relative to their center of mass is proportional to the velocities themselves, which results in the addition of the following term to the right-hand sides of equations (4.1.1–4.1.2):

$$m_i \frac{\alpha\eta j^2}{2nT_i}(\vec{v} - \vec{U}) \ , \qquad (4.1.6)$$

where T_i is the local ion energy averaged over the distribution function. The quantity α is assumed to be small and independent of the plasma parameters such that ion heating via this particular mechanism is much lower than electron heating. This mechanism, however, affects the spreading of the IDF and, consequently, the reflection of some of the ions off the CSW front, which means that this mechanism is essential.

Maxwell equations are expressed as

$$\frac{\partial B}{\partial x} = -\frac{4\pi}{c} j \ , \tag{4.1.7}$$

$$\frac{\partial B}{\partial t} = -c\frac{\partial E_y}{\partial x} \ . \tag{4.1.8}$$

Equations (4.1.1–4.1.8) define the problem if the quantities η, χ, and α, which are treated here as phenomenological parameters, are known. We assume that, for sufficiently small η and χ, which mainly determine the width of the resistive jump, their value and specific dependence on the plasma parameters should not affect the basic characteristics of a CSW. Therefore, in simulations, we assume that η = const and consider χ to be related to the magnetic diffusion coefficient $\kappa = \frac{c^2}{4\pi}\eta$ by the relationship

$$\chi = 1.5 n \beta_e \kappa \ ,$$

where $\beta_e = \frac{8\pi p_e}{B^2}$. Anomalous-resistivity assessment based on the theory of a weak turbulence for the ion–acoustic instability [4.14] yields

$$\kappa \sim a c_A \frac{c}{\omega_{pi}} \ ,$$

where c_A is the Alfven velocity and a is the dimensionless factor. The same factor determines ion heating via induced scattering of ion–acoustic noise by ions. The quantities a and α depend weakly on the plasma parameters $\left(a \sim \alpha \sim \left(\frac{n mc^2}{B^2} \frac{m}{m_i} \right)^{1/6} \right)$ and contain a small numerical factor. For our simulations, we took a = 0.2 and α = 0.1, basing on the plasma parameters in the CSW in the MAGO chamber.

At the initial time, the plasma is assumed to be cold: β_{e0} = 0, β_{i0} = 0.01. Plasma heating in CSW, of course, will be considerably higher than β_{i0}. The non-zero value of β_{i0} is required only to specify the initial Maxwellian IDF, which would remain Maxwellian if ion heating occurred solely due to (4.1.6). The simulations were performed for the velocities μ corresponding to both subcritical (u = 1 and 2) and supercritical (u = 3, 4, 6, and 10) CSW regimes.

4.1.2. Simulation results

Figures 4.1–4.3 show the ion distribution in the χ, v_x and χ, v_y phase planes and the magnetic field profiles for the times $t = 5$ and $t = 10$ for $u = 1$ (subcritical regime, in which there is almost no ion reflection off the resistive jump at the front, $M_A \cong 2$), $u = 3$ (supercritical regime, $M_A \cong 4.4$) and $u = 6$ (supercritical regime, $M_A \cong 8.5$). One can clearly see the difference between the subcritical and supercritical CSWs, which is also observed in the phase planes (Fig. 4.1 has no reflected ions, and Figs. 4.2 and 4.3 do), and in the magnetic field profiles (profiles B(χ) in Fig. 4.1 are monotone and steady-state; whereas in Figs. 4.2 and 4.3 they have a pedestal and an overshoot associated with the reflected ions, as well as an oscillatory structure downstream of the front; they are time-dependent, such that the wave propagation in this case is pulsating).

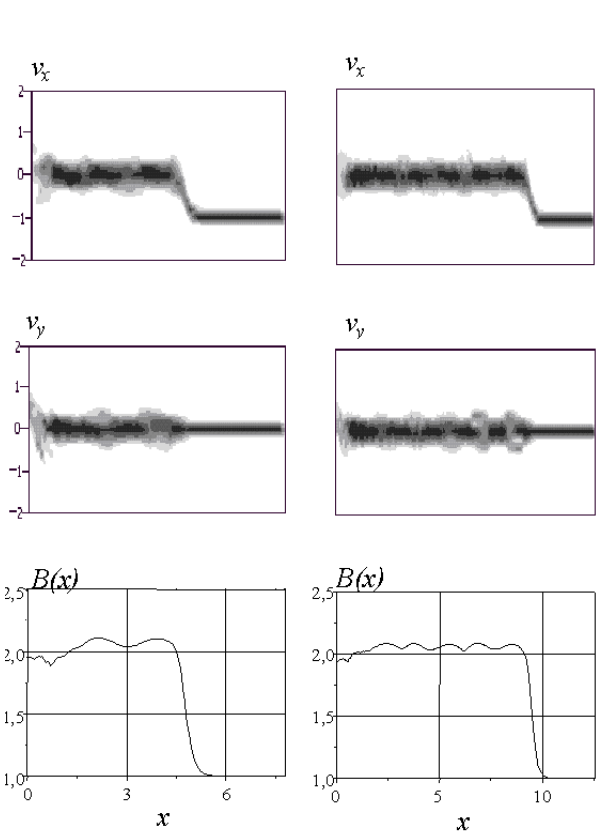

a) t = 5 b) *t* = 10

Fig. 4.1. The ion distribution in the χ, v_x and χ, v_y phase planes, and the magnetic field profiles B(x) in a CSW for the plasma flow velocity μ =1 at times a) t = 5; b) t = 10.

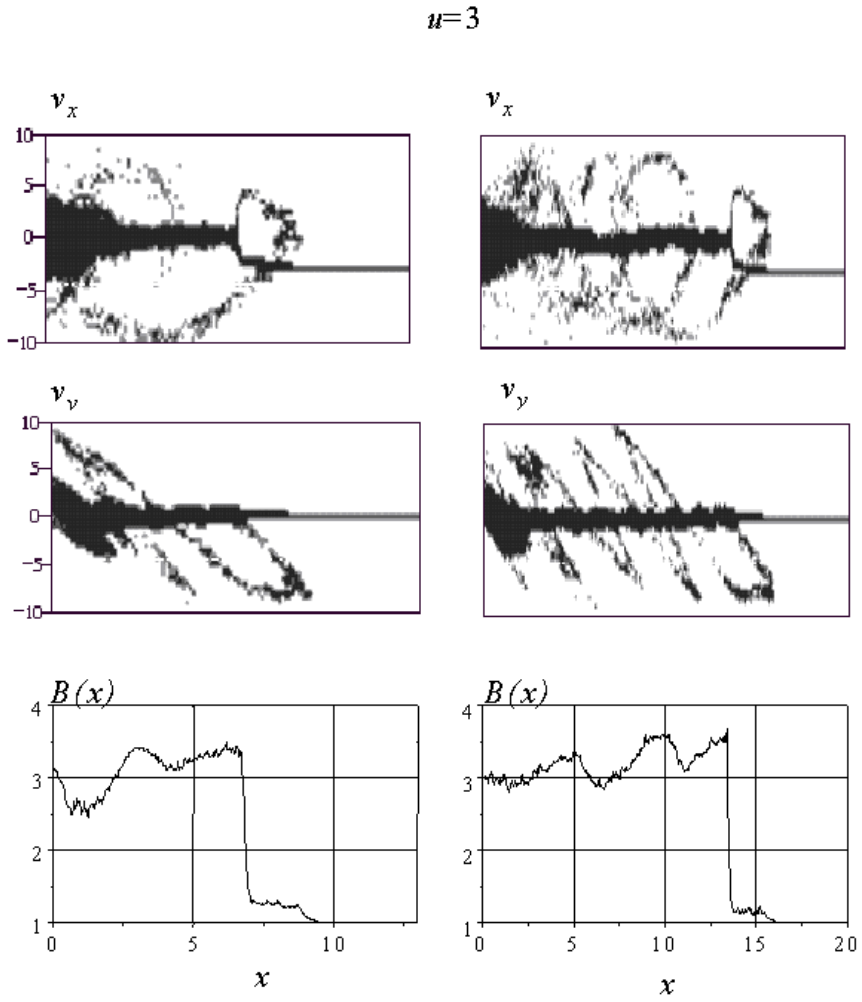

a) $t = 5$ b) $t = 10$

Fig. 4.2. The ion distribution in the x, v_x and x, v_y phase planes, and the magnetic field profiles B(x) in a CSW for the plasma flow velocity u =3 at times a) t = 5; b) t = 10.

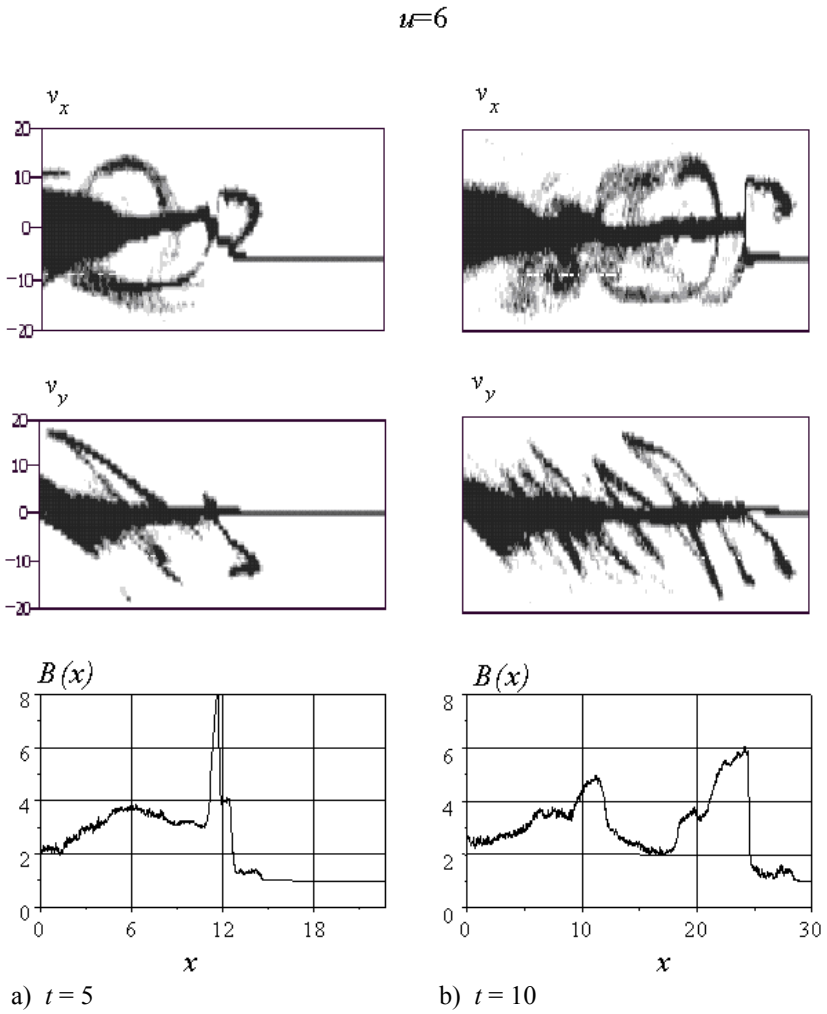

Fig. 4.3. The ion distribution in the x, v_x and x, v_y phase planes, and the magnetic field profiles B(x) in a CSW for the plasma flow velocity u = 6 at times a) t = 5; b) t =10.

The presence or absence of ions reflected from the front also determine the IDFs downstream of the front, which are shown in Fig. 4.4 for these CSWs for the time $t = 10$. To exclude the effects of the near-piston and near-front regions, the IDF was defined for the region $x_1 = 0.1x_F < x < 0.9\, x_F = x_2$. Since the Larmor gyration leads to equalization of velocities v_x and v_y, the figure shows IDFs in the total velocity $f(v)$, which are defined such that $f(v)dv$ is the fraction of ions in the velocity interval dv. Along with the IDFs, Fig. 4.4 shows the velocity distributions of the ion kinetic energy,

$v^2 f(v)$. Figures 4.4b and 4.4c, for supercritical CSWs, show that ions reflected from the front have very high velocities, and although the fraction of such ions is small, they make the main contribution to the thermal energy of ions downstream of the front.

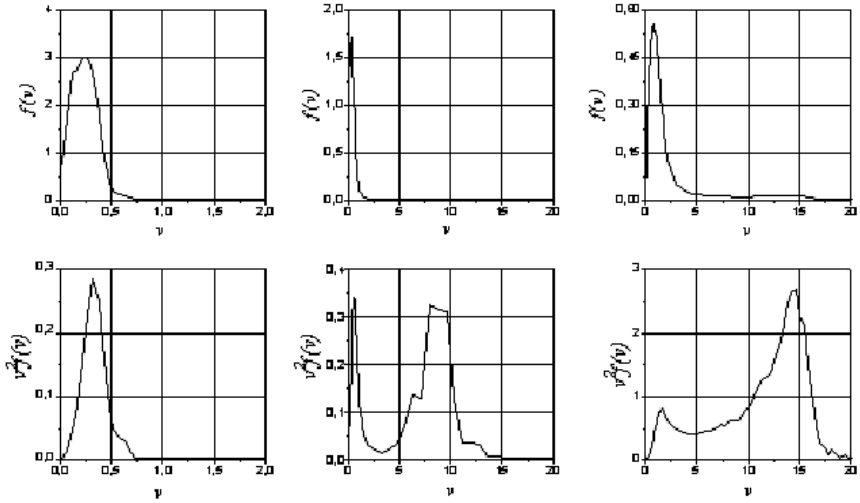

Fig. 4.4. The velocity IDFs, f(v), and velocity distribution of the ion kinetic energy, $v^2 f(v)$, downstream of the CSW front for plasma flow velocities a) u = 1; b) u = 3; and c) u = 6.

The basic results of the simulations performed, which characterize the plasma state downstream of the CSW front, are presented in Table 4.1. For different plasma velocities u, the table shows the following quantities:

- the computed Alfven-Mach number defined as $M_A = x_F / t + u$, where x_F is the shock front coordinate at $t = 10$;
- the average magnetic field $\bar{B}_1$ downstream of the shock front (in the region $x_1 < x < x_2$) or the compression ratio downstream of the front;
- fractions of the internal energy downstream of the shock front for different degrees of freedom: thermal energy of the electron

component W_e, thermal energy of the ion component W_i, energy contained in the magnetic field oscillations downstream of the front $W_B \sim \int_{x_1}^{x_2} \left(\frac{B^2}{2} - \frac{B_1^2}{2} \right) dx$;

- the ion velocity v_m corresponding to the median kinetic energy (the velocity that bisects the area under the curve $v^2 f(v)$).

Table 4.1. Basic results of simulations performed.

u	M_A	$\bar{B}_1$	W_e(%)	W_i(%)	W_B(%)	v_m	$M_A(\gamma = 5/3)$	v_1
1	1.95	2.05	84.7	15.3	0	0.33	1.94	4.1
2	3.1	2.81	84.3	15.6	0.1	7.1	3.09	6.6
3	4.35	3.18	78.7	21.1	0.2	8.2	4.32	9.3
4	5.66	3.3	72.6	27.1	0.3	9.8	5.59	12
6	8.46	3.23	52.7	46.7	0.6	13	8.18	18
10	14.5	3.13	29.1	70.4	0.5	15	13.4	29
1, D/T	1.96	2.04	73.4	11.1/15.3	0.2	0.48/0.42	1.94	4.0
3, D/T	4.45	3.01	55.5	31.5/12.5	0.5	7.5/1.6	4.32	9.1

*The last two lines of Table 4.1 represent the results of CSW simulations for a plasma with two ion species.

For comparison, the last two columns of Table 4.1 present the Alfven-Mach number corresponding to the shock Hugoniot with $\gamma = 5/3$ and the velocity v_r (with respect to the mean ion velocity) of the ions that were reflected from the front and penetrated through the front after the Larmor gyration. The velocity v_r is determined under the following assumptions:

- The shape of the CSW profile is rectangular (with the exception of a narrow peak at the front, where the reflection occurs);
- The reflected ions are a small fraction of the main-flow ions whose velocity (in the frame of reference related to the front) changes the sign from M_A to $-M_A$ at the instant of reflection; and
- The flow of reflected ions is rather weak and does not perturb the plasma. Therefore, these ions move in uniform electric and magnetic fields upstream and downstream of the front and, passing through the front, after Larmor gyration, are decelerated by the same potential as the main flow, i.e., in the frame of reference related to the front, v_x^2, decrease by the same value as for the ions from the main flow.

It can be seen from Table 4.1 that the fraction of ion heating grows with velocity u and Mach number and equals about a half for u = 6 and MA = 8.5. As a result, as follows from the comparison of M_A and M_A ($\gamma = 5/3$), the Hugoniot, which at small u coincides with that for $\gamma = 5/3$, starts to deflect from it with the growth of u and approaches the Hugoniot for $\gamma = 2$ corresponding to two degrees of freedom available in these simulations for ions. The fraction of the magnetic-field oscillations W_B in the internal energy of plasma proves small for any u: for small u because of a rather uniform magnetic field downstream of the front, and, for large u because the contribution of the magnetic-field energy to the energy balance becomes negligible. The estimate for the velocity v_r of the reflected ions agrees with the simulated characteristic ion velocity v_m downstream of the front for the flow velocities u = 2, 3, and 4, for which there are ions reflected from the front, but their fraction is small, and they do not introduce strong perturbations in plasma. Note that the ion spectrum obtained proves to be enriched with "superthermal" particles for any supercritical CSW. For example, the ratio of median kinetic energy $\frac{m_i v_m^2}{2}$ to the average "thermal" energy of ions downstream of the front is 42 for u =3.

CONCLUSION

For plasma with a single ion species, the fraction of electron heating in the total plasma heating downstream of the CSW front within the 1D simulation approach remains dominates up $M_A \sim 8$, whereas ion heating predominates for larger Mach numbers. Heating of the ion component is mainly determined by the ions that are reflected from the shock front and whose velocities downstream of the front are $\sim 2M_A$, which greatly exceeds "thermal" velocities. The velocity of such ions can be assessed satisfactorily, if these are assumed to form from the main flow due to the reflection from the front and to move then in the electric and magnetic fields of the main flow.

4.2. Instability of the Ion Distribution Function Downstream of the CSW Front. Time Evolution of the Distribution Function

Ions driven by the Lorentz force and Larmor gyration in strictly perpendicular CSW would move in a plane perpendicular to the magnetic field. As a result, ions downstream of the shock would have no velocities along the field. Such a situation is realized in the 1D simulations of Section 4.1, where the occurrence of longitudinal velocities is impossible by virtue of the problem setup. However, the anisotropic ion distribution forming downstream of the front proves to be unstable relative to perturbations with the wave vectors that have a component along the magnetic field. The growth of such perturbations and their effects on the distribution function may lead to a decrease of the anisotropy.

The development of unstable oscillations downstream of the CSW front in the quasi-linear approximation were studied by Yoon [4.12], where the IDFs for transverse and longitudinal velocities were assumed to be bi-Maxwellian, and oscillations and quasi-linear diffusion were assumed to result in changes of relevant temperatures and their equalization. The study showed that the anisotropy of such a distribution function decreases considerably. Nevertheless, if the real ion distribution is borne in mind, then the questions of whether the isotropization occurs for all regions of the IDF, how quickly this process runs for low and high velocities, and how real ion distribution affects the spectrum of oscillations remain unresolved. The question of the ion distribution function is also of practical importance to plasma facilities, including MAGO, where plasma is heated by means of the CSW, because in this case a large fraction of energy is contained in high-velocity ions, for which collisions are not very essential.

Heating of MAGO plasma as a result of "anomalous" friction against the anode, when the plasma passes through the nozzle, may also produce high-energy ions that, generally speaking, have anisotropic ion distribution with prevailing velocity directions perpendicular to the magnetic field (see Section 5.3). The information on high-energy ions was obtained by Burenkov *et al.* [4.13] by spectral measurements of thermonuclear neutrons. Those measurements did not reveal any velocity anisotropy for most of the neutron spectrum and, consequently, for high-energy ions. The explanation given for the results is that the ion distribution function contains a large fraction of high-energy ions, which becomes isotropic rather quickly due to the noise produced by the growing instability.

In this section, we will consider the development of the instability of the Alfven ion-cyclotron mode with a wave vector parallel to the magnetic field [4.8].

4.2.1. The Dispersion Relation for Oscillations Along the Magnetic Field

For oscillations along the magnetic field, i.e., $\vec{k} \parallel \vec{B} \parallel \vec{e}_z$, the dispersion equation [4.15]

$$\left| k^2 \delta_{ij} - k_i k_j - \frac{\omega^2}{c^2} \varepsilon_{ij} \right| = 0 \ ,$$

where e_{ij} is the tensor of dielectric permittivity, splits into two equations:

$$k^2 = \frac{\omega^2}{c^2} (\varepsilon_{xx} \pm i \varepsilon_{xy}) \ , \qquad (4.2.1)$$

and

$$e_{zz} = 0 \ .$$

We will consider only transverse waves described by Eq. (4.2.1). For this case, using the known components of tensor e_{ij} [4.16] and noting that, for the range of wave vectors $k \sim c/\omega_{pi}$ of interest, $\frac{\omega_e}{k v_{Te}} >> 1$, and for the frequencies $\omega \sim \omega_i$ of interest, $\omega << \omega_e$, we obtain the following dispersion equation:

$$k^2 = \frac{\omega^2}{c^2}\left(1 \pm \frac{\omega_{pe}^2}{\omega\omega_e} + \frac{2\pi e^2}{\omega^2}\int d\vec{p}\,\frac{(\omega - k v_\parallel)\frac{\partial f}{\partial p_\perp} + k v_\perp \frac{\partial f}{\partial p_\parallel}}{\omega - k v_\parallel \mp \omega_i} v_\perp\right). \qquad (4.2.2)$$

Assuming that wave velocities are small compared to the speed of light, we can ignore the 1 in the brackets of formula (4.2.2) (disregard of bias currents) and, proceeding to dimensionless units $k = k\frac{\omega_{pi}}{c}$, $\omega = \frac{\omega}{\omega_i}$, and $v = \frac{v}{c_A}$, rewrite Eq. (4.2.2) in the dimensionless form

$$k^2 = \mp\omega + \frac{1}{2}\int d\vec{v}\,\frac{(\omega - k v_\parallel)\frac{\partial f}{\partial v_\perp} + k v_\perp \frac{\partial f}{\partial v_\parallel}}{\omega - k v_\parallel \mp 1} v_\perp\,, \qquad (4.2.3)$$

where the function of velocity distribution is assumed to be normalized to 1

$$\int f\, d\vec{v} = 1\ .$$

Since, in an ideal case of a perpendicular perturbation-free CSW, ions move in the plane perpendicular to the magnetic field, parallel components of ion velocities right downstream of the front can be considered to be small. One can then expand the integral in the right-hand part of Eq. (4.2.3) in powers of $\frac{k v_\parallel}{1-\omega} << 1$ (here we treat only the case of the minus sign in (4.2.3); a solution for the plus sign can be obtained by replacing k with $-k$ and ω with $-\omega$)

$$k^2 = \frac{\omega^2}{1-\omega} - k^2\frac{\overline{v_\perp^2}}{2(1-\omega)^2} + k^2\frac{\overline{v_\parallel^2}}{(1-\omega)^3} - 3k^4\frac{\overline{v_\parallel^2 v_\perp^2}}{(1-\omega)^4} + \ldots \qquad (4.2.4)$$

(the bar above the squared velocity components means averaging over the distribution function).

If we ignore $\nu_{\|}$ completely, Eq. (4.2.4) transforms into a cubic equation for ω

$$k^2 = \frac{\omega^2}{1-\omega} - k^2 \frac{\overline{\nu_\perp^2}}{2(1-\omega)^2} \ ,$$

which has complex roots for sufficiently high k. As this equation has real coefficients, the imaginary part of one of the roots will be positive, i.e., such ion distribution is unstable. The roots of this equation for $\overline{\nu_\perp^2} = \beta_{i\perp} = 0.5$ are shown in Fig. 4.5, which corresponds to the ion distribution downstream of the CSW obtained in the 1D simulation with the Mach number $M_A = 44$ (Fig. 4.4b). The unstable root of Eq. (4.2.4) at $k >> 1$ equals

$$\omega = 1 - \frac{1-\overline{\nu_\perp^2}/2}{2k^2} + i\sqrt{\frac{\nu_\perp^2}{2}}\left(1 - \frac{1}{k^2} - 3k^2 \frac{\overline{\nu_\|^2 \nu_\perp^2}}{\overline{\nu_\perp^2}}\right) \qquad (4.2.5)$$

Fig. 4.5. Frequency ω and increment γ of the Alfven ion-cyclotron oscillation mode along the magnetic field for $\beta_{i\perp} = 0.5$, $\beta_{i\|} \cong 0$.

Thus, the anisotropic ion distribution in velocities with small $\nu_{\|}$ is unstable,

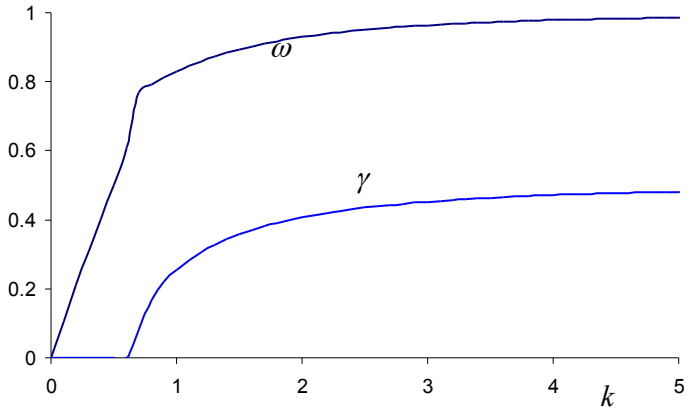

with characteristic wave vectors of the unstable mode being $k \sim \frac{\omega_{pi}}{c}$ and characteristic increments for plasma with β ~ 1 being $\gamma \sim \omega_i$.

4.2.2. Quasi-Linear Diffusion of the Distribution Function

The quasi-linear equation [4.17] that describes the variation of the IDF produced by noise with $\vec{k} \| \vec{B}$ can be written as

$$\frac{\partial f}{\partial t} = \pi \frac{e^2}{m_i^2} \int dk \left\{ \begin{array}{l} \frac{1}{\nu_\perp} \hat{R} \left[\frac{\nu_\perp}{2} |\vec{E}_k(n=1)|^2 (\hat{R} f) \right] \delta(\omega - \Omega_i - k\nu_\|) + \\ \quad + \frac{1}{\nu_\perp} \hat{R} \left[\frac{\nu_\perp}{2} |\vec{E}_k(n=-1)|^2 (\hat{R} f) \right] \delta(\omega + \Omega_i - k\nu_\|) \end{array} \right\}, \tag{4.2.6}$$

where m_i is the ion mass,

$$\hat{R} = \left(1 - \frac{k\nu_\|}{\omega} \right) \frac{\partial}{\partial \nu_\perp} + \frac{k\nu_\perp}{\omega} \frac{\partial}{\partial \nu_\|} \ ,$$

and $\vec{E}_k$ is the amplitude of electric field oscillations that can be expressed through the amplitudes of magnetic field perturbations

$$\vec{B}_k^1 = \frac{c}{\omega} [\vec{k}\, \vec{E}_k] \ .$$

If we focus primarily on the time history of the high-energy region of the IDF, for $\frac{k\nu}{\omega x} >> 1$, where $x = \frac{\nu_\|}{\nu}$, Eq. (4.2.6) can be written as

$$\frac{\partial f}{\partial t} = \frac{\partial}{\partial x} \frac{|\vec{B}_k^1|^2}{2} \frac{1 - x^2}{\left| \frac{\partial \omega}{\partial k} - \nu x \right|} \frac{\partial f}{\partial x} \ , \tag{4.2.7}$$

(oscillation frequency is assumed to satisfy the resonance condition of $\omega = 1 + k\,\nu\,x$, the imaginary part of frequency γ is assumed to be small), which corresponds to the diffusion over the angle variable with a fixed velocity modulus. The growth of magnetic field perturbations is described by the equation

$$\frac{\partial \left| \vec{B}_k^1 \right|^2}{\partial t} = 2\gamma \left| \vec{B}_k^1 \right|^2 \ . \tag{4.2.8}$$

Solving equations (4.2.3), (4.2.7), and (4.2.8) for the initial distribution function of Fig. 4.4b with $\beta_{i\perp} \sim 1$ and small perturbations $\vec{B}_k^1$ set in a wide range of wave numbers *k* has shown [4.8] that, in this case, the IDF becomes isotropic, although relatively slowly, over a period hundreds of times greater than the ion gyro time. The analysis of noise development has shown that the peak spectral noise density shifts from the initial wave number corresponding to the maximum increment in Fig. 4.5 towards smaller wave numbers $k \sim 1$.

As applied to the MAGO chamber plasma, that time is not very long and equals tenths of a microsecond, which is short compared with the characteristic time of a neutron pulse (see, for example, Fig. 2.5). In addition, if we consider plasma heating as a result of anomalous friction at the plasma chamber nozzle, this heating should result in predominant ion heating (Section 5.3), which should result in the growth of $\beta_{i\perp}$ and, according to (4.2.5), correspondingly faster growth of the instability and hence faster isotropization of the distribution function. Thus, the investigated instability growth can explain the absence of anisotropy in the spectra of the main body of thermonuclear neutrons in Burenkov *et al.* [4.13].

4.3. Two-Dimensional Hybrid Simulations

As we showed in Section 4.1, for Mach numbers that are not very large, the effects of plasma resistivity and Joule heating must be taken into account when considering CSW structure, and, according to Section 4.2, two-dimensional (2D) effects can play a major role in that structure. In this section, we study CSWs in the 2D approximation, with allowance for anomalous resistivity for a plasma in which the initial β value is equal to zero for electrons and is small but nonzero for ions.

4.3.1. Physical Model

Plasma flow is assumed to be 2D, and a CSW is assumed to propagate along the *x*-axis; all of the quantities are functions of *x* and *z* because of the presence of perturbations in the *z*-directions. The magnetic field and particle velocities can have all three components.

Electrons will be described using the same hydrodynamic variables as in Section 4.1, and ions will be treated within the kinetic approach with the same designations as in Section 4.1. As before, we assume that the plasma is quasi-neutral ($n = n_i$) ($n = n_i$).

Equations (4.1.1–4.1.5) in the 2D case are written as

$$m_i \frac{d\vec{v}}{dt} = e\left(\vec{E} + \frac{1}{c}[\vec{v}\,\vec{B}]\right) - e\eta\vec{j}\,, \tag{4.3.1}$$

$$-en\left(\vec{E} + \frac{1}{c}[\vec{v}_e\,\vec{B}]\right) - \nabla p_e + en\eta\vec{j} = 0\,, \tag{4.3.2}$$

$$\frac{\partial\left(\frac{3}{2}p_e\right)}{\partial t} = \mathrm{div}\left(-\frac{3}{2}\vec{v}_{ex}p_e + \chi\nabla T_e\right) - p_e\,\mathrm{div}\,\vec{v}_e + (1-\alpha)\eta j^2\,. \tag{4.3.3}$$

Similarly to the 1D simulations, we assume that a small fraction of Joule heating α is spent on ion heating, with the term of (4.1.6) added accordingly to the right-hand side of Eq. (4.3.1).

The Maxwell equations have the usual form

$$\mathrm{rot}\,\vec{B} = -\frac{4\pi}{c}\vec{j}\,, \tag{4.3.4}$$

$$\frac{\partial\vec{B}}{\partial t} = -c\,\mathrm{rot}\,\vec{E}\,. \tag{4.3.5}$$

The 2D problem is defined by equations (4.3.1–4.3.5) written in x, z-coordinates with the quantities η, χ, and α as described in Section 4.1.

4.3.2. Problem Statement

We studied the problem of a CSW in time-dependent formulation and assume that, as with the 1D simulations, there is an ideally conducting, rigid piston at $x = 0$ with an initially uniform plasma flowing onto it at a velocity of $-\mu$. To introduce perturbations, ions were assumed to be reflected off the piston as off a surface with a slope

$$\frac{dx}{dz} = 0.05\sin\frac{\pi z}{2z_0}\,,$$

where $2z_0$ is the width of the computation region in the z-direction and, despite the surface slope assumed for the process of ion reflection, the surface itself was considered flat. In simulations, the boundary points $z = z_0$ and $z = -z_0$ were assumed to be related through the periodicity conditions. Due to the problem's nonlinearity and instability, assigning a perturbation in the form of a single mode resulted in the generation of various shorter wavelength perturbation modes in the course of a run.

We shall express values in the units defined at the beginning of this Chapter, and as in Section 4.1, we assume that $\beta_{e0} = 0$, $\beta_{i0} = 0.01$.

The major difficulty in the numerical simulations of this problem involves the necessity of resolving small spatial scales near the CSW front. According to the 1D simulations in Section 4.1, the spatial mesh Δx of the grid used to compute average plasma variables (density, velocity, temperature, etc.) should meet the condition $\Delta x \le 0.5\frac{a}{u}$ (for the units adopted). For the 2D simulations, this condition proves to be too cumbersome, so we did not adhere to it at all times, especially for CSW with high Mach numbers. 2D simulations with different meshes show that small departures from it do not lead to a considerable change in the results. That appears to be because CSW fronts in the 2D case are usually inclined with respect to the incident flow, and the effective velocity of the plasma flow onto the front proves to be smaller than M_A.

4.3.3. Simulation Results

Numerical simulations have shown that 2D effects are negligible for CSWs with $u = 1$, $M_A \cong 2$, which means that one can use 1D simulation results for CSWs with subcritical Mach numbers.

Two-dimensional effects become more pronounced starting with $u = 3$. That is illustrated in Fig. 4.6, which shows 2D reliefs of the magnetic field component β_z and plasma density n at the time $t = 15$, and Fig. 4.7, which shows the x-profiles of the following parameters: the z-averaged magnetic field component β_z and plasma density, their maximum and minimum values along the z-axis, and the maximum values of the magnetic field components $B_{x,y}$ along the z-axis (in our problem setup, these components are odd functions of z, and their maxima coincide in absolute value with their minima) for the same time. The results illustrated in Figs. 4.6 and 4.7 were obtained in the simulation performed with $z_0 = 5$, with the spatial steps of the mesh being $\Delta x = 0.05$ and $\Delta z = 0.1$. Figures 4.6–4.7 show that the magnetic field oscillations excited downstream of the CSW front are characterized by amplitudes $\delta B_x \sim \delta B_y \sim 0.2$, and the oscillations of δB_z along the x-direction have approximately the same wavelength as those in the 1D case and a somewhat smaller amplitude.

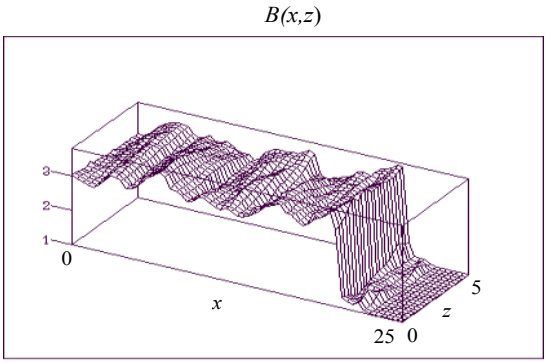

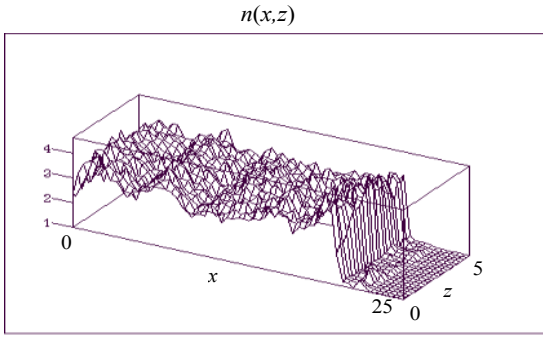

Fig. 4.6. Reliefs of the magnetic field component B_z and plasma density n for a CSW with u =3 at the time t =15.

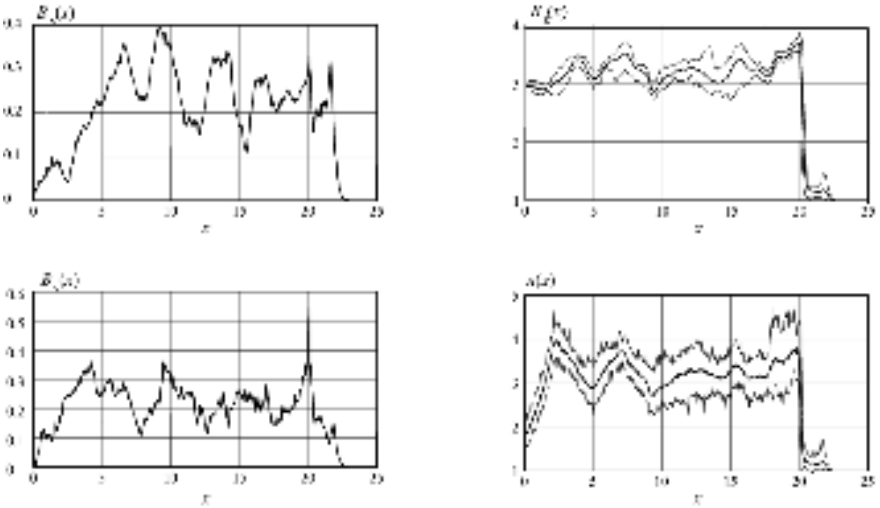

Fig. 4.7. The x-profiles of the maximum values (along the z-axis) of the magnetic field components $B_{x,y}$, the maximum, minimum, and averaged values (along the z-axis) of magnetic field component B_z, and plasma density n for a CSW with u = 3 at the time t = 15.

The amplitude distribution of the magnetic field oscillation modes downstream of the front as functions of the harmonic number m (reflecting dependence on z of the form $\exp(2\pi imz / z_0)$ is depicted in Fig. 4.8a and shows that excited downstream of the front are, primarily, the first three harmonics of B_x, B_y oscillations with characteristic wave numbers of $k \sim 1$, which is in rough agreement with the results of quasi-linear approach of Section 4.2. The characteristic mode amplitudes of oscillations of different harmonics in the x and y directions differ by no more than a factor of two. In this sense, there is isotropy for oscillations in these directions downstream of the front.

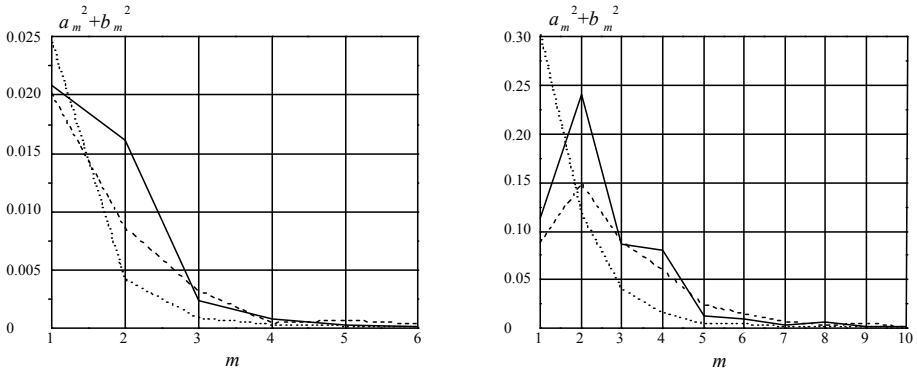

a) b)

Fig. 4.8. Squared amplitudes of the modes of the magnetic field oscillations downstream of the front for CSWs with u = 3 (a) and u = 6 (b) at the time t =15. Solid, dashed, and dotted curves show the squared amplitudes of B_x, B_y, and B_z, respectively.

The ion distributions in the phase planes (x, v_x) and (x, n_y) of Fig. 4.9 have an oscillatory structure and show the presence of ions reflected from the front. The ion distribution in the phase plane x, n_z indicates a trend of broadening with distance from the front—the process of noise-induced isotropization of the distribution function discussed in Section 4.2. On the whole, however, the 2D wave propagation pattern in Figs. 4.6–4.9 for $u = 3$ is qualitatively close to the 1D pattern, and for this supercritical CSW the reflected ions, as with the 1D simulations, are manifested both in the phase planes and on the graphs of the magnetic field $B_z(x)$ and density $n(x)$ profiles in the form of the foot and the overshoot. The 2D simulations, as with the 1D simulations, show the unsteady, pulsating nature of wave propagation.

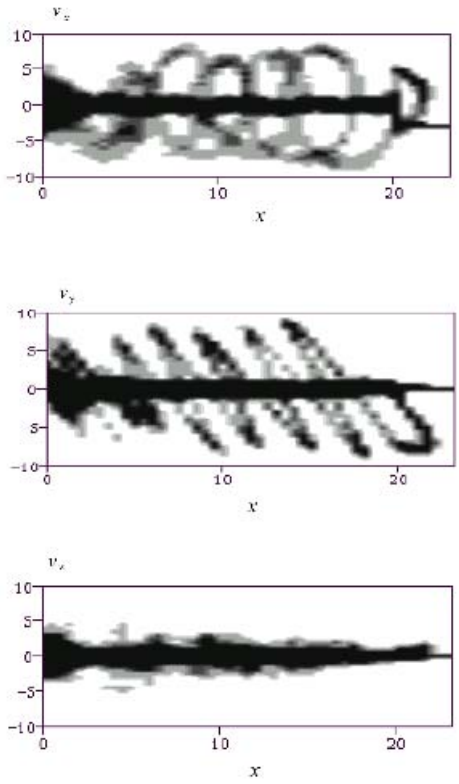

Fig. 4.9. Ion distribution in the phase planes (x, v_x), (x, v_y), and (x, v_z for a CSW with u = 3 at the time t = 15.

In the case of a CSW with $u = 6$, the 2D effects become substantial. The reliefs of the magnetic field component B_z and plasma density (Fig. 4.10) from the simulations with z_0=10.5, Δx =0.06, and $\Delta_Z = 0.3$ illustrate an essentially 2D CSW structure, which is particularly distorted in the front region and is similar to the wave structure calculated by Thomas [4.5] for M_A ~13, $\beta_{eo} = 4$, $\beta_{i0} = 0.5$ and zero plasma resistivity. The profiles of the maximum, minimum and average values for the magnetic field component B_k and plasma density along the z-axis in Fig. 4.11 show that the magnetic field oscillations excited at the CSW front have characteristic amplitudes of $\delta B_x \sim \delta B_y \sim 3$ and somewhat higher values of δB_z, δn, (which is related to the z-nonuniformity of the density and B_z overshoot, which forms when the incident ion flow is reflected from the front, and to the distortion of the shape of the CSW front). Those oscillations are dampened downstream of the front and have a relatively small value of $\delta B_x \sim \delta B_y \sim \delta B_z \sim 0.8$. Figures 4.10–4.11 show the damping of oscillations with distance from the front.

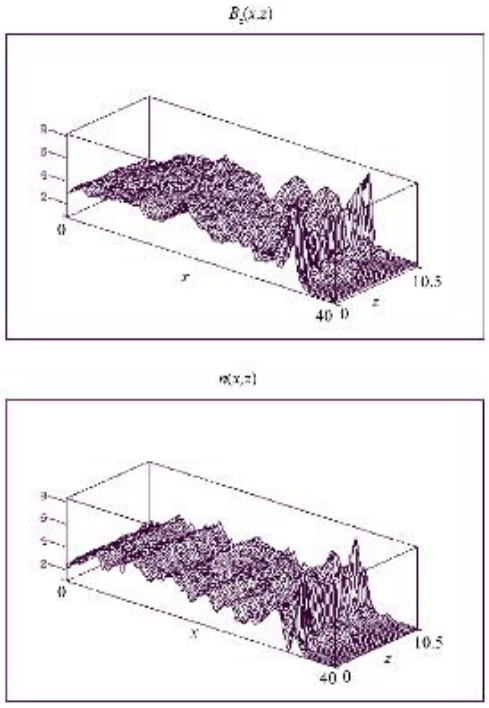

Fig. 4.10. Reliefs of the magnetic field component B_z and plasma density n for a CSW with u = 6 at the time t = 15.

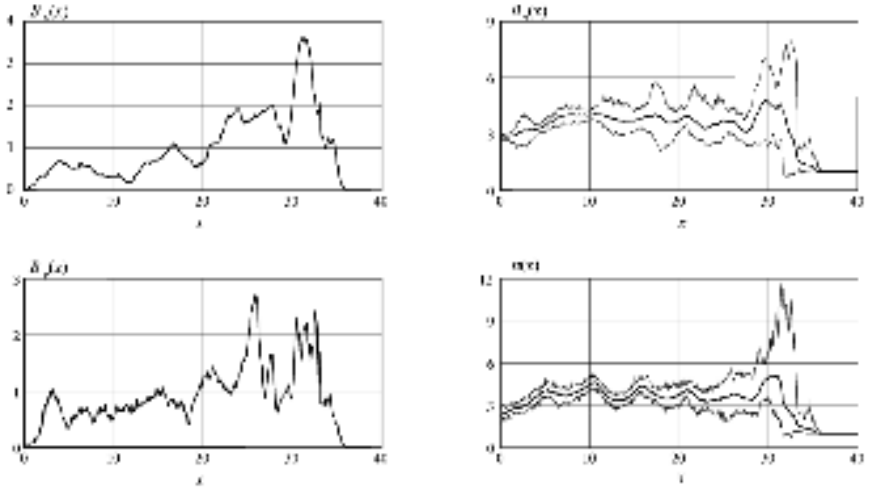

Fig. 4.11. The x-profiles of the maximum values (along the z-axis) of the magnetic field components $B_{x,y}$ and the maximum, minimum, and averaged values (along the z-axis) of the magnetic field component B_z and plasma density n for a CSW with u = 6 at the time t =15.

Figure 4.8b, which depicts the distribution of the modes of the magnetic field oscillations downstream of the front as functions of the harmonic along z, shows that the characteristic wave numbers of oscillations downstream, in this case $k \sim 0.9$, become somewhat smaller than those in the case of a CSW with u = 3, and similarly to the case of u = 3, there is isotropy for the oscillations of B_x, B_y.

The ion distributions in the phase planes (x, v_x) and (x, v_y) for $u = 6$ (Fig. 4.12) are seen to be more smeared than in the 1D case (Fig. 4.3) and when $u = 3$ (Fig. 4.9), and the reflected ion flows become less distinct as distance from the front increases. This is attributed to the larger role of the two-dimensionality in this case than in the case of u =3 and the loss of coherence for regions with different coordinates z. The ion distribution in the phase plane (x, v_z) roughly maintains its width with increasing distance from the front (i.e., the ions acquire their velocities v_z near the front and more or less maintain them at greater distances).

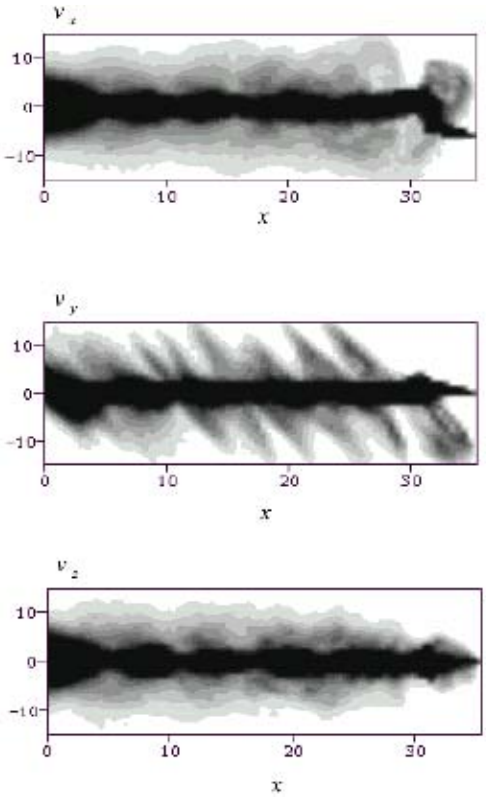

Fig. 4.12. Ion distribution in the phase planes (x, v_x), (x, v_y), and (x, v_z) for a CSW with $u = 6$ at the time $u = 15$.

The presence/absence of ions reflected from the shock front is also established by the IDFs downstream of the front, which are shown in Fig. 4.13 for the two CSWs under discussion at the time $t = 15$. To eliminate the effect of the zones near the piston and the shock front, the distribution function was calculated for the region $x_1 = 0.1x_F < x < 0.9x_F = x_2$, where x_F is the CSW front coordinate. Since the Larmor gyration results in the equalization of the velocity components v_x and v_y, the figure depicts the IDFs with respect to the total velocity, $f(v)$, and modulus v_z, such that $f(v)dv$ and $f(nz)dv_z$ are equal to the proportions represented by the ions in the interval of velocities dv and $d|v_z|$. Along with the IDFs, Fig. 4.13 shows the functions $v^2 f(v)$ and $v_z^2 f(v_z)$, which represent the velocity distribution of the ion kinetic energy. One can see from Fig. 4.13 that, as with the 1D case (Fig. 4.4), the ions that have been reflected from the front have very high velocities, and, although the proportion represented by such ions is small, they make the principal contribution to the thermal energy of ions downstream of the front. By comparison with the 1D case, however, for a CSW with $u = 6$, the peak of the function $v^2 f(v)$, which corresponds to the reflected particles, is shifted towards smaller velocities v, possibly because of the 2D modulation of the CSW front and the corresponding reduction in the effective velocity of the plasma flow onto the front. The ion distribution over velocities v_z shows that the distribution function for a CSW with $u = 3$ undergoes almost no isotropization on the time scales under consideration, and that isotropization is pronounced only in the range of low velocities corresponding to the main (non-reflected) ion flow. For the case of a CSW with $u = 6$, the distribution function shows rather high isotropization, and, as the results in Section 4.2 suggest, the rate of the isotropization is higher for the small velocity range.

The principal simulation results characterizing the plasma state downstream of the CSW front are summarized in Table 4.2, which shows the following quantities:

the computed Alfven-Mach number defined as $M_A = x_F / t + u$, where x_F is the shock front coordinate at t = 15;

the average magnetic field $\overline{B}_z$ downstream of the shock front (in the region $x_1 < x < x_2$) or compression ratio downstream of the front; fractions of the internal energy downstream of the shock front for different degrees of freedom: thermal energy of the electron component W_e, the ion thermal energy $W_{i\perp}$ for velocity components x, y, the ion thermal energy W_{iz} for

velocity component z, and the energy contained in the magnetic field oscillations downstream of the front $W_B \sim \int_{x_1}^{x_2} \left(\frac{B^2}{2} - \frac{\overline{B}_z^2}{2} \right) dx$;

the ion velocity v_m v_m corresponding to the median kinetic energy (the velocity that bisects the area under the curve $v^2 f(v)$); the ratio of squared median velocity v_m to the average squared thermal velocity of ions v_{Ti}^2 .

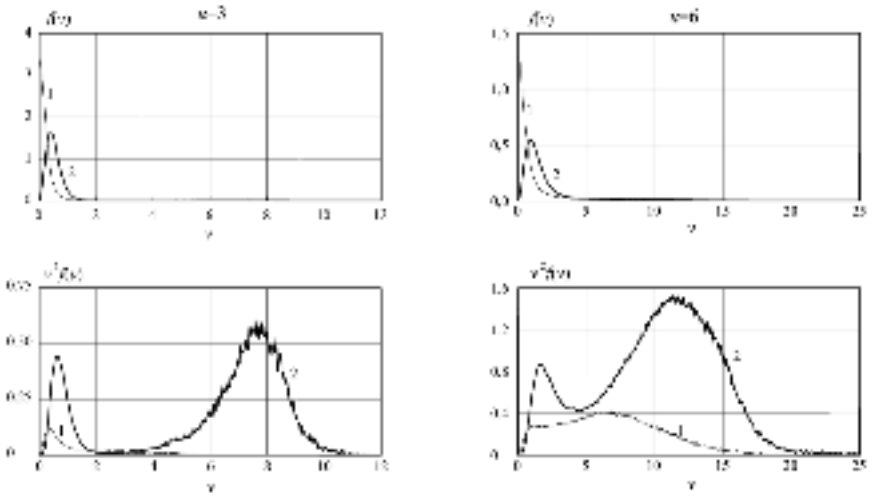

Fig. 4.13. Ion distribution f (v) over total velocity and the velocity distribution $v^2 f$ (v) of the ion kinetic energy (curves 2), and distributions f (v_z) and $v_z^2 f(v_z)$ over the modulus v_z (curves 1) downstream of the CSW front for the incident plasma flow velocities u =3 and u =6.

Table 4.2. Plasma State Downstream of Collisional Shockwave (CSW).

u	M_A	$\overline{B}_z$	W_e (%)	$W_{i\perp}$ (%)	W_{iz} (%)	W_B (%)	v_m	v_m^2 / v_{Ti}^2
3	4.36	3.18	75.4	22.4	1.9	0.3	7.2	29
6	8.17	3.72	51.3	35.5	12.5	0.7	11	7.3

The comparison of the data in Table 4.2 against the 1D simulation results presented in Table 4.1 shows that the 2D simulation for u = 3 yields nearly the same values for all the global plasma characteristics downstream of the front as does the 1D simulation. The results of the 1D and 2D simulations for u = 6, however, are considerably different. In the 2D simulations, the

values of M_A and $\overline{B}_z$ are close to the values determined by the Hugoniot with $\gamma = 5/3$, which is a result of the considerable isotropization of the IDF (the proportion of energy contained in the z component of velocity W_{iz} begins to be comparable with the proportions of energy in the x and y components of $W_{i\perp}/2$). As with the 1D simulations, the fraction accounted for by ion heating in the thermal energy of plasma equals about one-half for $u = 6$. As with the 1D simulations, the proportion represented by the magnetic field oscillations W_B in internal plasma energy turns out to be small for any u, despite the excitation of oscillations downstream of the front. And again, as with the 1D simulations, the ion spectrum for supercritical CSWs is rich with “superthermal" particles, which is shown by the ratio v_m^2 / v_{Ti}^2, although the median velocity v_m=11 for $u = 6$ is somewhat lower than in the 1D case, where it was v_m =13.

CONCLUSION

The role of 2D effects in the CSW structure is not particularly substantive for $M_A < 5$, and one can use 1D simulation results for such CSW (Section 4.1). For higher Mach numbers, the onset of instabilities and the 2D effects in the (x, z) plane play a very important role, especially in the vicinity of the CSW front, where large density and magnetic-field perturbations occur and magnetic-field components x and y are generated with an amplitude comparable to the perturbations of B_z. For large Mach numbers, the 2D effects cause isotropization of the IDF downstream of the CSW front and a decrease in the energy of the ions that have been reflected from the front. As with the 1D case, heating of the ion component is governed primarily by the ions that are reflected from the shock front and whose velocities downstream of the front are much higher than the ion “thermal” velocities.

4.4. Three-Dimensional Modeling

As shown by the results of three-dimensional modeling of CSWs with high Mach numbers (and with some additional restrictions, e.g., with the exclusion of any accounting of plasma electrical resistivity) [4.5], the presence of a third dimension introduces no fundamentally new physics; the simulation results are qualitatively and quantitatively close to those of the 2D simulations. In the 3D case, as with the 2D case, the instabilities developing downstream of the front leads to the equalization of the anisotropy of the ion temperature, which initially developed as a result of ion reflection from the front. We can hope that waiving the restrictions adopted by Thomas [4.5] would not change the conclusion on the qualitative and quantitative closeness of the 2D and 3D simulation results and that the 2D simulation results are applicable in the CSW description.

4.5. CSWs with Two Ion Species

In a multi-component plasma, where ions of different species have different charge-to-mass ratios z_i/m_i, those ions, moving in the same fields, will acquire different velocities, and a multi-velocity flow forms downstream of the front. Garanin examined a CSW in plasma with two ion species, zero resistance, and allowance for electron dispersion [4.18]. With a more realistic assumption of the presence of anomalous resistivity and zero electron dispersion, we can study such CSWs using numerical simulations in a hybrid model, as well as consider the question of whether a stationary solution can exist downstream of the resistive front where ions of different species gyrate in self-consistent fields. The case of small Mach numbers is of most interest for a plasma with several ion species, since at high Mach numbers a considerable portion of ions is reflected from the front, and the presence of several ion species should not change the general picture qualitatively. Since 2D effects do not exert much influence on CSWs with fairly small Mach numbers (as shown in Section 4.3), we will study a CSW with several ion types within a 1D setup.

4.5.1. Solution of Stationary Problem

A subcritical CSW in aninitially cold plasma with a single ion species is a resistive front (with the influence of some effective electron thermal conductivity). Downstream of the front, there is plasma with heated electrons and weakly heated ions, since the Joule heat for anomalous resistivity goes primarily to the heating of the electrons. The critical Alfven-Mach number for a purely resistive wave (for the electron adiabatic index $\gamma = 5/3$) is $M_* = 2.76$ (we will designate the Alfven-Mach numbers in this subsection by M), and when the electron thermal conductivity is taken into account, it is equal to $M_{**} = 3.46$ (see, for example, [4.19]).

We will consider the stationary structure of subcritical CSWs in plasma containing two ion species [4.7]. Downstream of the resistive front, those ions gyrate around each other. The multi-velocity flow that forms in such a solution should be unstable against stream instabilities; numerical simulations of CSWs in Section 4.5.2, however, show that such a solution lives for a long time. Important in that context is the question of the decay channels of such a solution and, accordingly, the final energy dissipation channels downstream of the front, i.e., the relative heating of the electron and ion components downstream of the front.

We will consider the structure of a transversal CSW in the rest frame of the shock front. The magnetic field is directed, as usual, along the z-axis, and the wave propagates along the x-axis. The set of equations describing the

structure of a stationary CSW in plasma with two ion species with the initial relative concentrations α_1 and α_2, includes the Maxwell equations

$$\frac{j}{\sigma} = \frac{c}{4\pi\sigma}\frac{\partial B}{\partial x} = \frac{v_{ex} B}{c} - E_y \ , \tag{4.5.1}$$

$$E_y = \text{const} = \text{M}\frac{c_A}{c} B_0 \ ;$$

the continuity equations for the ion components

$$n_1 v_{1x} = \text{const} = \alpha_1 \text{M} c_A n_0 \tag{4.5.2}$$

$$n_2 v_{2x} = \text{const} = \alpha_2 \text{M} c_A n_0 \ ; \tag{4.5.3}$$

the continuity equation for the electron component, which, when the quasi-neutrality condition $n_e = n_1 + n_2$ is taken into account, can be written in the form:

$$(n_1 + n_2) v_{ex} = \text{M} c_A n_0 \ ; \tag{4.5.4}$$

the equations of motion for the ion components,

$$m_i v_{ix} \frac{d v_{ix}}{d x} = e\left(E_x + \frac{v_{iy}}{c} B \right) , \tag{4.5.5}$$

$$m_i v_{ix} \frac{d v_{iy}}{d x} = e\left(E_y - \frac{v_{ix}}{c} B \right) - e\frac{j}{\sigma} \ ; \tag{4.5.6}$$

the equation of motion for the electron component,

$$-e n_e \left(E_x + \frac{v_{ey}}{c} B \right) - \frac{\partial p_e}{\partial x} = 0 \ , \tag{4.5.7}$$

where

$$n_e v_{ey} = n_1 v_{1y} + n_2 v_{2y} - \frac{j}{e} \ ;$$

and the equation for the electron energy

$$\frac{\partial}{\partial x}\left(-\frac{3}{2} v_{ex} p_e + \chi \frac{\partial T_e}{\partial x} \right) - p_e \frac{\partial v_{ex}}{\partial x} + \frac{j^2}{\sigma} = 0 \ .$$

In these equations, j is the current density, σ is the conductivity, B and $\vec{E}$ are the magnetic and electric fields, $\vec{v}_e$ and n_e are the electron velocity and electron density, $\vec{v}_i$ and n_i are the velocity and density of the ions of the i-th species, p_e and T_e are the electron pressure and electron temperature, χ is the electron thermal conductivity, n_0 and B_0 are the initial density and initial magnetic field, M is the Alfven-Mach number, and c_A is the initial Alfven velocity; it is assumed that for the electron gas $\gamma = 5/3$. Using the above basic equations, we can readily obtain the momentum and energy conservation laws:

$$m_1 n_1 v_{1x}^2 + m_2 n_2 v_{2x}^2 + p_e + \frac{B^2}{8\pi} = \left(\mathrm{M}^2 + \frac{1}{2}\right)\frac{B_0^2}{4\pi} \ , \qquad (4.5.8)$$

$$m_1 n_1 v_{1x} v_{1y} + m_2 n_2 v_{2x} v_{2y} = 0 \ , \qquad (4.5.9)$$

$$\frac{1}{2} m_1 n_1 v_{1x}(v_{1x}^2 + v_{1y}^2) + \frac{1}{2} m_2 n_2 v_{2x}(v_{2x}^2 + v_{2y}^2) + \frac{5}{2} p_e v_e - \chi \frac{dT_e}{dx} + \frac{c}{4\pi} E_y B$$

$$= \mathrm{M}\left(1 + \frac{\mathrm{M}^2}{2}\right) c_A \frac{B_0^2}{4\pi} \ . \qquad (4.5.10)$$

For M ~ 1 and $m_1 \sim m_2$, the characteristic spatial scale corresponding to the ion Larmor gyration is $\sim \frac{c_A}{\Omega_i} \sim \frac{c}{\omega_{pi}}$. On the other hand, according to the estimates given in Section 4.1 for the anomalous resistivity (and the corresponding electron thermal conductivity χ), the width of the CSW resistive front is much smaller than $\frac{c}{\omega_{pi}}$. This allows us to assume that a shock wave consists of a narrow resistive front where the ion gyration can be ignored and $v_{iy} = 0$, and of a subsequent structure where, over many periods of the ion gyration, the plasma resistivity and the heat conduction can be disregarded.

We will use the same dimensionless quantities as before: as the normalizing factors, we use density n_0, magnetic field B_0, velocity c_A, and mean ion mass $m = \alpha_1 m_1 + \alpha_2 m_2$. We express the time and length in units of the inverse initial ion gyrofrequency and of c / ω_{pi}, respectively (here, the ion gyrofrequency and the initial plasma frequency ω_{pi} are both expressed in terms of the mean ion mass). Using the condition of the magnetic field frozen into the electron component, which follows from disregarding the

resistance in (4.5.1), eliminating E_x by means of the equation (4.5.7), and disregarding the heat flux $-\chi\frac{\partial T_e}{\partial x}$ in the energy conservation law (4.5.10), we can write the equations (4.5.1–4.5.6) and (4.5.8–4.5.10), which determine the CSW structure downstream of the resistive front, as follows:

$$n_1 + n_2 = B\ , \tag{4.5.11}$$

$$n_1 u_{1x} = \alpha_1 \mathrm{M}\ , \tag{4.5.12}$$

$$n_2 u_{2x} = \alpha_2 \mathrm{M}\ , \tag{4.5.13}$$

$$B u_{ex} = \mathrm{M}\ , \tag{4.5.14}$$

$$m_i u_{ix}\frac{d u_{ix}}{d x} = -\frac{d B}{d x} - \frac{1}{B}\frac{d p}{d x} + (u_{iy} - \bar{u}_y) B\ , \tag{4.5.15}$$

$$m_i u_{ix}\frac{d u_{iy}}{d x} = -(u_{ix} - u_{ex}) B\ , \tag{4.5.16}$$

$$m_1 n_1 u_{1x}^2 + m_2 n_2 u_{2x}^2 + p_e + \frac{B^2}{2} = \mathrm{M}^2 + \frac{1}{2}\ , \tag{4.5.17}$$

$$\alpha_1 m_1 u_{1y} + \alpha_2 m_2 u_{2y} = 0\ , \tag{4.5.18}$$

$$\frac{\mathrm{M}}{2}\alpha_1 m_1 (u_{1x}^2 + u_{1y}^2) + \frac{\mathrm{M}}{2}\alpha_2 m_2 (u_{2x}^2 + u_{2y}^2) + \frac{5}{2} p_e u_e + \mathrm{M} B = \frac{\mathrm{M}^3}{2} + \mathrm{M}\ , \tag{4.5.19}$$

where $\bar{u}_y B = n_1 u_{1y} + n_2 u_{2y}$ (we denote the dimensionless velocities by the letter u and keep the above notations for the remaining quantities).

The plasma state immediately downstream of the resistive front can be determined from the condition $u_{iy} = 0$, equations (4.5.7–4.5.14, 4.5.17, 4.5.19), and the condition

$$m_2 u_2^2 - m_1 u_1^2 = \mathrm{M}^2 (m_2 - m_1)\ ,$$

which follows from (4.5.5) when ν_{iy} is disregarded. Using this initial plasma state as a boundary condition, we can obtain the CSW structure downstream of the resistive front by integrating the equations (4.5.11-4.5.19) and taking into account the fact that the pressure changes adiabatically downstream of the resistive front ($p_e \sim B^\gamma$). It is clear *a priori* that the wave structure will be periodic, since all of the quantities are determined from the conservation laws as functions of only one parameter (e.g., u_{1y}); and correspond to the above boundary plasma state at one of the points, where $u_{1y} = 0$. Integrating

the equation (4.5.16), divided by u_{ix}, we obtain the averaged density of each ion component (over the period of the wave structure), $\overline{n}_i = \alpha_i \overline{B}$, which implies that there will be no separation of different ion species in the wave.

In describing the ion motion downstream of the resistive front, we assume that the ion temperature is zero. It is of interest to consider what will happen with the ions whose energy is slightly different from the energy of the main stream. Linearizing the equations of motion (4.5.15–4.5.16), we obtain, for the purposes of describing the ions, a system of two first-order linear equations with periodic coefficients. This system can be reduced to the equation for small oscillations with periodically varying parameters. Depending on conditions, these equations may have either solutions with a nonincreasing amplitude or increasing solutions (the parametric resonance) [4.20]. In the first case we can determine how much, on average, the "temperature" (i.e., the energy spread) grows beyond the resistive front for each of the streams. The second case corresponds to the onset of an instability, and the increment of this instability can be determined.

Let us consider a plasma with two ion species whose masses differ by a factor of 1.5, $m_1 = 0.8$ and $m_2 = 1.2$, and whose initial concentrations are the same $\alpha_1 = \alpha_2 = 0.5$ (e.g., a DT plasma). Our calculations show that, in such a plasma, the critical Alfven-Mach number for a purely resistive wave is $M_* = 2.637$ and, with allowance for the electron heat conduction, it is equal to $M_{**} = 3.128$.

Figures 4.14 and 4.15 show the profiles of the ion densities, magnetic field, and ion velocitiesm u_{ix} and u_{iy} obtained by integrating the equations (4.5.11-19) numerically for CSWs with M = 2 and $M = M_{**} = 3.13$. We can see that the ion densities and velocities u_{ix} experience large-amplitude oscillations, whereas the amplitude of the magnetic filed oscillations is small. It is noteworthy that the oscillation amplitudes of the density and velocity u_x of the heavier ion component exceed those of the lighter component, although intuitively it would seem more difficult to swing the heavier mass. This effect, however, can be explained if we consider that, owing to the momentum conservation law, the heavier component exerts more of an effect on the magnetic field, enhancing the field in the regions of its low velocities u_{ix} and, accordingly, its higher densities. But enhancing the field requires increasing the density of both components, thereby increasing the oscillation amplitude of the heavier component and reducing that of the lighter one.

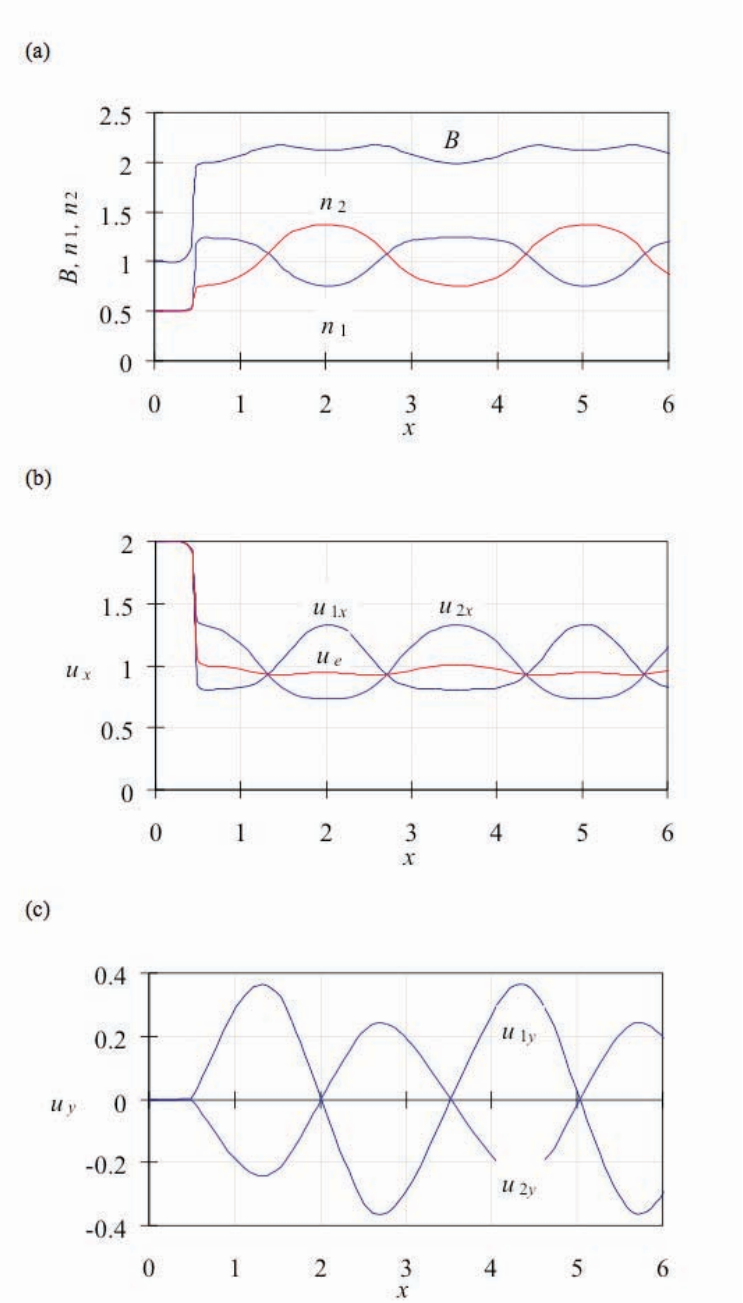

Fig. 4.14. CSW with M = 2: (a) profiles of the ion densities n_1 and n_2 and magnetic field B(x), (b) profiles of the ion (u_{1x} and u_{2x}) and electron (u_{ex}) velocities, and (c) profiles of the ion velocities u_{1y} and u_{2y}.

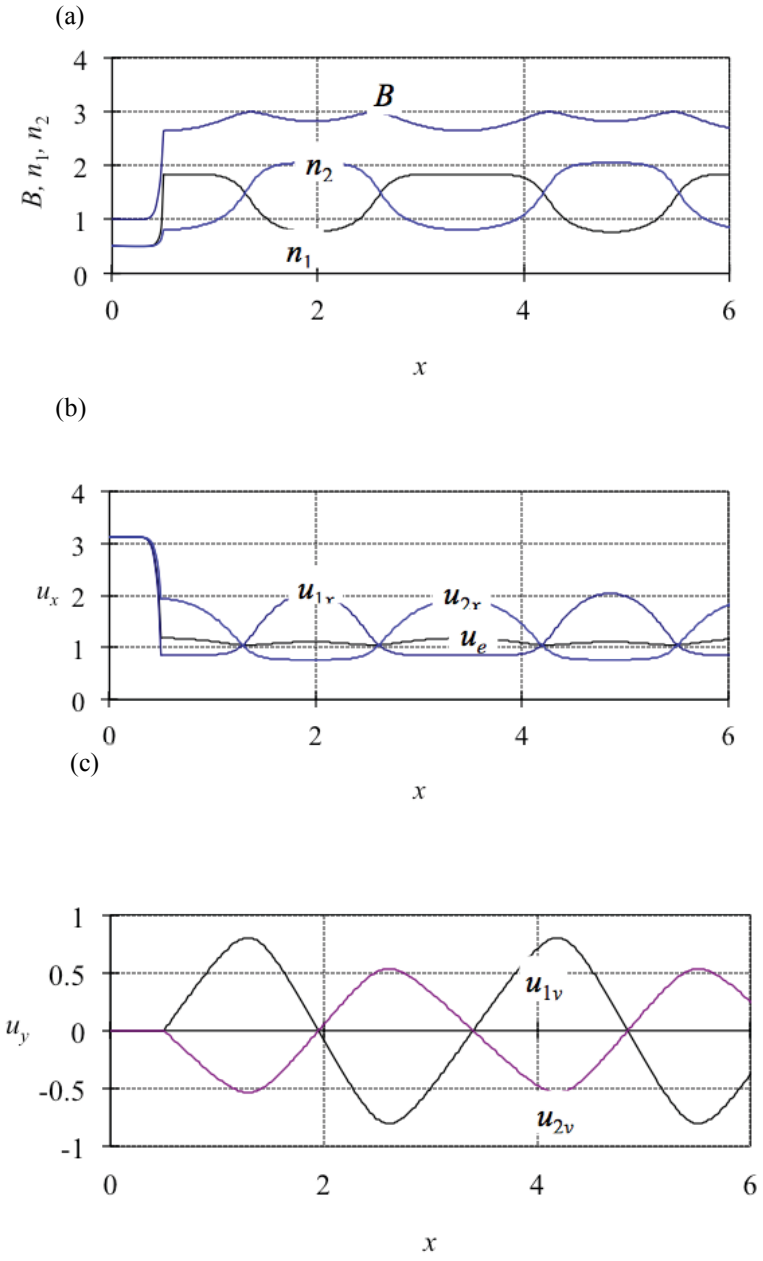

Fig. 4.15. CSW with M = 3.13: (a) profiles of the ion densities n_1 and n_2 and magnetic field B(x), (b) profiles of the ion (u_{1x} and u_{2x}) and electron (u_{ex}) velocities, and (c) profiles of the ion velocities u_{1y} and u_{2y}.

A study of the behavior of particles whose velocities differ slightly from the velocity of the main stream shows that, at small Alfven-Mach numbers M, their motion is stable. As M increases, the heavier ions first, and then the lighter ions, enter into parametric resonance with the wave. The critical Alfven-Mach numbers of these transitions are $M_{2*} = 2.278$ and $M_{1*} = 2.605$ for the heavier and lighter ions, respectively. The deviation δu_x of the velocities of the both ion species from the velocities of the two main streams, as a function of the x coordinate for both stable ion motion and parametric resonance, is illustrated by Fig. 4.16 for the Alfven-Mach number M = 2.5, which is subcritical for the lighter ions and supercritical for the heavier ones.

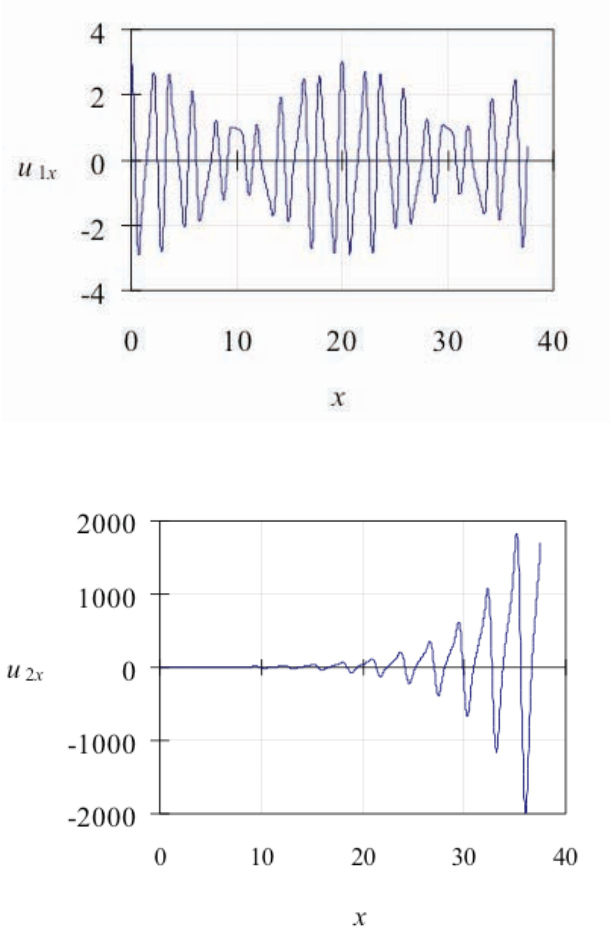

Fig. 4.16. Deviations δu_{ix} of the ion velocities from the velocities of the two main streams for lighter and heavier ion components for a CSW with M = 2.5.

Table 4.3 gives some of the calculated characteristics of the plasma state downstream of the CSW front, as functions of Alfven-Mach number:

- the Alfven-Mach number M;
- the oscillation period, X_p;
- the mean magnetic field $\overline{B}$ downstream of the wave front;
- the distribution of the internal plasma energy downstream of the wave front in terms of different degrees of freedom: the thermal energy of the electron component W_e, the mean kinetic energies W_{ix} and W_{iy} of the ion species in the x and y directions relative to the mean plasma velocity downstream of the front, and the energy $W_B \sim \int \left(\frac{B^2}{2} - \frac{B_1^2}{2} \right) dx$ of the magnetic field oscillations downstream of the front;
- the amplification factors k_i of the temperatures of ion components in the case of stable motion of perturbed particles ($M < M_i$) or increments γ_i (per unit of length) for parametric resonance ($M > M_i$).

Table 4.3. Plasma State Downstream of CSW as Function of M.

M	X_p	B	(W_e %)	W_{1x} (%)	(W_{2x} %)	W_{1Y}(%)	W_{2y}(%)	W_B(%)	k_1/γ_1	k_2 / γ_2
1.5	3.7	1.61	77.5	2.5	8.6	6.2	4.2	1.0	3	2.8
2	3.0	2.10	83.5	2.5	5.5	4.9	3.2	0.4	5.9	7/0
2.5	2.9	2.47	85.7	2.4	4.4	4.4	2.9	0.2	9.7/0	0.19
2.64	2.8	2.56	86	2.3	4.3	4.3	2.9	0.2	0.08	0.24
3	2.9	2.76	86.8	2.2	3.9	4.1	2.8	0.2	0.26	0.32
3.13	2.9	2.83	87.1	2.2	3.8	4.1	2.7	0.1	0.28	0.33

We should expect that as a result of the development of downstream instabilities and of dissipation, which leads to a homogeneous plasma state, the energy of the ion components will remain in the ions. Therefore, we can ascertain the final ratio of electron heating to ion heating in the CSW from the ratio of W_e to W_i. Table 4.3 shows that, for the Alfven-Mach numbers under consideration, the fraction accounted for by electron heating is the dominant fraction and even increases somewhat with M.

4.5.2. Results of One-Dimensional Simulations in the Hybrid Model

For 1D simulation of CSWs with two ion species, we used the same physical model and problem formulation as in Section 4.1, although, of course, the specific mass for each species was used in the equations of motion for the ions (4.1.1–4.1.2). The value of the anomalous resistivity, a, and the parameter α, which determines the fraction of the Joule heat spent on the ion heating, were the same. As in Section 4.5.2, we considered CSWs in plasma consisting of two ion species that differed in mass by a factor of 1.5 and had the same initial concentrations.

Figures 4.17 and 4.18 show the ion distribution in the x, v_x and x, v_y phase planes and the magnetic-field and density profiles of both ion components at $t = 10$ for $u = 1$ and $u = 3$.

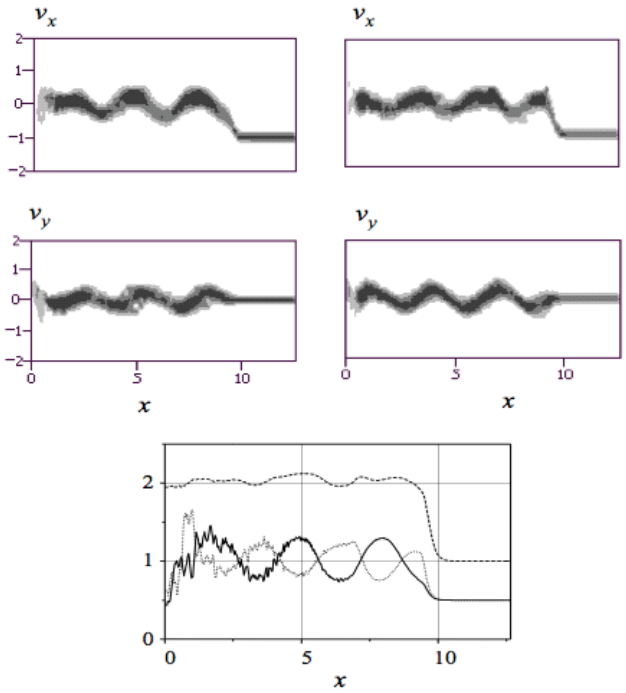

Fig. 4.17. The distributions of ions in the x, v_x and x, v_y phase planes and the magnetic-field and ion density profiles for CSWs with two ion species with identical initial concentrations and a mass ratio of 1/1.5 for an incident plasma velocity of u =1 at t =10. On the graphs for the distribution of ions in the phase planes: left distribution of heavy ions; right, distribution of light ions. On the graph of the magnetic-field and density profiles: the dashed line represents the magnetic field B(x); the solid line represents the density of the heavy ions; the dotted line represents the density of the light ions.

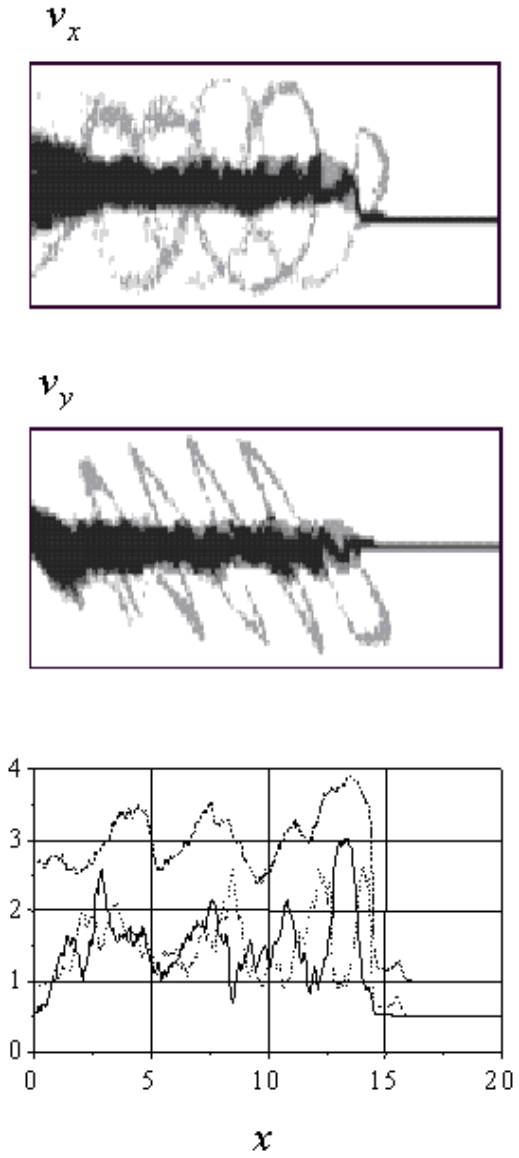

Fig 4.18. The distributions of ions in the x, v_x and x, v_y phase planes and the magnetic-field and ion density profiles for CSWs with two ion species with identical initial concentrations and a mass ratio of 1/1.5 for an incident plasma velocity of u =3 at t =10. The dashed line represents the magnetic field B(x); the solid line represents the density of the heavy ions; the dotted line represents the density of the light ions.

The functions of the ion velocity distribution downstream of the front for these CSWs at t = 10 are shown in Fig. 4.19.

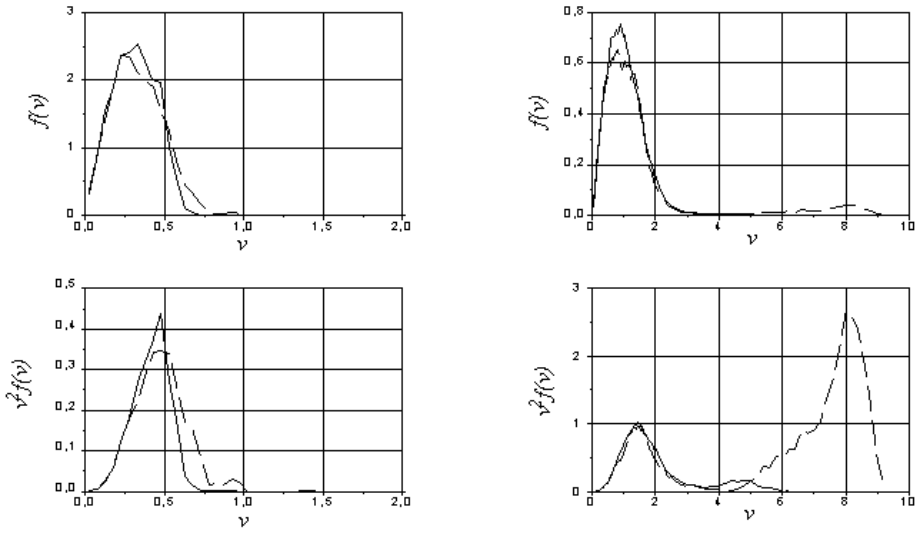

(a) $u = 1$ (b) $u = 3$

Fig. 4.19. Ion velocity distribution functions f (v) and the velocity distribution of the ion kinetic energy $v^2 f(v)$, downstream of the CSW front, with two ion species with identical initial concentrations and a mass ratio of 1/1.5 for an incident plasma velocity of (a) u =1 and (b) u =3. The solid lines represent heavy ions, and the dashed lines represent light ions.

The last two lines of Table 4.1 present the basic results of simulations of CSWs with two ion species, and v_y was determined for the lighter ions, which are more readily reflected from the spikes of the magnetic field.

Figure 4.17, for $u = 1$, shows that, in the subcritical regime, with two ion species, there are, just as in the problem with a single ion species, no reflected ions, and the CSW has a stationary structure. However, with ions of different species, the CSW pattern manifests substantive qualitative peculiarities. At the resistive front, different components that have different masses, when moving in the same field, acquire different velocities v_x. As a result, in accordance with the stationary solution of Section 4.5.1, Larmor gyration of ions of different species downstream of the resistive front begins around a common center of mass, and a stationary, two-stream movement forms within the system of the front. Observed downstream of the wave front is a periodic structure with large periodic oscillations of the densities

of ions of different species and with the magnetic-field oscillations that are more noticeable than those in Fig. 4.1. The presence of the two-stream movement downstream results in a considerable increase in the ion-heating fraction by comparison with the case of one ion species, as is seen from data presented in the table. From Fig. 4.19, we see that there are no superthermal particles in the ion spectra, and that Fig. 4.19 and Table 4.1 show that the heating of the light ions and that of the heavy ions are of the same order.

Figure 4.18 shows the reflection of ions at the front for supercritical CSWs ($u = 3$), and only the lighter ions are reflected from the front; whereas all the heavy ions passed through the CSW front are inside a diffuse beam in the phase plane. Figure 4.19 also shows the presence of a large fraction of the superthermal ions (in which most of the energy is contained) in the light component. As is shown in Table 4.1, the fraction of the ion heating is more than twice as large it is in the case of a single ion species and is about a half of the total plasma heating downstream of the CSW front.

CONCLUSION

In a plasma with two ion species a subcritical CSW has, downstream of the resistive front, a stationary, periodic structure with two flows corresponding to the two ion species. For plasma consisting of the ions that differ in terms of the charge-to-mass ratio by a factor of 1.5 and have the same concentrations, the critical Alfven-Mach number for a purely resistive wave is $M_* = 2.637$ and, when accounting for electron heat conduction, $M_{**} = 3.128$.

A two-stream CSW at the Alfven-Mach numbers above a certain value is unstable because of the onset of the parametric resonance, which leads to a thermal spread of the initially cold ions.

In a supercritical CSW, only the lighter ion species is reflected from the front, and the reflection is more intense than in a single-species CSW.

For any type of CSW (subcritical and supercritical), the fraction of ion heating is larger than with a plasma with a single ion species.

REFERENCES

4.1 R.Z. Sagdeyev. "Collective Processes and Shock Waves in Low-Density Plasma," Voprosy teorii plazmy: Sb. Statey (Reviews of Plasma Physics: Collection of Papers). Ed. M. A. Leontovich. Moscow: Atomizdat [Publishing House], Vol. 4, pp. 20–80, 1964.

4.2 D. Biskamp. "Collisionless Shock Waves in Plasmas," *Nucl. Fusion,* Vol. 13, No. 5, pp. 719–740, 1973.

4.3 Yu.A. Berezin, V.A. Vshivkov. "Arbitrary-Amplitude Shock Waves in Low-Density Plasma with Magnetic Field," *Fizika Plasmy* [Plasma Physics], Vol. 3, No. 2, p. 365 (*Sov. J. Plasma Phys.,* Vol. 3, p. 207) 1977.

4.4 M.M. Leroy, D. Winske, C.C. Goodrich, C.S. Wu, K. Papadopoulos. "The Structure of Perpendicular Bow Shocks," *J. Geophys. Res.,* Vol. 87, No. A7, pp. 5081–5094, 1982.

4.5 V.A. Thomas. "Dimensionality Effects in Hybrid Simulations of High Mach Number Collisionless Perpendicular Shocks," *J. Geophys. Res.,* Vol. 94, No. A9, pp. 12009–12014, 1989.

4.6 S.F. Garanin, A.I. Golubev, N.A. Ismailova. "One-Dimensional Hybrid Simulation of Transverse Collisionless Shock Waves," *Plasma Phys. Reports,* Vol. 25, No. 10, pp. 794–802 (Translated from *Fizika Plasmy,* Vol. 25, No. 10. pp. 862–871), 1999.

4.7 O.M. Burenkov, S.F. Garanin. "Shock Wave Structure in a Cold Collisionless Plasma with Two Ion Species in a Magnetic Field," *Plasma Phys. Reports,* Vol. 25, No. 8, pp. 637–641 (Translated from *Fizika Plasmy,* Vol. 25, No. 8. pp. 695-699), 1999.

4.8 S.F. Garanin, S.D. Kuznetsov. "Time Evolution of the Ion Distribution Function in the Perpendicular Collisionless Shock Wave," *Physica Scripta,* Vol. T84, pp. 154–155, 2000.

4.9 S.F. Garanin, A.I. Golubev, N.A. Ismailova. "Two-Imensional Modeling of a Transverse Collisionless Shock Wave." *Plasma Phys. Reports,* Vol. 26, No. 5, pp. 397-404; *Fizika Plasmy,* Vol. 26, No. 5. pp. 426-433), 2000.

4.10 V.P. Bashurin, S.F. Garanin, A.I. Golubev. "Numerical Modeling of a Shock Wave with an Infinite Mach Number in Collisionless Magnetized Plasma," *VANT* [Aspects of Atomic Science and Technology]. Methods and Programs for the Numerical Solution of Problems of Mathematical Physics Series, No. 2(13), pp. 21–28, 1983.

4.11 S.F. Garanin and A.I. Golubev. “Study of Transverse Waves in Collisionless Magnetized Plasma,” *VANT,* Theoretical and Applied Physics Series, No. 1, pp. 18–25, 1985.

4.12 P.H. Yoon. "Quasilinear Evolution of Alfven-Ion-Cyclotron and Mirror Instabilities Driven by Ion Temperature Anisotropy," *Phys. Fluids B,* Vol. 4, No. 11, pp. 3627–3637, 1992.

4.13 O.M. Burenkov, V.B. Yakubov, S.F. Garanin, A.N. Demin, V.I. Dudin, V.P. Korchagin, I.V. Morozov, V.N. Mokhov, E.S. Pavlovskii, V.K. Chernyshev. "Study of Plasma in MAGO Chamber in Terms of Neutron Self-Radiation,” *Fizika Plasmy,* (Russian Plasma Phys. Reports), Vol. 23, No. 3, pp. 203–209, March 1997.

4.14 L.A. Artsimovich, R. Z. Sagdeyev. *Fizika Plazmy Dlya fizikov* (Plasma Physics for Physicists). Moscow; Atomizdat [Publishing House], 1979.

4.15 E.M. Lifshits, L.P. Pitayevsky. *Fizicheskaya Kinetika* [Physical Kinetics]. Moscow: Nauka [Publishing House], 1979; Oxford: Pergamon, 1980.

4.16 A.F. Aleksandrov, L.S. Bogdankevich, A.A. Rukhadze. *Osnovy Electrodinamiki Plasmy* (Fundamentals of Plasma Electrodynamics). Moscow: Vusshaya shkola [Publishing House], 1978.

4.17 A.I. Akhiyezer, I.A. Akhiyezer, R.V. Polovin, A.G. Sitenko, K.N. Stepanov. *Elektrodinamika Plazmy* (Plasma Electrodynamics). Moscow: Nauka [Publishing House], 1974.

4.18 S.F. Garanin. “Study of Shock Wave in Collisionless Magnetized Plasma with Two Ion Species,” *VANT,* Theoretical and Applied Physics Series, No. 2, pp. 12–16, 1985.

4.19 A.L. Velikovich, M.A. Liberman. *Fizika Udarnykh Voln v Gazah i Plazme* (Physics of Shock Waves in Gases and Plasma). Moscow: Nauka [Publishing House], 1987.

4.20 L.D. Landau, E.M. Lifshitz. *Mekhanika* [Mechanics]. Moscow: Nauka [Publishing House], 1973; Pergamon, Oxford, 1976.

5. HALL EFFECT, DRIFT STREAMS, AND NEAR-ELECTRODE PLASMA FLOWS

5.1. Dynamics of Magnetic Field Penetration into Magnetized Plasma

An important role is played in the dynamics of magnetized plasma ($\omega_e\tau_e >> 1$) by the Hall effect—magnetic flux transport by current. Estimations of this effect suggest that, generally speaking, for non-one-dimensional problems, its influence on magnetic field dynamics should be $\omega_e\tau_e$-times greater than magnetic diffusion influence.

For plasma with small characteristic dimensions $a << c / \omega_{pi}$, at small characteristic times, $t << \omega_i^{-1}$, the ion motion can be disregarded (the case of electron magnetic hydrodynamics [5.1]) and, magnetic field dynamics are described by equations (4.3.4–4.3.5) and (4.3.2), which in the case of motionless ions has the form:

$$\vec{E} = \frac{1}{c}\left[\frac{\vec{j}}{en}, \vec{B}\right] + \vec{j}/\sigma - \nabla p_e / en \quad . \tag{5.1.1}$$

(p_e is electron pressure). For simplicity, we restrict ourselves to the model of isothermal plasma with constant conductivity and $p_e << B^2/8\pi$. In this case, the equation for the magnetic field is written as follows:

$$\frac{\partial \vec{B}}{\partial t} = -\mathrm{rot}\left[\frac{\vec{j}}{en}, \vec{B}\right] + \frac{c^2}{4\pi\sigma}\Delta\vec{B} \quad , \tag{5.1.2}$$

where the first term of the right-hand side describes the magnetic field transport by current, and the second term describes the magnetic diffusion. For this model, let us consider a 2D problem of magnetic field penetration into plasma [5.2]. Problems of this kind for some plasma density distributions have been solved analytically with a quasi-one-dimensional formulation [5.1] and numerically with a 2D stationary [5.3] formulation.

The diffusion term in (5.1.2) can be disregarded everywhere except the zones with high magnetic-field gradients, that is, magnetic-field jumps. Thus, the role of the diffusion term is reduced to, primarily, the spreading of magnetic-field jumps. In the zero approximation, the solution with the jumps can be built while disregarding the diffusion. In the next approximation, the problem of the spreading of the jumps attributed to diffusion is simplified by the fact that, near the jumps, it is sufficient to take into account just the derivatives in the direction perpendicular to a jump, since they make the chief contribution.

Now we will show that the problem with a purely azimuthal magnetic field and a density depending solely on r and z is, in the zero approximation, reduced to a plane problem. In fact, in this case, equation (5.1.2), in the absence of the diffusion term, can be written as

$$\frac{\partial B}{\partial t} = \frac{\partial}{\partial z}\left[\frac{cB}{4\pi enr}\frac{\partial}{\partial r}(rB)\right] - \frac{\partial}{\partial r}\left[\frac{cB}{4\pi en}\frac{\partial}{\partial r}B\right]$$

or, after the substitutions $I = rB$, $\nu = nr^2$, $\xi = \ln r$,

$$\frac{\partial I}{\partial t} = \left(\frac{\partial}{\partial \xi}\frac{I^2}{2}\right)\left(\frac{\partial}{\partial z}\frac{c}{4\pi e\nu}\right) - \left(\frac{\partial}{\partial z}\frac{I^2}{2}\right)\left(\frac{\partial}{\partial \xi}\frac{c}{4\pi e\nu}\right),$$

which is equivalent to the plane case

$$\frac{\partial B}{\partial t} = \left(\frac{\partial}{\partial x}\frac{B^2}{2}\right)\left(\frac{\partial}{\partial y}\frac{c}{4\pi en}\right) - \left(\frac{\partial}{\partial y}\frac{B^2}{2}\right)\left(\frac{\partial}{\partial x}\frac{c}{4\pi en}\right) \qquad (5.1.3)$$

For that reason, we limit ourselves hereinafter to an analysis of a planar problem.

Assume that, at the initial moment, a field $B_1 > B_0$ is applied to the boundary of plasma with the constant magnetic field B_0. We look for the solution of the equation (5.1.3) in the form

$$B = (B_1 - B_0)\eta(t - f(\vec{r})) + B_0 ,$$
$$\eta = \begin{cases} 0 & \text{at} \quad t - f(\vec{r}) < 0; \\ 1 & \text{at} \quad t - f(\vec{r}) > 0. \end{cases}$$

Then for f we obtain the equation:

$$\frac{c(B_1 + B_0)}{8\pi e}\left[\left(\frac{\partial f}{\partial x}\right)\left(\frac{\partial}{\partial y}\frac{1}{n}\right) - \left(\frac{\partial f}{\partial y}\right)\left(\frac{\partial}{\partial x}\frac{1}{n}\right)\right] = 1 , \qquad (5.1.4)$$

which can be solved by integration along characteristics. If, we assume that $f = f(x(t, s), y(t, s))$, where s is the coordinate along the plasma boundary, and $x(t, s)$, $y(t, s)$, satisfies the equations

$$\frac{\partial x}{\partial t} = \frac{c(B_1 + B_0)}{8\pi e}\left(\frac{\partial}{\partial y}\frac{1}{n}\right); \qquad \frac{\partial y}{\partial t} = -\frac{c(B_1 + B_0)}{8\pi e}\left(\frac{\partial}{\partial x}\frac{1}{n}\right),$$

then (5.4) yields $\frac{df}{dt} = 1$. Since $f = f(x(0, s), y(0, s)) = 0$, then $f = t$. Thus, $x(t, s)$, $y(t, s)$, are the coordinates of the jump boundary, and the 2D problem for the magnetic field is reduced to a one-dimensional problem for the movement of the jump boundary along the density n isolines.

In this zero approximation, it is also easy to determine the total voltage, U, across the jump. Integrating the electric field in equation (5.1) over the jump region perpendicular to the current, we find

$$U = \int \vec{E}\, d\vec{l} = \frac{B_1^2 - B_0^2}{8\pi en}\ , \qquad (5.1.5)$$

which for $B_0 = 0$ coincides with the results Kingsep *et al.* and Gordeyev *et al.* [5.1, 5.3] and exceeds the ohmic voltage $\sim \frac{c(B_1 - B_0)}{\sigma}$ by a factor of $\omega_e\tau_e$.

Now let us consider how the resistance of the plasma bridge between two metal electrodes varies in this approximation. Such a problem is of interest in the analysis of the operation of plasma opening switches [5.3 and 5.4]. We take as an example the case in which the bridge is contained between two parallel walls, and density n depends solely on the coordinate perpendicular to the walls and instantly falls off at the boundaries to which magnetic fields B_0 and B_1 are applied (see Fig. 5.1). We assume that the density grows near the walls (the walls themselves in this approximation can be considered to be plasma with infinite density). The motion of the magnetic-field jump for this example is shown in Fig. 5.1. As for the voltage, on the left boundary it is constant and equals $\frac{B_1^2 - B_0^2}{8\pi en_{\min}}$ (n_{min} is the minimum density), while on the right boundary initially it is $\frac{B_1^2 - B_0^2}{8\pi en_a}$ (n_a is the plasma density at the anode interface), which is due to fast magnetic-field penetration along the plasma-anode interface ($\nabla(1/n)$ is infinite). Then, as the jump arrives along the isolines with smaller density, the voltage grows. If the maximum gradient $1/n$ is realized not on the anode, but at an intermediate point, then after the jump arrives along this isoline the voltage on the right boundary equals

$$\frac{B_1^2 - B_0^2}{8\pi e}\left(\frac{1}{n_1(t)} - \frac{1}{n_2(t)} + \frac{1}{n_a}\right)$$

($n_1(t)$ and $n_2(t)$ are the densities along whose isolines the jump arrived to the right boundary by the time t). With time, $n_1(t)$ approaches n_{min}, and $n_2(t)$ approaches n_a, and thus the voltage on the right boundary approach the voltage on the left boundary. As a result, a stationary distribution of the magnetic field with a jump passing along the density isoline, $n = n_{min}$, sets in.

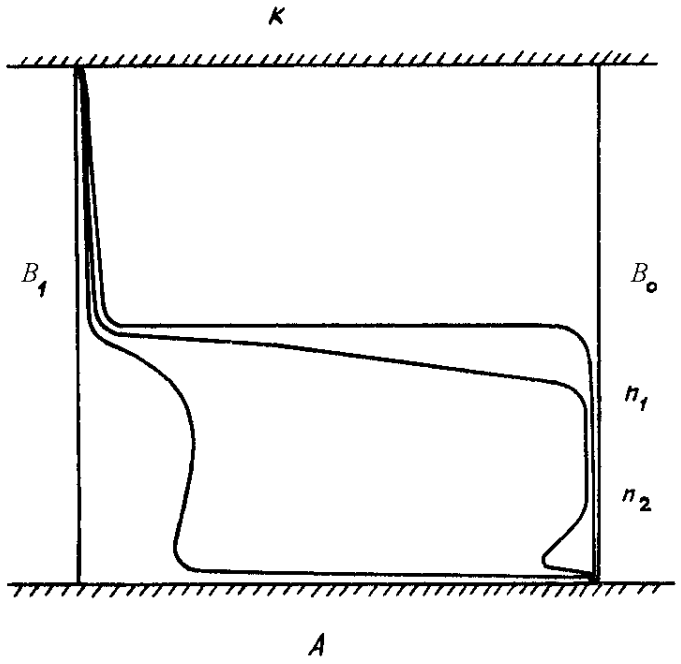

Fig. 5.1. Magnetic-field jump motion in the plasma bridge with the density growing towards the walls (A is the anode, K is the cathode).

A similar qualitative consideration of the problem is also easy to perform for any other density distribution. Thus, in the case of plasma bridge whose density goes to infinity on the electrodes and to zero at the vacuum interface (such density distribution seems to be natural since the hydrodynamic motion should lead to the zero plasma density at the interface, and the processes of plasma cooling on metal walls should lead to the plasma pushing toward the walls), the isolines take the form shown in Fig. 5.2, and the distribution of the magnetic field with a jump is set along the density isoline—the separatrix, which starts from the left boundary intersection with the cathode and enters the point of the right boundary intersection with the anode, is set. The voltage that sets in here (5.1.5) will be determined by this density.

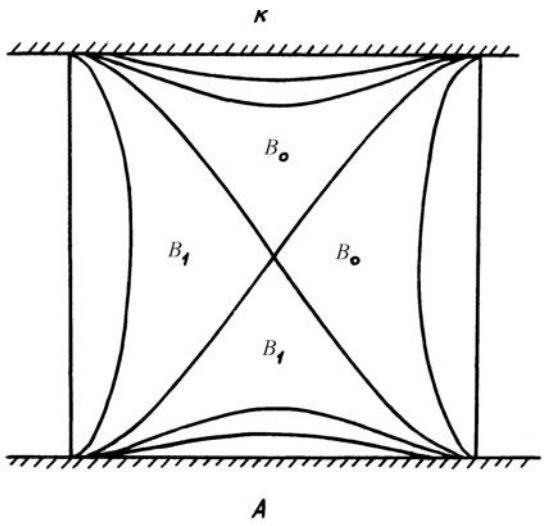

Fig. 5.2. Density isolines in the plasma bridge where the plasma density goes to infinity on the walls and to zero on the boundaries (A is the anode, K is the cathode).

Note that the total electric resistance of the plasmoid in this approximation turns out to be independent of the conductivity, but is determined solely by the magnetic field and the density spatial distribution. Therefore, the original assumption about the constant plasma conductivity should have no influence on this result; it should be true for the real conductivity, which is dependent on the coordinates (only if the condition $\omega_e\tau_e>>1$ is fulfilled). Here, the analogy with the shock wave in hydrodynamics, where the viscosity affects the front width only, but does not affect the Hugoniot, is appropriate.

Thus, in the general case of nonhomogeneous plasma, the magnetic field evolution in electron magnetic hydrodynamics leads to occurrence of discontinuities spread over the width determined by the magnetic diffusion. There exist, however, degenerate cases in which the magnetic field in the main plasma volume is distributed continuously. Homogeneous plasma can serve as such an example for the plane problem. Let us consider the magnetic field dynamics in that case. The Hall terms in the equation (5.1.2) for this problem equal zero, and the equation (5.1.2) is reduced to ordinary magnetic diffusion

$$\frac{\partial B}{\partial t} = \frac{c^2}{4\pi\sigma}\Delta B \equiv \kappa \Delta B \ .$$

The difference from a common diffusion problem consists in the boundary conditions on the metal surface, which follow from the condition that the tangent component of the electric field should be equal to zero

$$\frac{\partial B}{\partial \xi} = \frac{\sigma B}{enc}\frac{\partial B}{\partial \tau} = \omega_e \tau_e \frac{\partial B}{\partial \tau} \qquad (5.1.6)$$

($\frac{\partial B}{\partial \tau}$, $\frac{\partial B}{\partial \xi}$ are the tangent and the normal magnetic field derivatives).

Given that $\omega_e\tau_e >> 1$, the current lines (magnetic field isolines) enter the electrodes at a small angle. After the magnetic field B_1 is applied to the plasma boundary, there will be diffusive penetration of the magnetic field through the boundary as deep as $\sim\sqrt{\kappa t}$, and rapid propagation of the magnetic field along the anode as far as $\sim\omega_e\tau_e\sqrt{\kappa t}$. After the wave goes out along the anode to the other boundary, we can assume that there is the magnetic field B_1 on one boundary and on the anode, and the magnetic field B_0 on the other boundary and on the cathode; the subsequent dynamics are determined by the diffusion problem with these boundary conditions. That is, for the main plasma volume, there will be slow relaxation with diffusion times to the $\Delta B = 0$ state and with discontinuous boundary conditions on the intersections of one boundary with the cathode and the other boundary with the anode (points of inflow and outflow of magnetic flux). The magnetic field distributions in the vicinity of these points are qualitatively similar. Let us find, as an example, this distribution in the vicinity of the first boundary intersection with the cathode (inflow point). Let this boundary make the angle ϕ_0 with the cathode. Since in accordance with (5.1.6) the magnetic field should slowly change along the electrode, we look for the solution in the form

$$B = B_1[1-\phi g(\mathrm{r})]$$

(ϕ is the angle read from the plasma boundary; r is the distance from the boundary–cathode intersection; and $g(r)$ is the slowly changing function) which approximately satisfies the Laplace equation $\Delta B = 0$. Then, using the boundary condition (5.1.6) we get

$$\ln\frac{r}{r_0} = \frac{\phi_0}{\chi}[\ln(g\phi_0) - g\phi_0] \ .$$

The constant r_0 is determined from the condition, which on the characteristic problem dimensions a $g\phi_0 = 1 - \frac{B_0}{B_1}$, that is

$$\ln\frac{a}{r_0} = \frac{\phi_0}{\chi}\left[\ln\left(1-\frac{B_0}{B_1}\right) - 1 + \frac{B_0}{B_1}\right] .$$

In this case, the characteristic magnetic-field change takes place at distances exponentially small relative to the parameter $\chi\left(\sim a\exp\left(-\frac{1}{\chi}\right)\right)$. The total voltage applied in the region of the considered point

$$U = \int \frac{cB_1}{4\pi\sigma} g\frac{dr}{r} = \frac{B_1^2 - B_0^2}{8\pi en}$$

coincides with (5.1.5), as expected.

The qualitative consideration of the magnetic-field dynamics for other cases of density distribution (only if the density does not strongly fluctuate on small scales, as in Chukbar and Yankov [5.4]) also shows that these dynamics tend to generate discontinuities—current layers —and voltage (5.1.5) at those discontinuities. Thus, if the Hall effect is taken into account in magnetized plasma, the plasma's resistance increases by a factor of $\sim\omega_e\tau_e$.

5.2. Near-Anode Detached Magnetized Plasma Flows

The equations of magnetic hydrodynamics (3.3.1–3.3.2, 3.3.5) are widely used for the calculation of plasma flows in a magnetic field. In the case of ideal magnetic hydrodynamics, the equations can be written as follows:

$$\begin{aligned} &\frac{\partial\rho}{\partial t} + \operatorname{div}\rho\vec{v} = 0 \\ &\rho\frac{d\vec{v}}{dt} = -\nabla p + [\vec{j},\vec{B}]/c \\ &\vec{E} = -[\vec{v},\vec{B}]/c \ , \end{aligned} \qquad (5.2.1)$$

When kinetic phenomena are taken into account, additional terms are introduced into these equations. Evaluation of different kinetic effects [5.5] for flows of magnetized ($\omega_e\tau_e >> 1$) hydrogen plasma with low $\beta = 16\pi nT / B^2$ in a transverse magnetic field shows that the most significant

role should be played by the Hall effect—magnetic flow transport by current. The influence of the Hall effect on the flow is characterized by the parameter $c/\omega_{pi}a$ (a is the characteristic spatial flow scale); however, as will be shown below, in a number of cases it can be considerably larger.

The study of the role of the Hall effect in plasma flow in a transverse magnetic field is the focus of a large number of papers both of a general nature [5.6] and with respect to flows in plasma accelerators [5.7–5.10] and near-anode flows in plasma focus [5.11].

Taking into account the Hall effect is sometimes impossible without taking into account the finite plasma conductivity because otherwise, as is shown in Section 5.1, it can lead to the formation of jumps, infinitely fast plasma detachment from the anode (see below) and other paradoxical events. Since plasma conductivity depends on the temperature, heat transport must be calculated as well. As a result, the problem of flow calculation becomes rather complex, because the presence of the Hall effect makes it at least a 2D problem, and the difficulties of calculating magnetothermal processes are added to the difficulties of the 2D calculations.

Therefore, in this Section we limit our discussion to an isothermal plasma model with constant conductivity, which will allow us to perform a qualitative or semi-quantitative analysis of some flows. Taking into account the Hall effect and the finite conductivity leads to the generalized Ohm law (5.1.1), which, when the ion motion is taken into account, is written as

$$\vec{E}+[\vec{v},\vec{B}]/c=\frac{1}{c}\left[\frac{\vec{j}}{en},\vec{B}\right]+\vec{j}/\sigma-\nabla p_e/en \quad , \tag{5.2.2}$$

and to the following equation for the magnetic field, which follows from the Maxwell equations (4.3.4), (4.3.5) and (5.2.2)

$$\frac{\partial\vec{B}}{\partial t}=\mathrm{rot}[\vec{v},\vec{B}]-\mathrm{rot}\left[\frac{\vec{j}}{en},\vec{B}\right]+\frac{c^2}{4\pi\sigma}\Delta\vec{B} \tag{5.2.3}$$

(because the plasma is isotherma, $p_e = p_e(n)$, the last term in the Ohm law (5.2.2) does not contribute to (5.2.3)).

For this model, following Garanin and Mamyshev [5.12], we consider certain properties of plasma flows driven by a piston—magnetic or rigid, i.e., we assume that at the initial moment, there is a magnetic-field jump or a rigid, ideally conducting, moving wall at the interface of the plasma and a transverse magnetic field.

If the ion motion is not taken into account, the dynamics of the magnetic field in magnetized plasma result in an increase in the magnetic field in the vicinity of the anode (see Section 5.1). But when the ion motion is taken into account, plasma should be driven away from the anode and its density decreased down to point of detachment.

5.2.1. Near-anode plasma flow driven by a magnetic piston

At the initial moment, we assume the plasma to be homogeneous, $n = n_0$, with a constant magnetic field $B = B_0$. The plasma thermal pressure is assumed to be proportional to the density $p = \beta B_0^2 n / 8\pi n_0$ and low ($\beta >> 1$), and at the plasma boundary there is a constant magnetic field B = $B_1 > B_0$. We are going to seek a stationary solution for the near-anode flow.

Choosing the system of coordinates in which x is perpendicular to the anode surface and y is parallel to the surface, and using the dimensionless variables $x = x4\pi\sigma c_A/c^2$, $y = y4\pi\sigma c_A/c^2$, $h = B/B_0$, $\rho = \rho/\rho_0$, $u_x = v_x/c_A$, and $u_y = v_y/c_A$ ($c_A = B_0 / \sqrt{4\pi\rho_0}$), we can write the system of equations (5.2.1 and 5.2.3) in the form

$$\begin{gathered}
\rho\left(u_x\frac{\partial u_x}{\partial x}+u_y\frac{\partial u_x}{\partial y}\right)=-\frac{\partial}{\partial x}\left(\frac{h^2}{2}+\frac{\beta}{2}\rho\right), \\
\rho\left(u_x\frac{\partial u_y}{\partial x}+u_y\frac{\partial u_y}{\partial y}\right)=-\frac{\partial}{\partial y}\left(\frac{h^2}{2}+\frac{\beta}{2}\rho\right), \\
\frac{\partial}{\partial x}(\rho u_x)+\frac{\partial}{\partial y}(\rho u_y)=0 \\
\frac{\partial}{\partial x}(hu_x)+\frac{\partial}{\partial y}(hu_y)=\Delta h+\frac{1}{\chi}\left\{\left(\frac{\partial}{\partial x}\frac{1}{\rho}\right)\left(\frac{\partial}{\partial y}\frac{h^2}{2}\right)-\left(\frac{\partial}{\partial y}\frac{1}{\rho}\right)\left(\frac{\partial}{\partial x}\frac{h^2}{2}\right)\right\}
\end{gathered} \qquad (5.2.4)$$

($\chi = e\,c\,n_0/\sigma B_0 \sim 1$ $\omega_e\tau_e << 1$). The boundary conditions on the metal surface—the normal velocity component and the tangential component of the electric field are equal to zero—in these variables are

$$u_x\,|_{x=0} = 0$$
$$\frac{1}{\chi\rho}\frac{\partial}{\partial y}\left(\frac{h^2}{2}+\frac{r\beta}{2}\rho\right)+\frac{\partial h}{\partial x}\,|_{x=0} = 0\ , \qquad (5.2.5)$$

(r is the fraction of the electron pressure in the total thermal pressure).

Since the Hall effect leads to rapid movement of the magnetic field to the anode ($\chi << 1$), and the thermal pressure is low and cannot hold the plasma near the wall for a long time, we should expect motion with a high velocity $u_y >> 1$. Then we can assume that $u_y = D$ is constant and disregard the y derivatives in the term Δh. In this case, we can reduce the problem to a one-dimensional non-stationary problem by introducing the notation $y = Dt$, after which the system (5.2.4–5.2.5) takes the form

$$\rho\frac{du}{dt} = -\frac{\partial}{\partial x}\left(\frac{h^2}{2}+\frac{\beta}{2}\rho\right)\ ,$$

$$\frac{d\rho}{dt}+\rho\frac{\partial u}{\partial x} = 0\ ,$$

$$\rho\frac{d}{dt}\left(\frac{h}{\rho}\right) = \frac{\partial^2 h}{\partial x^2}+\frac{1}{\chi D}\left\{\left(\frac{\partial}{\partial x}\frac{1}{\rho}\right)\left(\frac{d}{dt}\frac{h^2}{2}\right)-\left(\frac{d}{dt}\frac{1}{\rho}\right)\left(\frac{\partial}{\partial x}\frac{h^2}{2}\right)\right\}\ , \qquad (5.2.6)$$

$$u\,|_{x=0} = 0\ ,$$

$$\frac{1}{\rho}\frac{d}{dt}\left(\frac{h^2}{2}+\frac{r\beta}{2}\rho\right)+\chi D\frac{\partial h}{\partial x}\,|_{x=0} = 0$$

d/dt is the Lagrangian derivative, and the subscript x is omitted in the velocity u_x. The dimensionless quantities χ and D enter the system (5.2.6) only in the form of a product. Thus, the solution will depend solely on two dimensionless quantities: β and $\gamma \equiv \chi D$.

Now let us analyze the qualitative behavior of the solution for the linearized system (5.2.6), i.e., we assume that $h \cong 1$, $\rho \cong 1$, and $u << 1$, which is true at the initial stage of the developing solution. The linearization of (5.2.6) yields the equations

$$\frac{\partial u}{\partial t} = -\frac{\partial}{\partial x}\left(h + \frac{\beta}{2}\rho\right),$$
$$\frac{\partial \rho}{\partial t} + \frac{\partial u}{\partial x} = 0, \qquad (5.2.7)$$
$$\frac{\partial h}{\partial t} - \frac{\partial \rho}{\partial t} = \frac{\partial^2 h}{\partial x^2}$$

and the boundary conditions

$$u|_{x=0} = 0$$
$$\frac{\partial}{\partial t}\left(h + \frac{r\beta}{2}\rho\right) + \gamma \frac{\partial h}{\partial x}|_{x=0} = 0. \qquad (5.2.8)$$

We look for the solution for $\delta h = h - 1$, $\delta \rho = \rho - 1$, and u in the form proportional to $\exp(\lambda t - kx)$, exponentially attenuating away from the front. Then for the dependence $k(\lambda)$ we obtain from (5.2.7) the dispersion equation

$$\frac{\beta}{2}k^4 - \left[\lambda^2 + \lambda\left(1 + \frac{\beta}{2}\right)\right]k^2 + \lambda^3 = 0, \qquad (5.2.9)$$

which has two positive roots:

$$k_{1,2} = \sqrt{\frac{\lambda(\lambda + 1 + \beta/2) \pm \sqrt{\lambda^2(\lambda + 1 + \beta/2)^2 - 2\beta\lambda^3}}{\beta}}.$$

We express the solution as the sum

$$\delta h = e^{\lambda t}(b_1 e^{-k_1 x} + b_2 e^{-k_2 x}),$$
$$\delta \rho = e^{\lambda t}\left[b_1\left(1 - \frac{k_1^2}{\lambda}\right)e^{-k_1 x} + b_2\left(1 - \frac{k_2^2}{\lambda}\right)e^{-k_2 x}\right], \qquad (5.2.10)$$
$$u = \lambda e^{\lambda t}\left[\frac{b_1}{k_1}\left(1 - \frac{k_1^2}{\lambda}\right)e^{-k_1 x} + \frac{b_2}{k_2}\left(1 - \frac{k_2^2}{\lambda}\right)e^{-k_2 x}\right],$$

and we find the coefficients b_1 and b_2 from the boundary conditions (5.2.8). The condition of consistency of the resulting system of equations provides the equation for λ:

$$\frac{1+\frac{\beta}{2}\left(1-\frac{k_1^2}{\lambda}\right)}{\frac{\lambda}{\gamma k_1}\left[1+\frac{r\beta}{2}\left(1-\frac{k_1^2}{\lambda}\right)\right]-1} = \frac{1+\frac{\beta}{2}\left(1-\frac{k_2^2}{\lambda}\right)}{\frac{\lambda}{\gamma k_2}\left[1+\frac{r\beta}{2}\left(1-\frac{k_2^2}{\lambda}\right)\right]-1} \quad . \qquad (5.2.11)$$

Taking into account the fact that β is small, we can simplify the formula (5.2.11):

$$\gamma = \frac{(1-r-r\lambda)}{1+\lambda}\sqrt{\beta\lambda/2(1+\lambda)} + \lambda/\sqrt{1+\lambda} \quad . \qquad (5.2.12)$$

For $\lambda >> 1$ the equation (5.2.12) yields $D \cong \sqrt{\lambda}/\chi$. Since in this case the main contribution to the magnetic-field derivatives in (5.2.8) is provided by the term b_2 from (5.2.10), for which in this limit $k_2 \cong \sqrt{\lambda}$, this corresponds to the generation of shock wave propagating perpendicularly to the current flowing into the anode at a small angle $\chi \cong \lambda / k_2 D \cong \sqrt{\lambda}/D$.

The solution (5.2.10) is applicable as long as $\delta\rho << 1$. To determine the qualitative dependence of $\delta h_1 \equiv h_1 - 1 \equiv B_1/B_0 - 1$ on γ and β, we can assume that this solution is true up to $\delta\rho = -1$ ($\rho = 0$). Using this condition, the condition that the velocity equals zero at the boundary (5.2.8), and equation (5.2.9), we find that

$$\delta h_1 = \frac{\beta}{2} + \sqrt{\lambda\beta/2} \quad . \qquad (5.2.13)$$

The formulas (5.2.12–5.2.13) provide the connection between the wave velocity and the magnetic-field jump. For $\delta h_1 >> \beta$ it follows that $\lambda = 2\delta h_1^2/\beta$, and from (5.2.12) it follows that the wave velocity $D = \lambda/\chi\sqrt{1+\lambda}$ should be high because of both the smallness of χ and the smallness of β.

Thus, on large scales (by comparison with that of the wave structure), a narrow vacuum wedge that detaches the plasma is formed. The connection between the wedge apical angle ($\delta h_1 - \beta/2$) and the motion velocity D is determined by solving the nonlinear system of equations (5.2.6), which has weak initial perturbations (5.2.10). Such a nonlinear problem has been solved numerically for $\gamma = 0.74$, $\beta = 0.2$, and $r = 0.5$. The flow lines of the obtained solution (the plasma particle trajectories) in the t, x variables are shown in Fig. 5.3. As a result of the numerical solution it was determined that $\delta h_1 = 0.27$, while the formulae (5.2.12–5.2.13) yield for these parameters $\delta h_1 = 0.43$.

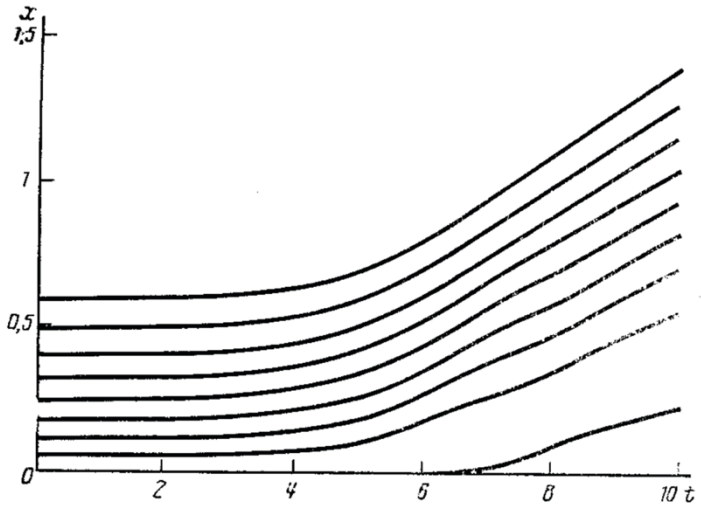

Fig. 5.3. Current flow lines of the detaching near-anode flow caused by the magnetic piston.

Note that the supersonic propagation of the shock wave moving along the channel with low density had also been discovered in pure hydrodynamics [5.13]. The difference here in the solution with the motion along the anode consists in the fact that the wave itself makes the channel as it delivers the magnetic flux to the anode.

5.2.2. Near-anode flow driven by a rigid, ideally conducting piston

When a rigid, ideally conducting piston (high-density plasma can be such piston) moves in a plasma, the formation of a plasma-detaching vacuum wedge moving at a high velocity (higher than that of the shock wave created by the piston) is impossible, because, unlike with the preceding problem, there is no unlimited source of magnetic flux. Indeed, the magnetic flux

contained within the vacuum wedge should grow $\sim t^2$. However, the zone encompassed by the hydrodynamic motion and from which the magnetic flux may derive (the zone downstream of the shock wave beyond the near-anode area) grows $\sim t$. Therefore, in this problem, the stationary motion of the vacuum wedge growing unrestrictedly is impossible; the wedge must collapse for large times near the anode, and an MHD shock wave will be moving. That shock wave has, however, a specific near-anode structure in which the detaching magnetic pressure generates a vacuum region.

We perform the evaluations of the characteristic parameters of the formation of a shock wave with a low Mach number $D = 1 + \varepsilon$, $\varepsilon << 1$. As before, we assume that the plasma thermal pressure is low ($\beta << 1$) and that the plasma is initially homogeneous. The formulae (5.2.12–5.2.13) show that applying a fairly small magnetic-field differential δh_1 is sufficient for the plasma detachment. Therefore, we can suppose, that the near-anode shock wave structure has the form shown in Fig. 5.4: initially there is a tearing wedge with $\delta h_1 << \varepsilon$ (in this sense, the shock wave's Mach number should not be too close to 1); then the vacuum region collapses. Thus, the entire stationary problem splits into two fragments with different characteristic scales, which should be connected with each other: the vacuum wedge generation, and the vacuum region collapse.

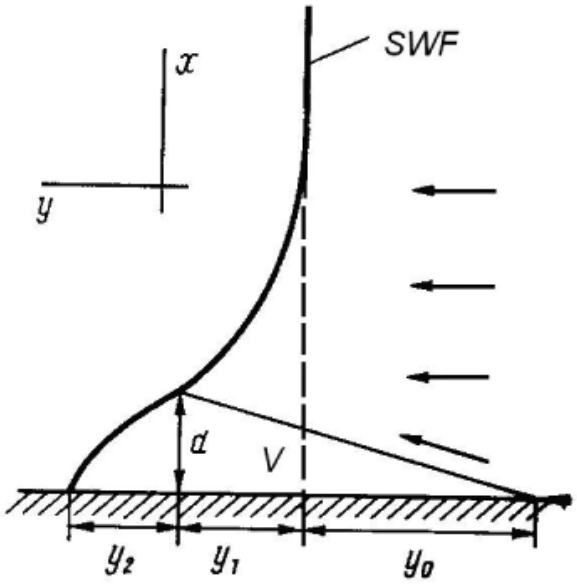

Fig. 5.4. Near-anode shock wave structure (SWF – position of shock wave front, V – vacuum region)

The dynamics of the vacuum wedge formation are described by the equations (5.2.4–5.2.5), in which we cannot now assume u_y to be constant. In the wave's frame of reference, when $y \to \infty$, $u_y \to D$. For a qualitative analysis of the solution, we can use, as before, the linearized system (5.2.4–5.2.5), in which ∂_u/∂_y is excluded from the equation of motion for u_y and the continuity equation. As with the previous problem, if we take the perturbations of the form $\exp(\lambda y - kx)$, we can get the equation for λ:

$$\left[\sqrt{\frac{\beta}{2\lambda}}(1-r)-\frac{\chi}{\lambda}\right]\sqrt{D-1-\beta/2-\lambda}+1=0 \quad . \qquad (5.2.14)$$

As with the derivation of (5.2.13), if we "extend" the solution of the linearized equations to $\delta\rho = -1$, we find

$$\delta h_1 = \frac{r+\chi\sqrt{2/\beta\lambda}}{2/\beta-\chi\sqrt{2/\beta\lambda}}$$

or, since it is assumed that $\delta h_1 << \varepsilon << 1$,

$$\delta h_1 = \frac{r\beta}{2}+\chi\sqrt{\beta/2\lambda} \quad . \qquad (5.2.15)$$

The formulae (5.2.14–5.2.15) yield in parametric form (over λ) the dependence of δh_1 on D. Here the apical angle of the vacuum wedge is now equal to $(\delta h_1 - \beta/2)\sqrt{2\varepsilon}$ [5.14], and if its length is y_0, then its width, which is collapsed by the shock wave, equals

$$d = y_0(\delta h_1 - \beta/2)\sqrt{\beta/2\lambda} \quad .$$

The problem of the collapse of the vacuum gap by the shock wave and its connection to the problem of the generation of the vacuum wedge [5.12] is rather complex, and we will not present its solution here. We will merely show the dependence obtained as a result of the solution of this problem:

$$d = C\frac{\varepsilon^{6.5}}{\chi^2\beta(\delta h_1-\beta/2)^3} \quad ,$$

where the constant C is determined from the solution of the problem of the collapse of the vacuum gap. Formula (5.2.16) provides the vacuum gap width if the quantity δh_1 is known from the solution (5.2.4–5.2.5) (approximately it is (5.2.13)).

Formation of the near-anode vacuum zone is also possible at the motion of a compressing (shockless) wave. The magnetic-field gradients needed for this can be estimated as $\partial h/\partial y \sim \varepsilon/y_0$.

The considered qualitative features of plasma flows may occur in the MAGO chamber, plasma accelerators [5.15 and 5.7], a plasma focus with the discharge sliding along the anode [5.16], and other plasma facilities with substantial magnetic-field dynamics. Since taking into account the Hall effect leads to a distinction between the anode and the cathode, for a number of experimental facilities, including the MAGO chamber, it is possible to explain the change in their operation when the polarity of the electrodes changes.

5.3. Formation of Electrode Sheaths in Connection with the Acceleration of a Magnetized Plasma

In a facility such as a plasma accelerator, a plasma opening switch, or a dense plasma focus, plasma with frozen-in magnetic field moves along electrodes in a direction transverse to the magnetic field. A sheath (near-boundary layer) forms close to the plasma/surface interface, which can be examined either with an MHD approximation if problem distance and time scales are large enough or with the kinetic approach if particle collisions over the time and the distance scales of interest are rare and the plasma can be considered collisionless.

Within the MHD approach to the examination of near-electrode layers and their structure, the problem can be set up as follows. Let plasma with a frozen-in magnetic field move along electrodes in a direction transverse to the magnetic field. One can then consider a one-dimensional electrode-sheath problem, in which all quantities depend solely on the coordinate perpendicular to the electrode surface and on time. In the problem, one can take into account viscous heating of plasma, its cooling due to heat conductivity, and other kinetic processes, as well as the effects of plasma acceleration and the electric current normal to the electrode, which, thanks to the Hall effect, brings the magnetic flux toward the anode and away from the cathode. In this case, the plasma mass will build up in the near-cathode region and become depleted in the near-anode region. It turns out that the MHD approximation is inadequate for describing the situation near the anode: in this region, plasma density quickly drops to zero, whereas the current remains constant. In order to overcome this difficulty, one should incorporate some non-hydrodynamic effects (primarily, electron dispersion).

For the collisionless kinetic case, some of the ions from the electrode sheath, when they collide with the wall, are absorbed by the electrode material, and others return to the flow with a loss of momentum and energy.

A self-consistent collisionless interaction between reflected ions and those in the basic stream results in the ion gyration of the basic stream towards the electrode. A specific instability arises, as a result of which development an increasing number of ions collide with the wall, which leads to anomalous "viscosity" on a scale of the ion Larmor radius. As with the MHD approach, one can consider a one-dimensional problem of a near-electrode layer in a low-density plasma in which all quantities depend solely on the coordinate perpendicular to the electrode surface and solve it in this collisionless case with the particle-in-cell (PIC) method.

5.3.1. MHD Approach

As mentioned in Section 5.2, the applicability of the MHD approach is, generally speaking, determined by the smallness of the parameter $\xi \equiv \frac{c}{\omega_{pi} a}$ (a is the characteristic spatial scale of the flow). For $\xi << 1$, the plasma flow can be described by the ideal MHD equations, and the effect of the electrodes that bound the plasma region, by the boundary conditions that, in the case of the magnetic field that is parallel to the electrodes, amount to the ideal sliding condition. Near the electrodes, the plasma flows along the electrode surfaces, being accelerated or slowed down by the Lorentz force $\frac{1}{c}[\vec{j}\vec{B}]$ (the plasma is assumed to be cold, $\beta \equiv \frac{8\pi p}{B^2} << 1$). Sheaths are formed near the electrode surfaces, where viscous plasma heating and plasma cooling as a result of heat conductivity take place. An important role may be played in the electrode sheaths by the Hall effect, which brings the magnetic flux to the anode, thereby causing plasma rarefaction near the anode, and takes it away from the cathode, thereby causing plasma compression near the cathode.

Interest in studying electrode sheaths in magnetohydrodynamics is due to three things. First, of interest are plasma characteristics in these sheaths and how they differ from those of bulk plasma, which can be important for diagnostics. Second, the sheath thickness and the mass of the plasma in the sheaths can be large enough to affect the operation of many plasma devices (for instance, MAGO chamber). Third, there is fundamental interest because MHD proves to be inadequate for describing the electrode sheaths, particularly for describing the near-anode plasma. As we will show, the density of plasma accelerated near the anode rapidly drops to zero, generating a vacuum similar to that formed by a shock wave front near the anode (Section 5.2). However, if, in the case of a shock wave, times were assumed to be long enough for the development of a steady-state two-dimensional structure with a current-free vacuum region, in the case of interest to us, when

a bulk plasma flow is determined by magnetic hydrodynamics and times are not too long, the current is governed by the MHD problem and it should flow across the region with zero density in the MHD approximation. The MHD approach, therefore, is inadequate in the near-anode region, and nonhydrodynamic effects need to be taken into account.

An attempt to consider near-electrode layers with the approach discussed here was made by Garanin [5.17], who presented results corresponding to large plasma acceleration distances. That study, however, did not take into account such important phenomena as boundary-layer turbulence [5.14] or anomalous plasma resistivity stemming from the development of a lower hybrid drift instability. In this section, following Garanin [5.18], we will incorporate these effects and consider plasma acceleration over shorter distances. We will also consider the motion of low-density plasma along the electrodes, in which the plasma can become heated to high temperatures, thus making it possible to explain neutron generation near the nozzle in the MAGO chamber at high anisotropy of neutron energy distribution [5.19].

One-dimensional problem. We assume that the electrode sheath thickness is small by comparison with the characteristic spatial scales of the full MHD problem. Then, we can consider a nonsteady one-dimensional problem in which all of the quantities depend solely on the coordinate perpendicular to the electrode surface and on time. We assume that, far from the electrodes, the plasma is homogeneous, with density n_0, temperature T_0, a magnetic field $\vec{B}_0$ parallel to the electrode surface, and constant current density $\vec{j}$ perpendicular to the surface. The Lorentz force $\frac{1}{c}[\vec{j}\vec{B}]$ causes the acceleration of both surface and bulk plasma along the surface.

Let the coordinate normal to the surface be x, and let the magnetic field be directed along the z-axis; then, the electric field and velocity acquired by the plasma will be directed along the y-axis. Since the electrode sheath is assumed to be rather thin, one can assume that the total pressure has enough time to be equalized along x; i.e.,

$$p + \frac{B^2}{8\pi} = P_0 \ , \qquad (5.3.1)$$

where the total pressure P_0 depends solely on time (in fact, we are solving problems, in which P_0 is constant, and density n_0, temperature T_0 and magnetic field B_0 experience slight time variations due to the Joule heating and thermal expansion). In addition to (5.3.1), the following MHD

equations will determine the electrode sheath dynamics: the equation of motion for the velocity v along y,

$$\rho\frac{dv}{dt}=\frac{jB}{c}-\frac{\partial\pi_{xy}}{\partial x}\ , \tag{5.3.2}$$

where π_{xy} is the xy component of the viscous stress tensor, which is equal to

$$\pi_{xy}=-\eta\frac{\partial v}{\partial x}\ ; \tag{5.3.3}$$

the equation for the magnetic field

$$\rho\frac{d(B/\rho)}{dt}=-c\frac{\partial E}{\partial x}\ , \tag{5.3.4}$$

where the Lagrangian electric field equals

$$E=-RjB-\frac{c}{4\pi\sigma}\frac{\partial B}{\partial x}-N\frac{\partial T}{\partial x}\ ; \tag{5.3.5}$$

and the heat-transfer equations for plasma ions

$$\frac{3}{2}n\frac{dT_i}{dt}-T_i\frac{dn}{dt}=-\frac{\partial q_i}{\partial x}+\eta\left(\frac{\partial v}{\partial x}\right)^2+Q_i \tag{5.3.6}$$

and plasma electrons

$$\frac{3}{2}n\frac{dT_e}{dt}-T_e\frac{dn}{dt}=-\frac{\partial q_e}{\partial x}+\frac{j^2}{\sigma}-\frac{j}{en}\frac{\partial(nT_e)}{\partial x}-\alpha j\frac{\partial T_e}{\partial x}+$$
$$+\frac{c}{4\pi}\frac{\partial B}{\partial x}\left(\frac{c}{4\pi\sigma}\frac{\partial B}{\partial x}+N\frac{\partial T_e}{\partial x}\right)-Q_i\,, \tag{5.3.7}$$

where

$$q_i=-\kappa_i\frac{\partial T_i}{\partial x}\ , \tag{5.3.8}$$

$$q_e=-\kappa_e\frac{\partial T_e}{\partial x}+\frac{c}{4\pi}NT_eB\frac{\partial B}{\partial x}-\left(\alpha+\frac{5}{2e}\right)jT_e\ . \tag{5.3.9}$$

Here η is the plasma viscosity; σ is the plasma conductivity; κ_1 is the ion thermal conductivity; κ_e is the electron thermal conductivity; and *R, N,* and α describe the Hall and Nernst effects and heat carried by the current, respectively. All of these coefficients depend on the degree of plasma magnetization. The term Q_i accounts for the energy exchange between electrons and ions. The formulas for all of these quantities are presented in Braginskii [5.20].

Note that, for our problem in a magnetized plasma, $(\omega\tau)_i >> 1$, and the plasma viscosity and heat-conductivity spatial scales become, at a certain stage, smaller than the ion Larmor radii because of the smallness of the viscosity and heat conductivity plasma coefficients. Consequently, the MHD approximation and the relevant transport coefficients, strictly speaking, are not applicable. For a qualitative description of the resulting transport problem in the context of the MHD approach, we incorporated the following additional terms into the coefficients η and κ_i in equations (5.3.3) and (5.3.8) for $(\omega\tau)_i >> 1$:

$$\eta_{an} = \frac{nT_i}{8\omega_i}\frac{x}{r_{Li}}\left(1-\frac{x}{r_{Li}}\right), \qquad \kappa_{ian} = \frac{nT_i}{4M_i\omega_i}\frac{x}{r_{Li}}\left(1-\frac{x}{r_{Li}}\right), \tag{5.3.10}$$

which are nonzero for distances from the electrode surface x smaller than the ion Larmor radius r_{Li} (M_i is the mass of an ion). Those terms should describe the kinetic ion fluxes that carry the momentum and heat from the wall plasma to the wall.

Since high current velocities u can develop in the wall layer for $T_e \le T_i$, a lower hybrid drift instability and the associated anomalous resistance can develop. We took the effect of that resistance into account by following the lead of Davidson and Gladd [5.21] and letting it, for a magnetized plasma, be equal to

$$\frac{1}{\sigma_{an}} = \begin{cases} 4\pi\sqrt{\frac{\pi}{2}}\frac{M_i u^2}{T_i}\frac{mc}{eB}\sqrt{\frac{m}{M_i}} & \text{for} \quad \frac{M_i u^2}{T_i} < 3 \\ 12\pi\sqrt{\frac{\pi}{2}}\frac{mc}{eB}\sqrt{\frac{m}{M_i}} & \text{for} \quad \frac{M_i u^2}{T_i} > 3 \end{cases} \tag{5.3.11}$$

and adding the relevant anomalous contribution to the electron thermal conductivity,

$$(\kappa_e)_{an} = 1.5 n \beta_e \frac{c^2}{4\pi\sigma_{an}} \ .$$

MHD instability resulting from high velocity gradients (Section 7.1) may develop in the wall layers, resulting in a turbulent boundary layer [5.14]. To take those effects into account, we introduced a turbulent diffusion coefficient equal to

$$0.1 x \delta v \ , \qquad (5.3.12)$$

where δv is characteristic velocity variation in the vicinity of coordinate x. We took as well into account the contributions to the viscosity, to the magnetic diffusion coefficient, and to the coefficients for electron and ion thermal conductivities corresponding to that turbulent diffusion coefficient.

The initial conditions for a deuterium plasma were chosen to be as follows: a spatially constant temperature $T_i = T_e = T_0 = 2$ *eV*=2, zero velocity $v = 0$, constant magnetic field $B = B_0 = 10^5$G, and densities $n = n_0 = 6 \cdot 10^{17}$ cm^{-3} (to describe the main plasma flow through the nozzle of the MAGO plasma chamber) and $n = n_0 = 1.5 \cdot 10^{16}$ cm^{-3} (to describe the residual plasma flow through the nozzle).

The boundary conditions for equations (5.3.2–5.3.3) are

$$v(x = 0) = 0 \ , \qquad \frac{\partial v}{\partial x}(x = \infty) = 0 \ .$$

At the boundary $x = 0$, the electric field was specified to correspond to magnetic diffusion into a copper wall

$$E = -\frac{B}{c}\sqrt{\frac{\chi_{Cu}}{\pi t}} \ , \qquad (5.3.13)$$

where χ_{Cu} is the magnetic diffusion coefficient for copper. At $x = \infty$, the gradients were assumed to be absent, and from (5.3.5) the electric field was determined to be equal to

$$E_H = -jBR \ . \qquad (5.3.14)$$

The temperatures T_i and T_e, at the boundary $x = 0$ were set to be

$$T_i = T_e = 0 \ ,$$

and for $x = \infty$, we assigned

$$\frac{\partial T_i}{\partial x} = \frac{\partial T_e}{\partial x} = 0$$

in which case, the electron heat flux is equal to

$$q_e = -\alpha T_e j \ .$$

Consideration of the anode and cathode problems with the use of equations (5.3.1–5.314) differs in the sign for *j*: for the anode, this sign is positive, and for the cathode, negative. The value of current *j* for our one-dimensional problems is chosen to be $j = \frac{c}{4\pi}\frac{B}{L}$, where *L* = 5 cm; i.e., *j* = ± 16 kA/cm^2, which approximately corresponds to the MAGO chamber conditions.

Cathode sheath. The mass of the plasma, from which the magnetic flux emanates and which is pressed against the cathode is determined by the relationship

$$\int n\,dx = \frac{|j|t}{e} \ . \qquad (5.3.15)$$

For small times, while the plasma viscosity and viscous plasma heating are negligible, that plasma mass will be accumulated in the sheath, whose thickness is governed by magnetic diffusion and electron thermal conductivity. For that to happen, the rates of magnetic diffusion and electron heat conduction should be of the same order of magnitude. For a low-β plasma, that means that

$$\chi = \frac{c^2}{4\pi\sigma}\beta \sim \frac{\kappa_e}{n}$$

or

$$(\omega\tau)_e \sim 1 \ .$$

Since, in this case, the thickness *x* of the cathode sheath will be determined by

$$x \sim \sqrt{\chi t} \ ,$$

the main plasma characteristics of the sheath will be described by the following self-similar dependences:

$$T \sim \frac{(j\sqrt{4\pi})^{1/2}\lambda^{1/2}e^{5/4}m^{1/4}c^{1/4}}{(B_0/\sqrt{4\pi})^{1/4}}t^{1/4} \ ,$$

$$n \sim \frac{(j\sqrt{4\pi})^{3/4}(B_0/\sqrt{4\pi})^{5/8}}{\lambda^{1/4}e^{9/8}c^{5/8}m^{1/8}}t^{3/8} \ , \qquad (5.3.16)$$

$$x \sim \frac{(j\sqrt{4\pi})^{1/4}\lambda^{1/4}e^{1/8}c^{5/8}m^{1/8}}{(B_0/\sqrt{4\pi})^{5/8}}t^{5/8} \ ,$$

where λ is Coulomb logarithm and m is the mass of the electron.

The numerical solution results of our one-dimensional problem for $n_0 = 6 \cdot 10^{17}$ cm^{-3} validates those dependences. For example, by the time $t = 0.1$ μs (when viscous plasma heating is still negligible), formulas (5.3.16) yield the characteristic quantities $T = 4$ eV, $n = 9 \cdot 10^{17}$ cm^{-3}, and $x = 0.04$ cm, and the profiles of the respective quantities in Fig. 5.5a obtained in the one-dimensional simulation agree with those estimates. The electron and ion temperatures by that time are essentially the same. According to (5.3.2), the value for the bulk plasma velocity

$$v = \frac{jB_0}{cn_0M_i}t \qquad (5.3.17)$$

by this time is $v_\infty = 0.8 \cdot 10^7$ cm/s. A decrease in the plasma velocity in the cathode sheath at that time is governed by the elevated plasma density and turbulent viscosity near the cathode (5.3.12).

At the next stage, turbulent diffusion starts to dominate magnetic diffusion, and the mass of the plasma involved in turbulent mixing becomes greater than the mass from which the magnetic flux emanated (5.3.15). A comparison of (5.3.15) and the turbulent mixing zone with coefficient of (5.3.12), in which the scale of velocity is determined by (5.3.17), shows that this happens at $t \sim 0.1\omega_i^{-1}$. The viscous plasma heating becomes substantial, but one can assume that $\beta << 1$, the electron and ion temperatures start to differ from one another, and the ion temperature is governed solely by viscous heating due to the friction of plasma moving with the velocity of (5.3.17) against the wall

$$T_i \sim \frac{j^2B_0^2}{M_ic^2n_0^2}t^2 \ . \qquad (5.3.18)$$

The characteristic scale of the electrode sheath is on the order of $0.1vt$, where the velocity v is determined by (5.3.17), and it increases with the square of time. According to (5.3.15), the characteristic plasma density compression decreases in inverse proportion to t. The characteristic electron temperature is governed by the electron-ion heat exchange and has smaller growth than the ion temperature.

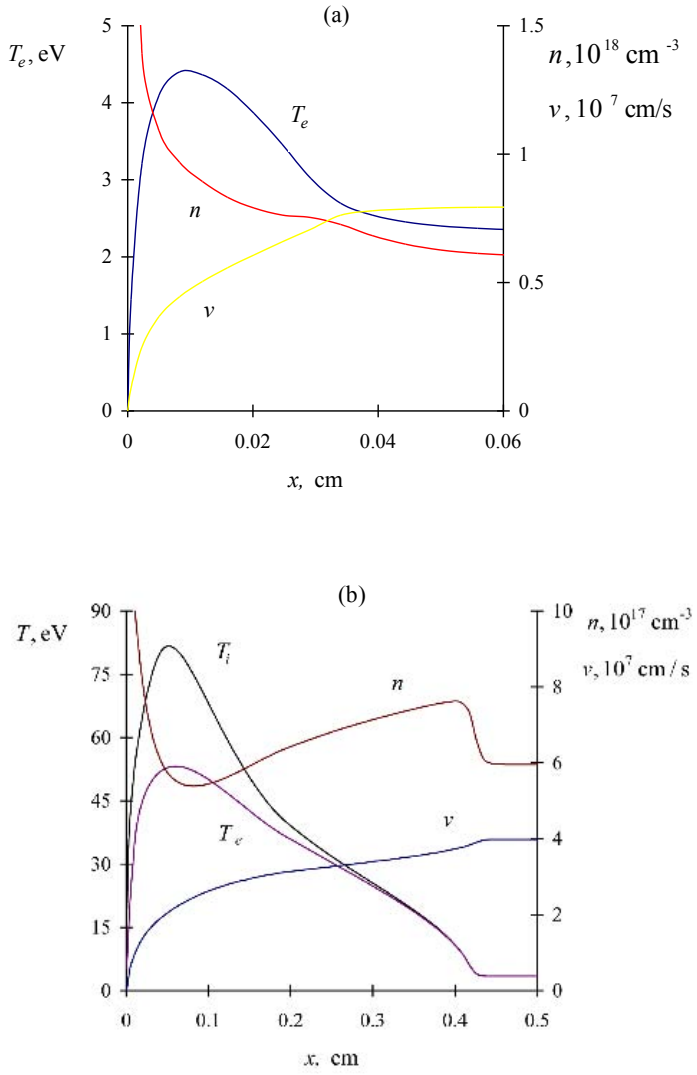

Fig. 5.5. Cathode sheath plasma temperature, density, and velocity profiles for $n_0 = 6 \cdot 10^{17}$ cm^{-3}, $T_0 = 2$ eV, $B_0 = 10^5$ G, and $j = -16$ kA/cm^2 at the times (a) $t = 0.1$ μs ; (b) $t = 0.5$ μs.

The profiles of the quantities that refer to this stage of the cathode sheath evolution in the one-dimensional problem for $t = 0.5$ μs are depicted in Fig. 5.5b. The bulk plasma velocity at this time is $n_\infty = 4 \cdot 10^7$ cm/s, and the maximum $\beta = 0.46$.

In order to characterize plasma deposition onto the cathode surface, which may be of interest for many MHD problems as a measure of the cathode sheath influence on the MHD flow, Fig. 5.6 shows the decrease in the bulk plasma mass due to plasma deposition onto the cathode $n_0 \Delta x$ as a function of time. In accordance with (5.3.15), Δx grows approximately linearly with time until viscous plasma heating and the growth of β come into play, which results in plasma pushing back from the electrode.

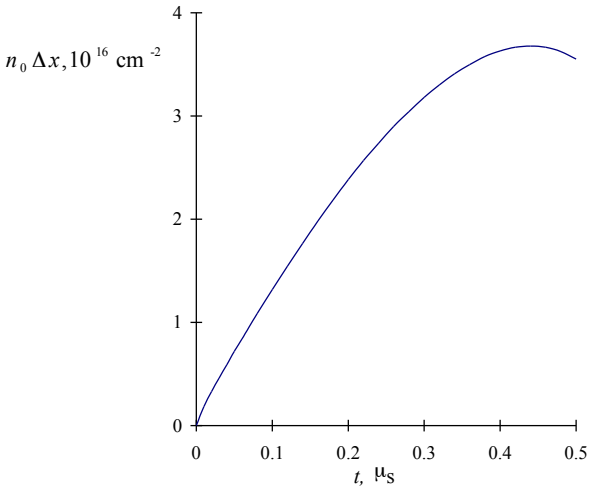

Fig. 5.6. Decrease in the bulk plasma mass $n_0 \Delta x$ as a result of the deposition of plasma onto the cathode as a function of time.

In the case of acceleration of a low-density plasma ($n_0 = 1.5 \cdot 10^{16}$ cm^{-3}), the thickness of the cathode sheath increases much more rapidly. An essential role in the formation of the sheath is played by anomalous ion viscosity and thermal conductivity (5.3.10) (near the cathode, at distances on the order of the ion Larmor radius) and anomalous electron resistivity and thermal conductivity (5.3.11). The profiles of the quantities for this case at the time $t = 55$ ns are shown in Fig. 5.7, when the velocity of the bulk plasma is $v_\infty = 1.75 \cdot 10^8$ cm/s. Fig. 5.7 demonstrates that for such plasma flow velocities, the ions in the cathode sheath are heated to temperatures on the order of several keV, and electrons are heated to fractions of a kiloelectron-volt, and the sheath thickness is several millimeters.

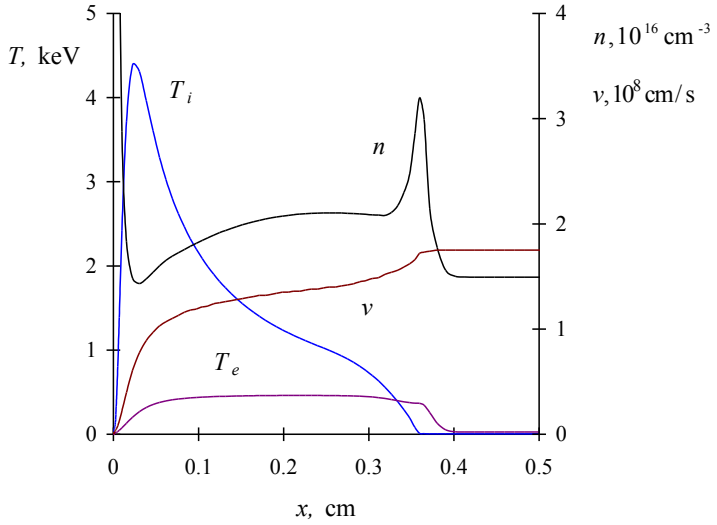

Fig. 5.7. Cathode sheath plasma temperature, density, and velocity profiles for $n_0 = 1.5 \cdot 10^{16}$ cm^{-3}, $T_0 = 2$ eV, $B_0 = 10^5$ G, and $j = -16$ kA/cm^2 at the time $t = 55$ ns.

Anode sheath. At the initial stage of the evolution of the anode sheath, in the MHD approximation, the magnetic flux is carried toward the anode, thereby separating the plasma from the surface. As in the cathode sheath, the dependence of the main plasma parameters on time will be described for short times by the self-similar formulas (5.3.16), with the difference being that t is replaced with $|t_0 - t|$, where t_0 is a certain point of time, i.e., in this approximation, the plasma density will fall off to zero over a finite time interval. At the same time, it is stipulated in the problem setup that the current continues to flow through the sheath. This contradiction can only be resolved by introducing additional kinetic effects and by treating the problem on small spatial scales, for which the MHD approximation is, strictly speaking, inapplicable. In our study, we do that by taking electron inertia into account, i.e., considering the spatial scales of $\sim c/\omega_{pe}$. However, while preserving the MHD description, we do that in the following qualitative fashion. In Ohm's law (5.3.5), we include terms related to electron inertia assuming that there is enough time for the quasi-steady-state approximation to get established for electrons; i.e., we will not include the time derivative term $\frac{\partial \vec{v}_e}{\partial t}$ and will keep only the derivative $v_{ex}\frac{\partial \vec{v}_e}{\partial x}$. That will provide an additional term to (5.3.5)

$$E_{me} = \frac{mc}{4\pi e^3}\frac{j}{n}\frac{\partial}{\partial x}\left(\frac{1}{n}\frac{\partial B}{\partial x}\right), \quad (5.3.19)$$

and the corresponding contribution to the equation for the electron temperature

$$-\frac{c}{4\pi}\frac{j}{n}\frac{\partial B}{\partial x}E_{me}$$

As a result of the presence the additional term in Ohm's law, the possibility of compensating for the first Hall term in equation (5.3.5) (which is $\sim\frac{1}{n}$, since, for a magnetized plasma, $R=\frac{1}{nec}$) opens up even for very small densities. Then, beginning with time t_0, when, according to formulas (5.3.16) with $|t_0 - t|$ in place of t, a vacuum region must form, the region will contain plasma with a density exponentially decreasing from the hydrodynamic boundary (but not zero density). The width of that region will grow with the entry into it of magnetic flux from infinity.

The presence of a current flowing through this low-density region may lead to its strong acceleration and, in the real 2D problem, its replacement with a higher-density plasma from a region with different coordinates y, where current j are weaker and where this vacuum region is smaller or not present at all. In order to describe this effect qualitatively, we will assume that the additional electric field is added to (5.3.13) at the wall interface:

$$E'=-\frac{4\pi}{c^2}j\int(v-v_\infty)\left(1-\frac{\rho}{\rho_\infty}\right)dx \ ,$$

where v_∞ and ρ_∞ are the velocity and the density of plasma far from the electrode.

One-dimensional simulations of the evolution of the anode sheath were performed with account taken of the contribution of E' to the boundary condition at the anode surface and of the effect of electron inertia (5.3.19). To simplify the numerical solution, we increased the coefficient in (5.3.19) by a factor of 100 (otherwise, we would have had to resolve very small spatial scales).

Fig. 5.8a shows profiles of temperature, density, and velocity at time t = 60 ns, which corresponds to the transition from self-similar dependences (5.3.16) to a linearly expanding, low-density region where electron inertia has a substantial effect. At this time, plasma velocity has a maximum $v_{max} = 6.1\cdot10^6$ cm/s at the distance $x = 9.5\cdot10^{-3}$ cm from the anode surface,

the plasma velocity far from the anode being $v_\infty = 4.8 \cdot 10^6$ cm/s. By this time, the impact of the additional field E' on the processes near the anode is still negligible and constitutes 0.01% of the Hall electric field E_H (5.3.14), which delivers the magnetic flux from the depth of the plasma. The electric field (5.3.13), which corresponds to magnetic flux losses into the electrode material by this time, is 14 % of E_H.

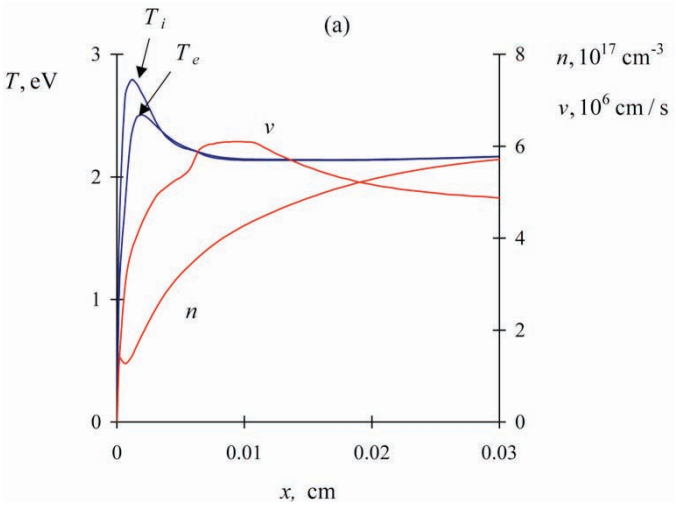

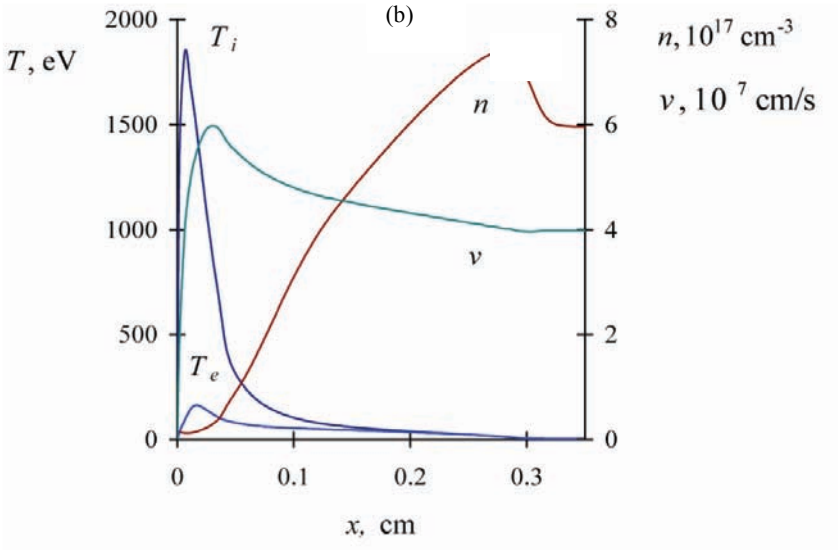

Fig. 5.8. Anode sheath plasma temperature, density and velocity profiles for $n_0 = 6 \cdot 10^{17}$ cm^{-3}, $T_0 = 2$ eV, $B_0 = 10^5$ G, and $j = 16$ kA/cm^2 at the times (a) $t = 60$ ns; (b) $t = 0.5$ μs.

The plasma density in the anode sheath continues to decrease, and magnetic flux leakage due to the hydrodynamic motion represented by E' plays no role of substance. The decrease in the plasma density results in a considerable growth of the plasma velocities and ion temperatures due to the friction between the plasma and the anode surface (see Fig. 5.8b, which corresponds to the time $t = 0.5$ μs). At this time, E' is 58% of E_H, and the electric field (5.3.13), because of diffusion into the copper wall, falls to just 4.7% of E_H. By this time, the electron component of the plasma gets also noticeably heated (to fractions of a kiloelectron-volt) due to electron acceleration by the Hall electric field. Plasma velocity near the wall $v_{\max} = 6 \cdot 10^7$ cm/s exceeds that of the bulk plasma, $v_\infty = 4 \cdot 10^7$ cm/s.

Fig. 5.9 shows the profiles of the anode sheath parameters for the case of acceleration of a low-density plasma at the same time, t = 55 ns, as that in Fig. 5.7 for the cathode sheath. We can see that the plasma velocities in direct proximity to the anode are extremely high, $v_{max} = 5.1 \cdot 10^8$ cm/s, and exceed considerably the bulk velocity; the electron and ion temperatures are also high, $T_{i\,max} = 160$ keV and $T_{e\,max} = 48$ keV. According to Fig. 5.9, DD fusion neutrons can be generated in the plasma sheath near the anode. If we assume that the anode area in the region of the nozzle of the MAGO chamber is S =170 cm^2 and estimate the characteristic time during which a low-density plasma flows through the nozzle as ~ $3 \cdot 10^{-7}$ s —which is based on the time over which the current at the chamber input rapidly ramps down (Fig. 2.5)—then, for the temperature and density profiles shown in Fig. 5.9 and under the assumption that the plasma ions obey the Maxwellian distribution, we obtain a neutron yield of about ~ $1.6 \cdot 10^9$. That yield agrees with the yield measured experimentally in the "nose" region of a neutron pulse ($5.5 \cdot 10^9$ neutrons, which is about 6% of the total number of neutrons in the pulse [5.19]) if we bear in mind that, by comparison with the Maxwellian spectrum, the ion spectrum should be enriched with a large number of high-energy ions produced when a high-velocity ion flow is scattered by the wall. The characteristic velocity $v = 2.2 \cdot 10^8$ cm/s and characteristic temperature T_i =27 keV of the neutron-generating plasma also agree with the experimentally measured characteristics in this part of the neutron pulse obtained on the basis of the spectrum of emitted fusion neutrons [5.19].

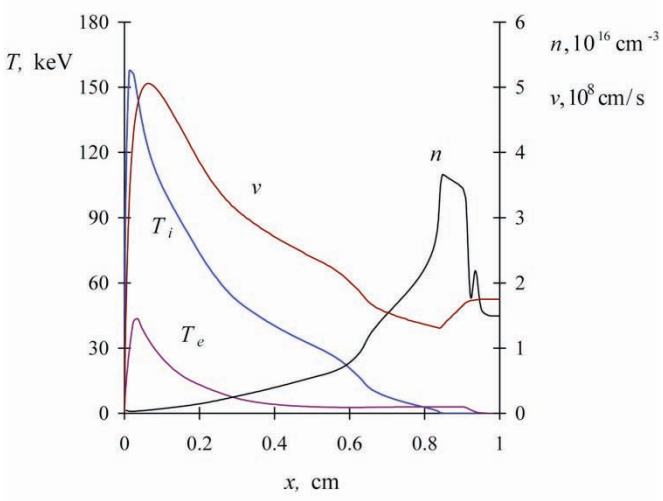

Fig. 5.9. Anode sheath plasma temperature, density and velocity profiles for $n_0 = 1.5 \cdot 10^{16}$ cm^{-3}, $T_0 = 2$ eV, $B_0 = 10^5$ G, and $j = 16$ kA/cm^2 at the time $t = 55$ ns.

A comparison of the anode and cathode sheaths for low-density plasma in Figs. 5.7 and 5.9 show that the difference in the heating of the near-electrode plasmas is quite considerable. For example, the neutron yield from the cathode sheath (Fig. 5.7) should be about two orders of magnitude lower than that from the anode sheath; accordingly, the ion temperature $T_i \sim 4$ keV and flow velocity $v = 7 \cdot 10^7$ cm/s of the neutron-generating plasma in the cathode sheath should be lower than those in the anode sheath.

Presumably, the great differences in the structure of the cathode and anode sheaths may explain the variation in the MAGO chamber operation and the drop in the neutron yield when electrode polarity is switched.

CONCLUSION

A numerical solution of the one-dimensional problem describing the evolution of the cathode sheath in the case of acceleration of a magnetized plasma by a current of constant density shows that, at small times (when plasma velocity is low and viscous plasma heating is negligible), a region of dense plasma forms near the cathode in which the plasma mass increases linearly with time and the electron magnetization parameter is $(\omega\tau)_e \sim 1$. As the plasma velocity increases and plasma turbulence develops, for times $t \sim 0.1\omega_i^{-1}$, viscous plasma heating becomes substantial, ion temperature begins to grow quadratically with time, and the characteristic spatial scale also grows quadratic ally with time and constitutes ~4 % of the entire path of the plasma along the electrode.

An analysis of the anode sheath shows that the MHD approach is inadequate to describe the sheath: in the MHD approximation, the plasma density in the sheath drops to zero, whereas the current density, as determined by the problem as a whole, remains constant. In order to overcome this difficulty, one must go beyond the scope of the MHD approach and take into account electron dispersion. Then, the plasma density in the anode sheath remains finite, although low. A low-density plasma in the anode sheath can be accelerated by the Lorentz force to velocities much higher than the plasma velocities far from the anode and can be heated to high temperatures as a result of the friction against the wall. As in the case of a cathode sheath, the characteristic ion temperatures in the anode sheath on long time scales are determined by the squared plasma velocity, and the characteristic spatial scales are governed by the zone of turbulent mixing. Plasma heating in the anode sheath can initiate fusion reactions, which may explain the generation of DD-neutrons with an anisotropic energy and direction distribution in MAGO experiments.

5.3.2. Kinetic Approach as Applied to Collisionless Magnetized Plasma

Thus, within the above MHD approximation, we assumed that there is an anomalous viscosity that, in terms of magnitude, is equal to $\frac{nT_i}{\omega_i}$ (n is plasma density, T_i is ion temperature, ω_i – is ion cyclotron frequency) and that acts at distances from the electrode surface smaller than the ion Larmor radius r_{Li}. This viscosity resulted in plasma flow deceleration on scales of the Larmor radius determined from the flow velocity v_0, $r_{Li} = v_0/\omega_i$. For the qualitative description of the near-electrode flow using viscosity in the MHD approximation on the r_{Li} scales to be valid, one must know whether the entire flow on those scales will experience deceleration or whether only the ions located at a distance of the Larmor radius from the electrodes that corresponds to the thermal velocity of the plasma flow (which is considered smaller than v_0) will be scattered on the electrodes.

Using the MHD approach, it was shown that thermonuclear neutrons that, because of high flow velocities, have an anisotropic energy distribution that can be generated in the near-anode zone of the MAGO chamber nozzle, which agrees with time-of-flight neutron spectrum measurements [5.19]. However, the neutron yield calculated under the assumption of the Maxwellian ion distribution proved to be somewhat smaller (approximately by a factor of 3) than the experimentally measured yield. The question arises, can that difference be explained by the real ion distribution in the near-electrode plasma with account taken of the kinetics of the ions?

Following Garanin *et al.* [5.22], we will now use particle-in-cell numerical simulations to consider the near-electrode plasma flows in order to answer these questions.

Problem setup. Let us consider a time-dependent one-dimensional problem, in which all quantities depend solely on the coordinate perpendicular to the electrode surface and on time. For large distances from the electrodes, the plasma is assumed to homogeneous, having density n_0 and moving at a velocity $\vec{v}_0$ across the magnetic field $\vec{B}_0$. The velocity $\vec{v}_0$ and field $\vec{B}_0$ are parallel to the electrode surface. We will designate the coordinate perpendicular to the surface as x and assume that the magnetic field is directed along z; then, the velocity $\vec{v}_0$ will be directed along y. We will assume the plasma to be cold: $\beta \equiv \frac{8\pi p_0}{B_0^2} << 1$ (p_0 is initial thermal pressure of the plasma).

When ions collide with the electrode located at x= 0, they can be reflected back into the flux. We will assume that the ions scattered on the electrode fly out into the plasma with the Lambert angular distribution, and we will consider two options for the ion reflection off the electrode: elastic with conservation of energy, and inelastic, with loss of 90% of the energy. The plasma is assumed to be quasi-neutral, the magnetic diffusion coefficient is taken to be small, such that the magnetic field is essentially frozen into the matter, and the Joule heating is disregarded.

Instability of initial plasma state. Let us assume that a small fraction of ions from the flow that have velocity components directed to the electrode due to thermal spreading is scattered elastically on the electrode. Initially, when the influence of these scattered particles is small, their motion can be considered as occurring against an assigned background of the main flow, i.e., they will move in the crossed electric and magnetic fields. For the main stream, the effect of these particles can be analyzed on the basis of perturbation theory, taking into account for it only the appearance of velocities v_x, which originally were equal to zero.

A qualitative analysis of such a linearized problem performed for high M_A numbers under the assumption that the instability growth increment is larger than ω_i yields the following expression for the increment

$$\lambda = \frac{3}{2}\omega_i \ . \qquad (5.3.20)$$

Results of numerical simulations. Fig. 5.10 plots the distribution of the magnetic field (and, hence, the plasma density coinciding with it) and the average velocity v along the electrode for the flow of residual plasma through the MAGO chamber nozzle, with a bulk velocity of $v_0 = -2\cdot10^8$ cm/s, a density of $n_0 = 1.5\cdot10^{16}$ cm^{-3}, in the magnetic field $B_0 = 10^5$ G ($M_A = 1.57$), at sequential times t = 0.5, 1, and $2\cdot10^{-8}$ s for elastic reflection of the ions from the electrode. This figure shows that the mass of plasma reflected from the electrode grows with time, leading to ion flow deceleration on Larmor radius scales, i.e., the specific anomalous viscosity comes into effect near the electrodes. The magnetic field profiles display oscillations, which are indicative of an evolving two-stream instability. Note that, in the simulations, the role of these instabilities, in accordance with their theory, diminishes with increasing M_A.

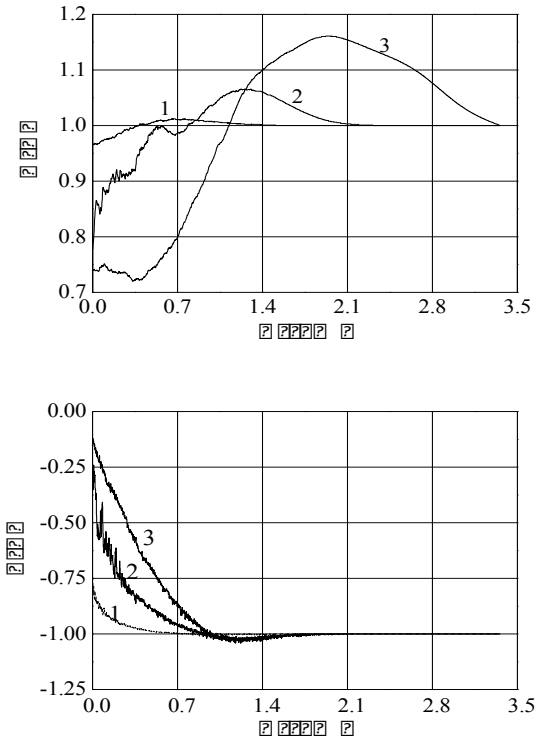

Fig. 5.10. Distribution of magnetic field B and average velocity v along the electrode (in units of initial B_0 and v_0) for the flow with bulk velocity $v_0 = -2\cdot10^8$ cm/s, density $n_0 = 1.5\cdot10^{16}$ cm^{-3}, in magnetic field $B_0 = 10^5$ G, at times t = 0.5, 1, and $2\cdot10^{-8}$ s (curves 1, 2, 3, respectively).

Figure 5.11 shows the resulting ion "thermal" velocity distribution $f(v)$ in the frame of reference system related to the local average velocity ($f(v)\,dv$ is equal to the fraction of the particles in the velocity interval dv) at a distance of 0.7 cm from the electrode, which equals 1.7 r_{Li}, as well as the velocity distribution for ion kinetic energy (i.e., the quantity $v^2 f(v)$) obtained for the time $t = 2 \cdot 10^{-8}$ s. It can be seen from the figure that ions that constitute a small fraction of the total number of the particles account for most of the "thermal energy" of the ion component. These are the ions that have been reflected off the wall, and it is those ions that make the principal contribution to thermonuclear reactions, when they collide with the main flow ions. What will that result in? First, the rate of thermonuclear reactions will become somewhat higher. Second, which is even more interesting in the context of neutron spectrum measurements in MAGO experiments [5.19], the velocity of neutron-generating plasma may exceed the average mass velocity. Thus, taking into account the kinetics to explain the results of Burenkov *et al.* [5.19], one must assume that the residual plasma density is higher than that used in the simulations in the hydrodynamic approximation (Section 5.3.1), and, consequently, the plasma will acquire a lower velocity. As a result, the neutron yield from such plasma will increase in the simulations in proportion to, roughly speaking, the squared density will agree with the experiment.

For early times, when the fraction of reflected particles is small, their number should increase exponentially in accordance with the linear theory of instability. In the simulations, we actually observed the exponential increase of the number of reflected particles with time. The increments of this growth proved close to the theoretical estimate (5.3.20), and the increments decreased somewhat with decreasing M_A, i.e., magnetic pressure of the reflected ions impedes the inflow of new ions from the main flow to the wall.

Figure 5.12 plots the dependence of the loss of the longitudinal component (along the electrode) of plasma momentum, converted to plasma layer thickness (measured in r_{Li}) corresponding to a full plasma stop, on the Alfven-Mach number M_A. We can see that this quantity remains nearly constant in a wide range of M_A and equals $\approx 0.5 r_{Li}$, i.e., this distance can be considered to be the point of full stop of the flow.

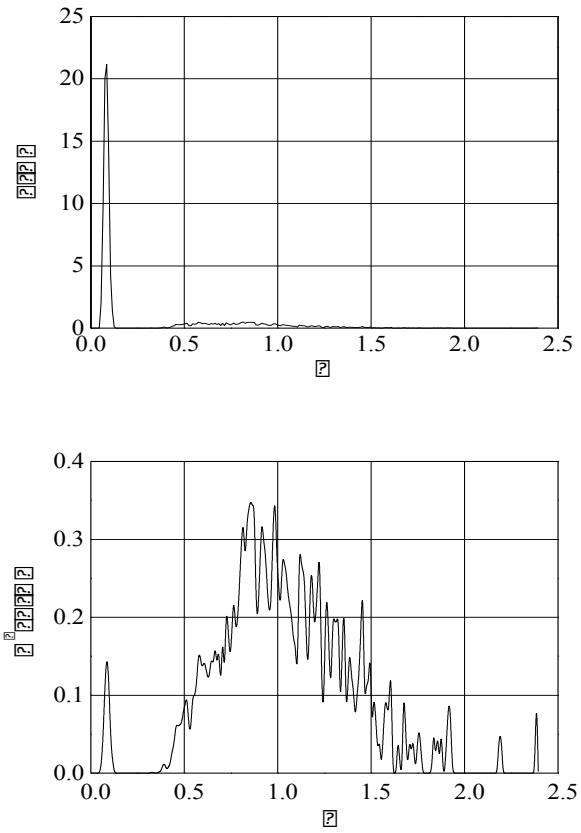

Fig. 5.11. Ion "thermal" velocity distribution f (v), and the velocity distribution for ion kinetic energy $v^2 f(v)$ *for the simulation with* $M_A = 1.57$ *at a distance of 0.7 cm from the electrode, at the time* $t = 2 \cdot 10^{-8}$ *s. Velocities are measured in the units of* v_0.

For very high flow velocities, the assumption that the ion scattering on the wall is inelastic may be valid. It turned out that in the simulations in this case, there was no linear stage of the flow swing instability development with the exponential growth due to a high density of reflected particles near the electrode; instead, there is immediate onset of a nonlinear stage. The simulation for $M_A = 1.57$ revealed that the loss of the longitudinal component of plasma momentum in this case was equivalent to a plasma layer thickness of $\approx 0.46 r_{Li}$.

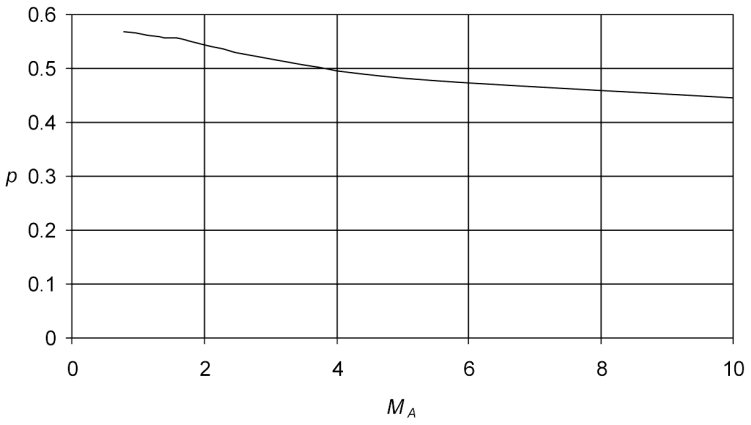

Fig. 5.12. Dependence of loss of longitudinal plasma momentum component converted to plasma layer thickness (measured in r_{Li}*),* $p = \int \frac{dx}{r_{Li}} \frac{n}{n_0} \left(1 - \frac{\nu}{\nu_0}\right)$ *on the Alfven-Mach number* $\mathrm{M_A}$.

CONCLUSION

The reflection off the electrode of ions of the moving stream leads to the turning of the flow fraction that is located at a distance of ~r_{Li} from the electrode towards the electrode and results in effective deceleration of that part of the flow. The ions scattered from the electrode can generate thermonuclear neutrons when they collide with ions of the main flow, and the velocity of this neutron-generating plasma can be markedly higher than the average mass velocity.

5.4. Role of Drifts in Magnetized Plasma of the MAGO System

As shown in Section 2.1.2 above, the body of experimental and simulated data enables us to believe that DT plasma with the following parameters is reliably produced in experiments with the large MAGO chamber in a coaxial cylindrical volume having a height of 8 cm, an outer radius of R ~ 10 cm, and an inner radius of 1.2 cm:

average density $n = 8 \cdot 10^{17} \mathrm{cm}^{-3}$,
average temperature $T = 250$ eV,
characteristic current in the plasma $I \sim 4$ MA,
characteristic magnetic field in the plasma $B \sim 0.16$ MG,
characteristic $\beta \sim 0.6$.

Those parameters make the plasma suitable for ignition in its quasi-spherical compression. If the plasma is compressed adiabatically to a radius of R ~1.7 cm and a characteristic height of ~1.4 cm (exposed to magnetic and thermal pressure, the radius of the metal rod decreases from 1.2 cm to about 0.8 cm), the plasma will have a density of $n = 2 \cdot 10^{20}$ cm^{-3}, a characteristic temperature of T =10 keV, a characteristic current in plasma of I ~ 70 MA, a characteristic magnetic field in plasma B ~ 10 MG, and a characteristic $\beta \sim 2$. If the plasma is compressed at a velocity of $v \sim 10^6$ cm/s, the characteristic time of its compression will be $\tau \sim 9 \cdot 10^{-7}$s, and the Lawson criterion, $n\tau \sim 2 \cdot 10^{14}$ cm^{-3}s, will be met.

For the compression to be adiabatic, it is necessary that the various losses not be large. Classical electron and ion heat conductivities of magnetized plasma cause losses of the order of the Bohm heat conduction (see Section 6) and they can be taken into account in direct one-dimensional simulations (see Chapter 7). Other important losses include those associated with drifts of charged particles in the magnetic field and resulting in heat and magnetic flux transfer. These losses and their associated fluxes do not contain collision frequencies and are therefore collisionless. In studying the processes of thermonuclear energy release, it is also important to address the issue of α-particles confinement in a magnetic field so that their energy is released in the fuel, increasing its temperature and amplifying its reactivity or heating up the cold parts of the fuel.

5.4.1. Role of Collisionless Losses in MAGO Plasma

The simplest example of collisionless drift losses is heat transport by the current. In the MAGO chamber, currents flow from one metal electrode to the other. Low-temperature electrons emitted by the cathode, when they move with the current, replace hot electrons of the plasma, thereby cooling it. The current velocity of electrons is equal to $u \sim I / e\pi R^2 n$, and the effect of their transport on plasma cooling can be estimated as the ratio of their displacement when they are transported by the current to the characteristic system size

$$\frac{u\tau}{2l} \sim \frac{I\tau}{2e\pi R^2 nl} \sim \frac{I\tau}{2eN}, \qquad (5.4.1)$$

where N is the total number of particles in the chamber (the multiplier 2 indicates that electrons carry only half of the energy). The number of particles does not change with plasma compression. If the quasi-spherical compression proceeds at a constant velocity, the duration of the characteristic inductance drop is shorter than the time τ of the plasma

compression, and the current grows faster than $1/\tau$. Hence, the stage of the highest compression is the most dangerous for plasma cooling by current transport. When we substitute the above plasma parameters of this stage into formula (5.4.1), we obtain $\frac{u\tau}{l} \sim 0.1$. Thus, the effects of plasma cooling by the current under such conditions can be pronounced, but not fatal.

One can easily estimate the effects of charged-particle drifts on plasma cooling. The drift velocities are equal to

$$u \sim \frac{r_{e,i}}{R} v_{T\,e,i} \sim \frac{cT}{eBR} \sim \beta \frac{I}{4\pi n e R^2} \quad . \tag{5.4.2}$$

They differ from the current velocity by only a factor of $\beta/4$. Since β grows during quasi-spherical compression, the states of highest compression are, as in the case of plasma cooling by current transport, the most dangerous for plasma cooling. Since $\beta/4 \sim 0.5$ in this state, the role of these drifts can also be assessed as pronounced, at ~ 0.1, but not fatal. Magnetic flux transport by current (the Hall effect) has a comparable influence on the plasma state. Formula (5.4.2) shows that the drift-induced losses in a system with $l \sim R$ produce losses that are literally the same as those associated with the Bohm diffusion, but they have no small numerical multiplier (1/16) appearing in the Bohm diffusion coefficient.

It should be noted that in the MHD description of plasma in 2D simulations, all those drifts can be taken into account in the form of the Hall effect, Leduc–Righi effect, and heat transport by current [5.20].

5.4.2. Confinement of α-Particles in Magnetic Field

The rate of α-particle deceleration in the plasma is determined by formula [5.23]

$$\gamma(\mathrm{s}^{-1}) \sim 1.6 \cdot 10^{-9} n(\mathrm{cm}^{-3}) \lambda / T(eV)^{3/2},$$

where λ is the Coulomb logarithm. Since the residence time of α-particles in the DT plasma is limited by their drift, $\tau \sim l/u$ ($u \sim \frac{2c\varepsilon}{3zeBr}$ is the drift velocity of a charged particle with the charge ze and energy ε in the magnetic field B decreasing in terms of the radius as l/r), the fraction of energy deposited by the particle in the plasma can be estimated as $\gamma l/u$. To enable good confinement of α-particles, this fraction should be large. In our

case, for the above plasma parameters, this fraction is ~ 0.3 and depends on the parameters ~ $Inl/T^{3/2}$. Thus, in order to improve α-particle confinement, one must increase the current in the plasma, the plasma density, or the dimensions of the plasma.

But if the objective is to transfer the energy release from hotter layers to colder layers, α-particles will be capable of performing this function, because their energy release increases with decreasing plasma temperatures. One should keep in mind that α-particle drift takes place along the Z-axis, and therefore the hot and cold regions of the fuel after the compression should also be located along the Z-axis. It should be noted also that heat transport by the electron current proceeds along the Z-axis as well, but in the opposite direction, and both effects can offset each other to a certain extent.

REFERENCES

5.1 A.S. Kingsep, K.V. Chukbar, V.V. Yankov. "Electron Magnetohydrodynamics," *Voprosy Teorii Plazmy: Sb. Statey* (Reviews of Plasma Physics: Collection of Papers). Ed. B.B. Kadomtsev. Moscow: Energoatomizdat [Publishing House], No. 16, pp. 209–250, 1987.

5.2 S.F. Garanin. "Dynamics of Magnetic Field Penetration into Magnetized Plasma," *VANT* [Aspects of Atomic Science and Technology]. Theoretical and Applied Physics Series, No. 3, pp. 12–16, 1989.

5.3 A.V. Gordeev, V.V. Zazhivikhin, A.V. Gulin, O.M. Drozdova. "On Some Physical Processes in Low-Density Plasma Opening Switches," *VANT,* Thermonuclear Fusion Series. No. 1, pp. 76–77, 1988.

5.4 K.V. Chukbar, V.V. Yankov. "Magnetic Field Evolution in Plasma Opening Switches," *ZhTF* (Journal of Technical Physics), Vol. 58, No. 11, pp. 2130–2135, 1988.

5.5 E.M. Lifshitz, L.P. Pitayevskiy. *Fizicheskaya Kinetika* [Physical Kinetics]. Moscow: Nauka [Publishing House], 1979.

5.6 K.V. Brushlinskiy, T.A. Ratnikova. "Some Issues of Two-Fluid MHD with a Transverse Magnetic Field," *Matematicheskoye Modelirovaniye* (Mathematical Modeling), v. 8, No. 2, pp. 75–90, 1996.

5.7 K.V. Brushlinskiy, A.I. Morozov. "Simulations of 2D Plasma Flows in Channels," *Voprosy Teorii Plazmy: Sb. Statey* (Reviews of Plasma Physics: Collection of Papers). Ed. M. A. Leontovich. Moscow: Atomizdat [Publishing House], No. 8, pp. 88–163, 1974.

5.8 K.V. Brushlinskiy, T.A. Ratnikova. "Hall Effect in the MHD Model of Plasma Flow in Channels," *Izv. RAN. MZhG* [Bulletin of the Russian Academy of Sciences. Mechanics of Fluids and Gases], No. 5, pp. 56–65, 1995.

5.9 K.V. Brushlinskiy, T.A. Ratnikova. "Numerical Model of Near-Electrode Instability in Plasma Accelerator Channels," *Fizika Plasmy* [Plasma Phys. Reports], Vol. 21, No. 9, pp. 784–790, 1995.

5.10 K.V. Brushlinskiy, T.A. Ratnikova. "Hall Corrections to Plasma Flow Simulations in Near-Electrode Layers of Coaxial Channels," *ibid*., Vol. 23, No. 2, pp. 126–130, 1997.

5.11 P.V. Sasorov. "On the Effect of Z-Pinch Current Shell Sliding Along the Anode)," *ibid.,* Vol. 16, No. 10, pp. 1236–1244, 1990.

5.12 S.F. Garanin, V.I. Mamyshev. “Otryvayushchie Prianodnye Techeniya Zamagnichennoy Plazmy (Near-Anode Magnetized Plasma Detachment Flows),” *ibid.,* Vol.. 16, No. 10, pp. 1218–1225, 1990.

5.13 V.I. Artemyev, I.E. Markovich, I.V. Nemchinov, V.A. Sulyayev. “Two-Dimensional Self-Similar Motion of a Strong Shock Wave Over a Heated Surface,” *DAN SSSR* (Sov. Phys. Dokl.), Vol. 293, No. 5, pp. 1082–1084, 1987.

5.14 L.D. Landau, E.M. Lifshits. *Gidrodinamika* (Fluid Mechanics). Moscow: Nauka [Publishing House], 1986.

5.15 A.I. Morozov, L.S. Solovyev. “Steady-State Plasma Flows in Magnetic Fields,” *Voprosy teorii plazmy: Sb. Statey* (Reviews of Plasma Physics: Collection of Papers). Ed. M. A. Leontovich. Moscow: Atomizdat [Publishing House], No. 8, pp. 3–87, 1974.

5.16 V.V. Vikhrev, S.I. Braginskii. “Z-Pinch Dynamics,” *Voprosy Teorii Plazmy: Sb. Stratey* (Reviews of Plasma Physics: Collection of Papers). Ed. M. A. Leontovich. Moscow: Atomizdat [Publishing House], No. 10, pp. 243–318, 1980.

5.17 S.F. Garanin. “Near-Electrode Layers Originating at Magnetized Plasma Accelerating,” in *XXIII International Conference on Phenomena in Ionized Gases, July 17–22, 1997, Toulouse, France, Proceedings,* Contributed Papers, Vol. 4. Fourth, pp. 158–159. Eds. M. C. Bordage and A. Gleizes. 1997.

5.18 S.F. Garanin. “Formation of Electrode Sheaths During the Acceleration of a Magnetized Plasma,” *Fizika Plasmy* [Plasma Phys. Reports], Vol. 26, No. 4, pp. 283-291 *Fiz. Plasmy*, Vol. 26, No. 4. pp. 309–317), 2000.

5.19 O.M. Burenkov, S.F. Garanin, A.N. Demin, V.I. Dudin, V.P. Korchagin, I.V. Morozov, V.N. Mokhov, E.S. Pavlovskii, V.K. Chernyshev, V.B. Yakubov, "Study of Plasma in MAGO Chamber from Neutron Self-Radiation,” *Fizika Plasmy* [Plasma Phys. Reports], Vol. 23, No. 3, pp. 203–209, March 1997.

5.20 S.I. Braginskii. “Transport Processes in a Plasma,” *Voprosy Teorii Plazmy: Sb. Statey* (Reviews of Plasma Physics: Collection of Papers). Ed. M.A. Leontovich. Moscow: Atomizdat [Publishing House], No. 1, pp. 183–272, 1963. Reviews of Plasma Physics. Consultants Bureau, New York, v. 1, p. 205, 1965.

5.21 R.C. Davidson, N.T. Gladd. “Anomalous Transport Properties Associated with the Lower-Hybrid-Drift Instability,” *Phys. Fluids,* Vol. 18, No. 10. pp. 1327-1335, 1975.

5.22 S.F. Garanin, A.I. Golubev, N.A. Ismailova. “Boundary Layer Formation in a Flow of Collisionless Magnetized Plasma,” *Proc. 13th Int. Conf. on High-Power Particle Beams,* K. Yatsui and W. Jiang, Nagaoka University of Technology, Vol. 1, pp. 68-71, 2001.

5.23 B. A. Trubnikov. "Particle Collisions in a Fully Ionized Plasma,” *Voprosy Teorii Plazmy: Sb. Statey* (Reviews of Plasma Physics: Collection of Papers). Ed. M.A. Leontovich. Moscow: Atomizdat [Publishing House], No. 1, pp. 98–182, 1963. *Reviews of Plasma Physics*. Consultants Bureau, New York, Vol. 1, p. 105, 1965.

6. SURFACE DISCHARGES IN STRONG MAGNETIC FIELDS

In many problems of physics and engineering related to megagauss magnetic fields, situations are encountered in which magnetic fluxes cross interfaces between condensed matter (metal or insulator) and vacuum or plasma. If one restricts oneself to considering the case that is most commonly used in applications, in which the magnetic field is parallel to the interface and the magnetic flux is transferred perpendicularly to the surface, then schematically these situations can be depicted as they are in Fig. 6.1. The transition of magnetic flux through the interface may be accompanied by surface discharges or flows that, generally speaking, affect the operation of given units. In a number of cases, the space scale of such discharge areas can be small by comparison with the characteristic scale of the problem as a whole, and the physics of such discharges can be studied assuming that they can be described by a plane 1D problem (with a coordinate perpendicular to the interface). Let us list the particular situations corresponding to the schemes in Fig. 6.1 with different directions of the magnetic flux.

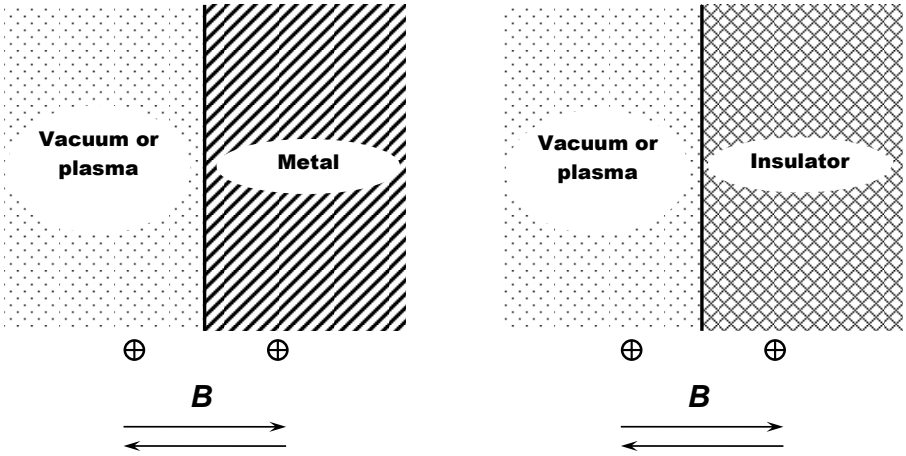

Fig. 6.1. Schemes of magnetic flux transfer through the interface between condensed matter and a vacuum or plasma.

1. Magnetic flux flows from vacuum to metal. This is magnetic field diffusion into metal, which is important for the problems of obtaining megagauss magnetic fields, condensed liner implosion through the use of strong magnetic fields, etc. This problem will be considered in accordance with Garanin *et al.* [6.1].

2. When plasma with a magnetic field comes in contact with metal, cooling processes begin that may amplify for a magnetized plasma if, as a result of magnetic diffusion, the plasma loses the magnetic flux and becomes demagnetized. Such problems are important for plasma confinement by walls in many applications, including the MAGO/MTF systems. Plasma cooling was considered by Vekshtein [6.2] for relatively low energy densities, when the metal does not explode, and by Garanin and Mamyshev [6.3] for higher energy densities, with account taken of the explosion of the metal wall caused by the heat flow from the plasma.

3. In the case in which the magnetic field outside the metal begins to decrease abruptly, and the metal, at least in the skin layer, contains a larger field, the magnetic flux tends to leave the metal. The diffusion starts and the material (if the metal is in a liquid state) escapes into the open space. Such a situation (magnetic spallation) sometimes occurs in the course of liner acceleration, and has a number of interesting features. This problem is considered in Garanin *et al.* [6.4].

4. When magnetic flux is transferred through the insulator surface, a breakdown may occur on its surface, which restricts the energy flux delivered through the surface (the *H*-thrown discharge). In addition, evaporation of the insulator in the discharge and the presence of an ionized vapor moving together with magnetic field lines can be detrimental, if the magnetic flux delivered through the surface is used to drive liners or plasma. In the first case, the additional vapor mass will make the liner heavier and will slow its acceleration; in the second case, the vapor may contaminate the plasma with the insulator impurities, which is very significant in the approaches using pure hydrogen plasma, such as MAGO and plasma focus. *H*-thrown discharge problems are considered in Garanin *et al.* [6.5] and Garanin and Karmishin [6.6].

5. When magnetic flux from a vacuum or plasma region enters a more dense plasma or insulator, surface discharges (H-pressed discharges) that impede the movement of the magnetic flux through the surface may occur [6.7, 6.8]. Depending on the system, these discharges may play either a negative role—in systems in which the energy must be

delivered through the insulator surface—or a positive role—in systems in which the magnetic flux must be confined in the plasma area (magnetic flux losses associated with field reversal in theta-pinch, magnetic flux confinement in the MAGO chamber, etc.). Related to the problem of *H*-pressed discharge is the problem of the cooling of magnetized plasma that is in contact with condensed material [6.9]. A general quantitative approach to consideration of a surface discharge at the interface between a plasma with arbitrary β and an insulator, which includes the problem of magnetic flux loss from a plasma into an insulator and the problem of plasma cooling, was developed by Garanin [6.10].

Surface discharges complicate the diagnostics of strong magnetic fields, because the probes that measure such fields (*B*-dot probes and Faraday loops) are usually placed in the insulator through whose surface the magnetic flux is transferred. As a result of the discharge, the field near the probe may turn out to be smaller than the field that needs to be measured. The rapid progress in modern high energy density and megagauss-field physics and engineering requires clear understanding of physical effects and characteristics of surface discharges in strong magnetic fields in order to include and simulate them in different systems.

In this section, we will consider the surface discharges that are most important for applications, excluding only magnetic spallation, which is of narrower interest. First, let us consider the *H*-pressed discharges since their qualitative features also play important role for other surface discharges.

6.1. Diffusion of Strong Magnetic Field into Plasma or Insulator

In the development of systems that use strong magnetic fields and corresponding electromagnetic energy densities, the need arises in various units and devices to transfer electromagnetic energy through the surface of an insulator. Such a transfer may cause a surface breakdown of the insulator and its subsequent development. In this case, a part (or all) of the current is diverted to the discharge, with a resulting decrease in the power and magnetic flux being transferred to load through the insulator surface. If the magnetic flux leaves a vacuum or plasma towards the insulator, the surface discharge is called magnetopressed, or *H*-pressed, because, in this case, the magnetic pressure presses the ionized vapor in the discharge to the insulator surface.

The following situation (see Fig. 6.2) can serve as an example of the *H*-pressed discharge problem: first, the current in a circuit surrounding some region with a magnetic field increases, with the magnetic flux entering this region through the insulator. Then the current powering the circuit begins to decrease, and the magnetic flux starts leaving the region. A voltage is

generated on the insulator surface, which can cause insulator surface breakdown. As a result of the development of a surface discharge (in which the magnetic pressure presses the material to the insulator, since the magnetic field in the circuit is stronger than that of the powering side), the discharge will impede the exit of the magnetic flux from the region. Another example of an *H*-pressed discharge is a discharge on the insulator surface occurring in the measurement of magnetic fields in some region with probes placed into the insulator. When the insulator or cold dense plasma are placed into a magnetic field and the magnetic field penetrates such a region, the formation of an *H*-pressed discharge is also possible.

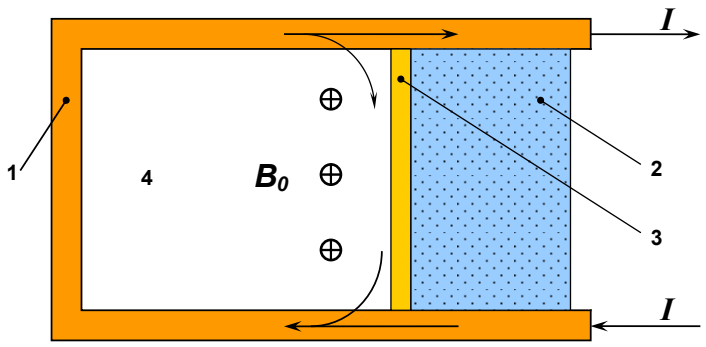

Fig. 6.2. Formation of H-pressed discharge on the insulator surface: 1) conductive walls; 2) insulator; 3)discharge plasma; 4) working space.

In terms of dimensions, the magnetic field penetration into the insulator is described by the equation of diffusion, in which the magnetic diffusion coefficient, *D*, is inversely proportional to the conductivity (proportional to the electrical resistivity) of the wall material. Knowing the diffusion coefficient *D*, we can evaluate the depth of the magnetic field penetration into the material (the skin-layer thickness):

$$\delta \sim \sqrt{Dt} \ ,$$

where *t* is the characteristic time of magnetic field application to the wall boundary. In the majority of cases of interest in terms of applications, we can assume that the vapor plasma generated in the discharge manages to reach equilibrium with the forces from the magnetic field *B*; therefore, we can assume that the total pressure (of the matter and the magnetic field $B^2/8\pi$)) at every moment in time is constant over the entire zone of the discharge. The discharge zone itself can be regarded as a flat layer, because its thickness is usually small by comparison with the size of the device.

As the discharge develops, a plasma whose conductivity depends primarily on temperature and increases with temperature is generated on the insulator surface. The question arises: How does one determine the characteristic conductivity of the discharge for a given magnetic field level *B,* and thus the thickness of the zone of discharge, δ, and, accordingly, all the discharge parameters (discharge resistance, voltage across it, etc.)? With conductivity growing with temperature, the following scenario would seem to be possible: an increase in the heating of the discharge zone by Joule heating results in increased conductivity and further heating until the entire current begins to flow over a thin layer of extremely heated plasma. This scenario, which attempts to describe the discharge evolution solely in terms of conductivity without accounting for any other phenomena can be called infinitely fast discharge skinning into an infinitely thin layer.

There exists, however, a process limiting the overheating of the current-carrying plasma layer. That process is thermal conductivity. Because of thermal conductivity and plasma layer cooling due to radiation, the plasma is not overheated.

The *H*-pressed discharge on the insulator surface can be looked upon as a special case of magnetic field diffusion into plasma of infinite density. Therefore, we can consider the general set-up of the problem of magnetic field diffusion into plasma. We will study the case of rather strong magnetic fields so that the discharge plasma can be regarded as completely ionized.

We can distinguish three main phases in the process of magnetic field diffusion into dense plasma: 1) the radiation losses are small in comparison with the Joule heating, and the electron thermal conductivity and thermoelectric effects (Nernst effect) play the main role in limiting the skinning of the magnetic field; 2) the radiation losses start to offset the Joule heat release, and the discharge becomes stationary; 3) the discharge radiation heats the internal plasma layers, the heat diffusion is determined by the radiative heat conduction, and the magnetic diffusion and radiation temperature conductivity coefficients become of the same order.

We assume that all the quantities depend on the *X* coordinate and time *t*, the magnetic field, *B*, and the electric field, *E*, are perpendicular to each other and the *X* axis, the characteristic times are larger by comparison with those of gas dynamic, such that the total pressure in the system managed to become equalized:

$$p + B^2 / 8\pi = B_0^2 / 8\pi \qquad (6.1.1)$$

(p is the thermal pressure, B_0 is the magnetic field at the interface with the vacuum).

The equations for magnetic and electric fields and the plasma thermal balance written in the Lagrangian variables have the following form:

$$\frac{dB}{dt} - \frac{B}{\rho}\frac{d\rho}{dt} = -c\frac{\partial E}{\partial X} \ ,$$

$$\frac{\partial B}{\partial X} = -\frac{4\pi}{c} j \ ,$$

$$E = \frac{j}{\sigma} - \frac{\beta_\Lambda}{e}\frac{\partial T}{\partial X} \ , \qquad (6.1.2)$$

$$\rho\frac{d\varepsilon}{dt} - \frac{p}{\rho}\frac{d\rho}{dt} = -\frac{\partial Q}{\partial X} + jE - J \ ,$$

$$Q = -\chi\frac{\partial T}{\partial X} + \frac{b_\Lambda T}{e} j \ ,$$

where ρ is the plasma density; ε is the internal energy; σ, χ, b_Λ are the transverse conductivity, the thermal conductivity and the thermoelectric coefficient, respectively; j is the bulk power of the radiation losses; Q is the heat flux density. We assume that at the initial moment, the magnetic field in plasma equals zero, and the plasma is homogeneous.

6.1.1. Magnetic field diffusion into hydrogen plasma for small times

First, let us consider magnetic field diffusion into plasma for small times, when the radiation is negligible, and electron transport coefficients play the principal role. In this case, the coefficients of magnetic diffusion and thermal conductivity are of the same order for the degree of electron magnetization $\omega_e\tau_e \sim 1$, and it is convenient to choose as units of measurement for temperature T and electron density N

$$[T] = \left(\frac{B_0}{\sqrt{8\pi}} c\lambda z e^3\sqrt{m}\right)^{2/5} \ , \qquad (6.1.3)$$

$$[N] = \frac{B_0^2}{8\pi} / [T] \qquad (6.1.4)$$

(z is the ion charge, λ is the Coulomb logarithm). Using the self-similar variable

$$\xi = \frac{e^{1.1} m^{0.1} (\lambda z)^{0.2}}{(B_0^2/8\pi)^{0.65}} \frac{\int N\,dx}{\sqrt{t}} \qquad (6.1.5)$$

and introducing the dimensionless functions

$$T = [T]\Theta(\xi)$$

$$N = [N]n(\xi)\,,$$

$$B = B_0\, h(\xi)$$

$$E = \frac{(em)^{0.1}(\lambda z)^{0.2}(B_0^2/8\pi)^{0.35}}{c^{0.3}\sqrt{t}}\varepsilon(\xi)\ , \qquad (6.1.6)$$

$$Q = \frac{(em)^{0.1}c^{0.7}(\lambda z)^{0.2}(B_0^2/8\pi)^{0.85}}{\sqrt{t}}q(\xi)\ ,$$

$$X = \frac{(em)^{0.1}c^{0.7}(\lambda z)^{0.2}}{(B_0^2/8\pi)^{0.15}}x(\xi)\ ,$$

the system of equations (6.1.1 and 6.1.2) can be written as

$$n\Theta(1+1/z)+h^2=1\ ,$$

$$\frac{d\varepsilon}{d\xi}=\frac{\sqrt{2\pi}\xi}{n}\left(\frac{dh}{d\xi}-\frac{h}{n}\frac{dn}{d\xi}\right),$$

$$\frac{dh}{d\xi}=-\frac{3\Theta^{3/2}}{4\alpha n}\left(\varepsilon+\beta n\frac{d\Theta}{d\xi}\right),$$

$$q=-\frac{\beta n\Theta}{\sqrt{2\pi}}\frac{dh}{d\xi}-\frac{3\gamma n}{4\sqrt{2\pi}}\Theta^{5/2}\frac{d\Theta}{d\xi}\ , \qquad (6.1.7)$$

$$\xi\left[\frac{5}{4}(1+1/z)n\frac{d\Theta}{d\xi}+h\frac{dh}{d\xi}\right]=n\frac{dq}{d\xi}+\frac{n\varepsilon}{\sqrt{2\pi}}\frac{dh}{d\xi}\ ,$$

$$\frac{dx}{d\xi}=1/n\ ,$$

where α, β, and γ depend on the degree of magnetization

$$y \equiv \omega_e \tau_e = \frac{3h}{2n}\Theta^{3/2} \tag{6.1.8}$$

and are determined by the approximate formulae [6.11]

$$\begin{aligned} \alpha &= 1 - \frac{\alpha_1' y^2 + \alpha_0'}{\Delta} \ , \\ b &= \frac{y(\beta_1'' y^2 + \beta_0'')}{\Delta} \ , \\ \gamma &= \frac{\gamma_1' y^2 + \gamma_0'}{\Delta} \ , \\ \Delta &= y^4 + \delta_1 y^2 + \delta_0 \end{aligned} \tag{6.1.9}$$

(the coefficients' designations in (6.1.9) coincide with the those in Braginskii [6.11]).

The boundary conditions of the system (6.1.7) are

$$\begin{aligned} h(0) = 1, \quad h(\infty) = 0 \ , \\ n(\infty) = n_\infty \ , \\ q(0) = q(\infty) = 0 \ . \end{aligned} \tag{6.1.10}$$

Using the equations (6.1.7) and the boundary conditions (6.1.10), we can obtain the expansion $n(\xi), \Theta(\xi), q(\xi)$ for $\xi \to 0$, taking into account that for $\xi \to 0$ $n \to 0, y \to 0$, and using the analytical expressions for the kinetic coefficients for high magnetization [6.12]:

$$\begin{aligned} n &\sim \xi^k \ , \\ \Theta &\sim \xi^{4k-2} \ , \\ q &\sim \xi^{5k-2} \ , \end{aligned} \tag{6.1.11}$$

$$k = \frac{5z^2 + 4(\sqrt{2}-1)z + 4}{9z^2 + (8\sqrt{2}-7)z + 10} \ .$$

The considered phase of the diffusion is important for hydrogen plasma ($z = 1$) only. For $z > 1$, because of the big radiation losses, the transition to the stationary discharge regime takes place too early, when the condition (6.1.1) is not yet satisfied and the material inertia cannot be disregarded.

Now let us consider the solution (6.1.7) for $z = 1$. In this case the expansions of (6.1.11) yield the following:

$$n \sim \xi^{0.457} ,$$

$$\Theta \sim \xi^{-0.172} ,$$

$$q \sim \xi^{0.286} ,$$

that is, the temperature at the vacuum interface goes to infinity. The results of the numerical calculation of system (6.1.7) for $n_\infty = \infty$ are shown in Fig. 6.3. The value of the electric field at the vacuum interface ε_0 is shown in Fig. 6.4 as the function of n_∞. The electric field ε_0 for large n_∞ tends to the constant value $\varepsilon_0 \cong 2.04$, whereas, for low n_∞, it becomes proportional to $n_\infty^{3/4}$, as one would expect.

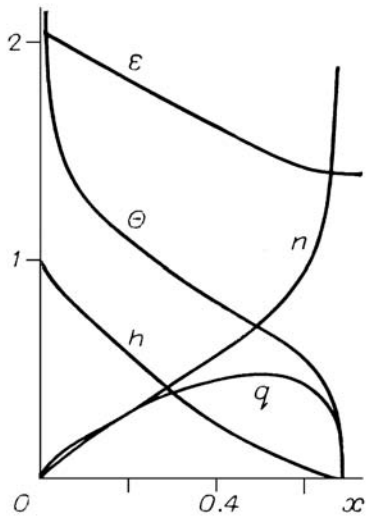

Fig. 6.3. Profiles of the electric field ε, temperature Θ density n, magnetic field h, and heat flow q for magnetic field diffusion into a plasma with infinite density $n_\infty = \infty$.

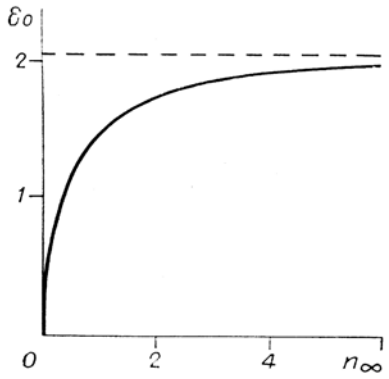

Fig. 6.4. Dependence of electric field at the vacuum interface on plasma density for magnetic field diffusion into plasma.

It should be borne in mind, however, that for

$$n_\infty << \left(\frac{m}{m_i}\right)^{0.1} / z^{0.4}$$

(m_1 is the ion mass) the ion thermal conductivity is more important than electron thermal conductivity. In this case, the plasma can be regarded as isothermal with temperature $\Theta = 1/[n_\infty(1 + 1/z)]$. The numerical solution of the magnetic field diffusion equations for this case shows, that the isothermality approximation is fulfilled quite well in low-density plasma and with account taken of electron transport coefficients only; thus, the solutions of the equations (6.1.7) can also be used for very low plasma densities. Thus, the value $\varepsilon(0) = 1.58$ coincides quite well with $(\Theta_\infty^{3/4}\varepsilon(0)$ for $n_\infty \to 0, \quad \Theta_\infty \to \infty$ in Fig. 6.4: $(\Theta_\infty^{3/4}\varepsilon(0))_{n_\infty \to 0} \cong 1.51$.

6.1.2. Phase of Stationary Discharge

As the thickness of the discharge zone increases, the rate of the Joule heat release per unit volume decreases, and the radiation losses determined by temperature (6.1.3) and density (6.1.4) remain unchanged. Therefore, over the course of time, the discharge transits to the stationary phase, where the Joule heat release is offset by the radiation losses. It is reasonable to consider this phase of the discharge only for plasma with infinite density $n_\infty = \infty$ (or an insulator), because radiation cooling of the plasma not involved in the discharge leads to, sooner or later, $Q_\infty \to 0$ and, consequently, to $n_\infty = \infty$. This transition process itself has a nonstationary character and is not self-similar. It is easy to ascertain that at the stationary phase the thickness of the discharge zone is small by comparison with the radiation path, so the radiation can be regarded as volume radiation.

In strong magnetic fields, bremsstrahlung radiation, whose volume power is

$$J_B = \frac{32}{3}\sqrt{\frac{2T}{\pi m}}\frac{zN^2e^6}{mc^3\hbar}$$

plays the main role for hydrogen plasma. The dimensionless quantities for this phase of the discharge can be selected conveniently in accordance with the formulae (6.1.3–6.1.6), where the time t is replaced by the quantity

$$\tau = \frac{B_0^2}{8\pi J_B([T],[N])} \quad . \tag{6.1.12}$$

In this stationary case, the second equation of the system (6.1.7) turns into

$$\varepsilon = \text{const} \quad , \tag{6.1.13}$$

the last equation is written as

$$\frac{dq}{d\xi} = -n\sqrt{\Theta} - \frac{\varepsilon}{\sqrt{2\pi}}\frac{dh}{d\xi} \quad , \tag{6.1.14}$$

and the rest of the equations remain unchanged. The solution of the system (6.1.7) with the given changes is shown in Fig. 6.5. The electric field here is ε=1.16.

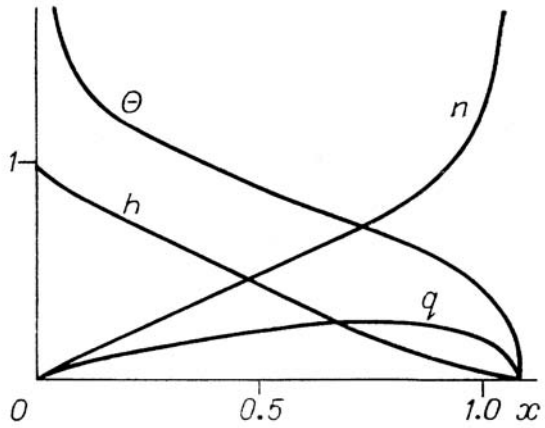

Fig. 6.5. Profiles of temperature Θ, density n, magnetic field h, and heat flux q in the stationary discharge with energy sink by means of bremsstrahlung radiation.

Recombination and line radiation play an essential role for plasma with $Z > 1$. For the temperatures and densities (6.1.3 and 6.1.4) in the megagauss magnetic fields, the volume radiation of such plasma can be approximately written as the dependence [6.13]:

$$J_R(T, N) = R\frac{e^{10}}{\hbar^3 c^3}\frac{Z^4}{z}\frac{N^2}{\sqrt{mT}} \tag{6.1.15}$$

(R is the dimensionless constant). So, when the quantity

$$\tau = \frac{B_0^2}{8\pi J_R([T],[N])} \tag{6.1.16}$$

is used instead of t in (6.1.7)—similarly to (6.1.12)—for the dimensionless quantities (6.1.3–6.1.6), all the equations (6.1.7) remain unchanged, with the exception of the second one, which turns into (6.1.13), and the last one, which has the form

$$\frac{dq}{d\xi} = -n/\sqrt{\Theta} - \frac{\varepsilon}{\sqrt{2\pi}}\frac{dh}{d\xi} \ . \tag{6.1.17}$$

The solution of the system (6.1.7) with those changes with the coefficients of (6.1.9) for $z = \infty$ is shown in Fig. 6.6. The electric field here is $\varepsilon = 5.58$. The discharge shown in Fig. 6.6 can be interpreted as an H-pressed discharge on the insulator surface. Note, that for large z, the temperature at the plasma-vacuum interface turns into 0, unlike $z = 1$. This behavior is governed by the expansion (6.1.11) and is a result of the more substantial effect (by comparison with that of $z = 1$) of thermoelectric heat fluxes on the heat balance near the boundary $\xi = 0$.

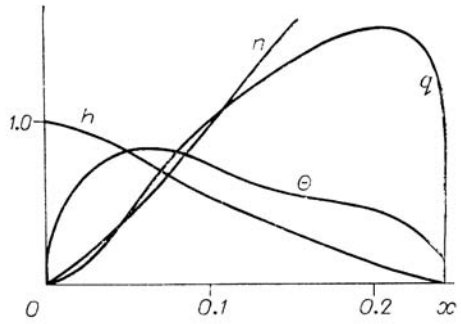

Fig. 6.6. Profiles of temperature Θ, density n, magnetic field h, and heat flow q in the stationary discharge with the energy sink by means of recombination radiation and line radiation.

Let us present the characteristic numerical values of discharges in hydrogen and plexiglass $H_8C_5O_2$ in magnetic fields of the megagauss range.

For hydrogen in such fields, the Coulomb logarithm is λ =7.5

$$[T] = 74 eV \cdot B_0^{0.4}(MG) \ ,$$

$$[N] = 3.3 \cdot 10^{20}\, cm^{-3} \cdot B_0^{1,6}(MG) \ .$$

In Fig. 6.3, the unit of measurement for distance is

$$[X] = 0.19 cm \sqrt{t(\mu s)} / B_0^{0.3}(MG) \ ,$$

and for the electric field, it is

$$[E] = 0.38 \frac{kV}{cm} \cdot B_0^{0.7}(MG) / \sqrt{t(\mu s)} \ .$$

In Fig. 6.5, the unit of measurement for distance is

$$[X] = 0.095 cm / B_0(M) \ ,$$

and for the electric field, it is

$$[E] = 0.78 \frac{kV}{cm} \cdot B_0^{1.4}(MG) \ .$$

If we assume that the start of the transition from the regime of Fig. 6.3 to the regime of Fig. 6.5 is determined by the coincidence of the electric fields E_∞ in Fig. 6.3 and E in Fig. 6.5, and at the finish of the transition, the field E_0 (Fig. 6.3) coincides with E, the characteristic times of the transition start, t_s, and finish, t_f, are the following:

$$t_s = 0.35 \mu s / B_0^{1,4}(MG) \ ,$$

$$t_f = 0.75 \mu s / B_0^{1.4}(MG) \ .$$

The setting time of the start of the Fig. 6.3 regime, when the material inertia can be disregarded and the condition (6.1.1) begins to be fulfilled is

$$t = 6 \cdot 10^{-3} \mu s / B_0(MG) \ .$$

6.1.3. Magnetic Field Diffusion Guided by Radiative Heat Conduction

For a dense plasma or an insulator, the radiation from the stationary discharge area gradually heats the internal layers, where noticeable electric conductivity appears, and the magnetic field starts diffusing inwards, heating the plasma, which is accompanied by heat transfer to the next layers. Thus, the next phase of the magnetic field diffusion is formed, which will be considered using the example of strong field diffusion into plexiglass.

Using the Saha equation with multiple ionization [6.15], radiation paths for multiple ionization [6.15] and electrical conductivity of the Lorentz electron gas (see Section 3.3.3) in the temperature range of 3–30 eV and density range of 10^{-3}–10^{-5} g/cm^3, we can obtain the power form of the temperature and density dependence of the equation of state, the radiation path l, and the magnetic diffusion coefficient κ:

$$p/\rho = 0.17T^{1.19}/\rho^{0.06} \ ,$$

$$l = 2\cdot 10^{-9}T^{2.14}/\rho^{1.86} \ ,$$

$$\kappa = 0.17/(T^{0.86}\rho^{0.14}) \ ,$$

the adiabatic index is $p/\varepsilon\rho + 1 = 4/3$ (the units are g, cm, μs, and temperature is in eV).

Let us choose the units of measurement for the temperature $[T]$ and density $[\rho]$ such that the coefficients of temperature conductivity and magnetic diffusion are of the same order

$$\sigma_{SB}[T]^4 l([T],[\rho])/(B_0^2/8\pi) = \kappa([T],[\rho])$$

($\sigma_{SB} = 1.03 \cdot 10^{-6}$ is the Stefan-Boltzmann constant), the heat pressure is of the order of the magnetic pressure

$$p([T],[\rho]) = B_0^2/8\pi \ .$$

Then

$$[T] = 17\,eV\cdot B_0^{0.62}(MG) \ ,$$

$$[\rho] = 5.7\cdot 10^{-3}\frac{g}{cm^3}\cdot B_0^{1.35}(MG) \ .$$

Using the self-similar variable

$$\xi = \frac{1000 \int \rho \, dx \, (g/cm^2)}{B_0^{0.99}(MG)\sqrt{t(\mu s)}}$$

and introducing the dimensionless functions

$$T = [T]\Theta(\xi) \ ,$$

$$\rho = [\rho] n(\xi) \ ,$$

$$B = B_0 \, h(\xi) \ ,$$

$$E = 1.8 \frac{kV}{cm} \cdot \frac{B_0^{0.64}(MG)}{\sqrt{t(\mu s)}} \varepsilon(\xi) \ ,$$

$$X = 0.88 \, cm \cdot \frac{\sqrt{t(\mu s)}}{B_0^{0.36}(MG)} x(\xi)$$

$$Q = 3.5 \cdot 10^9 \frac{W}{cm^2} \cdot \frac{B_0^{1.64}(MG)}{\sqrt{t(\mu s)}} q(\xi) \ ,$$

the system of the equations (6.1.1 and 6.1.2) can be presented as

$$\Theta^{1.19} / n^{0.94} + h^2 = 1 \ ,$$

$$\frac{d\varepsilon}{d\xi} = \frac{\sqrt{2\pi}\xi}{n} \left(\frac{dh}{d\xi} - \frac{h}{n} \frac{dn}{d\xi} \right) ,$$

$$\frac{dh}{d\xi} = -\frac{1}{2\sqrt{2\pi}} \frac{\Theta^{0.86}}{n^{0.86}} \varepsilon \ ,$$

$$q = -\frac{16}{3} \frac{\Theta^{5.14}}{n^{0.86}} \frac{d\Theta}{d\xi} \ , \qquad (6.1.18)$$

$$\frac{dq}{d\xi} = \frac{\varepsilon^2}{4\pi} \frac{\Theta^{0.86}}{n^{0.86}} + 0.59\xi \left(3 \frac{\Theta^{0.19}}{n^{0.06}} \frac{d\Theta}{d\xi} - \frac{\Theta^{1.19}}{n^{1.06}} \frac{dn}{d\xi} \right) ,$$

$$\frac{dx}{d\xi} = 1/n \ .$$

From (6.1.18) and the boundary conditions $h(0) = 1$, $\varepsilon(0) = \text{const}$, and $q(0) = \text{const}$, we have the expansion for $\Theta(\xi)$ and $n(\xi)$:

$$\Theta(\xi)\big|_{\xi\to 0} \sim \xi^{0.23} \ ,$$

$$n(\xi)\big|_{\xi\to 0} \sim \xi^{0.51} \ .$$

The solution of the system (6.1.18) with the boundary condition $n(\infty) = \infty$ is shown in Fig. 6.7. The characteristic times of the start, t_s, and finish, t_f, of the transition from the Fig. 6.6. regime to the Fig. 6.7. regime can be evaluated if we equate the Fig. 6.6 regime electric field to the Fig. 6.7 electric fields $E(\infty)$ and $E(0)$, respectively:

$$t_s = 0.029\,\mu s/B_0^{1.12}(MG) \ ,$$

$$t_f = 0.038\,\mu s/B_0^{1.12}(MG) \ .$$

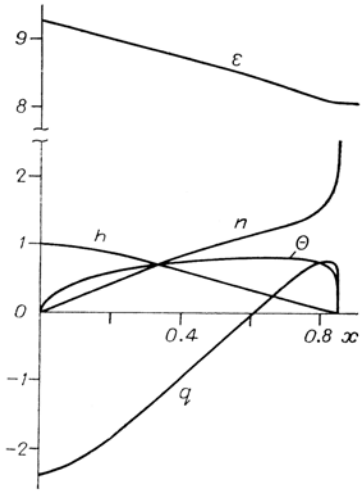

Fig. 6.7. Profiles of the electric field ε, temperature Θ, density n, magnetic field h, and heat flux q for the magnetic-field diffusion, guided by radiative heat conduction, into plasma with infinite density $n_\infty = \infty$.

For the magnetic-field diffusion into the insulator, the finite discharge resistance leads to penetration of the magnetic flux into the insulator and, if the circuit behind the insulator is closed, the magnetic field will grow there (and the magnetic fields at the inlet to the insulator and inside it will start getting equalized).

Note that the considerations developed above for ultrahigh magnetic-field penetration into material require more accurate quantitative determination, both with respect to theoretical models and simulations, and with respect to the comparison of theory and experiment. At present, there are almost no experimental studies devoted specifically to the *H*-pressed discharge, although it occurs in many experiments at different facilities and its effects prove to be important. To give an example that demonstrates the influence of the *H*-pressed discharge on experimental results, one can refer to the experiments in which a strong magnetic field was generated in a dielectric tube with magnetic flux compression by a plasma liner [6.16]. In these experiments, the *H*-pressed discharge on the outer surface of the tube impeded the magnetic-field generation inside the tube during magnetic flux compression by the liner. Thus, it played a negative role. As a result, in some shots, instead of a 1 MG field that could be expected if the magnetic flux could freely flow into the tube, the field penetrating into the tube with the first magnetic flux compression by the liner was as small as about 0.2 MG. However, after the flux compression, the *H*-pressed discharge, this time produced on the inner tube surface, facilitated magnetic field containment inside the tube and consequently played a positive role. Another example showing the significance of the *H*-pressed discharge is the difference between the computed and measured magnetic field derivatives in the MAGO plasma chamber experiments (Section 2). While the experimental and calculated results agreed in general, the experimental waveforms were observed to be smoother and to have significantly smaller amplitudes of magnetic field derivatives. This can be attributed to the effects of the *H*-pressed discharges on the surface of the insulators, where the probes were installed.

6.2. Diffusion of Megagauss Fields into a Metal

Material conductivity changes due to the heating of the walls by the current flowing over the skin layer. As a result, the metal conductivity decreases, then with higher fields, the material vaporizes, and, if the substance transforms to plasma, its conductivity can increase again.

The opinion is expressed at times in the literature to the effect that when a conductor explodes in strong fields, a cold nonconducting gas is generated, which expands from the metal boundary across the field. Physical observations borne out by corresponding calculations, however, show that, in reality, this does not happen in the fields on the order of several megagauss. Indeed, the radiation emitted from a hot metal surface with a temperature in the electronvolt range contains hard radiation quanta that ionize the vapor that is formed and thus produce seed ionization. For low densities, the degree of this ionization near the vapor boundary should be independent of the density. Thus, at the vapor boundary, there is constant conductivity within an arbitrarily small density. The presence of an electric field that forms as a result of diffusion into the metal and that is increased as a result of the vapor movement across the magnetic field leads to the Joule heat release in a unit of

volume that is independent of the density and, hence, infinitely large per unit mass for an arbitrarily small density at the vapor–vacuum interface. This leads to an inevitable gas breakdown, the creation of a plasma piston that prevents gas expansion, and the formation of a conducting plasma layer instead of a nonconducting expanding gas, just as the calculations show.

Thus, the material transforms into a plasma whose conductivity grows with heating. As a result, the penetration of super-strong magnetic fields into materials turns out to be a rather complicated phenomenon accompanied by material vaporization and plasma formation. Although this penetration is diffusive, it is interesting to ask, What is the value of the effective diffusion coefficient, and what state of matter determines it?

In seeking to answer these questions, some authors consider only the plasma forming at the boundary with the metal—even in fields on the order of one megagauss—similarly to the *H*-pressed discharge on the insulator surface that was discussed in Section 6.1.3, and without taking into account the presence of metal under the plasma layer. The reasoning of Section 6.1.3, however, cannot be applied to the plasma discharge on the metal surface, because the plasma discharge, shunted by the metal conductivity (even reduced as a result of Joule heating) sharply reduces the electric fields in the plasma, and, as a result, only a small fraction of the current flows over it even for the fields on the order of dozens of megagauss (with ideal metal conductivity, the discharge over the plasma is generally impossible because energy can be supplied to this discharge from the magnetic field only, and the magnetic field energy cannot decrease, since the magnetic flux has no place to expand).

In many papers that consider the motion of liners driven by a strong magnetic field, the relevant MHD problems are considered without taking into account the heat conduction in plasma layers. In such consideration, numerical calculations (for grids not very fine) can be quantitatively correct for liner parameters on the whole; but one should bear in mind that this description has internal contradictions and will not yield correct results for rather fine grids. Let us show this with the example of a Lagrangian grid in a 1D calculation.

Since, in a Lagrangian calculation that disregards heat conduction, the characteristic mass scale of the generated plasma ρx (ρ is the plasma density and x is the layer thickness) is determined by the grid resolution

$$\rho x \sim \Delta m , \tag{6.2.1}$$

we examine the plasma behavior on that scale if the characteristic magnetic B and electric E fields are determined by the diffusion into the metal adjacent to the plasma. The characteristic plasma pressure is determined by its Joule heating:

$$p \sim \sigma E^2 t ,$$

where σ is the plasma conductivity and t is the characteristic time. For a thin plasma layer, the equilibrium condition should be satisfied with good accuracy:

$$p \sim \frac{\sigma E}{c} Bx \,. \tag{6.2.3}$$

From expressions (6.2.1) and (6.2.2), it follows that the layer thickness increases with time as

$$x \sim \frac{cEt}{B} \,. \tag{6.2.4}$$

Inserting the dependences for pressure $p \sim z\rho T$ (z is the degree of ionization of a multiply ionized plasma and T is the characteristic temperature) and for conductivity $\sigma \sim T^{3/2}/z$ into (6.2.2) and taking into account (6.2.1) and (6.2.4), we obtain

$$\frac{\sqrt{T}}{z^2} \sim \frac{B\Delta m}{E^3 t^2} \,. \tag{6.2.5}$$

For a multiply ionized plasma with $z \sim Z$ (Z is the nucleus charge), and $z^{4/3} \sim T$, and using the expression (6.2.5), we find that the plasma temperature $T \sim \dfrac{E^3 t^2}{B\Delta m}$ is inversely proportional to the grid resolution and grows with time until the plasma pressure $p \sim \dfrac{E^{17/4} t^{5/2}}{B(\Delta m)^{3/4}}$ becomes equal to the magnetic pressure and the plasma shields the metal. But if the plasma is heated to the level of $z \sim Z$ and z becomes independent on the temperature, the temperature rise becomes so rapid that it should be described using the differential form of (6.2.2), i.e., $\rho \dfrac{dT}{dt} \sim T^{3/2} E^2$, and, using the equilibrium condition (6.2.3), for the temperature rise, we obtain

$$\frac{dT}{dt} \sim \frac{T^{5/4} E^{3/2}}{\sqrt{B\Delta m}} \,. \tag{6.2.6}$$

From (6.2.6) it follows that if the degree of ionization reaches the level $z \sim Z$, then, the temperature goes to infinity over the finite period of time $\tau \sim \sqrt{B\Delta m} / E^{3/2} T_0^{1/4}$ (T_0 is the temperature corresponding to the degree of ionizationz $z \sim Z$), and the finer the grid, the smaller the time. In fact, of course, the temperature grows until the plasma thermal pressure becomes equal to the magnetic pressure and the metal is shielded.

Thus, the use of rather fine grids in calculations makes it possible to obtain plasma shielding of the skin layer in the metal. In many cases, for real grids, this shielding may not manage to develop within times of interest. Since for

fields $B < 10$ MG, with correct accounting taken of the plasma area, its role is insignificant in the current shunted from the metal and in the mass involved in the skin layer, the error in its description (even by several magnitudes) may remain, on the whole, insignificant for the description of the liner. In any case, however, one should be able to evaluate correctly the characteristics of the plasma layers and understand that improperly accounting for them can lead to incorrect results.

6.2.1. Formulation of the One-Dimensional Problem

Let us consider magnetic-field diffusion into a metal on the basis of an example of diffusion from a vacuum into a semi-infinite copper wall. We will perform the calculations in a 1D MHD formulation on a Lagrangian grid. We will assume that all the quantities depend on the coordinate x and time t, and the magnetic field B and the electric field E are perpendicular to each other and to the x axis. At the initial time, cold copper occupies the region $x > 0$, the magnetic field in this region is equal to zero, and the magnetic field on the material boundary is specified as a function of time $B_0(t)$. The calculations took into account hydrodynamic motion, magnetic diffusion, electronic heat conduction, and radiative heat transfer in the "forward-reverse" approximation.

The equation of state, conductivity, electron thermal-conduction coefficient, and the radiation paths for copper used in the simulations had the following form [6.3]:

The equation of state of copper (in cm, g, μs, temperature in eV) was determined by the formulas:

$$\varepsilon(\rho,T)=\varepsilon_1(\rho)+\varepsilon_2(\rho,T)+\varepsilon_S(\rho,T)\ ,$$

$$p(\rho,T)=p_1(\rho)+p_2(\rho,T)+p_S(\rho,T)\ ,$$

where $\varepsilon_1 = 2.32/\rho_0)(\delta^{2.1}/2.1 - \delta^{1.5}/1.5 + 4/21)$, $p_1 = 2.32(\delta^{3.1} - \delta^{2.5})$ ($\rho_0 = 8.9\text{g/cm}^3$, $\delta = \rho/\rho_0$); $\varepsilon_2 = 0.0121T^{3/4}\delta^{5/6}$, $p_2 = (10/3)\varepsilon_2\rho$; $\varepsilon_S = (0.965/A) \cdot [1.5(1 + z)T + Q(z)]$, $p_S = (0.965/A)\rho(1 + z)T$; A is atomic weight equal to 63.5; z was determined by approximate solution of the Saha equation for multiple ionization [6.15] by means of the transcendent equation $I(z + 0.5 = T \ln(317\, AT^{3/2}(z\rho))$; $I/(z)$ represents the ionization potentials; $Q(z)$ is input for ionization $Q(z) = \sum_1^z I(z)$. The copper conductivity σ was calculated in the plasma range ($\rho < 0.28$ g/cm^3) using the formulas from Silin [6.17].

For

$$z > 1 \qquad \sigma = 0.871 \cdot 10^8 \frac{3.25 + 1.41/z}{1 + 1.41/z} \frac{T^{3/2}}{z\lambda} ,$$

$$\lambda = \ln\left(1 + \frac{0.052}{z}\sqrt{\frac{AT^3}{\rho z(1+z)}}\right); \tag{6.2.7}$$

for

$$z < 1 \qquad \sigma = \frac{1}{0.594 \cdot 10^{-8} \frac{\lambda}{T^{3/2}} + 1.3 \cdot 10^{-9} \frac{1-z}{z}} ,$$

$$\lambda = \ln\left(1 + 0.037\sqrt{\frac{AT^3}{\rho z}}\right);$$

in the condensed phase range ($\rho > 2.8$ g/cm^3)

$$\sigma = \frac{4.83 \cdot 10^8}{\varepsilon - 0.0004}\delta , \tag{6.2.8}$$

and in the intermediate range (0.28 g/cm^3 $< \rho <$ 2.8 g/cm^3) σ was determined based on density interpolation between (6.2.7) and (6.2.8). The electron thermal conductivity in copper was considered nonmagnetized and was found from the Wiedemann-Franz law

$$\chi = \frac{\pi^2 kT}{3e^2}\sigma$$

(k is Boltzmann constant). For radiation energy transfer, we used the "forward-reverse" approximation [6.15] with the path $l = \frac{2}{3} l_R$ ($l_R$is Rosseland path) to provide the correct limiting transition to the heat conductivity equation. Here, the path was temperature- and density-dependent (gray matter) and equaled [6.15]

for $z > 1$

$$l_R = 9.5 \cdot 10^{-12} \frac{T^{7/2}}{\rho^2} \frac{A^2}{z^3} ;$$

for $z < 1$

$$l_R = 9.5 \cdot 10^{-12} \frac{T^{7/2}}{\rho^2} \frac{A^2}{z^2} .$$

As regards the boundary condition that determines the radiation propagation, two variants are possible: in one case, it is assumed that all of the radiation leaves the surface (an open system), and in the other case, the radiation flux on the boundary is equal to zero (a closed system). The second variant is possible if the magnetic field diffuses from a cavity whose walls are under identical conditions. Most of the calculations were performed for the open-system formulation, and only some (for purposes of comparison) were performed for the closed-system formulation.

Most of problems considered the case of a constant magnetic field on the plasma boundary, $B_0 = const$. That case offers an advantage in that the problem thus becomes close to self-similar, and, therefore the profiles of all quantities are easily recalculated from one time for other times. Indeed, for real times that are not too short (in excess of a few nanoseconds), the hydrodynamic motion is considerably faster than the diffusion, and it can be assumed that the total pressure (thermal plus magnetic) can become equalized over the skin-layer area. The magnetic diffusion and the thermal conductivity in this case should provide the dependence of all quantities on the self-similar variable $x/\sqrt{t}$ only. In principle, a deviation from this self-similar dependence could be caused by the radiation transport in the phase when the radiation path becomes comparable with the plasma layer thickness. In reality, however, we found the calculations with $B_0 = const$. to be in good agreement with the self- similar dependence (see the next section).

The calculations disregarded some phenomena that, in principle, could affect the pattern of the magnetic-field diffusion. First, the equation of state (EOS) that we employed had no two-phase (liquid-vapor) states. Decay into phases occurred automatically in the calculations, but only if the material fell into the thermodynamically unstable region $\partial p/d\rho \ (\partial p/\partial\rho)_T < 0$, and, therefore, the states of an overheated liquid and overcooled vapor were allowed. As a result, the calculations did not take into account some metal vaporization into a vacuum for relatively low fields $B_0 < 1.5$ MG, in which plasma may not have formed. However, the influence of this effect is not very significant. Calculations with two-phase equations of state show that for fields $B_0 \sim 1$ MG, not more than a few percent of the skin layer evaporates.

Second, the radiation transport was considered in a gray matter approximation, which could not provide a detailed account of the gas-breakdown and plasma-formation phenomena that were discussed in the introduction. These delicate phenomena can be of special interest in studies of the beginning of plasma formation for relatively low fields $B_0 < 1.5$ MG.

However, as was mentioned above, these effects concern a small mass fraction and generally should not be too significant in terms of the description of field diffusion into a metal.

Third, we did not take into account the dependence of electrical conductivity and thermal conductivity on the degree of plasma magnetization, or thermoelectric phenomena (Nernst effect). Generally speaking, these effects could influence the behavior of the plasma quantities near the boundary with vacuum, in the zone where the radiation transport is not yet very important since in this area the degree of electron magnetization $\omega_e\tau_e$ can be on the order of unity. This zone itself, however, occupies a fairly small percentage of the entire plasma layer in most of whose mass the role of radiation is significant, and therefore inaccuracy in the description of this zone has virtually no effect on the description of the skin layer in the metal as a whole.

6.2.2. Open-system Calculations for a Constant Magnetic Field on the Boundary

Profiles obtained in calculations for B_0 = 1, 2, 5 and 10 MG at the moment t = 1 μs of the magnetic field $B(x)$, the density $\rho(x)$, and temperature $T(x)$ of a material are presented in Fig. 6.8, which shows how the skin-layer structure changes as the magnetic field increases. For B_0 = 1 MG, the copper present in the skin layer is in the condensed phase only. For B_0 = 2 MG, the skin-layer structure next to the condensed phase has also a two-phase liquid-vapor region (for purposes of discernibility, the density fluctuations in the two-phase region on the plot given in Fig. 6.8b are smoothed) and a plasma area, which can also be divided into a zone of radiative thermal conduction and a zone of electron thermal conduction at the boundary with the vacuum, where the radiation is almost negligible. Our calculations in this problem formulation (open system, B_0 = *const*.) showed that the transition from the single-phase structure of the skin layer (Fig. 6.8a) to a composite multiphase structure (Fig. 6.8b) takes place roughly when B_0 = 1. 6 MG. Then, as the magnetic field B_0 increases, the two-phase region in the skin layer disappears, and for larger fields, the skin layer (see Fig. 6.8c and d) consists only of a condensed phase and a plasma area, in which it is possible distinguish a zone of radiative thermal conduction (with a temperature decreasing toward the vacuum, which is explained by the plasma cooling that results when the radiation exits through the surface) and a zone of electron thermal conduction with a temperature increasing toward the vacuum. It should be noted that, as Fig. 6.8d shows, when B_0 = 10 MG, a rather large contribution to the heating of the material (commensurate with Joule heating) in the dense region is made by shock-wave heating, which is significant for high fields in this formulation, where the magnetic field is applied to the surface instantaneously.

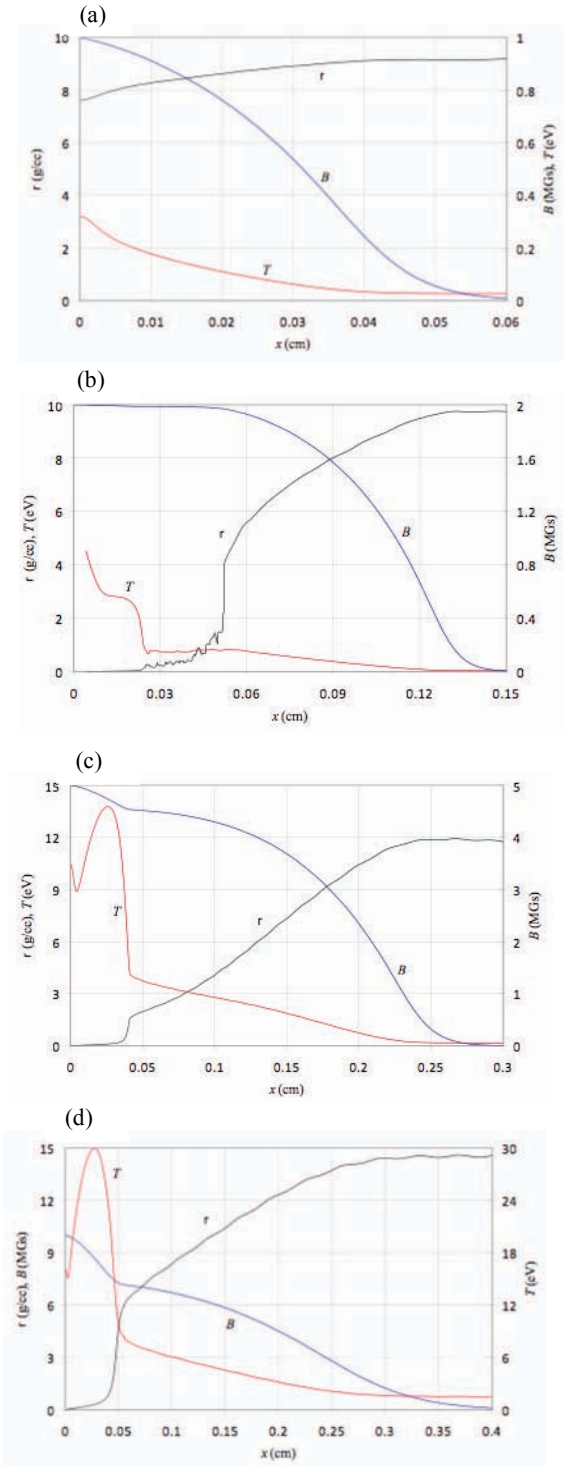

Fig. 6.8. Profiles of the magnetic field $B(x)$ and density $\rho(x)$ and temperature $T(x)$ of a material, calculated for an open system for a constant magnetic field on the boundary B_0 = 1 (a), 2 (b), 5 (c), and 10 MG (d) at t = 1 μs.

For all fields $B_0 \leq 10$ MG, the plasma area is small and occupies only a small fraction of the skin layer. This is also confirmed by Table 6.1, where the thickness of the skin layer and its mass at $t = 1\ \mu s$ are shown for the considered fields. A comparison of these values shows that, for these fields, the mean material density in the skin layer is rather high and corresponds to the density of the condensed phase (although it is hardly possible to speak of a condensed phase here in a material heated strongly by a shock-wave when $B_0 = 10$ MG). The skin-layer thickness, itself as a function of B_0, increases rapidly in the range of 1–2 MG as a result of the nonlinear diffusion and the appearance of the two-phase and plasma areas. Then for large fields, the skin-layer thickness increases more slowly, and in the range of 5–10 MG, the increase ceases since the density (and the conductivity along with it) in the material of the skin layer increases as the field increases, including in the plasma area. It is interesting, that in the entire range of 1–10 MG, the mass of the skin layer increases monotonically as the field increases, approximately following the law $m \sim B_0^{0.72}$. According to the data of Table 6.1, the fraction of the current shunted in the plasma area is small for fields $B_0 \leq 5$ MG, and only for $B_0 =$ 10 MG does it have an appreciable value.

Table 6.1. Properties of the Skin Layer as a Function of Magnetic Field B_0.

Magnetic field B_0, MG	1	2	5	10
Skin-layer thickness $x(t)$ (cm) (determined as $\frac{1}{B_0}\int B\,dx$, where the integral is taken over the material area) at $t = 1\ \mu$s	0.0297	0.106	0.175	0.168
$x(1\mu s) / x(0.1\mu s)\sqrt{10}$	1.00	1.03	1.03	1.03
Skin-layer mass $m(t)$ (g/cm^2) (determined as $\frac{1}{B_0}\int B\rho\,dx$) at $t = 1\ \mu$s	0.252	0.416	0.797	1.31
$m(1\mu s) / m(0.1\mu s)\sqrt{10}$	1.00	1.00	1.01	1.04
Fraction of current shunted in the plasma area, %	0	0.7	9	25

Let us consider the question of the dependence of the obtained profiles on time, i.e., how the real time dependence of the quantities in the skin is close to the self-similar one, in which all quantities should depend on the ratio $x/\sqrt{t}$ only. The values given in Table 1—$x(t_2)\sqrt{t_1} / x(t_1)\sqrt{t_2}$ (where $x(t)$ is the skin-layer thickness, and t_1 and t_2 are different times) and $m(t_2)\sqrt{t_1} / m(t_1)\sqrt{t_2}$ (where $m(t)$ is the skin-layer mass), which for strict

self-similarity should be equal to unity—can serve as a measure of deviation from this dependence. The data of Table 1 show that, indeed, for all the considered fields, the skin-layer dynamics in this formulation are close to the self-similar dynamics. Small deviations from self-similarity are explained by the larger role of radiation with increasing time, resulting in a reduction of the temperature of the plasma area and, accordingly, an increase of its relative thickness.

6.2.3. Effect of the Radiation Boundary Conditions on the Skin-Layer Structure

Let us consider how the skin-layer structure changes if the radiation flux on the boundary is equal to zero (a closed system). This situation is exemplified by magnetic flux compression in a cavity. Calculated profiles of the magnetic field $B(x)$ and density $\rho(x)$ and temperature $T(x)$ of material that correspond to this case for $t = 1$ μs and $B_0 = 2$ MG are shown in Fig. 6.9.

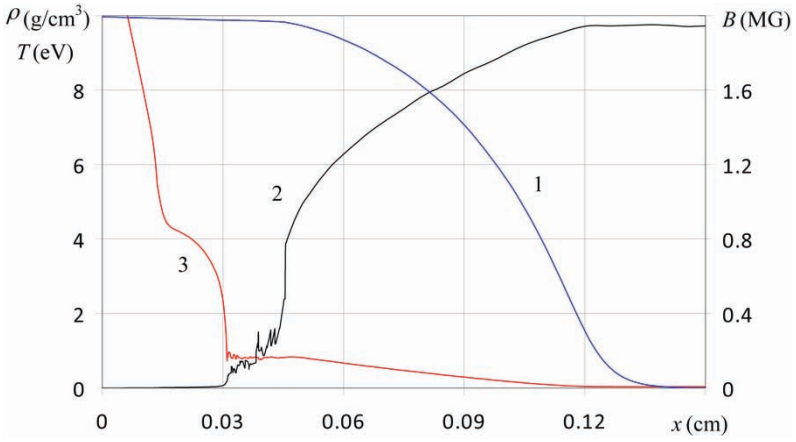

Fig. 6.9. Profiles of the magnetic field B(x) (1) and density ρ(x) (2) and temperature T(x) (3) of material that are calculated for a closed system for a constant magnetic field on the boundary $B_0 = 2$ MG at $t = 1$ μs.

A comparison of Fig. 6.9 and Fig. 6.8b shows that, as one might expect, the temperature in the plasma area of the closed system is a little higher (in the zone of radiative thermal conduction in Fig. 6.8b, it is about 3 eV; whereas in Fig. 6.9, it is about 4 eV). There is also a decrease of the thickness of the two-phase zone in the closed system. As a result, the skin layer in the closed system is thinner than in the open system. However, the skin-layer masses in both cases are approximately identical (in the closed system, it is 0.6 % lower).

6.2.4. Effect of Smooth Growth of the Magnetic Field on the Skin-Layer Structure

The calculations described here assumed that the magnetic field is instantaneously applied to the metal boundary and then remains constant. In the majority of real problems, the magnetic field at the boundary grows gradually, and this, of course, changes the skin-layer structure. In the case of a smoothly growing field for moderately strong fields, the magnetic diffusion into metal can be calculated without accounting for thermal conduction, which cannot be done when the field is switched on instantaneously. Indeed, when the field is switched on instantaneously for the self-similar law of electric field variation at the boundary $E \sim 1/\sqrt{t}$, the integral over time corresponding to the Joule heating of the material at the boundary diverges for small times. Therefore, for the description of the material heating near the boundary, the thermal conduction should be taken into account, which distributes the heat released near the boundary over some area. As a result, if, in problems of diffusion of a moderately strong field (up to 1 MG) into a metal, the volumetric heating for a smoothly growing field is equal to approximately $B^2 / 8\pi$ [6.18], for instantaneous field switching, it is considerably higher near the boundary (for the case shown in Fig. 6.8a, by a factor of approximately 2.6).

The effect of the smooth growth of the magnetic field at the boundary on the skin-layer structure in megagauss fields is illustrated by Fig. 6.10, where the profiles of the magnetic field $B(x)$, material density $\rho(x)$ and temperature $T(x)$ are shown at $t = 1$ μs calculated for a magnetic field growing linearly with time for $dB_0/dt = 5$ MG μs, so that at t = 1 μs the magnetic field on the boundary is equal 5 MG. A comparison of Fig. 6.10 and Fig. 6.8.c shows that in the case of megagauss fields, the skin-layer heating is also smaller for a smoothly growing magnetic field than for instantaneous switching. Accordingly, in the case of a smoothly growing magnetic field, a plasma layer is formed for higher magnetic fields than in the case of instantaneous switching. In the present calculation, plasma formation occurred when the magnetic field at the boundary reached a value of 3 MG, which is almost twice as larger as that for instantaneous switching.

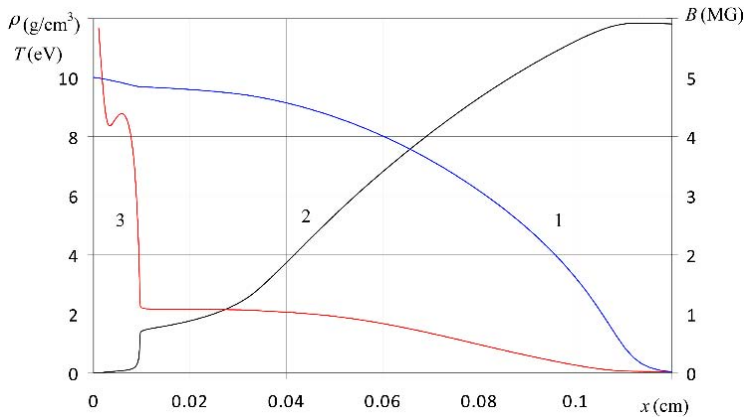

Fig. 6.10. Profiles of the magnetic field B(x) (1), density ρ(x) (2) and temperature T(x) (3) of material that are calculated for an open system with a linearly growing magnetic field at the boundary for dB/dt =5 MG μs at t = 1 μs.

CONCLUSION

The explosion of a conductor for fields in excess of $B \approx 1.5–3$ MG leads to the formation of a conducting plasma layer at the boundary with the vacuum. For fields $B < 10$ MG, the role of this layer in the current shunted from the metal and the plasma mass involved in the skin layer is small, but is of fundamental importance since incorrectly accounting of it (for example, in numerical calculations without thermal conduction on sufficiently fine grids) can lead to complete shunting of the current into the plasma layer. For a correct description of the skinning of megagauss fields in a metal, one needs to take into account electron thermal conduction and radiative heat transport.

For magnetic fields at the metal boundary in excess of $B_0 \sim 1.5–3$ MG, the skin layer consists of a condensed phase area with a density on the order of the initial density, a two-phase liquid-vapor area, and a plasma area, which can also be divided into an area of radiative thermal conduction and an area of electron thermal conduction at the very boundary with the vacuum. A two-phase liquid-vapor area is formed for fields of $B_0 \approx 1.5–4$ MG, depending on the dynamics of the magnetic field at the boundary and the radiation boundary conditions.

Numerical calculations of megagauss-field diffusion with a constant magnetic field at the boundary $B_0 = const$. have shown that for all fields in the range $B < 10$ MG for times greater than a few nanoseconds, the dependence of all quantities in the skin layer is described with high accuracy by a self-similar dependence, where all the quantities depend on the variable $x / \sqrt{t}$.

A comparison of closed and open systems shows that the temperature in the plasma area in a closed system is a little higher (for example, for B_0 = 2 MG, in the zone of radiative thermal conduction in the open system, it was about 3 eV, whereas in the closed system it was about 4 eV).

The heating of the skin layer is considerably smaller for a smoothly growing magnetic field than for instantaneous switching. Accordingly, in this case the formation of a plasma layer occurs with higher magnetic fields than it does in the case of instantaneous switching.

If one compares the characteristic spatial scales and temperatures for the cases of the magnetic-field diffusion into metal and an *H*-pressed discharge, one finds that the thickness of the skin layer for the magnetic field diffusion into a metal is much smaller than that of the *H*-pressed discharge area. This can be explained by the substantial effect exerted by the conductive material underlying the plasma layer, which, although it has lost its initial conductivity, still remains rather conductive. This material still has higher conductivity than the insulating plasma in the *H*-pressed discharge and, in contrast to the insulating plasma, does not allow the magnetic field to diffuse inwards the material. Shunting of the current flowing through the plasma by the current flowing through this material leads to much smaller plasma Joule heating than in the case of the *H*-pressed discharge, and hence to much lower temperatures. Thus, if, for B_0 = 5 MG in the *H*-pressed discharge on the insulator surface, the characteristic temperature of the plasma layer is 30 eV, it is on the order of 10 eV for the diffusion into metal.

At present, the processes of plasma formation on the surface of thick metal, in response to a pulsed multi-megagauss magnetic field, are investigated in well-diagnosed experiments [6.19, 6.20]. The theoretical simulation results of these experiments [6.21] based on the presented concepts of the diffusion of megagauss fields into a metal agree with experimental data [6.19, 6.20].

6.3. Discharge Produced During Magnetic Flux Transfer from Plasma to the Insulator

The vacuum in the problem of an *H*-pressed discharge can be treated as a special case of zero-density plasma. For a number of problems, it is important to take that discharge into account in the case of a plasma with finite density. An even more general case is the case of an arbitrary-β plasma that is in contact with an insulator. Consideration of this case is important for many applications, such as wall confinement of magnetized plasma, liner compression of magnetized plasma, etc., when it is necessary to take into account magnetic-flux and plasma losses due to the field diffusion and heat conduction to the wall. The role of a discharge occurring in plasma when the

magnetic flux flows out of it should be particularly substantial for hydrogen plasma, whose conductivity can be high by comparison with the conductivity of the plasma in the *H*-pressed discharge on the wall surface. In this case, if the hydrogen plasma density proves to be insufficiently small, discharge resistance will be determined by the discharge in the hydrogen plasma.

Let us consider the development of this discharge in the following setup: there is hydrogen plasma with a magnetic field confined by a rigid non-conducting insulator wall. This case was addressed qualitatively by Vekshtein [6.7, 6.9], and the resulting effective diffusion factor for a plasma with $\beta << 1$ ($\beta = 16\pi N_0 T_0 / B_0^2$ is the ratio of plasma thermal pressure to the magnetic pressure; N_0, T_0, B_0 is the density, temperature and magnetic field in plasma far from the discharge region) proved to be on the order of $D \sim cB_0 /4\pi eN_0$; for $\beta >> 1$, it was on the order of $D \sim cT_0/10eB_0$.

In this section, following Garanin [6.10], we will provide a quantitative analysis of the near-wall current layer structure and formulate the boundary condition with which the influence of this discharge on the plasma motion in the bulk volume can be described.

Let all quantities depend on the X coordinate and the time t; let the magnetic field B and the electric field E be perpendicular to each other and the X axis; and let the characteristic times be large by comparison with the gas-dynamic times, such that the total pressure in the system manages to equalize:

$$2NT + B^2 / 8\pi = p_0 \equiv 2N_0 T_0 + B_0^2 / 8\pi \ . \qquad (6.3.1)$$

Plasma density in the bulk of the volume is assumed to be small by comparison with the density in the near-wall discharge region. In this case, as shown in Vekshtein [6.7], the problem is quasi-stationary, i.e., in the equations of the magnetic and electric fields and of the thermal balance of the plasma in the discharge region, one can disregard time derivatives and consider the electric field and the energy flux to be constant. These equations will then take the form

$$E = -\frac{c}{4\pi\sigma}\frac{\partial B}{\partial X} - \frac{b_\Lambda}{e}\frac{\partial T}{\partial X} \ ,$$
$$Q = -\chi\frac{\partial T}{\partial X} - \frac{cT}{4\pi e} b_\Lambda \frac{\partial B}{\partial X} + \frac{c}{4\pi} EB \ . \qquad (6.3.2)$$

The mass of plasma accumulated in the near-wall layer is

$$a = \int_0^{X_0} N\, dX \tag{6.3.3}$$

(X_0 is the boundary of the discharge region). The wall is assumed to be a plane $X = 0$, and plasma occupies the region of $X > 0$. Then, the boundary conditions for equations (6.3.1) and (6.3.2) are

$$T(0) = 0 \ ,$$

$$B(0) = B_1 \ , \tag{6.3.4}$$

$$N(X_0) = 0$$

(B_1 is the magnetic field in the insulator). The energy flux flowing into the discharge region from the plasma is $Q = \frac{c}{4\pi} EB_0 + 5N_0T_0v$ (v is the velocity of the inflowing plasma). Because of the freezing-in of the magnetic field into the plasma far from the insulator,

$$v = cE / B_0 \tag{6.3.5}$$

and, consequently,

$$Q = \frac{c}{4\pi} EB_0 \left(1 + \frac{5}{4}\beta\right). \tag{6.3.6}$$

At the plasma/insulator boundary, the plasma stays non-magnetized by virtue of (6.3.4). In this region, the factors χ, b_Λ increase with distance from the wall and temperature; characteristic dimensions X corresponding to temperature T grow in accordance with (6.3.2), and discharge plasma accumulates. With plasma magnetization, the factors χ, b_Λ decrease; consequently, the characteristic dimensions X and, simultaneously, density decrease. Therefore, the major contribution to the plasma mass accumulating in the discharge will be that of the region in which magnetization of electrons is $\omega_e\tau_e \sim 1$. It is natural to choose p_0 as a unit of measurement for pressure, and to choose [T] and [N] as units of

measurement for temperature and density such that $p = p_0$ and $w_e\tau_e \sim 1$ for $T = [T]$, $N = [N]$ (see Section 6.1). Based on these conditions, we get

$$[T] = \left(\sqrt{p_0}\, c\lambda e^3 \sqrt{m}\right)^{2/5} ,$$

$$[N] = p_0^{4/5} / \left(c\lambda e^3 \sqrt{m}\right)^{2/5} . \qquad (6.3.7)$$

For choosing a measurement unit for the coordinate X, it is convenient to use equations (6.3.2) and substitute $[T]$ and $[N]$ from (6.3.7) as temperature and density. Then, introducing the dimensionless coordinate $x = -\dfrac{E}{e^{0,2} m^{0,2} c^{0,4} \lambda^{0,4} p_0^{0,2}} X$ (the electric field E is negative) and the dimensionless

$$\theta(x) = T / [T] ,$$

$$n(x) = N / [N] ,$$

$$h(x) = B / \sqrt{8\pi p_0} , \qquad (6.3.8)$$

$$\xi = -eEa / p_0 ,$$

we can rewrite equations (6.3.1–6.3.3) as follows:

$$2n\theta + h^2 = 1 ,$$

$$\frac{4}{3}\frac{\alpha}{\theta^{3/2}} h' + b\theta' = 1 , \qquad (6.3.9)$$

$$b\theta h' + \frac{3}{4}\left(\gamma + \frac{\gamma_i}{\sqrt{912A}}\right)\theta^{5/2}\theta' = \frac{1 + 1.25\beta}{\sqrt{1+\beta}} - h ,$$

$$\xi = \int_0^{x_0} n\, dx ,$$

where α, b, γ are defined in Section (6.1), and

$$\gamma_i = \frac{2y_i^2 + 2{,}64}{y_i^4 + 2{,}7y_i^2 + 0{,}677} \ ,$$

($y_i = y/\sqrt{912A}$, A is the atomic weight). Here, as distinct from Section 6.1, we take into account the term γ_i, representing ion heat conductivity, which is a small correction. The inclusion of ion heat conductivity, however, changes the solution behavior in the region of high magnetization $x \cong x_0$. Boundary conditions of (6.3.4) in the new notation will be given by

$$h(0) = h_1 \ ,$$

$$\theta(0) = 0 \ , \qquad (6.3.10)$$

$$n(x_0) = 0 \ ,$$

where

$$h_1 = B_1/\sqrt{8\pi p_0} \ .$$

Let us estimate the magnitudes of the quantities that characterize the discharge region at high β. In this case, it follows from equations (6.3.9) that thermoelectric transport of magnetic flux makes the main contribution to the electric field, and heat conductivity to the energy flux. Then, given that $y \sim 1$ in the discharge region, we obtain $h \sim 1/\sqrt{\beta}$, $T \sim \beta^{0.2}$, $n \sim \beta^{-0.2}$, $x \sim \beta^{0.2}$, and $\xi \sim 1$. Thus, the parameter ξ, which characterizes the accumulated mass, is weakly dependent on β, changing only when $\beta \sim 1$.

Results of numerical simulations of system (6.3.9) with boundary conditions (6.3.10) for h_1 0; 0.5; 0; 0.5, β = 0; 0; 10; 10, A = 2 are shown in Figs. 6.11–6.12, and the plot of ξ as a function of β and h_1, in Fig. 6.13 (h_1 = 0; 0.25; 0.5; 0.75 are represented by lines 1–4).

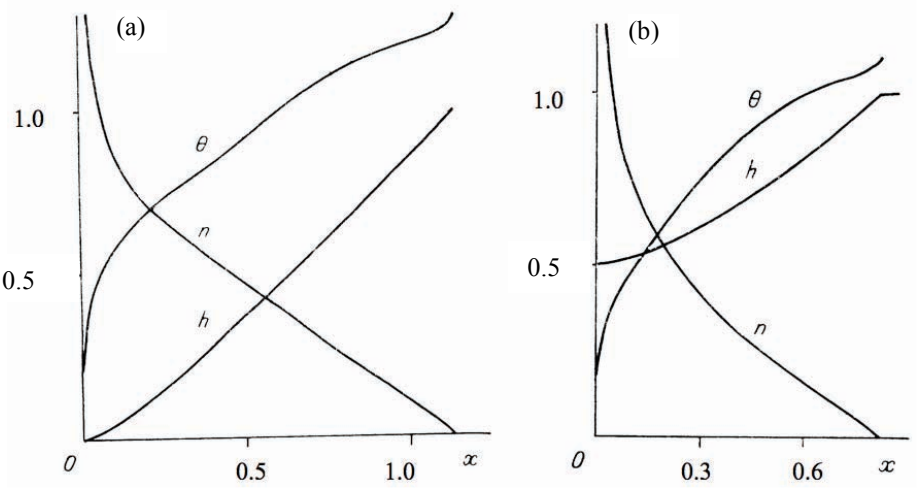

Fig. 6.11. Profiles of temperature θ, density n, and magnetic field h in a plasma with $\beta = 0$ in contact with an insulator with magnetic field: (a) $h_1 = 0$; (b) $h_1 = 0.5$.

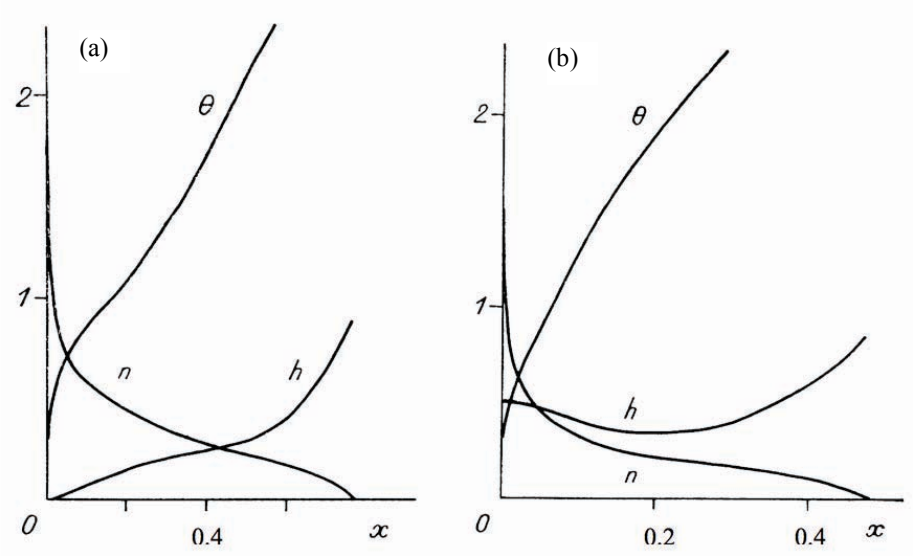

Fig. 6.12. Profiles of temperature θ, density n and magnetic field h in a plasma with $\beta = 10$ in contact with an insulator with magnetic field: (a) $h_1 = 0$; (b) $h_1 = 0.5$.

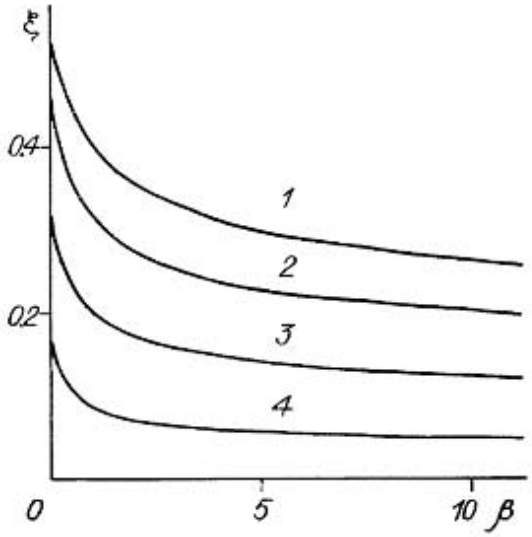

Fig. 6.13. Mass ξ of plasma deposited on the insulator as a function of β for h_1 = 0; 0.25; 0.5; 0.75, represented by lines 1–4.

The simulations show that thermoelectric processes, which play the central role in the magnetic flux transfer for $\beta >> 1$ and which result in the export of magnetic flux even into an insulator with a higher magnetic field (Fig. 6.12b) than in the plasma, are numerically not very essential for β >> 1. For example, if we assume $b = 0$ in equations (6.3.9), the value of ξ for β = 0 and $h_1 = 0$ will decrease by only 13 %. A noticeable decrease in ξ (by about 30%) with thermoelectric fluxes turned-off is observed only for β ≈10. A very small contribution to the accumulated mass ξ is made by the ion heat conductivity, which is a correction of $\sim 1/\sqrt{912A}$, the turning off of which for β = 0 and $h_1 = 0$ leads to the decrease of ξ by 2 %.

Let us consider plasma deposition dynamics. The rate of mass accumulation $\frac{da}{dt} = N_0 v$, in accordance with (6.3.5) and (6.3.8), is determined by the differential equation

$$a\frac{da}{dt} = \xi(\beta, h_1)\frac{c}{e}\frac{p_0 N_0}{B_0} \quad , \qquad (6.3.11)$$

which for the total volume of plasma can be treated as a boundary condition describing plasma and magnetic-flux losses. For $B_0(t) = const.$, $N_0(t) = const.$, $p_0(t) = const.$, $B_1(t)$ *const.*, and $\beta(t) = const.$, plasma deposition is governed by the diffusion law

$$a = \sqrt{2\xi \frac{c}{e} \frac{p_0 N_0}{B_0} t} \ ,$$

$$E = \sqrt{\frac{\xi}{2ec} \frac{p_0 B_0}{N_0 t}} \ , \qquad (6.3.12)$$

$$[X] = \frac{e^{0.7} m^{0.2} c^{0.9} \lambda^{0.4}}{p_0^{0.3}} \sqrt{\frac{2N_0 t}{\xi B_0}} \ .$$

The effective diffusion factor in this case is $D \sim 2\xi c p_0 / e N_0 B_0$, which, for $\beta << 1$, when $\xi \cong 0.5$ (Fig. 6.13), yields $D \sim cB_0/8\pi eN_0$ and approximately corresponds to the estimate of Vekshtein [6.7], and for $\beta >> 1$, when $\xi \cong 0.25$ (Fig. 6.13), yields $D \sim cT_0/eB_0$ and exceeds the estimate of Vekshtein [6.9] and the Bohm heat conductivity by approximately an order of magnitude.

Let us now address the issue of the conditions for the applicability of the above megagauss range of magnetic fields and $\beta \sim 1$. Plasma density N_0 should be much smaller than the plasma density in the discharge region, i.e., in accordance with Section 6.1, $N_0(cm^{-3}) < 3 \cdot 10^{20} B^{1.6}(MG)$. In this case, one can consider the problem to be quasi-stationary and can employ equations (6.3.2) and the boundary condition $N(X_0) = 1$. For $N_0(cm^{-3}) > 3 \cdot 10^{20\ B1.6}$ (MG), plasma density in the discharge region is on the order of N_0, and the simulations performed are inapplicable. The condition that radiation losses in the discharge region can be disregarded yields solution of the near-wall discharge problem. We restrict ourselves to the

$$N_0(cm^{-3})t(\mu s) < 0.8 \cdot 10^{20} B^{0.2}(MG) \ . \qquad (6.3.13)$$

In addition, we ignored the role of the *H*-pressed discharge in the insulator, i.e., the magnetic flux flowing from the discharge through the plasma external to the insulator is assumed to be too small for the formation of an *H*-pressed discharge in the insulator. This means that electric fields (6.3.12) should be smaller than the fields obtained in Section 6.1. For the PMMA insulator, this condition for t $t(\mu s)<0.03/B^{1.12}\,(MG)$ yields

$$N_0(cm^{-3})t(\mu s)>9\cdot 10^{15}B^{0.6}(MG)\ ; \qquad (6.3.14)$$

and for

$$t(\mu s)0.03/B^{1.12}(MG)\ ,$$

$$N_0(cm^{-3})>2\cdot 10^{17}B^{1.72}(MG)\ . \qquad (6.3.15)$$

If condition (6.3.13) is violated, i.e., with rather large time scales, the discharge will enter the stationary stage described in Section 6.1. If conditions (6.3.14) and (6.3.15) are violated, i.e., with rather small densities of the hydrogen plasma, the *H*-pressed discharge discussed in Section 6.1 will occur on the insulator surface.

6.4. Magnetized Plasma Cooling at the Exploding Metal Wall/Plasma Interface

In a number of cases, cooling of the magnetized plasma at the cold wall/plasma interface, which is accompanied by the interaction of magnetic and thermal processes, as shown above, results in anomalously high effective heat conductivity and magnetic diffusion coefficients. Indeed, for hydrogen plasma cooling at the interface with an insulator or dense multi-charge plasma, effective heat conductivity proves to be on the order of the Bohm heat conductivity (Section 6.3).

For the cooling of plasma bounded by a rigid, ideally conducting wall, the increase in heat conductivity by comparison with the classical magnetized heat conductivity, as shown by Vekshtein [6.2], is not appreciable and is possible only for plasmas with $\beta >> 1$. In this case, the metal wall can be considered rigid, ideally conducting if it does not explode when exposed to a heat flux from the plasma, i.e., its thermal conductivity in a condensed phase proves to be sufficient to remove heat without vaporization. This condition is fulfilled for relatively low energy densities (for instance, for plasma with T_0 = 1 keV and β =1, it is satisfied at $B_0 \leq 0.2$ MG). For higher energy densities, the presence of a metal layer exploded by the heat flux substantially changes the nature of cooling and increases the heat losses of

the plasma. This particular case is discussed in this section. Magnetic fields, however, are considered to be not very high ($B_0 < 10$ MG), because for $B_0 > 10$ MG, when the skin layer is exploded by Joule heat and the metal becomes non-conductive, the problem reduces to the problem of plasma cooling at the plasma/insulator interface considered in Section 6.3.

Let us use the same problem geometry and designations as in Section 6.3. Characteristic time scales will, as before, be assumed to be large by comparison with the gas-dynamic scales, so that the total pressure, both in the hydrogen plasma and in the metal vapor, manages to equalize, and equation (6.1.1) holds true. Equations for the magnetic and electric fields and plasma heat balance have the form of (6.1.2).

It turns out that, depending on the hydrogen plasma density, there are two cooling modes: for higher density, the key role, as with plasma cooling at the plasma/insulator interface, is played by processes in the near-wall plasma layer; for lower density, it is played by processes in the metal vapor. In both cases, however, effective heat conductivity of the plasma may greatly exceed the classical conductivity.

6.4.1. Cooling of Dense Plasma

The presence of anomalously high effective heat conductivity coefficients indicates that, as already mentioned in Section 6.3, the problem for the hydrogen plasma is quasi-stationary: hydrogen plasma density at the plasma/wall interface is high by comparison with the density N_0, and in equations (6.1.2) for the magnetic and electric fields and plasma heat balance in the near-wall region, we can disregard time derivatives and assume the electric field and the energy flux to be constant. Then, equations (6.1.2) will take the form of (6.3.2) with the energy flux Q equal to that of (6.3.6) flowing into the discharge region from the plasma.

In ionized vapors, the leading role in heat transfer is played by radiation. As a result of the radiative heat conductivity, the mass of the vapor in the discharge region greatly exceeds the mass of the plasma. Therefore, the temperature of the vapor is markedly lower than that of hydrogen plasma, and the hydrogen plasma temperature at the plasma/vapor interface can be assumed to be zero.

Thus, if the magnetic field B_1 at the hydrogen plasma/vapor interface is known, the boundary conditions for (6.3.2) will be as follows:

$$T(0) = 0\,,$$

$$B(0) = B_1\,, \tag{6.4.1}$$

$$N(-X_0) = 0$$

(for the vapor boundary, we assume $X = 0$, for the discharge region boundary, $X = -X_0$), and for the plasma, the problem reduces to the problem of plasma cooling at the plasma/insulator interface (Section 6.3).

As the major contribution to the mass of the plasma accumulated in the discharge is made by the region in which electron magnetization is $\omega_e\tau_e \sim 1$, and the total pressure p_0 is specified, for the transition in (6.3.2) to dimensionless quantities it will be natural to use p_0 as a pressure unit and take temperature and density units of measure from (6.3.7).

Introducing the dimensionless coordinate x and the dimensionless temperature θ, density n, magnetic field h and plasma mass

$$\xi = eEa\,/\,p_0 \tag{6.4.2}$$

in accordance with (6.3.8), we can rewrite the system of equations (6.3.2) in the form of (6.3.9). The boundary conditions (6.4.1) in the dimensionless variables will be written as (6.3.10) (here, E is assumed to be positive, and since X is negative, x is positive).

The rate of accumulation of the plasma mass is described by the differential equation (6.3.11). The quantity ξ as a function of β and h_1 is shown in Fig. 6.13.

For a complete statement of the problem, we must determine the magnetic field B_1. For sufficiently high plasma density, this can be done by using a system of ordinary differential equations. Indeed, in accordance with (6.3.11) and (6.4.2), discharge resistance in the hydrogen plasma falls as density N_0 increases, whereas discharge resistance in the metal vapor does not depend on N_0; therefore, for a sufficiently high-density magnetized hydrogen plasma, the conductivity of the vapor can be disregarded, and the magnetic field in the vapor can be considered to be constant ($B = B_1$). To calculate it, we use the condition of magnetic flux conservation

$$\frac{d}{dt}(B_1 X_1) = cE \tag{6.4.3}$$

for a vapor layer of thickness X_1 and the condition of energy conservation, assuming the vapor to be an ideal gas with adiabatic index γ:

$$\frac{d}{dt}\left(\frac{p_1 X_1}{\gamma-1}\right)+p_1\frac{dX_1}{dt}+\frac{d}{dt}\left(\frac{B_1^2}{8\pi}X_1\right)+\frac{B_1^2}{8\pi}\frac{dX_1}{dt}=\frac{c}{4\pi}EB_0\left(1+\frac{5}{4}\beta\right) \qquad (6.4.4)$$

(p_1 is the thermal pressure of the vapor, which is constant because of the constancy of $B = B_1$ and equilibrium condition (6.1.1)). Note that the energy conservation condition is used only if the system geometry is such that the energy flux from the vapor surface is completely offset by the flux from the surrounding walls (closed system). The opposite limiting case, in which the radiation flux from the wall is not offset at all, is discussed in Section 6.4.2. The set of equations (6.3.11) and (6.4.2–6.4.4), together with the equilibrium condition $p_1 + B_1^2/8\pi = p_0$, completely determines the cooling of dense plasma.

When $p_0 = const.$, $N_0 = const.$, $B_0 = const.$, $\beta = const.$, and $p_0 = const.$, we find from (6.3.11) and (6.4.2–6.4.4) that plasma deposition proceeds according to the diffusion law

$$a=\sqrt{2\xi\frac{c}{e}\frac{p_0 N_0}{B_0}t}\ ,$$

$$E=\sqrt{\frac{\xi}{2ec}\frac{p_0 B_0}{N_0 t}}\ , \qquad (6.4.5)$$

$$X_1=\sqrt{\frac{2\xi c}{e}\frac{p_0 B_0 t}{N_0 B_1^2}}\ ,$$

and the dimensionless magnetic field h_1 is obtained from the algebraic equation

$$h_1^2\frac{\gamma-2}{\gamma-1}-h_1\frac{2+2.5\beta}{\sqrt{1+\beta}}+\frac{\gamma}{\gamma-1}=0\ ,$$

i.e.,

$$h_1(\beta)=\frac{1}{(2-\gamma)\sqrt{1+\beta}}\left\{\sqrt{1+\beta\left[1+\left(\frac{25}{16}\beta+\frac{3}{2}\right)(\gamma-1)^2\right]}-(\gamma-1)(1+5\beta/4)\right\} \quad .(6.4.6)$$

For $\beta\to 0$, $h_1\to 1$, and for $\beta\to\infty$, $h_1\cong\frac{0.4\gamma}{(\gamma-1)\sqrt{\beta}}\to 0$; thus, in accordance with Section 6.3, for $\beta\to 0$, $\xi\to 0$, and for $\beta\to\infty$, $\xi\to$ const. The dependence $\xi(\beta,h_1(\beta))$ for $h_1(\beta)$ from (6.4.6)—obtained by means of equations (6.3.9) for the set of coefficients α, b, γ from Epperlein and Haines [6.22] (somewhat more accurate than (6.1.9)) for $\gamma = 1.21$∗—is depicted in Fig. 6.14 (Curve 1). For comparison, the same figure shows the dependence $\xi(\beta,h_1(\beta))$ for the set of coefficients (6.1.9) (Curve 2). Note that although the difference between the coefficients from Epperlein and Haines [6.22] and (6.1.9) is rather considerable (for instance, for *b* it gets as high as 30 %), the difference between the values of $\xi(\beta)$ does not exceed 6 %. This points to a weak dependence of ξ on the values of transport coefficients; in addition, apparently, mutual offsetting between different-sign deviations of Epperlein and Haines [6.22] from (6.1.9) for different $\omega_e\tau_e$ is substantial.

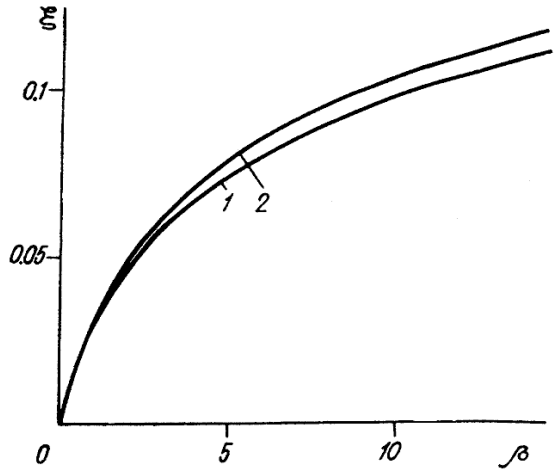

Fig. 6.14. Plasma mass deposited on the exploding metal ξ as a function of β for the set of transport coefficients from [6.22] (Curve 1) and for the set of coefficients (6.1.9) (Curve 2).

∗ $\gamma = 1.21$ approximates the adiabatic index of copper vapors in megagauss magnetic fields (see the next section)

Since for high β, $h_1 \cong 0$, the effective diffusion coefficient $D \sim 2\xi cp_0/eN_0B_0$ for the dense plasma cooling at the interface with an exploding metal wall proves to be the same as for plasma cooling at the plasma/insulator interface ($\xi(\beta \to \infty) \cong 0.2$, $D \sim cT_0 / eB_0$) and exceeds the Bohm heat conductivity by an order of magnitude; while for $\beta \approx 1$, when $\xi \approx 0.03$, it proves to be on the order of the Bohm coefficient.

The theoretical results presented here that describe dense plasma cooling near the exploding metal wall were verified by numerical simulations of the cooling of deuterium plasma with $T_0 = 0.5$ keV, $B_0 = 0.5$ MG, and $\beta = 1$ near a copper wall. The simulations took into account the hydrodynamic motion, the magnetic diffusion and electron heat conductivity (both for deuterium and for copper). In addition, for deuterium, we took into account an additional contribution to the electric field and the heat flux due to the Nernst effect (summands with the factor b_Λ in (6.1.2)) and ion heat conductivity; for copper, we accounted for the radiative heat transport. The transport coefficients α, b, γ in deuterium were found from the formulas of Epperlein and Haines [6.22], and γ_1, from Braginskii [6.11] (Section 6.3). The equation of state, conductivity, electron thermal conductivity, and the radiation paths for copper used in the simulations were determined by formulas presented in Section 6.2.1. The boundary condition for the radiation propagation was zero radiation flux at the discharge region boundary (closed system). Initial copper was considered to have normal density $\delta = 1$ and a temperature close to room temperature, $\varepsilon = 0.0013$.

Fig. 6.15 shows temperature and magnetic-field profiles, obtained using equations (6.3.9) (solid curves) and numerical simulations (dashed curves). The comparison shows satisfactory agreement. Much better agreement is observed for the volume of cooled plasma. In numerical simulations, the plasma thickness decreased by that time by $\Delta X = 0.042$ cm, and according to (6.4.5), the deposited plasma thickness should be $\Delta X = 0.045$ cm.

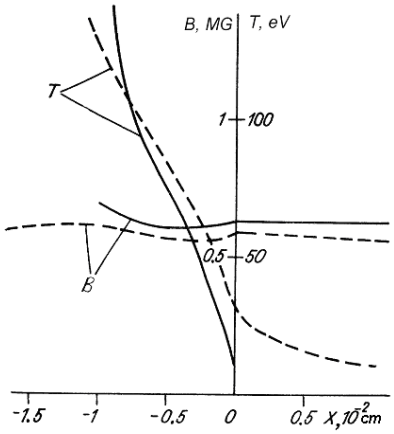

Fig. 6.15. Profiles of temperature T and magnetic field B at time t = 0.085 μs for the cooling of deuterium plasma with $T_0 = 0.5$ keV, $B_0 = 0.5$ MG, and $\beta = 1$ near the copper wall, obtained using equations (6.3.9) (solid curves) and numerical simulations (dashed curves).

6.4.2. Shunting Metal-Vapor Discharge

In sufficiently low-density hydrogen plasma, as opposed to the case considered in Section 6.4.1, the conductivity of metal vapor predominates, and the metal-vapor discharge that thereby shunts the hydrogen-plasma discharge plays the key role. Let us consider a problem, in which, at the initial time, plasma whose temperature, density and magnetic field are constant throughout the volume is in contact with a cold copper wall. The key factor in the heat transfer through the metal vapor is radiation whose transport in the context of long time scales for a closed system is found from the heat conduction equation. Since this problem has no characteristic length scale, its solution is self-similar, and the heat conduction and magnetic diffusion determine the diffusive nature of the self-similarity. The consideration of this problem differs from that of the problem of magnetic-field diffusion into the insulator accompanied by radiative heat conductivity (Section 6.1.3) solely in terms of the boundary conditions.

For the equation of state, free radiation path and conductivity of copper vapor, we assume the power dependence on temperature and density. Then, using the formulas from Section 6.2.1 for these quantities in the temperature range of 3–30 eV and the density range of 10^{-3}–10^{-1} g/cm^3, we approximately obtain the following dependences (in cm, g, μs, and temperature in eV): $p/\rho = 0.0075T^{1.67}/\rho^{0.14}$, $l_R = 10^{-6}T/\rho^{1.64}$, $\sigma = 2.7\cdot 10^8 T^{0.92}\rho^{0.2}$, adiabatic index $\gamma = p/\varepsilon\rho + 1 = 1.21$. In order to convert to dimensionless variables, the units of measurement for temperature [T] and density $[\rho]$ are chosen as in Section 6.1, such that the heat conductivity and magnetic diffusion coefficients $\kappa = c^2/4\pi\sigma$ are of the same order of magnitude—$\sigma_{SB}[T]^4 l_R([T],[\rho])$ / $p_0 = \kappa([T],[\rho])$—and thermal pressure is on the order of the assigned p_0, $p([T],[\rho]) = p_0$; then, $[T] = 12\,eV\,p_0^{0.31}$ (GPa), $[\rho] = 0.01\,g/cm^3\,p_0^{0.57}$ (GPa).

Using the self-similar variable $\varsigma = 390\int \rho\, dX(g/cm^2) / \left[\sqrt{t(\mu s)}\, p_0^{0.37}(GPa)\right]$ and introducing dimensionless functions

$$T = [T]\theta(\varsigma) \ ,$$

$$\rho = [\rho] n(\varsigma) \ ,$$

$$B = \sqrt{8\pi p_0}\, h(\xi) \ ,$$

$$E = 0.63 \frac{kV}{cm} \frac{p_0^{0.3}(GPa)}{\sqrt{t(\mu s)}} \varepsilon(\varsigma) \ ,$$

$$Q = 2.5 \cdot 10^8 \frac{W}{cm^2} \frac{p_0^{0.8}(GPa)}{\sqrt{t(\mu s)}} q(\varsigma) \ ,$$

$$X = 0.25\, \mu s \frac{\sqrt{t(\mu s)}}{p_0^{0.2}(GPa)} x(\xi) \ ,$$

we rewrite equations (6.1.1) and (6.1.2) as follows:

$$\theta^{1.67} n^{0.86} + h^2 = 1 \ ,$$

$$\frac{d\varepsilon}{d\varsigma} = \frac{\xi}{n}\left(\frac{dh}{d\varsigma} - \frac{h}{n}\frac{dn}{d\varsigma}\right) \ ,$$

$$\frac{dh}{d\varsigma} = -\frac{1}{2}\frac{\theta^{0.92}}{n^{0.8}} \varepsilon \ ,$$

$$q = -\frac{16}{3}\frac{\theta^4}{n^{0.64}}\frac{d\theta}{d\varsigma} \qquad (6.4.7)$$

$$\frac{dq}{d\varsigma} = \frac{\varepsilon^2}{2}\frac{\theta^{0.92}}{n^{0.8}} + \frac{5}{6}\varsigma\left(\frac{14}{3}\frac{\theta^{0.67}}{n^{0.14}}\frac{d\theta}{d\varsigma} - \frac{\theta^{1.67}}{n^{1.14}}\frac{dn}{d\varsigma}\right) \ ,$$

$$\frac{dx}{d\varsigma} = 1/n \ .$$

Let us determine boundary conditions for equations (6.4.7). A heat flux at the plasma boundary ($\varsigma = 0$) can be calculated as the difference between the total energy flux coming to the discharge region from the plasma $(c/4\pi)EB_0(1+5\beta/4)$ and the electromagnetic energy flux $(c/4\pi)EB_1$

(B_1 is magnetic field at the hydrogen plasma/vapor interface). Thus, one of the boundary conditions at this interface is the relationship between the heat flux and electric field, which is written in dimensionless variables as

$$q(0) = \left[\frac{1 + (5/4)\beta}{\sqrt{1+\beta}} - h_1 \right] \varepsilon(0) \ . \tag{6.4.8}$$

The second boundary condition results from the fact that the vapor discharge shunts the hydrogen-plasma discharge, i.e., for the hydrogen-plasma discharge, in this case, we assume that $E = 0$, which means that, from (6.4.5), $\xi = 0$; since ξ becomes zero at $h_1 = 1$ 1, the boundary condition should be assumed to be

$$h_1 = 1 \ . \tag{6.4.9}$$

The boundary conditions at the interface of the nonvaporized metal and the vapor will consist in temperature, heat flux, and electric field equaling zero:

$$\theta(\varsigma_0) = q(\varsigma_0) = \varepsilon(\varsigma_0) = 0 \ . \tag{6.4.10}$$

By solving equations (6.4.9) with boundary conditions (6.4.10–6.4.12), and using the equation

$$\frac{da}{dt} = N_0 cE / B_0 \ ,$$

we determine the thickness of the deposited plasma:

$$\Delta X = 0.25 \mu s \frac{\sqrt{t(\mu s)}}{p_0^{0.2}(GPa)} \varepsilon(0) \sqrt{1+\beta} \ . \tag{6.4.11}$$

Let us estimate the orders of magnitude of the quantities that characterize the discharge region for large and small β. For $\beta >> 1$, one can disregard the role of the terms with magnetic field in the heat transfer equations and find the electric field from relationship (6.4.8); then, $\varepsilon(0) \sim \beta^{-0.03}$, $n \sim \beta^{-0.22}$, x $\sim \beta^{0.47}$, and $\varepsilon(0) \sim \beta^{-0.03}$, and the magnetic field exponentially decays with discharge-region depth. For $\beta << 1$, in the discharge region, $\theta^{1.67} n^{0.86} \sim \beta$, and from (6.4.7) we have

$$\theta \sim \beta^{0.42} \ ,$$

$$n \sim \beta^{0.35} \ , \tag{6.4.12}$$

$$x \sim \varepsilon(0) \sim \beta^{0.27} \ .$$

Some results of numerical simulations of system (6.4.7) with boundary conditions (6.4.8–6.4.10) are shown in Figs. 6.16 and 6.17. Fig. 6.16 depicts as functions of β the electric field at the entry point into the discharged $\varepsilon(0)$, the mass of the vapor in the discharge ς_0, the magnetic field at the interface with nonvaporized metal $h(\varsigma_0)$, and the ratio of vapor volume $X(\varsigma_0)$ to the volume of deposited plasma (6.4.11) $s = x(\varsigma_0) / \varepsilon(0)\sqrt{1+B}$. The solid curves in Fig. 6.17 are the profiles for magnetic field and temperature found by solving the equations of (6.4.7) and converted to dimension units for comparison with numerical simulation results for the case of the cooling of plasma with $B_0 = 1$ MG, $T_0 = 10$ keV, and $\beta = 1$ by the time $t = 0.035$ μs. The figure also shows numerical simulation data (dashed curves) obtained using the procedure described in Section 6.4.1. The numerical simulation yields a smaller size for the discharge region, which is due to the influence of the hydrogen-plasma discharge, which was not included in the calculations based on formulas (6.4.7). This difference also affects the thickness of deposited plasma, which, in accordance with (6.4.11), is $\Delta X = 0.047$ cm, whereas the numerical simulation yields $\Delta X = 0.036$ cm.

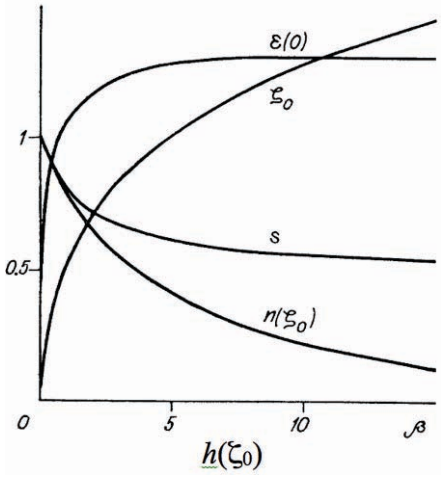

Fig. 6.16. Electric field at the entry point into the discharge ε(0), vapor mass in the discharge ς_0, magnetic field at the interface with nonvaporized metal $h(\varsigma_0)$, and ratio of vapor volume to volume of deposited plasma s as functions of β.

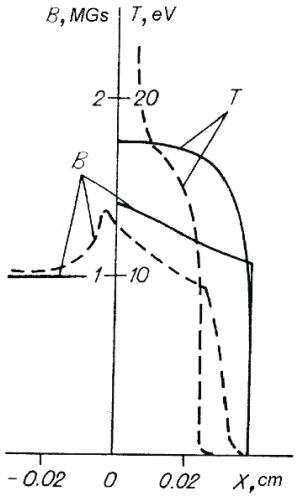

Fig. 6.17. Profiles of temperature T and magnetic field B at the time t = 0.085 μs for the cooling of deuterium plasma with $T_0 = 10$ keV, $B_0 = 1$ MG, and $\beta = 1$ near the copper wall, obtained using equations (6.4.7) (solid curves) and numerical simulations (dashed curves).

Until now, we have considered the system to be closed, such that the flux of energy emitted from the vapor surface was completely offset by the radiation coming from the surrounding walls. Let us move now to the case of an open system, whose geometry is such that the flux is in no way offset. Then, in the vapor, due to the heat release, the characteristic thermal pressure is much smaller than the magnetic and thermal pressure of the hydrogen plasma, $\beta_v << 1, \beta$, and it varies over time. To determine the dependence $\beta_v(t)$, we take into account that the heat flux from the surface, which in this case corresponds to blackbody radiation $\mathcal{Q} \sim T^4(t)$, should offset the heat coming from the plasma $\sim E(t) \sim \varepsilon(0)/\sqrt{t}$. Equating these fluxes and using the dependences of θ and $\varepsilon(0)$ on β from (6.4.12), we obtain $\beta_v \sim t^{-0.35}$, $X \sim t^{0.4}$. Thus, X grows more slowly than according to the diffusion law, and the vapor-discharge resistance in the open system is less than in the closed system.

Let us discuss the question of when plasma can be considered sufficiently dense, and when, for its cooling, we can use the results of Section 6.4.2 and when we can use the results of Section 6.4.3. To answer this question, as already mentioned, one should compare hydrogen-plasma discharge resistance with that of metal vapor (by comparing the thicknesses of the deposited plasma, calculated with formulas (6.4.5) and (6.4.11)). The governing mode will be that with a smaller thickness, although if the difference is not very large, one can expect an appreciable influence by the mode not taken into account (as for the case of Fig. 6.17), which reduces the thickness of deposited plasma. In any of these modes, however, if plasma magnetization is high enough, the effective heat conductivity can be markedly higher than the classical heat conductivity.

The high values of effective heat conductivity coefficients can make it difficult to produce a high-temperature magnetized plasma in the new systems for liner compression of plasma from an ultrahigh speed flow discussed in Turchi *et al.* [6.23].

6.5. Stationary Discharge during Magnetic Flux Transfer through the Insulator Surface

A qualitatively different type of surface discharge forms at the interface of the condensed matter and the vacuum (or plasma), when the magnetic flux flows out of condensed matter. Such a discharge may occur in different pulsed power systems during the transfer of electromagnetic energy through the insulator surface. Figure 6.18 shows diagrams of units in which energy is transferred to a vacuum, plalsma, and a liner. The

operation of such units may involve difficulties resulting from the insulator surface breakdown and its subsequent transition to a quasi-stationary discharge (*H*-thrown discharge; this term is used, because the ponderomotive force $\frac{1}{c}[jH]$ throws off the conducting ionized vapor from the insulator surface; see Fig. 6.19). In this case, part of the current delivered to the unit branches off to the discharge, resulting in a decrease in the power delivered to the load through the insulator surface.

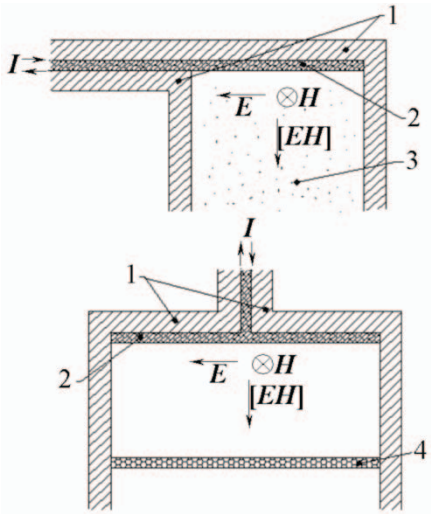

Fig. 6.18. Diagrams of units with electromagnetic energy transfer through the insulator surface: 1) conducting walls, 2) insulator, 3) plasma (or vacuum), 4) liner. The diagram shows the electric- and magnetic-field vectors, as well as the Umov-Poynting vector.

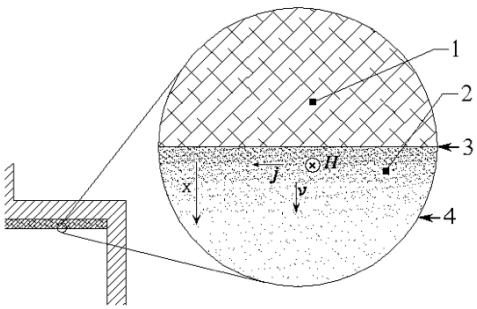

Fig. 6.19. Discharge zone: 1) nonvaporized insulator, 2) insulator vapor, 3) beginning of the discharge zone, 4) end of the discharge zone. The figure shows the current-density vector, magnetic-field vector, and velocity of matter vector, as well as the direction of the x coordinate.

In this case, since matter can expand together with the magnetic field, there is considerable hydrodynamic motion, which carries the magnetic flux along with matter away from the surface. In the case of an *H*-thrown discharge on the insulator surface, some of the Joule heat given off in the discharge is transferred by radiation or heat conduction to the insulator, causing its vaporization and conversion into plasma. The hydrodynamic outflow of matter and diffusive processes (magnetic diffusion and heat conduction) balance each other in the discharge region, producing a stationary discharge.

The possibility of the formation near the insulator surface of a stationary surface discharge that constrains the rate of outflow of magnetic field lines was demonstrated by Keck [6.24] and Workman [6.25]. Workman [6.25] developed a theory for such a discharge, in which a number of simplifying assumptions are used, including the assumption concerning complete single ionization of the insulator vapor flowing out of the discharge, which holds true for moderate magnetic fields, $B \sim 10^4$ G. In this Section, we consider a more general case of arbitrary multiple ionization, which is important for stronger magnetic fields, in particular those used in magnetic liner acceleration experiments, and which may be necessary for the analysis of liner implosion as applied to MAGO plasma compression.

Studies of the *H*-thrown discharge in strong magnetic fields were carried out by Garanin *et al.* [6.5] and Garanin and Karmishin [6.6]. The heat flux was determined by the blackbody radiation of ionized vapor flying away in Garanin *et al.* [6.5] and by the electron heat conductivity of the discharge plasma in Garanin and Karmishin [6.6].

In the case of interest here, as in the previous cases, the magnetic field B and electric field E are perpendicular to each other and parallel to the insulator surface, which is considered flat. A self-sustained surface discharge in the insulator vapor occurs because the ponderomotive force–induced plasma outflow from the surface is offset by the vaporization of new insulator portions by the heat fluxes from the plasma being carried off. The ionized vapor entering the discharge region is further heated up by Joule heat and is accelerated until the plasma velocity reaches the velocity v_1 of the outflow of the magnetic force lines and the electric field in the associated frame of reference becomes equal to zero.

Under typical experimental conditions, the thickness of the discharge zone x_B is small by comparison with the dimensions L of the region of insulator vapor motion (at $B \sim 10^4$ G, x_B proves to be on the order of 0.1 cm and decreases with B). Therefore, the setup time for the vaporization regime is small by comparison with the characteristic times for the variation of the magnetic

field and other quantities that influence the current layer. Consequently, the discharge can be considered stationary. When solving a complete magnetohydrodynamic problem that describes the operation of an experimental installation in which such a discharge takes place, the discharge zone can be replaced with an infinitely narrow jump of all MHD quantities. Our goal is to find conditions on this jump, so we need to find the dependence of the plasma outflow velocity v_1, as well as plasma density and temperature, on the value of magnetic fields in a nonvaporized insulator B_0 and at the exit from the current layer B_1.

An essential factor is that for obtaining these dependences it is strictly speaking insufficient to use only integral conservation laws relating quantities at the entry into the discharge region and at the exit from it; one should also solve the problem of the structure of that region. Workman [6.25] managed to do without solving this more complex problem thanks to an approximation in which the temperature of the plasma flowing out of the discharge was considered to be high enough for almost complete first ionization, but at the same time low enough to enable him to disregard further ionization, and the heat energy was considered low by comparison with the ionization energy, and the thermal pressure was considered low by comparison with the magnetic pressure. Our statement of the problem is free of such strict constraints [6.25]. In mathematical terms, it is an eigenvalue problem.

6.5.1. Discharge Maintained by Radiation

The dependence of all quantities in the discharge on the normal coordinate x is described by a system of stationary MHD equations:

$$\rho v = \text{const} \ ; \tag{6.5.1}$$

$$p + \rho v^2 + B^2 / 8\pi = \text{const} \ ; \tag{6.5.2}$$

$$\rho v (w + v^2 / 2) - Q - cEB / 4\pi = \text{const} \ ; \tag{6.5.3}$$

$$-\kappa \, dB / dx + vB = cE = \text{const} \ , \tag{6.5.4}$$

where $\rho(x)$, $v(x)$, $p(x)$, $B(x)$, $w(x)$, $Q(x)$, and $\kappa(x)$ are the current values of the density, velocity, pressure, magnetic field, specific enthalpy, heat flux, and magnetic diffusion coefficient, respectively; E is the electric field. The system of equations (6.5.1–6.5.4) represents the mass, momentum, energy and magnetic flux conservation laws in the frame of reference with a resting current sheath. One can consider this frame of reference to be identical to

the laboratory one, because the characteristic density in the current sheath turns out to be very small by comparison with the insulator density.

Solving this problem is made easier by the fact that, in cases of practical interest, consideration of the heat flux Q can be greatly simplified. Let us estimate the optical thickness of the current sheath x_B/l (l is the Rosseland mean free path of radiation, $x_B \sim \kappa/v$), proceeding from the diffusion approximation for describing the heat transfer. Within this approximation, the temperature conductivity and magnetic diffusion coefficients, $\sim l\sigma_{SB}T^4/\rho w$ and κ, respectively, should be of the same order of magnitude. Also, using the relationships

$$\rho w \sim \rho v^2 \sim B^2 / 8\pi$$

and p, λ and κ as power functions of ρ and T (see Section 6.1.2), we find

$$x_B / l \sim \kappa / lv \sim \sigma_{SB}T^4 / (\rho w v) \sim 0.2\, B^{0.14} \ ,$$

where B is measured in MG.

Thus, for a typical insulator containing light elements, for moderately high magnetic fields, the optical thickness of the current sheath is small. Therefore, the heat flux Q towards the insulator from the plasma flowing out of the current sheath and having a temperature of T_1 should be considered equal to $\sigma_{SB}T_1^4$ *, with this flux Q being almost constant over the thickness x_B, where all the other quantities (B, ρ, ν T, and gas-dynamic and magnetic energy fluxes) vary significantly. The absorption of the heat flux begins at distances of $x \sim l$, i.e., at the outlet of the current sheath to the insulator side, where the variations of the rest of the fluxes in equation (6.5.3) are small by comparison with their characteristic values in the current sheath. Consequently, the whole region is divided into two zones: Zone I of the current sheath, where Q in equation (6.5.3) can be disregarded, and Zone II of heat flux absorption, where in equation (6.5.3), apart from Q, one should leave only the terms of the first order of smallness for the velocity v.

The subscripts 0 will denote the quantities in the forepart of the discharge region (on the side of the nonvaporized insulator), and the subscripts 1,

* If the plasma in the complete magnetohydrodynamic problem is optically thick. Otherwise, the flux Q should be determined by the conditions of the complete problem, while within the H-thrown discharge problem of interest to us, this flux will be an external parameter (this case is discussed at the end of the section).

those in the rear part. As the insulator density is high, $v_0 = 0$. The heat flux does not penetrate deeply into the insulator, and therefore $Q_0 = 0$.

At the outlet of the current sheath, the current density is equal to zero, which is why it follows from (6.5.4) that

$$v_1 B_1 = cE \ . \tag{6.5.5}$$

We introduce dimensionless variables:

$$u \equiv v / v_1 \ ,$$

$$h \equiv B / B_1 \ ,$$

$$q \equiv Q / v_1 \cdot (B_1^2 / 8\pi) \ ,$$

$$p \equiv p / p_1 \ ,$$

as well as parameters μ and β:

$$\mu \equiv \rho_1 v_1^2 / (B_1^2 / 8\pi) \ ,$$

$$\beta \equiv p_1 / (B_1^2 / 8\pi) \ .$$

Then, assuming that the insulator vapor is a gas with the adiabatic index γ and using (6.5.1) and (6.5.5), we rewrite equations (6.5.2) and (6.5.3) in the dimensionless form

$$\beta p + \mu u + h^2 = \beta p_0 + h_0^2 = \beta + \mu + 1 \ ; \tag{6.5.6}$$

$$\frac{\gamma}{\gamma - 1} \beta p u + \mu u^2 / 2 - q + 2h = 2h_0 = \frac{\gamma}{\gamma - 1} \beta + \frac{\mu}{2} - q_1 + 2 \ . \tag{6.5.7}$$

From equations (6.5.6) and (6.5.7), one can derive a relationship between μ and β by using the smallness of q in Zone I. Disregarding q and excluding p from (6.5.6) and (6.5.7), we get

$$u = \left\{ \frac{\gamma}{\gamma - 1}(\beta + \mu + 1 - h^2) \pm \sqrt{D} \right\} / \frac{\gamma + 1}{\gamma - 1}\mu \ , \qquad (6.5.8)$$

where

$$D = \left[\frac{\gamma}{\gamma - 1}(\beta + \mu + 1 - h^2) \right]^2 - \frac{2(\gamma + 1)}{\gamma - 1}\mu \left(2 + \frac{\mu}{2} + \frac{\gamma}{\gamma - 1}\beta - 2h \right) . \qquad (6.5.9)$$

The analysis of formulas (6.5.8) and (6.5.9) with the use of the conditions of $\mu = 1$ at $h = 1$ and $u = 0$ at $h = h_0 > 1$ shows that for $h = 1$, the sign for the radical in (6.5.8) should be positive. On the other hand, at the point $h \cong h_0$, $u \cong 0$ at the interface between Zones I and II, this sign is negative, which follows from the condition of $p > 0$. As the rarefaction shock wave is unstable, the change in the radical sign should occur at $D = 0$. In this case, it follows from the condition $D \geq 0$ that dD/dh should be equal to zero at this point.

Based on these conditions, we find the relationship between μ and β in the parametric form

$$\mu = \frac{2h_*^2\gamma^2}{\gamma + 1} \frac{(h_* - 1)(\gamma h_* + 2 - \gamma)}{(\gamma h_* - \gamma + 1)^2} \ ; \qquad (6.5.10)$$

$$\beta = \mu(\gamma^2 - 1) / \gamma^2 h_* + h_*^2 - \mu - 1 \ , \qquad (6.5.11)$$

where h_* is the parameter.

Dimensionless quantities of the magnetic field h_0 and pressure p_0 in the insulator* can be calculated from equations (6.5.6) and (6.5.7)

$$h_0 = 1 + \mu / 4 + \beta\gamma / 2(\gamma - 1) \ ; \qquad (6.5.12)$$

$$p_0 = 1 + (1 + \mu - h_0^2) / \beta \ . \qquad (6.5.13)$$

* The presence of pressure $p_0 \neq 0$ in the insulator at high magnetic fields ($B \geq 10$ MG) may lead to the occurrence of pronounced electric conductivity, and the theory set forth here will be invalid in this case.

Note the presence of a limitation on the range of variation of μ and β. The analysis of the function $h(x)$ at $h, u \to 1$ (Eq. (6.5.4)) shows that the finite solution exists only if the following inequalities are fulfilled:

$$\gamma\beta < \mu \le 2 + \gamma\beta \, .$$

The dependence $\mu(\beta)$ found from equations (6.5.10) and (6.5.11) fulfills the first of them. The second inequality is nontrivial. It coincides with the condition for the total speed of sound c_1

$$c_1^2 \equiv B_1^2 / 4\pi\rho_1 + \gamma p_1 / \rho_1 \ge v_1^2 \ , \qquad (6.5.14)$$

which is necessary for the solution to be stable [6.26]. This limitation is associated with the existence of a limiting vaporization regime under which v_1 achieves its highest possible value, $v_{1\max} = c_1$ (similar to the Jouget combustion mode).

In order to obtain the value of velocity v_1, one must consider the process of heat absorption in Zone II in more detail. It is shown above that for the whole length of the current sheath, the heat flux is

$$Q \approx Q_1 = \sigma_{SB} T_1^4 \ , \qquad (6.5.15)$$

where T_1 is the vapor temperature in the rear part of the discharge region. Let us assume that the radiation free path depends only on density and temperature, $l(\rho,T)$ (the gray matter assumption). For the equation of state, free path and magnetic diffusion coefficient, let us take a power dependence on temperature and density:

$$p / \rho = A T^n / \rho^m \ ; \qquad (6.5.16)$$

$$l = \Lambda T^j / \rho^i \ ; \qquad (6.5.17)$$

$$\kappa = K / (\rho^k T^l) \ . \qquad (6.5.18)$$

Then, from (6.5.15) we obtain

$$q_1 = \sigma_{SB} \left(\frac{\beta}{A\mu} \right)^{4/n} \mu^{4m/n} \left(\frac{B_1^2}{8\pi} \right)^{4m/n-1} v_1^{8(1-m)/n-1} \ . \qquad (6.5.19)$$

Using the smallness of q in Eq. (6.5.7), leaving the major terms in the expansion for velocity u, we find

$$\frac{dq}{d\xi} - \frac{2lv_1}{\kappa} = \frac{\gamma}{\gamma - 1}\beta p_0 \frac{du}{d\xi} \ . \qquad (6.5.20)$$

Here, the function $q(\xi)$ is given by

$$q(\xi) = 2q_1 \int_0^1 \cos\theta \exp(-\xi / \cos\theta)\, d(\cos\theta)$$

for pure absorption of the Lambert source photons in Zone II, since by virtue of $q_1 << 1$, the temperature in Zone II is much lower than T_1. Proceeding to the variables

$$y \equiv \frac{q}{q_1} \ ,$$

$$z \equiv \frac{\gamma}{\gamma - 1}\frac{\beta p_0}{q_1} u$$

in equation (6.5.20) and using (6.5.16–6.5.18), we obtain

$$\frac{dz}{d\xi} + az^{\alpha} = \frac{dy}{d\xi} \ , \qquad (6.5.21)$$

where

$$\alpha = i - k + (j + l)(1 - m)/n \ ;$$

$$a = \frac{q_1^{\alpha - 1}}{\left(\frac{\gamma}{\gamma - 1}\beta p_0\right)^{\alpha}} \frac{2\Lambda(\beta p_0)^{(j+l)/n}}{KA^{(j+l)/n}} \frac{v_1^{1+2\alpha}}{\mu^{\alpha}\left(\frac{B_1^2}{8\pi}\right)^{i-k-(j+l)m/n}} \ . \qquad (6.5.22)$$

The solution $z(\xi)$ of the first-order differential equation (6.5.21) should fulfill two boundary conditions:

$$z \to [(\alpha - 1)a\xi]^{-1/(\alpha-1)} \ \text{ at } \ \xi \to 0 \ ; \qquad (6.5.23)$$

$$z(\xi) \to y(\xi) \ \text{ at } \ \xi \to \infty \ , \qquad (6.5.24)$$

so we have a problem of determining the eigenvalue of *a*. Condition (6.5.23) follows from the requirement of smooth transition to the solution in Zone I at $h \to h_0$. Condition (6.5.24) follows from the fact that the cause of initial insulator heating is the heat flux. If we insert the eigenvalue of *a* found after the solution of the problem into equation (6.5.22), we can calculate the velocity v_1.

Let us consider a specific, rather typical case. For PMMA $H_8C_5O_2$, using the values of the constants in formulas (6.5.16–6.5.18) in Section 6.1.3, we obtain $\alpha = 4.08$. The numerical solution of (6.5.21) with boundary conditions (6.5.23) and (6.5.24) yields a ≈ 2, and from (6.5.22),

$$v_1 = \frac{5.5 p_0^{0.061} \mu^{0.541}}{\beta^{0.345}} (B_1^2 / 8\pi)^{0.156} \qquad (6.5.25)$$

(in units of g, cm, and μs).

Note that the dependence of the solution obtained on the path value is very weak (the vapor velocity is $v_1 \sim l^{0.04}$). Therefore, it is natural to expect that the inaccuracy associated with the gray matter assumption will also have a weak effect on the result.

Combined with (6.5.10–6.5.13), formula (6.5.25) gives a correlation between the vapor velocity v_1 and the fraction of current diverted to the discharge (1-1/ h_0) as a function of the magnitude of magnetic field B_0. This particular correlation serves as a boundary condition in the complete MHD problem.

The limiting vaporization regime corresponding to the equality in formula (6.5.14) is represented by the following values of quantities:

$$\begin{aligned} \mu &= 2.12 , \\ \beta &= 0.091 , \\ h_0 &= 1.71 , \\ p_0 &= 3.04 , \\ v_{1\max} &= 17(B_0^2 / 8\pi)^{0.156} , \end{aligned} \qquad (6.5.26)$$

and the limiting power transferred through the insulator surface is equal to

`

The quantity q_1 for the example under consideration in the limiting regime,

$$q_1 = 0.099(B_0^2 / 8\pi)^{0.041},$$

is weakly dependent on B_0, and for $B_0 < 10$ MG it has a magnitude of $q_1 \leq 0.1 << 1$, which verifies our assumption that the radiation energy flux is small.

To illustrate the solution obtained, Fig. 6.20 shows the plots of the major magnetohydrodynamic quantities as a function of optical thickness x ($t^4 \equiv (T / T_1)^4$)) for the limiting regime.

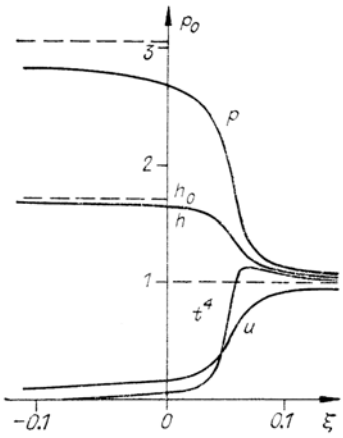

Fig. 6.20. Dimensionless pressure p, magnetic field h, biquadrate of temperature t^4, and velocity u as functions of optical thickness ξ in the limiting regime of the H-thrown discharge.

As the velocity v_1 decreases to a point below the limiting value, the fraction of current shunted to the discharge also decreases. For example, when $v_1 = 0.61 v_{1max}$, the fraction of shunted current becomes equal to $(1 - h_0^{-1}) = 0.11$ ($h_0 = 1.128$, $\mu = 0.31$, $\beta = 0.026$). However, if the boundary velocity of the vapor flow from the insulator in the complete MHD problem exceeds v_{1max}, there will be a rarefaction wave between the insulator and the boundary [6.26], since the vapor velocity near the insulator remains equal to n_{1max}.

E.S. Pavlovsky and V.B. Yakubov also obtained a numerical solution of the problem within the framework of a diffusion approximation in the description of heat transfer. Despite the formal inapplicability of that approximation, the results are rather close to those above. Specifically, the velocity v_{1max} depends on B_0 almost as it does in (6.5.26), and the difference for B_0 = 1 MG is on the order of only ~10%.

The range of applicability of the theory presented is bounded on the side of high magnetic fields by the values of $B \sim 10$ MG (see the footnote above on the insulator pressure). Apart from this, the theory should be applicable to all the cases in which it is possible to describe the equation of state, the path and conductivity of insulator vapor by power formulas (6.5.16–6.5.18) and in which the conditions of stationary vaporization are met. The latter assumes a fairly slow variation of the magnetic field over the time ~ l/v_1, during which insulator particles fly away a distance of about a photon path, such that the intensity of insulator surface irradiation varies slowly as well and corresponds to the intensity of blackbody radiation of vapor $\sigma_{SB} T_1^4$.

The values chosen for $H_8C_5O_2$ in formulas (6.5.16–6.5.18) are oriented to the magnetic fields of $B \sim 0.1 - 1$ MG and the velocity of $v_1 \sim 10^6$–10^7 cm/s in order to theoretically analyze the process of insulator vaporization in magnetic fields stronger than $B \sim 10^4$ G [6.24, 6.25]. Note that although these values of the parameters have not been calculated specifically for the fields of $B \sim 10^4$ G used in the experiments of Keck [6.24], the calculated results for the velocity v_1 and shock velocity in the magnetic shock tube show reasonably good agreement (taking into account the possible pronounced difference of the insulator irradiation intensity from blackbody radiation of the vapor because of small optical thicknesses in Keck [6.24]) with the experimental values in the order of magnitude and yield nearly the same dependence of velocities on the magnetic field: with B changing by an order of magnitude, velocities in the experiments changed by a factor of 2–3.

We also obtained formulas to describe the vaporization of ceramic insulator Al_2O_3 both for the case when the heat flux incident on the insulator surface equals $\sigma_{SB} T_1^4$ and for the case when it is defined from outside (determined by the whole body of plasma and dependent on the system geometry). In the units of g, cm, 10^{-7} s, for the first case:

$$v_1 = 0.611 \frac{p_0^{0.091} \mu^{0.536}}{\beta^{0.294}} B_1^{0.385} ,$$

and for the second case, the velocity

$$v_1 = 0.288 \frac{(\beta p)_0^{0.291} \mu^{0.616}}{Q^{0.424}} B_1^{1.43} \qquad (6.5.27)$$

depends on the flux Q incident on the insulator surface. Along with other formulas, these formulas make it possible, when the values of B_0 and B_1 are known, to also find the pressure p and the density ρ of the vapor flowing out of the discharge (for Al_2O_3, we assume $\gamma = 1.2$).

In Garanin *et al.* [6.27], we performed numerical simulations for experiments involving the acceleration of liners deposited on the surface of cylindrical PMMA $H_8C_5O_2$ and ceramic Al_2O_3 insulators, with account taken of the vaporization of these insulators induced by the radiation flux determined by the whole body of plasma (i.e., using formula (6.5.27) for Al_2O_3 and a similar formula for $H_8C_5O_2$). The range of magnetic fields in these experiments was $B \sim 0.6$ MG, and characteristic velocities were $\sim 5 \cdot 10^6$ cm/s. The simulations and the experiments demonstrated good agreement, and vaporization intensity for the ceramic insulator turned out to be higher than for PMMA in both simulations and experiments.

6.5.2. Discharge Maintained by Electron Thermal Conductivity

The effect of an *H*-thrown discharge can be reduced by attenuating the radiation fluxes, e. g., by changing the installation geometry, using special shields to protect the system from radiation, etc. Even in the absence of radiation, however, if a discharge occurs, it can further be maintained by the electron thermal conductivity of plasma and can result in branching of part of the current from the load and in the entry of the plasma of the insulator material into the load volume. In the absence of radiation flux, the deleterious effect of these processes is weaker. In this sense, discharges maintained by electron thermal conductivity are characterized by minimum values of the shunted current and flow of the insulator material into the load volume.

Here we analyze an *H*-thrown discharge for a ceramic insulator (Al_2O_3) in the range of high magnetic fields (above 0.1 MG) in the absence of radiation. For ionized insulator vapor, the Lorentz plasma approximation is used. The plasma is considered magnetoactive. The effect of magnetization on the thermal and electric conductivity is taken into account. In addition, the Nernst effect is included as well, which, generally speaking, makes a contribution to the heat flux of the same order of magnitude as electron thermal conductivity, and to the electric field, of the same order of magnitude as plasma resistivity.

In this case, the statement of the problem is the same as in the previous section (Fig. 6.19, system of equations (6.5.1–6.5.4)), but the heat flux is determined by the electron thermal conductivity and the Nernst effect, i.e.,

$$Q = -\chi \cdot \frac{dT}{dx} + \frac{b}{e} Tj \qquad (6.5.28)$$

(where χ is the electron thermal conductivity, j is the current density, and the coefficient b/e describes the Nernst effect). The problem allows arbitrary

multiple ionization of the insulator vapor. The presence of the Nernst effect also leads to the necessity of adding a corresponding term to the Ohm's law (6.5.4), which will take the following form:

$$E = \frac{j}{\sigma} + \frac{1}{c} vB - \frac{b}{e}\frac{dT}{dx} \quad . \tag{6.5.29}$$

For magnetoactive plasma:

$$\sigma = \frac{3T^{3/2}}{4\sqrt{2\pi m}e^2 Lz\alpha}$$
$$\chi = \frac{3T^{5/2}\gamma}{4\sqrt{2\pi m}e^4 Lz} \tag{6.5.30}$$

where L is the Coulomb logarithm, z is the root-mean-square ion charge, and the quantities α, b, γ in formulas (6.5.28–6.5.30) correspond to $\alpha_\perp$, β_Λ^{uT}, $\chi_\perp^e$ in Braginskii [6.11] and are calculated using approximate formulas

$$\alpha = 1 - \frac{\alpha_1' y^2 + \alpha_0'}{\Delta}$$
$$b = \frac{y(\beta_1'' y^2 + \beta_0'')}{\Delta} \quad . \tag{6.5.31}$$
$$\gamma = \frac{\gamma_1' y^2 + \gamma_0'}{\Delta}$$
$$\Delta = y^4 + \delta_1 y^2 + \delta_0$$

Here $y = \omega_e\tau_e$ is the degree of electron magnetization, and the coefficients (α_0', α_1', etc.) are chosen for the ion charge $z \to \infty$ by sequentially using the Lorentz plasma approximation, because the temperature in the discharge becomes rather high, as does, consequently, the degree of ionization.

The transport coefficients of a magnetoactive plasma are linked to the corresponding coefficients of a nonmagnetized Lorentz plasma σ_L, χ_L by the

relations $\chi = \frac{\gamma}{\gamma_0}\chi_L = 0.08\gamma\chi_L$ and $\sigma = \frac{\alpha_0}{\alpha}\sigma_L = \frac{3\pi}{32\alpha}\sigma_L$, where α and γ, according to (6.5.31), are determined by plasma magnetization and depend on T, ρ, and B, and α_0, γ_0 α_0, γ_0 are α and γ for zero degree of magnetization y.

By substituting the values of quantities at the inlet (subscript "0") and outlet (subscript "1") of the current sheath into conservation laws (6.5.1–6.5.4), on the basis of the changes made the set of equations defining the problem can be rewritten as

$$\begin{cases} \rho v = \rho_1 v_1 \\ \rho v^2 + p + \frac{B^2}{8\pi} = \rho_1 v_1^2 + p_1 + \frac{B_1^2}{8\pi} = p_0 + \frac{B_0^2}{8\pi} \\ \rho v\left(\frac{v^2}{2} + w\right) + \frac{c}{4\pi}EB - \chi\frac{dT}{dx} - \frac{bc}{4\pi e}T\frac{dB}{dx} = \rho_1 v_1\left(\frac{v_1^2}{2} + w_1\right) + \frac{c}{4\pi}EB_1 = \frac{c}{4\pi}E \\ -\kappa\frac{dB}{dx} + vB = cE + \frac{cb}{e}\frac{dT}{dx} \end{cases} \quad (6.5.32)$$

Assuming the ionized insulator vapor to be a gas with the adiabatic index γT and using an approximate calculation method for the region of multiple ionization (the multiple ionization Saha equation) [6.15] and the formulas for the thermal and electric conductivities of a nonmagnetized Lorentz plasma χ_L and σ_L [6.12], we obtain the interpolation formulas $p \sim T^m\rho^n$, $\chi_L \sim T^{l+i}\rho^j$, and $\kappa_L \sim T^{-i}\rho^{-j}$ and the effective adiabatic index in a certain interval of temperatures and densities for a specific type of insulator. We will use the units g, cm, and μs, MG for the magnetic field, and eV for the temperature. For the ceramic insulator (Al_2O_3) in the temperature range of 3–30 eV and in the density range of 10^{-5} – 10^{-3} g/cm^3, we obtained the following approximate formulas:

$$p(T,\rho) = 3.8\cdot 10^{-2}T^m\rho^n m = 1.417,\ n = 0.917$$
$$\chi_L(T,\rho) = 1.84\cdot 10^{-8}T^{1+i}\rho^j i = 0.825,\ j = 0.158$$
$$\kappa_L(T,\rho) = \frac{c^2}{4\pi\sigma_L(T,\rho)} = 0.173\cdot T^{-i}\rho^{-j}$$
$$\gamma_T = 1.2$$

The values of the quantities calculated using these formulas for the given temperature and density ranges, differ from those calculated using the Saha equation [6.15] and the refined Coulomb logarithm (Section 3.2.3) by no more than 5%.

In accordance with our method of solving such problems, the measurement units for the temperature [T] and density [ρ], which define the characteristic quantities of the problem, are found from the condition of equality of the magnetic diffusivity κ and the thermal diffusivity, $\kappa = (\gamma_T - 1)\,\chi_L\, T/\gamma_T p$ (assuming that the characteristic plasma magnetization $y \sim 1$, which follows from the equality of the magnetic diffusivity and the thermal diffusivity; for definiteness of the choice of measurement units, we will equate the values of the magnetic diffusivity and the thermal diffusivity for $y = 0$) and from the condition of equality of the thermal pressure to magnetic pressure (for definiteness, as a unit of measurement for pressure we will use the magnetic pressure at the outlet of the discharge region):

$$\begin{aligned} [p] &= p([T],[\rho]) = \frac{B_1^2}{8\pi} \\ \kappa_L([T],[\rho]) &= \kappa_{TL}([T],[\rho]) \end{aligned} .$$

Solving these two equations yields

$$\begin{aligned} [T] &= 101 \cdot B_1^{0.415} \\ [\rho] &= 8.37 \cdot 10^{-4} \cdot B_1^{1.54} \end{aligned} . \qquad (6.5.33)$$

We introduce dimensionless variables

$$\begin{aligned} t = \frac{T}{[T]},\ r = \frac{\rho}{[\rho]},\ u = \frac{v}{v_1},\ h = \frac{B}{B_1}, \\ p = \frac{p}{[p]} = \frac{p}{B_1^2/8\pi} = t^m r^n,\ \xi = \frac{x}{[x]}, \end{aligned} \qquad (6.5.34)$$

where [x] is found from the relation $[x] = \dfrac{\kappa_L([T],[\rho])}{v_1}$, which, in view of (6.5.33), yields

$$[x] = 1.71 \cdot 10^{-3} \sqrt{\frac{r_1}{\mu}} B_1^{-0.816} . \qquad (6.5.35)$$

We introduce the same dimensionless parameters as in Section 6.5.1

$$\beta = \frac{p_1}{B_1^2/8\pi}, \quad \mu = \frac{\rho_1 v_1^2}{B_1^2/8\pi} \qquad (6.5.36).$$

and the constant $g = 2\dfrac{\gamma_T}{\gamma_T - 1}$ and we proceed to consideration of the system (6.5.32). We substitute the relations $cE = v_1 B_1$ and $w = \gamma_T p/(\gamma_T - 1)\rho$ into the third and fourth equations and divide the first equation by $v_1[\rho]$, the second by $B_1^2/8\pi$, the third by $v_1 B_1^2/16\pi$, and the fourth by $v_1 B_1$. From the first equation, we obtain the relationship between the dimensionless density and velocity $r = r_1/u$. Substituting it into the other three equations (6.5.32), we arrive at the system

$$\begin{cases} \mu u + r_1^n t^m u^{-n} + h^2 = \mu + \beta + 1 \\ \mu u^2 + g r_1^n t^m u^{1-n} + 4h - 0.08\gamma g r_1^j t^{1+i} u^{-j} \dfrac{dt}{d\xi} - \sqrt{g} bt \dfrac{dh}{d\xi} = \mu + 4 + g\beta \\ -\dfrac{32\alpha}{3\pi} r_1^{-j} t^{-i} u^j \dfrac{dh}{d\xi} + uh = 1 + \dfrac{b\sqrt{g}}{4} \dfrac{dt}{d\xi} \end{cases} . \qquad (6.5.37)$$

Here, t, u, and h are unknown functions of the variable ξ, and μ, β, and r_1 are the parameters. From the first and the second equations in the system (6.5.37), setting $u = 0$ and disregarding the derivatives, we obtain the following expressions for the magnetic field and pressure in the insulator

$$\begin{aligned} h_0 &= \frac{1}{4}(\mu + 4 + g\beta) \\ p_0 &= \mu + \beta + 1 - h_0^2 \end{aligned} .$$

Using the chosen units of measurement, one can express the degree of magnetization of the insulator material plasma as

$$y = \omega_e \tau_e = \frac{3\pi}{32\sqrt{2}} \sqrt{\frac{\gamma_T}{\gamma_T - 1}} \left(1 + \frac{1}{z}\right) \cdot r_1^{j-n} t^{1+i-m} u^{n-j} h \ . \qquad (6.5.38)$$

Since we use the Lorentz plasma approximation, considering z large enough, we obtain for $\gamma_T = 1.2$

$$\omega_e \tau_e = 0.51 \cdot r_1^{j-n} t^{1+i-m} u^{n-j} h \quad .$$

Using the dimensionless variables, original equations (6.5.37) can be converted to the set of equations of the type

$$\begin{cases} a_1 \dfrac{dt}{d\xi} + b_1 \dfrac{du}{d\xi} = c_1 \\ a_2 \dfrac{dt}{d\xi} + b_2 \dfrac{du}{d\xi} = c_2 \end{cases} . \qquad (6.5.39)$$

Here, t and u are functions of the variable ξ, the coefficients a_1, a_2, b_1, c_1, and c_2 depend on t and u, and μ, β, and r_1 are the parameters.

To solve the problem, one must integrate equations (6.5.39) with the boundary conditions $u(0) \equiv u_0 = 0$, $t(0) \equiv t_0 = 0$, $u(\infty) \equiv u_1 = 1$, $t(\infty) \equiv t_1 = (\beta r_1^n)^{1/m}$ and three free parameters μ, β, and r_1.

The initial and terminal points are singular, and to come out of them, we used expansions in powers of ξ. The coming out of the terminal point was defined uniquely by the parameters and boundary conditions, and the coming out of the initial point contained an arbitrariness associated with the probability of a nonzero heat flux coming out from the discharge zone into the insulator.

The expansion near the initial point corresponds to the primary plasma heating via electron thermal conductivity (i.e., the Joule heat release in this region is small by comparison with the heating due to thermal conduction, and the heat flux at the discharge region boundary is equal to zero), and in the vicinity of the initial point, the plasma is not magnetized.

The expansion near the terminal point is determined by the exponential character of the MHD quantities' movement to their final values.

For the given discharge mode, which can be characterized by one parameter, for example, μ, it was necessary in solving the equations to select the two other parameters (β, r_1) in such a way as to obtain a solution with the given boundary conditions. In this case, it turned out to be necessary to pass through a singular point at which the flow velocity

becomes equal to the thermal sound velocity $v^2 = \gamma \frac{p}{\rho}$. By varying one parameter, one can manage to arrive at this singular point after coming out from the initial point by the specified expansion; by varying the other parameter, one can arrive at the same singular point coming out from the terminal point. As a result of the solution, for each μ we obtain particular values of β and r_1, i.e., the functions $\beta(\mu)$ and $r_1(\mu)$ characterizing different discharge modes.

Fig. 6.21 shows the structure of the current zone, i.e., the plots of the dimensionless MHD quantities as a function of the coordinate x at $\mu = 2$. Fig. 6.22 shows plots of $\beta(\mu)$ and $r_1(\mu)$.

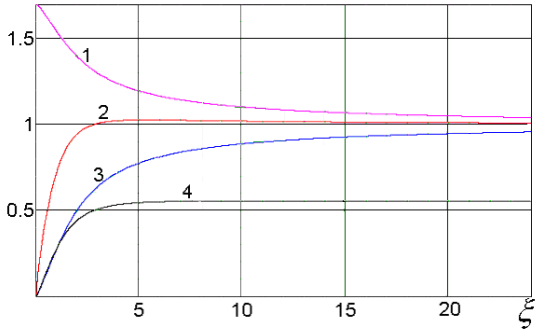

Fig. 6.21. Spatial distributions of the dimensionless MHD quantities for μ =2. 1) magnetic field h(ξ), 2) temperature t(ξ)/t1, 3) velocity u(ξ) u(ξ), 4) degree of magnetization y(ξ).

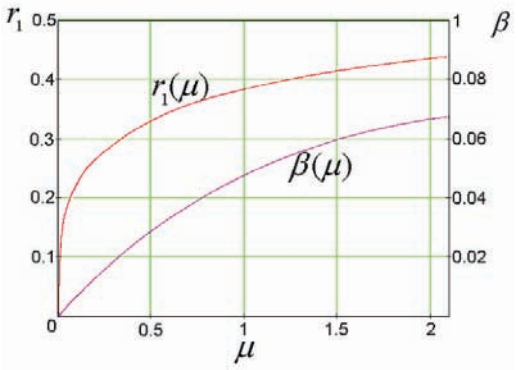

Fig. 6.22. Plots of the functions β(u) and r1(μ).

For the limiting insulator vaporization regime, the limitation (6.5.14)

$$\mu \le \mu_{\max} \equiv 2 + \gamma_T \beta$$

is satisfied by the calculated values $\mu_{\max} = 2.08$, $\beta_{\max} = 0.0675$, and $r_{1\max} = 0.439$.

The calculated values of the parameters μ, β, and r_1 and the corresponding values of dimensionless h_0 are given in Table 6.2. Table 6.3 presents the values of the magnetic field B_1, velocity v_1, density ρ_1 and temperature T_1 at the outlet of the discharge, as well as of the electric field E in kV/cm, all calculated in accordance with (6.5.33–6.5.34 and 6.5.36) using the formulas

$$\begin{aligned} B_1 &= \frac{B_0}{h_0} \\ T_1 &= t_1\left[T\right] = 101 \cdot \beta^{0.706} r_1^{-0.647} h_0^{-0.415} B_0^{0.415} \\ \rho_1 &= 8.37 \cdot 10^{-4} \cdot r_1 h_0^{-1.54} B_0^{1.54} \\ v_1 &= \sqrt{\frac{\mu B_1^2}{8\pi\rho_1}} = 6.9 \cdot \left(\frac{\mu}{r_1}\right)^{0.5} h_0^{-0.23} B_0^{0.23} \\ E &= \frac{v_1}{c} B_1 = 69 \cdot \left(\frac{\mu}{r_1}\right)^{0.5} h_0^{-1.23} B_0^{1.23} \end{aligned} \qquad (6.5.40)$$

for a magnetic field in the insulator $B_0 = 1$ MG.

Table 6.2. Dimensionless discharge parameters.

μ	β	r_1	h_1
0.01	0.00070	0.117	1.0046
0.1	0.0068	0.222	1.045
0.2	0.0130	0.265	1.089
0.5	0.0288	0.331	1.211
1	0.0477	0.384	1.393
1.5	0.0597	0.415	1.554
2	0.0668	0.436	1.700
2.08	0.0675	0.439	1.722

Table 6.3. The dependence of the major MHD parameters on discharge intensity for a magnetic field in the insulator B_0 = 1 MG.

μ	B_1, MG	v_1, $\frac{km}{s}$	ρ_1, $10^{-4}\frac{g}{cm^3}$	T, eV	E, $\frac{kV}{cm}$
0.01	0.995	20	0.98	2.4	20.0
0.1	0.957	46	1.73	7.8	43.9
0.2	0.918	59	1.94	10.8	53.9
0.5	0.826	81	2.06	15.7	67.0
1	0.718	103	1.93	19.2	74.1
1.5	0.643	118	1.76	20.4	76.2
2	0.588	131	1.61	20.6	76.9
2.08	0.581	132	1.59	20.5	76.9

Using formulas (6.5.40), one can suggest the following method for calculating the *H*-thrown discharge. From the formula for the electric field in (6.5.40), based on the initial fields *E* and *B* and using Table 6.3, we find the parameter μ. Next, using the known μ we recover β, r_1, and h_1 by means of Fig. 6.22. Then, using the remaining formulas of (6.5.40), we obtain all plasma parameters at the outlet of the *H*-thrown discharge zone in the absence of radiation flux. These parameters can be specified as the boundary conditions in full MHD simulations of particular assemblies and facilities.

It is worthwhile to compare the modes of an *H*-thrown discharge due to plasma radiation (radiation-maintained discharge, RMD) and the discharge maintained by electron thermal conductivity (electron-thermal-conductivity–maintained discharge, ETCMD). Figs. 6.23 and 6.24 show the plots of the mass flux and the fraction of the current shunted off to the discharge ($\delta I = 1 - \frac{1}{h_0}$) versus electric field for B_0 = 1 MG (the solid lines are the results of the ETCMD calculations including all essential effects; and the dashed lines are the results of the RMD calculations). The ETCMD case yields current branching that is one-tenth and mass flux that is one-fifteenth that of the radiation case for the field *E* corresponding to the limiting insulator vaporization mode (and maximum current diversion) in the RMD (radiative) case for B_0 = 1 MG. For *E* corresponding to $\delta I \approx 10\,\%$ in the radiative problem, the current branching for the ETCMD case is one-third that of the radiative case, and the mass flux is one-fourth. Thus, even for a discharge occurring on the surface, its adverse effect is smaller in the absence of radiation incident on the insulator surface (for example, if the insulator is shielded from radiation).

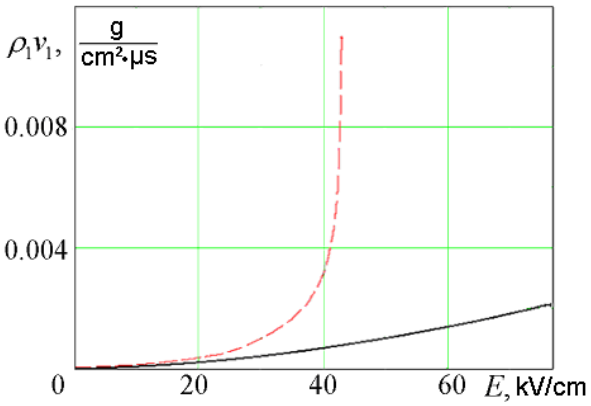

Fig. 6.23. Mass flux $\rho_1 v_1$ at the outlet of the discharge zone versus electric field E.

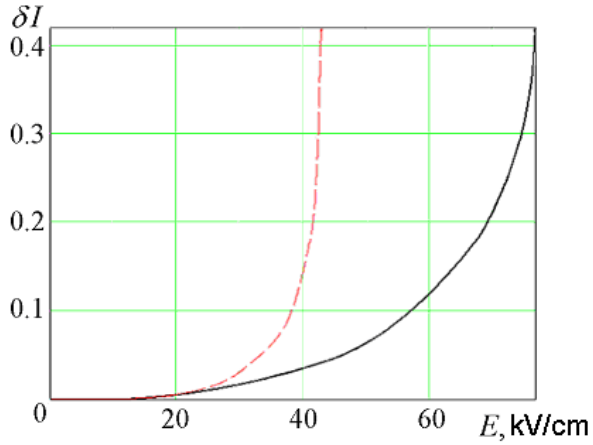

Fig. 6.24. Fraction of the current shunted off to the discharge δI versus electric field E.

CONCLUSION

We considered a plane problem for a stationary surface discharge that arises when a magnetic flux emerges through an insulator surface in strong magnetic fields. The discharge takes place via the insulator vapor, and part of the released Joule heat is transferred by radiation or thermal conductivity to the insulator and causes its evaporation. Essentially, obtaining a relationship between the quantities at the inlet and outlet of the discharge region requires more than using just the integral conservation laws; one must also solve the problem of the region's structure. To solve this problem, we consider a set of stationary MHD equations and account for heat transfer.

If the heat flux is determined by the radiative transfer, the radiation flux turns out to be small by comparison with the Joule heat and the material's energy flux. Using this circumstance and the assumption of gray matter and a power form of the equation of state, as well as of radiation path and conductivity dependent on temperature and density, we can solve the discharge problem analytically. We found the dependence of the velocity of the plasma flow from the discharge, as well as of plasma density and temperature, on the magnitude of magnetic fields in the nonvaporized insulator and at the outlet of the current sheath. It is shown that there is a limiting insulator vaporization mode in which the velocity of the plasma flow from the discharge reaches its maximum possible value. The velocity corresponding to the limiting vaporization mode is (for PMMA)

$$v_{1\max} = 17(B_0^2 / 8\pi)^{0.156},$$

(in the units of g, cm, μs), the fraction of current shunted to the discharge is $\alpha = 0.42$, and the limiting power transferred through the insulator surface is

$$v_1 B_1 B_0 / 4\pi = 20(B_0^2 / 8\pi)^{1.156} \quad .$$

The steady-state discharge conditions, when the magnetic field passes through the insulator surface, also exist if the discharge is maintained by electron thermal conductivity, subject to the involvement of all relevant effects, including plasma magnetization and Nernst effect.

If the insulator surface is protected from radiation, for the same magnitude of the electric field (e.g., for the same velocity of liner acceleration), the *H*-thrown discharge produces a much smaller adverse effect. In particular, the mass flux of the insulator material to the load volume is reduced by up to a factor of 15 by comparison with the radiation maintained discharge, and the branching of the current is reduced by up to a factor of 10, depending on the vaporization conditions (the higher the vaporization rate, the greater the differences).

The discharge characteristics obtained can be used as boundary conditions in calculations of different units, in which the magnetic flux is transferred through the insulator surface. If the radiation flux is unknown, the results obtained for the electron-thermal-conductivity–maintained discharge can be used to estimate the minimum discharge parameters.

The influence of the *H*-thrown discharge on the performance of physical facilities can be illustrated by MAGO experiments, in which the flow of a large amount of *H*-thrown discharge-vaporized insulator resulted in strong long-period magnetic field oscillations (Fig. 2.3) measured by B-dot probes in the chamber.

REFERENCES

6.1 S.F. Garanin, G.G. Ivanova, D.V. Karmishin, V.N. Sofronov. "Diffusion of a Megagauss Gield into a Metal," *PMTF* [J. Appl. Mech. Tech. Phys.], Vol. 46, No. 2, pp. 153–159, 2005.

6.2 G.E. Vekstein. "Magnetic and Thermal Processes in a Dense Plasma," *Voprosy Teorii Plazmy: Sb. Statey* (Reviews of Plasma Physics: *Collection of Papers*). Ed. B. B. Kadomtsev. Moscow: Energoatomizdat [Publishing House], No. 15, pp. 3–54, 1987. Consultants Bureau, New York, Issue 15, p. 153, 1990.

6.3 S.F. Garanin, V.I. Mamyshev. "Cooling of a Magnetized Plasma at the Boundary with an Exploding Metal Wall," *PMTF*, [J. Appl. Mech. Tech. Phys.], No. 1, pp. 30–37, 1990. Vol. 31, No. 1, pp. 28–34, 1990.

6.4 S.F. Garanin, S.D. Kuznetsov, V.B. Yakubov. "Expansion of Magnetized Fluid into Vacuum," *4th Zababakhin Scientific Talks*, Snezhinsk, Russia, pp. 280–286, 1995.

6.5 S.F. Garanin, E.S. Pavlovsky, V.B. Yakubov. "Stationary Discharge Accompanying Emergence of the Magnetic Flux Through the Surface of an Insulator," *PMTF*, [J. Appl. Mech. Tech. Phys.], Vol. 25, No. 2, pp. 171–176, 1984.

6.6 S.F. Garanin, D.V. Karmishin. "Stationary Discharge Sustained by Electron Thermal Conduction for Emergence of a Magnetic Flux Through an Insulator Surface." *PMTF*, [J. Appl. Mech. Tech. Phys.], No. 1, pp. 9–15, 1984. Vol. 45, No. 5, pp. 639–646, 2004.

6.7 G.E. Vekshtein. "Magnetic Flux Losses During the Formation of Reverse-Field Plasma Configuration," *DAN SSSR* [Sov. Phys. Dokl.], Vol. 247, No. 1, pp. 83–86, 1979.

6.8 S.F. Garanin. "Diffusion of a Strong Magnetic Field into a Dense Plasma," *PMTF*, [J. Appl. Mech. Tech. Phys.], No. 3, pp. 8–14, 1985. Vol. 26, No. 3, pp. 308–312, 1985.

6.9 G.E. Vekshtein. "Magnetic Field Evolution and Anomalous Heat Losses in a Dense Plasma," *ZhETF* [J. Exp. Theor. Phys.], Vol. 84, No. 2, pp. 549–563, 1983.

6.10 S.F. Garanin. "Discharge Arising with Magnetic Flux Outflow From Plasma to Insulator," *PMTF*, [J. Appl. Mech. Tech. Phys.], No. 6, pp. 13–16, 1987. Vol. 28, No. 6, pp. 816–819, 1987.

6.11 S.I. Braginskii. "Transport Processes in a Plasma," *Voprosy Teorii Plazmy: Sb. Statey* (Reviews of Plasma Physics: Collection of Papers). Ed. M.A. Leontovich. Moscow: Atomizdat [Publishing House], No. 1, pp. 183–272, 1963. Consultants Bureau, New York, Vol. 1, p. 205, 1965.

6.12 E.M. Lifshits, L.P. Pitaevsky. *Fizicheskaya Kinetika* [Physical Kinetics]. Moscow: Nauka, 1979. Pergamon, Oxford, 1980.

6.13 V.I. Kogan. "On the Role of Impurity Emissions in the Energy Balance of a Plasma Filament)," *DAN SSSR*, [Sov. Phys. Dokl.], Vol. 128, No. 4, 1959.

6.14 D.E. Post, R.V. Jensen, C.B. Tarter, W.H. Grassberger, W.A. Lokke. "Steady-State Radiative Cooling Rates for Low-Density, High-Temperature Plasmas," *Atom. Data and Nucl. Data Tables*, Vol. 20, No. 5, pp. 397–439, 1977.

6.15 Ya.B. Zeldovich, Yu.P. Raizer. *Fizika Udarnykh Voln I Vysokotemperaturnykh Gidrodinamicheskikh Yavleniy* [Physics of Shock Waves and High-Temperature Hydrodynamic Phenomena]. Moscow: Nauka, 1966. Vol. 1. Academic Press, New York, 1966.

6.16 S.A. Sorokin. "Generation of a Strong Magnetic Field Inside a Dielectric Tube," *ZhTF* [J. Tech. Phys.), Vol. 79, No. 6, pp. 43–47, 2009.

6.17 V.P. Silin. *Vvedeniye V Kineticheskuyu Teoriyu Gazov* (Introduction to the Kinetic Theory of Gases). Moscow: Nauka, 1971.

6.18 H. Knoepfel. *Pulsed High Magnetic Fields*. Moscow: Mir, 1972. North-Holland, Amsterdam, 1970.

6.19 S. Fuelling, T.J. Awe, B.S. Bauer, T. Goodrich, A. Haboub, V.V. Ivanov, V. Makhin, A. Oxner, R. Presura, R.E. Siemon. "A Zebra Experiment to Study Plasma Formation by Megagauss Fields," *IEEE Trans. Plasma Sci.,* Vol. 36, Pt. I, No. 1, pp. 62–69, Feb. 2008.

6.20 T.J. Awe, B.S. Bauer, S. Fuelling, R.E. Siemon. "Threshold for Thermal Ionization of an Aluminum Surface by Pulsed Megagauss Magnetic Field," *Phys. Rev. Lett.*, Vol. 104, No. 3, p. 035001, Jan. 2010.

6.21 S.F. Garanin, S.D. Kuznetsov, W.L. Atchison, R.E. Reinovsky, T.J. Awe, B.S. Bauer, S. Fuelling, I.R. Lindemuth, R.E. Siemon. "Numerical Simulations of Thick-Aluminum-Wire Behavior Under Megaampere-Current Drive," *IEEE Trans. Plasma Sci.*, Vol. 38, No. 8, Pt. I, pp. 1815–1821, 2010.

6.22 E.M. Epperlein, M.G. Haines. “Plasma Transport Coefficients in a Magnetic Field by Direct Numerical Solution of the Fokker-Planck Equation,” *Phys. Fluids*, Vol. 29, No. 4, 1986.

6.23 P.J. Turchi, N.F. Roderick, J.H. Degnan, M.H. Frese, D.J. Amdahl. “Preparation and Liner Compression of Plasma from an Ultrahigh Speed Flow,” *IEEE Trans. Plasma Sci.*, Vol. 36, Pt. I, No. 1, pp. 92-103, Feb. 2008.

6.24 J. Keck. “Current Speed in a Magnetic Annular Shock Tube,” *Phys. Fluids*, Vol. 7, No. 11, Pt. 2, pp. 5-16–5-27, 1964.

6.25 J.B. Workman. “Insulator Ablation in a Magnetic Piston Shock Tube,” *Phys. Fluids*, Vol. 8, No. 12, p. 2162, 1965.

6.26 L.D. Landau, E.M. Lifshitz. *Gidrodinamika* [Fluid Dynamics]. Moscow: Nauka, 1986. Fluid Mechanics, 2nd Ed. Addison-Wesley Publishing Co., Reading, MA, 1987.

6.27 S.F. Garanin, V.A. Demidov, A.N. Demin, V.I. Mamyshev, V.K. Chernyshev, V.A. Shevtsov. "Study of Ponderomotive Systems on Models," in *Megagauss Fields and Pulsed Power Systems,* Ed. V. M. Titov and G. A. Shvetsov, New York: Nova Science Publishers, pp. 713–717, 1990.

7. MAGNETOHYDRODYNAMIC (MHD) INSTABILITIES AND THEIR EFFECT ON PLASMA AND ITS COMPRESSION

As a rule, the magnetohydrodynamic (MHD) plasma flows in the MAGO-MTF systems are unstable. In order to analyze and understand the process of the development of these instabilities, we need to study their linear stage, which determines the conditions of their growth and the increments of the growth, the patterns of their development in the nonlinear stage, and, finally, the properties of the occurring turbulent flows and their effect on the system's operation. We will study MHD instabilities in that order in this chapter.

7.1. Linear-Theory Instability Development

The problem of a tangential discontinuity instability in a cold plasma with a magnetic field perpendicular to the velocity jump and the problem of a convective instability in an azimuthal field in the presence of acceleration, including problems of Rayleigh-Taylor and "sausage" instabilities in an azimuthal magnetic field as examples of limiting cases, will be evaluated as important problems in the study of the linear stage of development of MHD instabilities.

7.1.1. Instability of the Tangential Discontinuity in Cold Plasma with a Magnetic Field Perpendicular to the Velocity Jump

Landau [7.1] found that for sufficiently high velocity v, the tangential discontinuity in a compressible gas can be stable with respect to oscillations of the discontinuity surface with the wave vector $\vec{q}$ parallel to the velocity jump $\vec{v}$. Syrovatskiy [7.2] indicated that, in this case, the discontinuity remains unstable relative to oscillations with wave vectors directed at an angle to the velocity jump and satisfying the condition:

$$v\cos\phi<(c_1^{2/3}+c_2^{2/3})^{3/2}\ , \qquad (7.1.1)$$

where φ is the angle between $\vec{q}$ and $\vec{v}$, and c_1 and c_2 are the sound speeds on both sides of the discontinuity.

There is a broad class of MHD flows in which the magnetic field $\vec{B}$ is perpendicular to the velocity: Z- and Θ-pinches, plasma accelerators, explosive-magnetic generators, etc. For such flows, it is of interest to analyze the stability of tangential discontinuities. In this analysis, the case $\phi = 0$ (motion in a plane perpendicular to the magnetic field) is reduced to the hydrodynamic (HD) case, and the stability condition (7.1.1) holds for

sufficiently high velocities of the discontinuity. But the case in which $\vec{q}$ has a component along $\vec{B}$ can be stabilized as a result of the tension of the magnetic field lines. Thus, we can expect that such tangential discontinuities with high velocities can be stable or that the instabilities in them will develop more slowly than in the case of the HD discontinuities.

The case of a cold plasma with $\beta << 1$ (β is the ratio of plasma pressure to magnetic pressure) is of particular interest, because, for a plasma with $\beta >> 1$, the force effect of the magnetic field is not high and can be disregarded in the first approximation when the instability is considered. In that approximation, the discontinuity will be unstable for any velocities, just as it is in conventional HD. The case of an incompressible fluid (i.e., $\beta >> 1$, $c >> v$), considered for magnetic fields arbitrarily directed along both sides of the discontinuity [7.3], in the situation of interest to us, $\vec{B} \perp \vec{v}$, to be sure, yields an instability. Note that in the case of plasma motion along the magnetic field, the instability occurs at high velocities [7.3, 7.4].

Gonzales and Gratton [7.5] studied the stability of a tangential discontinuity for an arbitrary relative orientation of the vectors $\vec{B}$ and $\vec{v}$ and a continuous plasma density at the discontinuity. In this Section, we follow Garanin and Kuznetsov [7.6] and use a different method to analyze the instability. In the case of interest to us — $\vec{B} \perp \vec{v}$ and discontinuous plasma density—we obtained a relatively simple dispersion relation that allows us to prove that, a tangential discontinuity in this configuration is unstable for any velocity and to analyze the behavior of the growth rates.

Dispersion Equation

We choose the configuration with the magnetic field $\vec{B}_0$ aligned with the zaxis and parallel to the discontinuity plane $y = 0$ as the initial stationary solution. We assume that, for $y < 0$, medium 1 is immobile, and, for $y > 0$, medium 2 moves with velocity $\vec{v} \| x$ (Fig. 7.1). The equation for small oscillations of an immobile, ideally conducting cold plasma ($\beta = 0$) is written as follows [7.7]

$$\frac{\partial^2 \vec{\xi}}{\partial t^2} = c^2 \nabla_\perp \mathrm{div} \vec{\xi}_\perp + c^2 \frac{\partial^2 \vec{\xi}_\perp}{\partial z^2} , \qquad (7.1.2)$$

where $\vec{\xi}$ is the displacement of the plasma particles, $\nabla_\perp$ and $\vec{\xi}_\perp$ are the transverse components (with respect to $\vec{B}_0$) of the gradient operator and

displacement, respectively, and $c = \dfrac{B_0}{\sqrt{4\pi\rho}}$ is the Alfven velocity. The densities of media 1 and 2 are assumed to be different, ρ_1 and ρ_2, and, consequently, the velocities c_1 and c_2 in these media are also different. The transition from the plasma rest frame to the frame where the plasma moves with the velocity $\vec{v}$ is performed by the substitution of $\dfrac{\partial}{\partial t} \to \dfrac{\partial}{\partial t} + \vec{v}\nabla$.

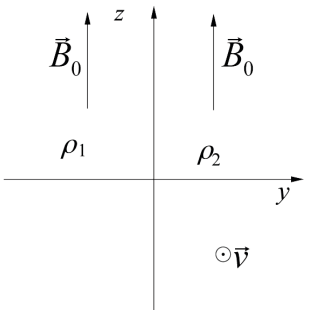

Fig. 7.1. Geometry of the problem.

The perturbation of the discontinuity surface is presented in the form

$$\exp(i\vec{q}\vec{r}) \ , \tag{7.1.3}$$

and the dependence of all quantities on the *y* coordinate and time is searched as

$$\exp(-i\omega t + i\kappa_{1,2} y) \ , \tag{7.1.4}$$

where κ_1 and κ_2 correspond to media 1 and 2, respectively.

We substitute dependences (7.1.3) and (7.1.4) into (7.1.2) to obtain

$$\omega^2 = c_2^2(q^2 + \kappa_2^2) \tag{7.1.5}$$

for medium 2 and

$$(\omega - \vec{v}\vec{q})^2 = c_1^2(q^2 + \kappa_1^2) \tag{7.1.6}$$

for medium 1 with allowance made for its motion.

The displacements ξ_y at the interface between these two media should obviously equal each other,

$$\xi_{y1}(y=0) = \xi_{y2}(y=0) \equiv \xi_y \ .$$

We can find one additional relationship between the displacements $\vec{\xi}$ of the interface, taking into account the fact that the magnetic-field pressures at the boundary are equal, $B_1^2 = B_2^2$ and expressing the magnetic field perturbation $\vec{B}'$ via $\vec{\xi}$ [7.6],

$$\vec{B}' = -\vec{B}_0 \mathrm{div}\vec{\xi}_\perp + B_0 \frac{\partial \vec{\xi}_\perp}{\partial z} ,$$

to obtain

$$q_x \xi_{x1} + \kappa_1 \xi_y = q_x \xi_{x2} + \kappa_2 \xi_y . \qquad (7.1.7)$$

for $y = 0$.

Relationships (7.1.5–7.1.7) and equation (7.1.2) yield the dispersion relation

$$\frac{(x^2 - c_2^2 \sin^2\phi)}{c_2^2 (x^2 - c_2^2)} = \frac{[(x - v\cos\phi)^2 - c_1^2 \sin^2\phi]}{c_1^2 [(x - v\cos\phi)^2 - c_1^2]} , \qquad (7.1.8)$$

where $x = \omega / q$. The obtained equation differs from HD [7.2] only by the fact that in the HD we have 0 instead of $\sin\phi$.

Both sides of the relation (7.1.8) coincide if $\left(\frac{x}{c_2}\right)^2 = \left(\frac{x - v\cos\phi}{c_1}\right)^2$.

Consequently, two of the six roots of (7.1.8) are known (these roots are real and do not lead to instability), and thus we can reduce the order of the equation. As a result, we obtain the following fourth-order equation with respect to x:

$$\frac{(x - v\cos\phi)^2 x^2}{c_1^2 c_2^2} = \frac{x^2}{c_2^2} + \frac{(x - v\cos\phi)^2}{c_1^2} - 1 + \cos^4\phi . \qquad (7.1.9)$$

The HD equation [7.2] again differs from (7.1.9) only by the fact that there should be 0 instead of $\cos^4\phi - 1$ on the right hand side.

Instability of the Tangential Discontinuity

For the velocities

$$v < (c_1^{2/3} + c_2^{2/3})^{3/2}$$

the case $\phi = 0$ (which is reduced to the HD case), will, as in hydrodynamics, result in instability. Therefore, to analyze whether the flow is stable, it is sufficient to consider only the following velocity range:

$$v > (c_1^{2/3} + c_2^{2/3})^{3/2} \quad . \tag{7.1.10}$$

To prove that the flow is unstable, it is sufficient to find just one angle φ, for which the flow is unstable. However, for (7.1.10), the velocity meets the condition

$$v > c_1 + c_2 \quad ,$$

and we can find the angle φ, for which

$$v\cos\phi = c_1 + c_2 \quad .$$

For this angle φ, the real roots of the equation (7.1.9) rewritten in the form:

$$\frac{(x - c_1 - c_2)^2}{c_1^2} = 1 + \frac{\cos^4\phi}{\frac{x^2}{c_2^2} - 1} \quad .$$

are determined by the points of intersection of the curves assigned by the left- and the right-hand sides of this equation (see Fig. 7.2). Fig. 7.2 shows that, in this case, there are only two real roots. Consequently, the other two roots are complex conjugate and, therefore one of them corresponds to the instability.

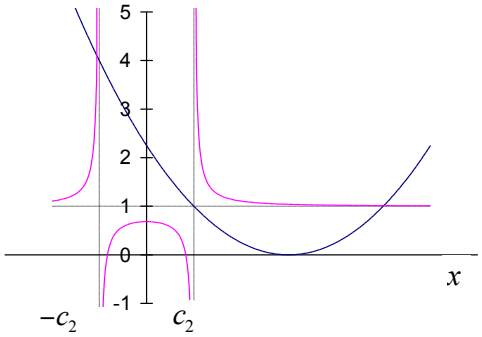

Fig. 7.2. Curves whose points of intersection determine the real roots of the dispersion equation for $v\cos\varphi = c_1 + c_2$.

Instability Increments and Domain

Although the MHD tangential discontinuity turns out to be unstable at any velocity (as in the HD case), it is of interest to consider the effect of the magnetic field on the instability increments and to compare them with the HD increments.

Below, for brevity, we will call $\gamma = \mathrm{Im}x$ as the "increment" (in fact, the increment equals $q\mathrm{IM}x$, i.e., it is proportional to the wave vector).

For definiteness, we assume that $c_1 > c_2$ and move to the dimensionless quantities by designating $u = \frac{v}{c_2}$, $c = \frac{c_1}{c_2}$, $x = \frac{x}{c_2}$, and $\gamma = \frac{\gamma}{c_2}$.

First, we consider the behavior of the increments in the case of identical media, $c = 1$. In this case, in the low velocity range, the analysis of the equation (7.1.9) shows that, for $u < \sqrt{3}$, the HD and MHD discontinuities yield the maximum increment at $\varphi = 0$, which is equal to

$$\gamma_{\max} = \sqrt{\sqrt{1+u^2} - 1 - \frac{u^2}{4}} \ . \qquad (7.1.11)$$

For $u > \sqrt{3}$ in the HD case, the increment is maximum when $\cos\phi = \frac{\sqrt{3}}{u}$ and remains equal to

$$\gamma_{max} = 0.5 \ . \qquad (7.1.12)$$

In the case of MHD, for velocities $u_0 > u > \sqrt{3}$ (where the velocity u_0 is determined such that

$$\cos^2\phi = \frac{u^2}{2}\left(\frac{1}{\sqrt{1-16/u^2}} - 1\right) \qquad (7.1.13)$$

is equal to unity), the maximum increment remains equal to (7.1.11), and, for $u > u_0$, it corresponds to the angle φ, determined from (7.1.13) and is equal to

$$\gamma_{max} = \sqrt{\frac{u^4}{8} - 1 - \frac{u^4}{8}\sqrt{1 - \frac{16}{u^4}}} \ .$$

The dependences of the maximum increments on the velocity for HD and MHD discontinuities for $c = 1$ are shown in Fig. 7.3a. For this case, Fig. 7.4a shows the domains of the angles corresponding to the instability as functions of u. The curves presented were obtained by solving equation (7.1.9) and the equation for conventional HD. Along with the instability boundaries, Fig. 7.4a shows the dependence $\varphi(u)$ corresponding to the maximum increment. From Figs. 7.3a and 7.4a, we can see that for high velocities in the MHD, the maximum increments and the instability domain are substantially smaller than those in the HD case, and we can expect these MHD discontinuities to spread into the turbulent areas considerably slower than HD discontinuities.

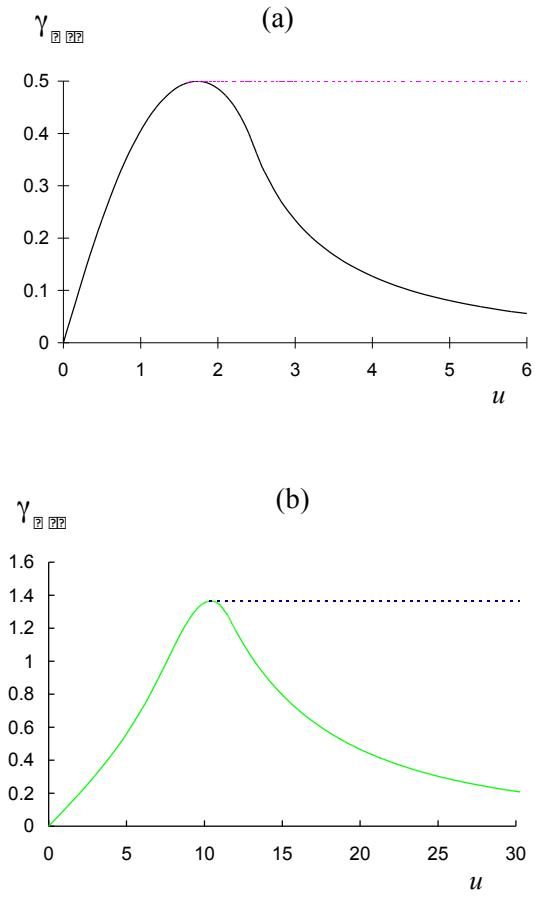

Fig. 7.3. Maximum increment versus the velocity in MHD (solid curves) and conventional HD (dashed lines) for (a) $c_1 = c_2$ and (b) $c_1 = c_2$.

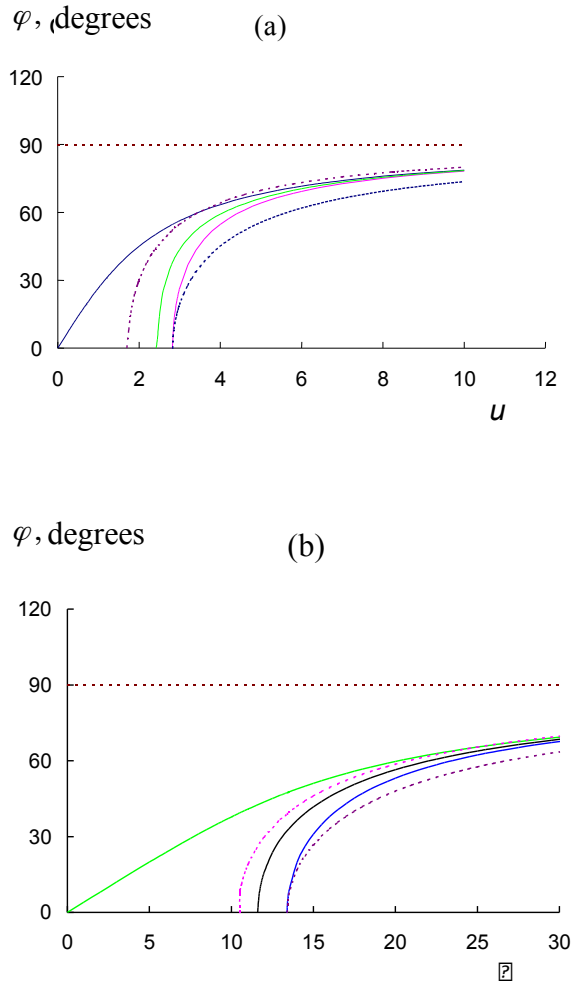

Fig. 7.4. Domains of the angles corresponding to the instability as functions of the velocity in the MHD (solid curves – domain boundaries) and conventional HD (dashed curves – domain boundaries) for (a) $c_1 = c_2$ and (b) $c_1 = 10\ c_2$.

Now, we examine the case $c >> 1$, when the densities of the media on both sides of the discontinuity are substantially different. In this limit, for both HD and MHD cases, the increments are maximum for the same angles φ. For $c - u >> c^{1/3}$, the maximum increments are also equal for both HD and MHD discontinuities and are equal to

$$\gamma_{max} = \frac{u}{\sqrt{c^2 - u^2}} \ .$$

For $u > c$, the angle corresponding to the maximum increments in HD and MHD cases is determined by the condition

$$cos\phi = \frac{c}{u} \ ,$$

and for $c^{5/4} >> u > c$, the maximum increments are the following:

$$\gamma_{max} = \frac{\sqrt{3}}{2}\left(\frac{c}{2}\right)^{1/3} \qquad (7.1.14)$$

for HD and

$$\gamma_{\max} = \frac{\sqrt{3}}{2}\left(\frac{c^5}{2u^4}\right)^{1/3}$$

for MHD. Comparison of the maximum increments and instability domains in MHD and conventional HD obtained from the solution of the equation (7.1.9) and the equation for conventional HD for $c = 10$ is presented in Figs. 7.3b, 4b. Here we see again that, for high velocities, the maximum increments and the instability domains for MHD-discontinuities can be substantially smaller than those in the HD case.

For high velocities $u >> c$ and arbitrary values of c in the MHD case, we obtain the maximum increment

$$\gamma_{max} = \frac{\sqrt{c}(c+1)^2}{2u^2} \ ,$$

which decreases as u increases. The angle at which the increment is maximum is determined by the relationship

$$cos\phi = \frac{c+1}{u} \ ,$$

whereas in the HD case, the maximum increments remain constant for $u \to \infty$, as can be seen from expression (7.1.12) for $c = 1$ and expression (7.1.14) for $c >> 1$.

CONCLUSION

We have shown that the MHD tangential discontinuity in a cold plasma with a magnetic field perpendicular to the velocity jump is unstable for any discontinuity velocities. However, for high discontinuity velocities in the MHD case, the increments and the wave-vector domain corresponding to the instability turn out to be substantially smaller than those in the HD case. Therefore such discontinuities in MHD should spread into turbulent areas considerably more slowly than in the HD case. This can lead to effective decrease of the turbulent viscosity for supersonic plasma flows, and make it possible to accelerate the plasma to high velocities in plasma accelerators using supersonic flows.

For example, in the MAGO chamber when plasma flows through the nozzle, the plasma velocity changes from $v = c$ in the narrowest region of the nozzle to $v \sim 4c$; simultaneously, the density changes across the nozzle approximately by an order of magnitude, and the velocity changes by a factor of three. This corresponds to the fact that for the maximum velocities $\frac{c_1}{c_2} \sim 3$, and the change of the velocity across the nozzle is $u = \frac{\Delta v}{c_2} \sim 8$.
Hence, in the region of the supersonic flow, the instability caused by such high velocity gradients can be suppressed by comparison with the HD-case.

Another example of the application of the obtained results is the supersonic flow in the Z-pinch waist (see Section 7.2.1). Due to the inhomogeneity of the plasma density on the radius, the plasma velocities on different radii may differ from one another considerably. The magnetic field penetrating the waist at different stages of its formation can also stabilize here the instability caused by the velocity gradients.

7.1.2. Convective instability in an Azimuthal Magnetic Field in the Presence of Acceleration

When plasma moves in an azimuthal magnetic field, convective instability may develop that is analogous to the convective instability of nonuniformly heated gas in a gravitational field [7.8]. Both acceleration of plasma (gravitational Rayleigh-Taylor instability) and the curvature of azimuthal magnetic field lines ("sausage" instability, whose development causes the magnetic flux "going down" to a smaller radius) can lead to the instability. Both in Rayleigh-Taylor and in "sausage" instabilities, the shortest wavelengths are known to be the most dangerous. In case of smooth distribution of density in the Rayleigh-Taylor instability or of the magnetic field in the "sausage" instability, which is realistic for most flows due to the presence of heat conduction, mixing, and magnetic diffusion, the increments

of those instabilities' developments, when the wavelength tends to zero, should tend to a constant limit that is dependent on the gradients of the corresponding quantities. We are going to consider the problem of the calculation of those limiting increments for the wavelengths that are short by comparison with the characteristic dimensions of the flows, for simultaneous action of Rayleigh-Taylor and "sausage" instabilities in the azimuthal magnetic field.

Assume that plasma is moving with the acceleration g directed along the radius, which means in the reference frame moving with it that it is in a gravitational field that has the acceleration $-g$ produced by inertial forces. All the quantities are considered to be dependent on r only. The plasma is assumed to be in hydrodynamic equilibrium

$$-\rho_0 g - \frac{\partial p_0}{\partial r} - \frac{1}{r^2}\frac{\partial}{\partial r}(r^2 B_0^2 / 8\pi) = 0 \ . \qquad (7.1.15)$$

The subscripts 0 designate the equilibrium quantities, and $B_0^2 / 8\pi \equiv p_B^0$ is non-perturbed magnetic pressure.

Now we write the system of equations determining the perturbed motion under the assumption that the perturbed quantities dependence on z* is expressed in the form of an arbitrary multiplier with short characteristic scales. The equation for the plasma elements' velocity in the radial direction $v = v_r$ is written as follows:

$$\rho_0 \frac{\partial v}{\partial t} = -\frac{\partial p_1}{\partial r} - \frac{1}{r^2}\frac{\partial (r^2 p_B)}{\partial r} - \rho_1 g \ , \qquad (7.1.16)$$

(the perturbed quantities are indicated by the subscript 1, and the magnetic pressure perturbation is designated by p_B^1). Since we consider the case of short wavelengths for which constant increments are expected, the leveling of the total pressure will take place going with magneto-sonic speed:

$$p_1 + p_B^1 = 0 \ . \qquad (7.1.17)$$

* We will not consider the perturbations along φ that bend the magnetic field lines, since it is clear ahead of time that the increments for such perturbations can only be smaller, which means that, these perturbations are less dangerous.

The motion will be also determined by the equation for conservation of magnetic flux and the equation for conservation of entropy, *S*, which will have the form (with the accuracy up to the quantities of the first order of magnitude):

$$\frac{\partial}{\partial t}\left(\frac{p_B^1}{\rho_0^2 r^2} - \frac{2p_B^0}{\rho_0^3 r^2}\rho_1\right) + v\frac{\partial}{\partial r}\left(\frac{p_B^0}{\rho_0^2 r^2}\right) = 0 \ , \tag{7.1.18}$$

$$\frac{\partial}{\partial t}S_1 + v\frac{\partial}{\partial r}S_0 = 0 \ . \tag{7.1.19}$$

The time dependence of the perturbed quantities will be sought in the form $\exp\gamma t$, where γ is the increment of the perturbations growth. When we change the time derivative $\partial/\partial t \to \gamma$, exclude *v* and p_B^1 from the equations (7.1.16-19) and express the entropy perturbation via the pressure and density perturbations using the formula

$$S_1 = \left(\frac{\partial S}{\partial p}\right)_\rho p_1 + \left(\frac{\partial S}{\partial \rho}\right)_p \rho_1 \ ,$$

we get

$$\begin{gathered}\gamma^2\left(\frac{p_1}{\rho_0 r^2} + \frac{2p_B^0}{\rho_0^3 r^2}\rho_1\right) - \left(\frac{2p_1}{r} - \rho_1 g\right)\frac{\partial}{\partial r}\left(\frac{p_B^0}{\rho_0^2 r^2}\right) = 0 \ , \\ \gamma^2\rho_0\left(\frac{\partial S}{\partial p}p_1 + \frac{\partial S}{\partial \rho}\rho_1\right) + \left(\frac{2p_1}{r} - \rho_1 g\right)\frac{\partial}{\partial r}S_0 = 0 \ .\end{gathered} \tag{7.1.20}$$

Equating the determinant of the system of equations (7.1.20) to zero, we get an expression for the increment, which is convenient to express via the pressure and density gradients, using the identity that follows from the Jacobian of the thermodynamic quantities

$$\frac{\left(\frac{\partial S}{\partial \rho}\right)_p}{\left(\frac{\partial S}{\partial p}\right)_\rho} = \left(\frac{\partial p}{\partial \rho}\right)_S = c^2 \ .$$

Finally, using the equilibrium condition (7.1.15), we can write the expression for the increment as follows:

$$\gamma^2 = \frac{g\left(g + \frac{c^2 + c_A^2}{\rho}\frac{\partial \rho}{\partial r} + 2\frac{c_A^2}{r}\right) + \frac{2}{\rho}\left[c^2 r \frac{\partial}{\partial r}\left(\frac{p_B}{r^2}\right) - \frac{c_A^2}{r}\frac{\partial}{\partial r}p\right]}{c^2 + c_A^2} \qquad (7.1.21)$$

(the equilibrium quantities are written with the zero subscripts omitted).

When the magnetic field is absent, the expression (7.1.21) gives the short-wave increment of the Rayleigh-Taylor instability

$$\gamma^2 = g\left(\frac{g}{c^2} + \frac{\partial \ln \rho}{\partial r}\right)$$

or, with the reversed sign, the square oscillation frequency for internal waves [7.8]. In this case, the condition of stability for the one-species gas (not mixed gases) reduces to the condition that the entropy must grow with height growth [7.8]

$$g\frac{\partial S}{\partial r} > 0 \ .$$

In the case of absence of the motion ($g = 0$, "sausage instability"), we can express the increment via the magnetic pressure gradient using the equilibrium equation (7.1.15)

$$\gamma^2 = \frac{c_A^2}{r^2}\left[\frac{\partial \ln p_B}{\partial \ln r} + \frac{2(c_A^2 - c^2)}{c_A^2 + c^2}\right], \qquad (7.1.22)$$

which yields the instability if the magnetic field decreases with the radius increasing more slowly than under the law

$$B \sim r^{-(c_A^2 - c^2)/(c_A^2 + c^2)}$$

(the instability condition [7.9]), i.e., for plasma with low β, the magnetic field should decrease more slowly than $r^{-1+5\beta/3}$ as the radius increases (for plasma with $\gamma = 5/3$); for plasma with high β, the field should increase faster than r. If plasma is an ideal gas with the adiabatic index γ, the expression for the increment can be rewritten as

$$\gamma^2 = -\frac{2c_A^2}{r^2}\frac{\partial \ln \Phi}{\partial \ln r} \ ,$$

where $\phi = p^{1/\gamma} r/B$ is a quantity proposed in Gerlakh *et al.* [7.10]. For stability, it is required that $\frac{\partial \Phi}{\partial r} > 0$. Note that for each plasma element the quantity ϕ is conserved in the adiabatic 2D flows. When $\frac{\partial \Phi}{\partial r} < 0$, the plasma elements with lower pressure (per unit of the frozen-in magnetic flux) are located on larger radii, and it is energetically advantageous for them to change their positions with the elements located on the smaller radii, and thus the instability develops.

The instability development (7.1.21) results in convection and mixing, in which the released "pinching" energy is converted into the kinetic energy, and then into heat. Such a process can be qualitatively interpreted as anomalous resistance. In 2D calculations, this instability is taken into account automatically, whereas in 1D calculations, which are usually performed in the channel approximation (i.e., along some mid-line in the chamber for dependences of the median channel radius *r* and its cross-section width on the path along the channel that correspond to the chamber geometry), it can be simulated using the exponential factors $ch(\int \gamma\, dt)$ in the coefficients of the magnetic diffusion and heat conductivity. The quantity determined by (7.1.21) can be taken as the increment γ.

7.2. Nonlinear Development of Instabilities

In the linear stage, the development of perturbations is exponential. However, after the perturbations grow so much that the linear equations become unusable, the nonlinear stage should come into force. We will consider some flows and their properties in the nonlinear stage. The analysis of these flows and their properties can be useful for the evaluation of turbulent flows developing when exposed to instabilities.

7.2.1. Nonlinear Stage of the Z-Pinch Instability

As we know, with the deviation of the Z-pinch configuration from the ideal cylindrical shape, an MHD instability develops. The linear stage of Z-pinch development was first studied by Trubnikov [7.11], Kruskal and Schwarzchild [7.12], and Shafranov [7.13]. The study of the nonlinear development of the most important type of instability—the "sausage" instability——is the focus of a number of papers referenced in the reviews of Vikhrev and Braginskii [7.14] and Dyachenko and Imshennik [7.15]. The study of the development of a waist in "sausage" instability with the simplifying assumption of plasma incompressibility was the focus of Book *et al*. [7.16], who performed a numerical study of the waist development in the context of the long-wave limit and concluded that the problems of the

nonlinear waist development in the short-wave limit and nonlinear development of the planar Rayleigh-Taylor instability are equivalent. In the long-wave limit, Trubnikov and Zhdanov [7.17] obtained a particular analytical solution describing waist development, starting with weak perturbations and going up to an essentially nonlinear stage. In this section, following the work of Garanin and Chernyshev [7.18], we will consider the main stages of the nonlinear development of the waist in an ideal magnetohydrodynamic setting and will show that the final stage of waist development is the stage described by the self-similar solution to which the solution of Trubnikov and Zhdanov [7.17] tends for high compressions.

Let us consider an infinite plasma cylinder that is homogeneous over its cross-section and whose plasma pressure is balanced by the magnetic forces of the current flowing along the cylinder. The plasma conductivity is assumed to be infinitely high such that the magnetic field inside the plasma equals zero. At the initial moment, there is a small perturbation that is periodic along the cylinder length and is axially symmetrical. For evaluation of instability development, in this case the effect of the magnetic field is reduced to the external pressure depending on the plasma boundary radius, r

$$p = p_0 R_0^2 / r^2 \tag{7.2.1}$$

(R_0, p_0 are the initial pinch radius and the pressure).

Initially, the perturbations in the linear stage develop according to the formulas of Trubnikov [7.11], Kruskal and Schwarzchild [7.12], and Shafranov [7.13], and each harmonic develops exponentially. The nonlinear stage starts when the radial perturbation amplitude is comparable either with the wavelength, λ (if $l << R_0$) or with the radius (if $l >> R_0$).

Numerical Simulation of Waist Development

Let us consider the question of which self-similar solution the waist development approaches for a wavelength that is greater than, or on the order of, the pinch radius ($l \geq R_0$). Different assumptions regarding waist dynamics leads to different time dependences of the characteristic quantities. Thus, for example, if we assume the compression to be adiabatic, the waist length l to be proportional to its radius R, and, consequently, the time of plasma outflow from the waist zone to be

$$t \sim l / v_T \sim R / v_T$$

(v_T is the sound speed in the waist), we get Vikhrev and Braginskii's [7.14] time dependences of the plasma radius, density ρ, and temperature T

$$R \sim t^{\gamma/(2\gamma-1)} ,$$
$$\rho \sim t^{-2/(2\gamma-1)} , \qquad (7.2.2)$$
$$T \sim t^{-2(\gamma-1)/(2\gamma-1)}$$

(γ is the plasma adiabatic index). If we assume the compression to be adiabatic and the waist length to be a fixed quantity, the characteristic quantities will change as follows:

$$R \sim t^{\gamma/(\gamma-1)} ,$$
$$\rho \sim t^{-2/(\gamma-1)} , \qquad (7.2.3)$$
$$T \sim t^{-2} .$$

But if we assume that the density to be fixed in terms of the order of magnitude, which is determined by the initial density, i.e., the waist configuration contains the shockwave, and $l \sim R$, then

$$R \sim \sqrt{t} ,$$
$$\rho \sim \text{const} , \qquad (7.2.4)$$
$$T \sim 1/t .$$

Besides the dependences (7.2.2–7.2.4), we can give examples of other possible regimes of waist development. A series of numerical hydrodynamic calculations were performed to determine which of the regimes is realized.

Figs. 7.5 and 7.6 present the waist shape $r(z, t)$ (half of the wavelength) for $\lambda = 4R_0$, $\gamma = 5/3$ for two variants of the initial perturbations:

$$r = 1 - 0.02\cos\frac{\pi z}{2} , \qquad (7.2.5)$$

$$r = 1 - 0.02\sum_{k=1}^{\infty}(0.2)^{k-1}\cos\frac{\pi k z}{2} = 1 - 0.02\frac{5\cos\frac{\pi z}{2} - 1}{5{,}2 - 2\cos\frac{\pi z}{2}} \qquad (7.2.6)$$

(hereinafter, the initial radius R_0, density ρ_0, and Alfven velocity $\sqrt{2p_0/\rho_0}$ are employed as the units of measurement).

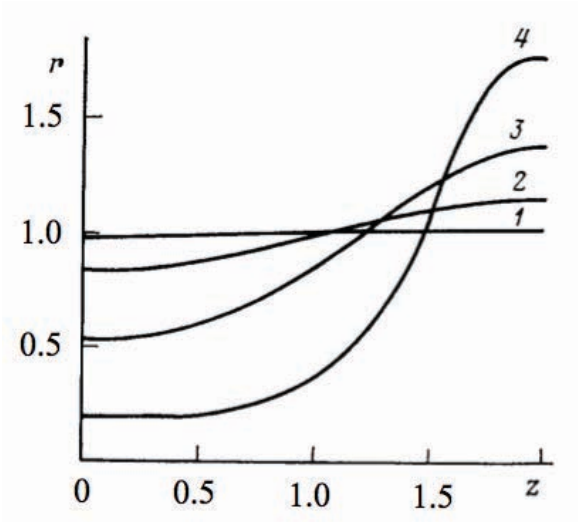

Fig. 7.5. Waist shape for the initial perturbation assigned in the form of (7.2.5) at different times: 1) t = 0; 2) t = 2.05; 3) t = 2.92; 4) t = 3.52.

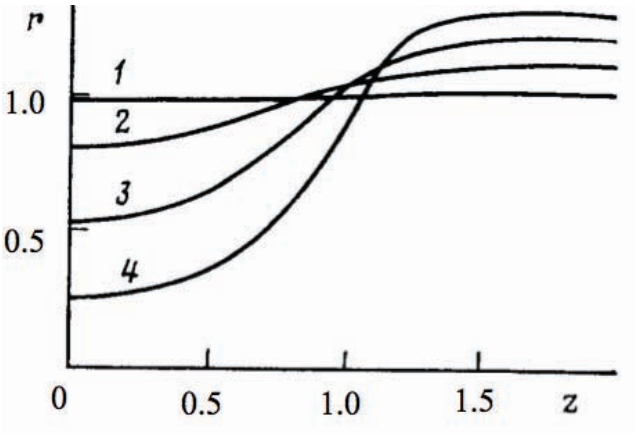

Fig. 7.6. Waist shape for the initial perturbation assigned in the form of (7.2.6) at different times: 1) t = 0; 2) t = 2.05; 3) t = 2.69; 4) t = 3.01.

Fig. 7.7 shows the waist minimum radius R versus time for the variant (7.2.5). It was not possible to achieve radial compressions R_0 / R that were higher than shown in the figures, because of the developing instabilities. Nevertheless, we managed to go farther than Book *et al.* [7.16], whose calculation achieved only $R_0 / R \approx 1.3$.

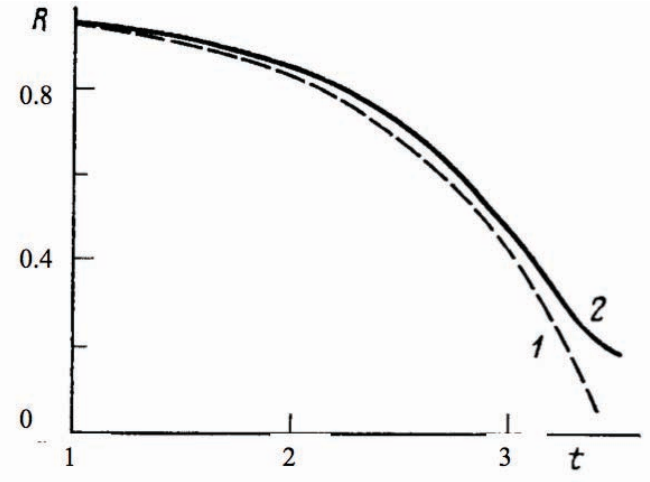

Fig. 7.7. Time dependence of the minimum waist radius for the initial perturbation assigned in the form of (7.2.5). Curve 1 represents exponential perturbation growth according to linear theory [7.11–7.13]; curve 2, the result of a numerical calculation.

The calculation results showed that the time dependence of the minimum radius up to considerably high compressions is described by linear theory (see Fig. 7.7), although the waist shape at that times is seriously distorted (see Figs. 7.5 and 7.6). Plasma compression in the waist is nearly isentropic: for the variant (7.2.5), the maximum volume change of the quantity $T^{3/2}/\rho$, which characterizes the entropy, is 9% when the radial compression is 5.2; for the variant (7.2.6), the maximum change of $T^{3/2}/\rho$ is 19% when the radial compression is 3.8. Another important conclusion from the calculation results is that the waist length does not decrease as the radius decreases (see Figs. 7.5 and 7.6).

Thus, the regime (7.2.3) with $l = const.$ is realized for nonlinear waist development. With the assignment of one harmonic, the waist length l tends to λ. If a set of harmonics is assigned with $\lambda >> R_0$, the waist length is determined by the characteristic length $l \leq \lambda$, which is formed at the moment of transition from the linear stage to the nonlinear stage.

Note that the waist development under consideration is unstable relative to the short-wave perturbations. The presence of an additional local perturbation with a length $\lambda' << \lambda$ should cause, against the backdrop of a large waist, the formation of a smaller waist with the length ~ λ', for which the larger waist can be regarded as a pinch homogeneous over its cross-section. We do not consider here the problem of what will happen in the presence of a spectrum of chaotic perturbations.

Self-Similar Stage of the Waist Development

When the characteristic quantities change in the regime (7.2.3), the pressure should set almost constant over the radius, because for $l >> r$, the outflow time is great by comparison with the time of the sound propagation along the radius. For the same reason, the compression remains isentropic. Plasma flow for sufficiently high compressions will be 1D along the axis, and the system of equations describing the plasma motion can be written in the form used by Vikhrev and Braginskii [7.14]

$$\frac{\partial}{\partial t}(\rho r^2)+\frac{\partial}{\partial z}(\rho r^2 v)=0 \ ,$$

$$\frac{\partial v}{\partial t}+v\frac{\partial v}{\partial z}=-\frac{1}{\rho}\frac{\partial p}{\partial z} \ , \qquad (7.2.7)$$

$$p=\frac{1}{2r^2}=\rho^{\gamma}/2 \ .$$

Let us introduce self-similar variables according to (7.2.3):

$$x=2z/l \ ,$$

$$\frac{1}{2}\frac{\gamma}{\gamma-1}\rho^{\gamma-1}=\frac{l^2}{4t^2}\phi(x) \qquad (7.2.8)$$

$$v=-\frac{l}{2t}u(x)$$

(time $t<0$). Then the system (7.2.7) is rewritten as

$$2/\phi-\frac{d}{dx}(u/\phi)=0 \ ,$$

$$u+u\frac{du}{dx}=-\frac{d\phi}{dx} \ . \qquad (7.2.9)$$

The boundary conditions for the system (7.2.9) are

$$u(0) = 0 \ , \qquad \phi(1) = 0 \ . \tag{7.2.10}$$

Since the system (7.2.9) does not explicitly contain x, it is equivalent to the equation

$$\frac{d\phi}{du}\left(\phi - \frac{u^2}{2}\right) + \frac{3}{2}\phi u = 0 \ , \tag{7.2.11}$$

which is homogeneous. Solving the equations of (7.2.11) and (7.2.9), with account taken of (7.2.10), we get

$$u = 2\sqrt{(\phi/4)^{3/2} - \phi/4} \ ,$$

$$x = \frac{[2 - (\varphi/4)^{1/3}]\sqrt{1 - (\varphi/4)^{1/3}}}{2} \ , \tag{7.2.12}$$

$$0 \le \phi \le 4$$

dependences that can be obtained from the analytical solution of Trubnikov and Zhdanov [7.17] for high compressions $R_0/R >> 1$. The plasma temperature T is proportional to ϕ, and the waist radius, r, is proportional to $\phi^{-\gamma/2}(^{\gamma-1})$. Fig. 7.8 shows the graphs $\phi(x)$, $u(x)$ and the self-simulated waist radius $\tilde{r} \equiv \phi^{-5/4}(x)$ for $\gamma = 5/3$.

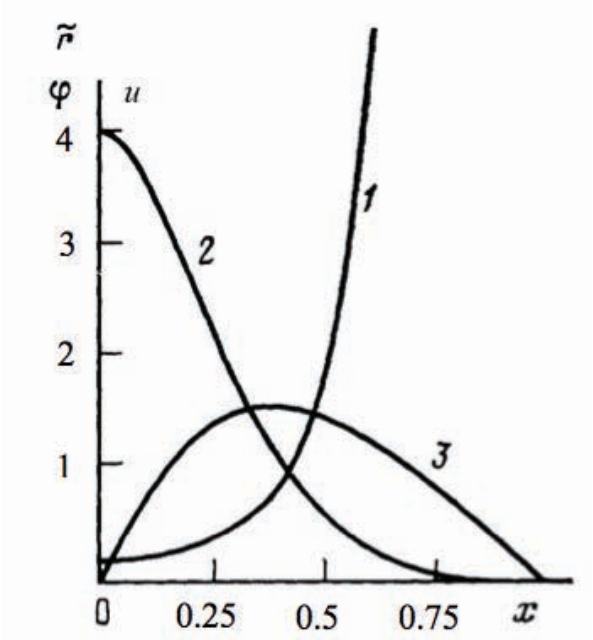

Fig. 7.8. Waist shape in self-similar stage $\tilde{r}(x)$ *(curve 1), temperature distribution along the waist length* $\phi(x)$ *(curve 2), and longitudinal velocity,* $u(x)$ *(curve 3).*

Pinch "Evaporation" Stage for Short Wave Lengths

For short wavelengths, $\lambda << R_0$, the instability development is reduced to a well-studied case of the nonlinear stage of the Rayleigh-Taylor instability [7.19–7.21]. In this case plasma plays the role of a heavy fluid, the magnetic field, that of a light fluid, and the role of acceleration is played by the quantity

$$g = 2p / \rho r .$$

The magnetic field will penetrate into the plasma as "bubbles" moving inward with the velocity $v \sim \sqrt{g\lambda}$, and plasma will "fall" along the radius with the acceleration g as "spikes" (see Fig. 7.9). This stage we shall call the stage of pinch "evaporation". The picture will qualitatively change when the bubbles approach the axis at a distance on the order of λ. Here the wavelength becomes of the same order with the radius, after which the waist development enters the stage considered above—the stage described by the self-similar solution.

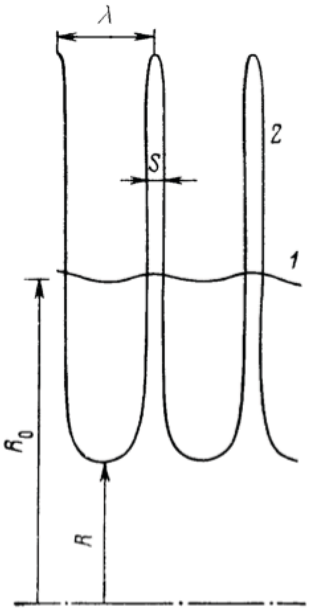

Fig. 7.9. Waist shape at the stage of the pinch evaporation (short wavelength): 1) initial perturbation; 2) developed stage.

Let us consider, in general terms, the pinch evaporation. The bubbles' velocity here will be greater than their velocity in the Rayleigh-Taylor instability because of the additional compression of the bulk mass by the pressure of (7.2.1), which increases as the radius decreases. The mass evaporation rate per unit of pinch length will be determined with the equation

$$\frac{dm}{dt} = -2v_0 m / R \ , \qquad (7.2.13)$$

where R is the radius of the nonevaporated portion of the pinch,

$$v_0 = \mathrm{F}\sqrt{g\lambda} \ , \qquad (7.2.14)$$

and the constant F is determined by the rise velocity of the bubbles in the Rayleigh-Taylor instability and approximately equals F ≅ 0.23 [7.20 and 7.21]. Then, with account taken of the fact that plasma compression proceeds adiabatically,

$$g = 1 / R^{(3\gamma-2)/\gamma} \ , \qquad (7.2.15)$$

$$v = F\sqrt{\lambda} / R^{(3\gamma-2)/2\gamma} , \tag{7.2.16}$$

and since for the adiabatic compression

$$m = R^{2(\gamma-1)/\gamma} \tag{7.2.17}$$

(the letter m designates the mass divided by π, for the purposes of simplicity) for the bubble rise velocity we get

$$\frac{dR}{dt} = -\gamma F\sqrt{\lambda} / (\gamma-1) R^{(3\gamma-2)/2\gamma}, \tag{7.2.18}$$

a quantity that is larger than the Rayleigh-Taylor quantity by a factor of $(\gamma/\gamma - 1)$. Therefore, if we take the time of evaporation of the entire pinch to be zero time, the pinch radius and time are connected by the relation

$$t = -\frac{2(\gamma-1)}{(5\gamma-2)F\sqrt{\lambda}} R^{(5\gamma-2)/2\gamma} . \tag{7.2.19}$$

The plasma leaving the bubble area after passing the distance ~ λ moves in a form of streams virtually freely, driven by the acceleration (7.2.15), since the pressure manages to equalize across the stream width.

Thus, the velocity of each element after evaporation is determined by the motion in the potential

$$U = \frac{\gamma}{2(\gamma-1)} / r^{2(\gamma-1)/\gamma} . \tag{7.2.20}$$

However in this case, since the motion of each plasma element starts with the velocity proportional to the small parameter $\lambda << 1$, the particles that emerged later from smaller radii will have velocities greater than those of the particles that emerged earlier. There is a danger that if the particles that emerged from smaller radii begin to catch up with the particles that emerged earlier, the stream cross-section can grow and close the pinch region from the current source. Let us consider this possibility.

The stream cross-section S will be determined from the continuity equation

$$2S\rho r dr = \lambda dm \ ,$$

that is,

$$S = \lambda r^{(2-\gamma)/\gamma} / 2\frac{dr}{dm} \ . \qquad (7.2.21)$$

The dependence $r(m, t)$ can be found using the connection between the mass and the initial radius of the emerged particle (7.2.17) and the energy conservation law for particle motion in potential (7.2.20)

$$\frac{1}{2}\left(\frac{\partial r}{\partial t}\right)^2 + \frac{\gamma}{2(\gamma-1)}\Big/ r^{2(\gamma-1)/\gamma} = \frac{\gamma}{2(\gamma-1)}\Big/ m \ . \qquad (7.2.22)$$

The solution of the equation (7.2.22) with initial conditions of (7.2.17) and (7.2.19) yields $r(m, t)$, and consequently, according to (7.2.21), $S(m, t)$, i.e., the implicit dependence of the stream cross-section on the radius.

Since the emerged particles pass the zone $r \sim 1$ in short times compared with (7.2.19), then if the $\partial r/\partial m$ sign change takes place for $r \sim 1$, the $\partial r/\partial m < 0$ will be also true for $r >> 1$. Hence, it is sufficient to consider the zone of $r >> 1$. For $r >> 1$ in (7.2.22) we can neglect the potential energy, and then using (7.2.17, 7.2.19) we can get

$$r = \frac{2\sqrt{\gamma(\gamma-1)}}{(5\gamma-2)F\sqrt{\lambda}}\left(\frac{\tau}{\sqrt{m}} + m^{3\gamma/4(\gamma-1)}\right) , \qquad (7.2.23)$$

where

$$\tau = \frac{(5\gamma-2)F\sqrt{\lambda}}{2(\gamma-1)}t$$

changes in the course of the pinch evaporation from –1 to 0. The formula (7.2.23) shows that $\partial r/\partial m$ does not turn into zero for $t < 0$. When we substitute (7.2.23) into (7.2.21), we get the dependence

$$S = \lambda\left[\frac{(5\gamma-2)F\sqrt{\lambda}}{2\sqrt{\gamma(\gamma-1)}}\right]^{2(\gamma-1)/\gamma} \frac{\left[\tau/\sqrt{m} + m^{3\gamma/4(\gamma-1)}\right]^{(2-\gamma)/\gamma}}{\left[-\tau/m^{3/2} + \frac{3\gamma}{2(\gamma-1)}m^{(4-\gamma)/4(\gamma-1)}\right]} , \qquad (7.2.24)$$

which, together with (7.2.23), describes the shape of the plasma stream leaving the pinch region.

We shall introduce here a description obtained as the result of the solution of equation (7.2.22) and correct for arbitrary radii $r >> \lambda$ with the accuracy of $\sim \lambda$ of the motion of the plasma stream with $\gamma = 5/3$

$$t = -\frac{4}{19F\sqrt{\lambda}} m^{19/8} + 10m^{7/4} y(\xi) \ , \qquad (7.2.25)$$

where

$$\xi = r^{1/5} / m^{1/4} \ ,$$

$$y(\xi) = \frac{\xi^3\sqrt{\xi^4 - 1}}{5} + \frac{3}{5}\frac{\sqrt{\xi^4 - 1}}{\xi} + \frac{3}{5\sqrt{2}} F\left(\arccos\frac{1}{\xi}, \frac{1}{\sqrt{2}}\right) - \frac{3\sqrt{2}}{5} E\left(\arccos\frac{1}{\xi}, \frac{1}{\sqrt{2}}\right),$$

$F(\phi, k)$, $E(\phi, \kappa)$ are the first- and second-kind elliptical integrals. It follows from the expression (7.2.25) that the derivative $\partial r/\partial m$, which should be substituted into (7.2.21) for obtaining the stream shape, equals

$$\frac{\partial r}{\partial m} = \sqrt{\frac{5}{2}} m^{1/4} \sqrt{1 - 1/\xi^4} \left(\frac{m^{5/8}}{2F\sqrt{\lambda}} - \frac{7}{4}\sqrt{10} y \right) + \frac{5}{4}\frac{r}{m} \ ,$$

and the velocity is determined by the formula

$$v = \sqrt{\frac{5}{2m}(1 - 1/\xi^4)} \ .$$

As for the rising bubble, for its description on the scale of $\sim\lambda$ we can use the known results of the nonlinear stage of the Rayleigh-Taylor instability [7.19–7.21] with account of the fact that, because of the additional compression of the entire plasma mass, on that scale plasma can be regarded as incompressible fluid moving with a speed equal to the difference between the velocities (7.2.18) and (7.2.14), i.e., with a speed of $v_0/(\gamma - 1)$.

CONCLUSION

For wavelengths $\lambda \geq R_0$, the nonlinear development of Z-pinch perturbations that are periodic along the length (but not necessarily harmonic) and are axially-symmetrical approaches the stage described by a self-similar solution, to which the analytical solution [7.17] reduces for high compressions. In the case of short wavelengths $\lambda << R_0$, the perturbation development goes through the stage of the nonlinear Rayleigh-Taylor instability, and the bubbles rising to the axis, after their dimension λ is on the order of the radius R, form the stage of the self-similar solution.

7.2.2. Periphery Plasma Motion Following Z-Pinch Waist Constriction

Section 7.2.1 shows that the final stage of the nonlinear Z-pinch instability development is the stage described by a self-similar solution, in which the waist length remains constant, and the radius depends on time as a power function (7.2.3). Density of the plasma around the waist was assumed to be sufficiently small and to have no effect on the waist movement.

The motion of the cold periphery plasma near the pinch waist was considered by Zhdanov and Trubnikov [7.22], who assumed the waist boundary to move in the periphery plasma at a velocity on the order of the Alfven velocity c_A. As a result of that assumption, there were high velocities of plasma motion and strong plasma heating. In reality, however, the waist velocity equals $\sim \frac{R}{l} v_T$, where v_T is the sound speed in the dense waist plasma, and the ratio of the waist boundary velocity to the Alfven velocity in the periphery plasma is $\sim \frac{R}{l}\frac{v_T}{c_A} << 1$, since $R << l$, and $\frac{v_T}{c_A} \sim \sqrt{\frac{\rho}{\rho_S}} << 1$ (ρ, ρ_S are the periphery and constriction plasma densities, respectively).

Thus, the problem contains a small parameter, $\mu = \frac{R}{c_A \tau} << 1$ ($\tau \sim l / v_T$ is the time of the waist breakup), and the problem of periphery plasma motion and its effect on the waist motion can be solved within the theory of perturbations. In the zero approximation, the current flowing through the waist can be considered constant, and the waist movement can be assigned. Then, considering the motion of the periphery plasma for the given boundary motion, one can determine the correction to the current that compresses the waist.

This problem is solved in this section following Garanin and Mamyshev [7.23]. The periphery plasma is assumed to be cold, the current I in the plasma at the initial time is constant $I = I_0$, the plasma density initially depends on the radius r as a power function,

$$\rho(r, R = R_0) = \rho_0 (r / R_0)^s \tag{7.2.26}$$

(R_0 is the initial waist radius). In accordance with (7.2.3), the time dependence of the waist radius is considered to be power-law,

$$-t / \tau = (R / R_0)^\alpha \ . \tag{7.2.27}$$

The calculations will be performed with logarithmic accuracy, $\sim 1/\ln\mu$.

In the first approximation, as the waist compresses, the current can be assumed to be constant in the region of $R < r < r_{\max}$ ($r_{\max}$ is the maximum radius that can be reached by acoustic perturbations). In this region, using the condition of magnetic flux conservation for each Lagrange particle $I/\rho r^2 = const.$, with (7.2.26) taken into account, one can easily obtain the density distribution

$$\rho(r) = \rho_0 \frac{i}{(r / R_0)^2} \left(\frac{r}{R} \right)^{(2+s)i} \tag{7.2.28}$$

($i = I/I_0$). The sound speed in this region will be

$$c_A = c_{A0} \frac{i}{(r / R_0)\sqrt{\rho / \rho_0}} = c_{A0} \sqrt{i} \left(\frac{R}{r} \right)^{(2+s)i/2} \tag{7.2.29}$$

(c_{A0} is the initial sound speed for $r = R_0$), and the order of magnitude of the maximum radius reached by the perturbations is $r_{\max} \sim c_A t$, where t is the characteristic time of the waist radius change from (7.2.27). Thus,

$$r_{\max} \sim R_0 \mu^{-2/(2+(2+s)i)} (R / R_0)^{(2\alpha+(2+s)i)/(2+(2+s)i)} \tag{7.2.30}$$

(for definiteness, we assume that $\mu = R_0/c_{A0}\tau$) .

As the characteristic times decrease with the decrease in the waist radius, one can assume that the magnetic field does not vary over these times for $r > r_{max}$. Using this circumstance, the dependence of current on the waist radius can be found with a logarithmic accuracy by striking the magnetic flux balance as the waist radius changes,

$$L\,di + 2i\frac{dR}{R} = 0 \qquad (7.2.31)$$

($L = 2\ln\frac{r_{max}}{R}$ is the inductance of the constant-current region). By integrating (7.2.31) and taking (7.2.30) into account, we obtain

$$R = R_0\mu^{\{[(2+(2+s)i)/(4+s)i]^{1-\alpha}-1\}/(1-\alpha)}, \qquad (7.2.32)$$

which is a relationship between the current and the waist radius. Since the magnetic field and the density cannot manage to change (they get frozen) at $r > r_{max}$ as the waist radius reduces from R to 0, using (7.2.28, 7.2.30, 7.2.32), we obtain the dependences of $r(i)$, $\rho(i)$* for $r > r_{max}$

$$\rho = \rho_0\mu^{2\{1-(2\alpha+(2+s)(2-\alpha)i)/[(4+s)i]^{1-\alpha}[2+(2+s)i]^{\alpha}\}/(1-\alpha)}. \qquad (7.2.33)$$

The curves $i(r)$ and $\rho(r)$ plotted on the basis of the formulas (7.2.28) at $r < r_{max}$ and (7.2.33) at $r > r_{max}$ for $\mu = 0.01$; $s = 0$; $\alpha = 0.4$ (which corresponds to $\gamma = 5/3$ in accordance with (7.2.3)), $R/R_0 = 0.032$ are shown in Figs. 7.10, a and b. The plot of the waist current as a function of time for the same case and based on formulas (7.2.27) and (7.2.32) is shown in Fig. 7.11. For comparison, these figures also show the results of 1D numerical magnetohydrodynamic simulation of periphery plasma motion with boundary motion defined in accordance with (7.2.27). The comparison shows that formulas (7.2.28, 7.2.32, and 7.2.33) provide a reasonable description of the periphery plasma motion, although the logarithmic accuracy is not high, ~ 1/ln100 ~ 0.2.

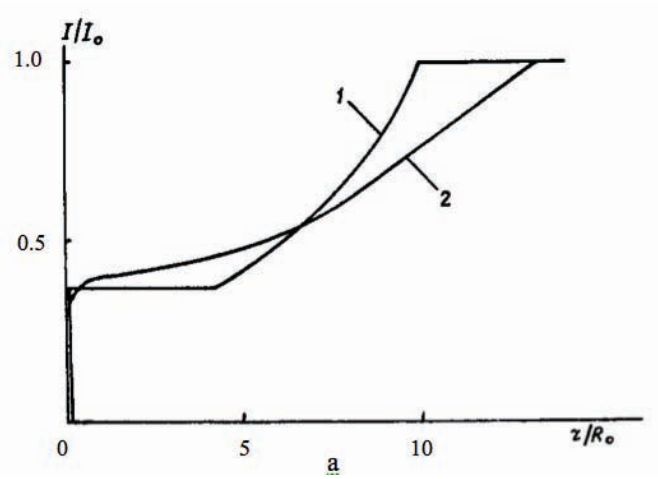

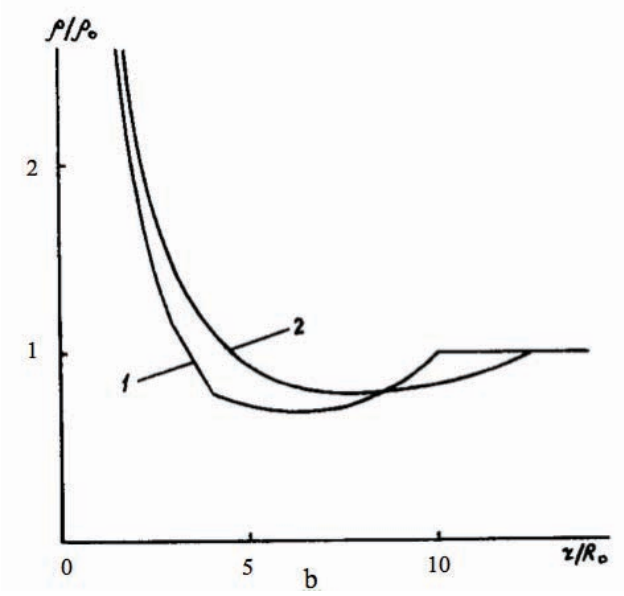

Fig. 7.10. Current in the periphery plasma (a) and plasma density (b) as a function of radius for $\mu = 0.01$; $s = 0$; $\alpha = 0.4$; $R/R_0 = 0.032$: 1) plots based on formulas (7.2.28 and 7.2.33); 2) results of numerical MHD simulation.

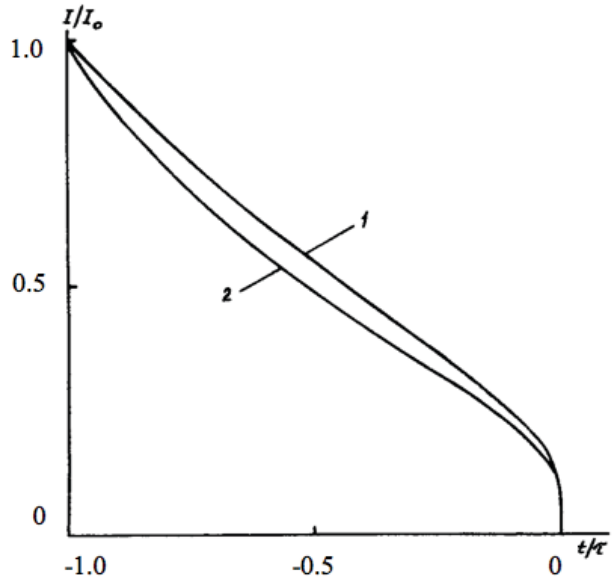

Fig. 7.11. Current in the waist as a function of time I(t) for $\mu = 0.01$; $s = 0$; $\alpha = 0.4$: 1) plots based on formulas (7.2.27, 7.2.32); 2) result of numerical MHD simulation.

Once the waist radius diminishes to zero (constriction breakup), the density and the magnetic field throughout the region $0 < r < R_0\mu^{-2/(4+s)}$ get distributed in accordance with the formulas of (7.2.33). Plasma velocities in this case can be disregarded because of the smallness of μ. The question arises of how the plasma will move farther.

The presence of the current gradient will result in plasma acceleration toward the axis and then deceleration in a weak shock diverging from the axis. Thus, the plasma downstream of the shock wave can be considered to be in mechanical equilibrium. Thermal pressure p of the downstream plasma can be determined from the equilibrium condition

$$\frac{\partial p}{\partial r} = -\rho_0 c_{A0}^2 \frac{R_0^2}{r^2} \frac{\partial}{\partial r} \frac{i^2}{2} ,$$

which, using current distribution of (7.2.33), gives

$$p = \rho_0 c_{A0}^2 \frac{R_0^2}{2r^2} i \frac{\partial i}{\partial \ln r} = \rho_0 c_{A0}^2 \frac{R_0^2}{r^2} \frac{i^2}{2} \frac{[(4+s)i]^{1-\alpha}[2+(2+s)i]^{1+\alpha}}{4\alpha \ln(1/\mu)} . \qquad (7.2.34)$$

The distribution of internal energy ε of plasma corresponding to (7.2.34)

$$\varepsilon = \frac{c_{A0}^2}{\gamma - 1}\frac{i^2}{2}\frac{[(4+s)i]^{1-\alpha}[2+(2+s)i]^{1+\alpha}}{4\alpha\ln(1/\mu)}\mu^{\left[\frac{(4+s)i}{2+(2+s)i}\right]^{\alpha}\frac{2(2+s)}{4+s}} \qquad (7.2.35)$$

has a maximum, which is achieved at

$$i = \left[\frac{3-\alpha}{\ln(1/\mu)\alpha(2+s)}\left(\frac{4+s}{2}\right)^{1-\alpha}\right]^{1/\alpha} \qquad (7.2.36)$$

and is equal to

$$\varepsilon_{\max} = \frac{2c_{A0}^2}{\gamma - 1}\left[\frac{3-\alpha}{2(2+s)}\right]^{\frac{3}{\alpha}-1}\frac{(4+s)^{3(1-\alpha)/\alpha}}{[\alpha\ln(1/\mu)]^{3/\alpha}}\exp\left(-\frac{3-\alpha}{\alpha}\right). \qquad (7.2.37)$$

Note that because of the presence of large numerical factors in real cases, in order to ensure applicability of formulas (7.2.34–7.2.37), one should use very large values of $\ln(1/\mu)$ *. In fact, it is necessary that

$$\beta = p/(B^2/8\pi) = \frac{[(4+s]^{1-\alpha}[2+(2+s)i]^{1+\alpha}}{4\alpha\ln(1/\mu)}$$

be small.

The equilibrium state of plasma after the shock propagation is stable with respect to convection, since $\frac{\partial \Phi}{\partial r} > 0$, where $\Phi = p^{1/\gamma}r/B$ (see Section 7.1). Consequently, the magnetized periphery plasma in the vicinity of the waist can exist for quite a long time (by comparison with hydrodynamic times). In addition, if we take into account that its temperature can be high due to the low density (despite the presence of the large factor $[\ln(1/\mu)]^{3/\alpha}$ in the denominator of (7.2.37)), it can generate a noticeable quantity of thermonuclear neutrons. Thus, a more consistent analysis of periphery plasma motion than that of Zhdanov and Trubnikov [7.22] does not rule out the possibility of neutron generation in it. In order to determine the neutron yield, certain experiments are required to explore the heating of the ion plasma component in a weak collisionless wave, since the wave propagating in the low-density magnetized periphery plasma is collisionless, and heating of a given plasma component is determined by its structure (see Chapter 4).

* Fig. 7.10 confirms this. For a moderately large value of $1/\mu = 100$, formula (7.2.33) describes the profile of $I(r)$ reasonably well, but the gradient of $I(r)$ is strongly overstated.

7.2.3. Self-Similar Evolution of Rayleigh-Taylor Instability at Corner Points

The Rayleigh-Taylor instability and its properties play an important role in magnetohydrodynamic problems. The flows associated with it often have a two-dimensional nature, because the tension of magnetic lines often precludes their bending and the onset of motions that affect one of the coordinates. The sausage instability in a short wave-length range is also equivalent to the problem of the evolution of the plane Rayleigh-Taylor instability for both its linear and nonlinear stage.

In Rayleigh-Taylor instability studies, one often uses the problem setup with periodic, constant wavelength perturbations [7.19–7.21, 7.24, 7.25]. In such a statement, the instability development problem in the nonlinear stage is reduced for large times to a steady-state problem, which simplifies its analysis [7.20, 7.21]. The characteristics obtained by solving the problem with periodic perturbations, such as the increments in a linear problem or the Froude number $F = v/\sqrt{g\lambda}$ (v is the bubble rise velocity, λ is the wavelength, g is the gravity acceleration) in the steady-state problem, are used to develop different instability models with a spectrum of modes [7.26, 7.27].

Localized perturbations studied by Volchenko *et al.* [7.28] and Garanin and Startsev [7.29] are another type of perturbation, the development of which has a universal nature. A possible type of perturbation without a characteristic dimension is a perturbation in the form of a dihedral angle (localized perturbations in the plane problem, i.e., perturbations in the form of a straight line drawn on the surface of a fluid, can be treated as a particular case of such perturbations for the angle equal to p). The problem of the evolution of such perturbations can be of interest in and of itself for practical applications and as auxiliary for building models.

A fundamental distinctive feature of the evolution of perturbations in the form of a corner (L-shaped perturbations) is their nonlinearity, because the perturbations are not small (their amplitude is on the order of the characteristic wavelength). The problem can be simplified substantially by considering self-similar solutions; but even in this case the problem remains quite complex, since self-similar solutions are, generally speaking, two-dimensional with respect to two spatial coordinates. Therefore, in this section, following Garanin [7.30 and 7.31], we consider the cases that allow for additional simplifications, and only as an example, we consider the numerical solution of a plane localized perturbation problem. The density of light fluid that supports a heavy fluid is assumed to be zero.

Let us consider the flow of a fluid in a gravitational field and supported from below by constant pressure p applied to its boundary, which can have an arbitrary shape. Thus, we suppose that heavy fluid is supported by an infinitely light fluid, the motion of which we may do not take into account. We assume that the heavy fluid is ideal and incompressible, and its flow is potential, and whose equations of motion are written as

$$\Delta\phi = 0 \ ; \tag{7.2.38}$$

$$\frac{\partial\phi}{\partial t} + \frac{1}{2}(\nabla\phi)^2 + \frac{p}{\rho} + g\,y = 0 \ ; \tag{7.2.39}$$

$$\frac{dX}{dt} = \frac{\partial\phi}{\partial x}|_s \ ; \tag{7.2.40}$$

$$\frac{dY}{dt} = \frac{\partial\phi}{\partial y}|_s \ ;$$

where $\varphi(\vec{r},t)$ is the velocity potential $\left(\vec{v} = \nabla\varphi\right)$, p is the pressure, ρ is the density, X and Y are the Lagrange coordinates of the boundary, and the subscript s denotes that the corresponding quantity is taken on a free surface. Since the pressure on the free surface is p = const, and the potential ϕ is defined with an accuracy to within an arbitrary function of t, the equation (7.2.39) on the surface takes the form

$$\frac{\partial\phi}{\partial t} + \frac{1}{2}(\nabla\phi)^2 + g\,y\,|_s = 0 \ . \tag{7.2.41}$$

Equations (7.2.38), (7.2.40), and (7.2.41) completely define the fluid flow.

Acute anglesAcute angles $\theta_0 < \pi/2$ (Fig. 7.12) represent the simplest case discussed by Garanin and Startsev [7.29]. For this case, we expand the potential φ in powers of $x - x_0(t)$, $y - y_0(t)$, where $x_0(t)$ and $y_0(t)$ are the angle vertex coordinates. The velocity potential satisfying (7.2.38) is written as

$$\phi(x,y,t) = \phi_0(t) + \phi_x(t)(x - x_0) + \phi_y(t)(y - y_0) +$$

$$\frac{\phi_{yy}(t)}{2}[(y - y_0)^2 - (x - x_0)^2] + \phi_{xy}(t)(x - x_0)(y - y_0) + o(\vec{r} - \vec{r}_0)^2 \ . \tag{7.2.42}$$

Substituting (7.2.42) into equations (7.2.40) and (7.2. 41) and expanding the equation of surface in powers of the distance from the corner point yields

$$\frac{d\phi_0}{dt} = \frac{\phi_x^2 + \phi_y^2}{2} - g\, y_0 \ ;$$

$$\frac{d\phi_x}{dt} = 0 \ ;$$

$$\frac{d\phi_y}{dt} = -g \ ; \qquad (7.2.43)$$

$$\frac{dx_0}{dt} = \phi_x \ ;$$

$$\frac{dy_0}{dt} = \phi_y \ ;$$

$$\frac{d\phi_{yy}}{dt} = \frac{1 - AB}{1 + AB}(\phi_{yy}^2 + \phi_{xy}^2) \ ;$$

$$\frac{d\phi_{xy}}{dt} = -\frac{A + B}{1 + AB}(\phi_{yy}^2 + \phi_{xy}^2) \ ;$$

(7.2.44)

$$\frac{dA}{dt} = 2\phi_{yy} A + \phi_{xy}(1 - A^2) \ ;$$

$$\frac{dB}{dt} = 2\phi_{yy} B + \phi_{xy}(1 - B^2) \ ,$$

where

$$A = tg\alpha \ , \ B = tg\beta \ .$$

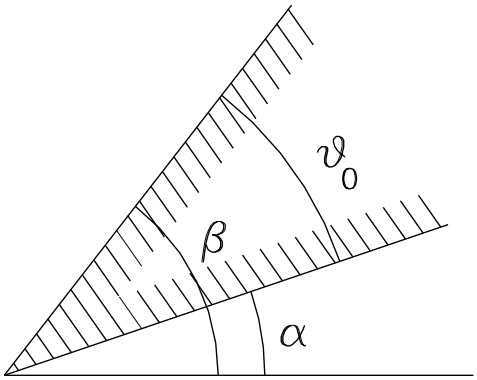

Fig. 7.12. The shape of the initial perturbation.

The system of equations (7.2.43) and (7.2.44) shows that, first, the flow near acute angles is independent of the flow of the rest of the fluid mass, because these equations do not include flow characteristics of other regions. Second, the corner point moves with constant acceleration, $-g$, which occurs due to the zero pressure gradient in it, and consequently, it falls freely. Third, the motion of the corner point and the rotation of the sides of the angle are independent, because systems (7.2.43) and (7.2.44) are decoupled. Fourth, the rotation and compression of the angle are determined only by initial conditions, and if the fluid was initially at rest ($\phi(\vec{r},0)=0$), it follows from (7.2.44) that the angle will neither continue to rotate nor be compressed, and it will fall freely like a rigid body whose side angles α and β will be rigidly fixed in space.

Self-similarity for angles larger than $\pi/2$

Now consider the case of angles $\theta_0 > \pi/2$. The fluid is assumed to be initially at rest. Then, at subsequent times, when the nonlinear terms are still small, and the surface has not had time to displace much, the flow in the bulk of the fluid will be determined by the linear problem

$$\Delta\phi = 0 \ ; \qquad (7.2.45)$$

$$\frac{\partial\phi}{\partial t} + gy\,|_s = 0 \ .$$

In this case, the expansion of the potential in powers of the distance from the angle's vertex at a sufficient distance from the vertex where the nonlinear terms are still insignificant, in addition to the powers of (7.2.42), the following terms will be present and will play an important role:

$$C g t |\vec{r} - \vec{r}_0|^n \cos n\theta \ , \qquad (7.2.46)$$

$n = k\pi/\theta_0$, k is an integer, θ is the angle counted from the angle bisector. Indeed, such terms satisfy the equations (7.2.45), and the lowest power n making the principal contribution to the expansion is $n = \pi/\theta_0$. When $\frac{\pi}{2} < \theta_0 < \pi$, the terms of the form (7.2.46) will be larger than quadratic terms, but smaller than linear terms in the expansion (7.2.42). Therefore, the motion of the corner point is still governed by the equation (7.2.43), i.e., it is a free fall. In the next approximation, however, the motion of the angle will already be related with the motion of the rest of the fluid through the coefficient C, which is determined by the solution of the linear problem (7.2.45) for all the fluid*. When $\theta_0 > \pi$, terms of the form (7.2.46) are larger than linear terms, and the motion induced by them becomes principal. In any case of $\theta_0 > \frac{\pi}{2}$, after the subtraction of the linear expansion terms (7.2.42) from the potential φ, the motion generated by the asymptotics (7.2.46) will be symmetric with respect to the bisector, which remains therewith motionless.

In the frame of reference related to the freely falling corner point, the motion at large distances from the corner point will be defined by the potential (7.2.46). The nonlinear terms in the equation (7.2.41) and the variation of the boundaries (7.2.40) will become significant at distances determined by the relationship

$$r \sim vt \sim \frac{\phi}{r} t \sim C g t^2 r^{n-1}$$

(here and below, we denote $r = |\vec{r} - \vec{r}_0|$). Thus, the nonlinear solution determining the angle region flow will be self-similar with a self-similar variable

$$\frac{r^{2-n}}{Cgt^2} \qquad (7.2.47)$$

and potential asymptotics (7.2.46) at large distances.

---

* It is easy to prove that the constant C should be positive. Indeed, if we introduce the potential $\varphi^* = \varphi + g\,yt$, for it the boundary conditions of (7.2.45) will be $\varphi^* \big|_S = 0$, $\varphi^* \ (y \to \infty)\ g\,yt$. The potential φ^* is a harmonic function; consequently, it cannot have a minimum, which means it must be positive everywhere. But that implies that the first nonlinear term in the expansion φ should also be positive.

Equations Describing the Flow for Close-to-Right Angles

The problem of a fluid flow near the angle can be simplified in the case of angles close to $\pi/2$. In this case, one can seek the solution of the problem (in the frame of reference related to the falling angle vertex) in the form

$$\phi = \frac{a(r,t)r^2}{2}\cos(2+\delta n)\theta \ ;$$

$$s = rA(r,t) \ , \tag{7.2.48}$$

where $a(r,t)$ is a function slowly varying with r, $\delta n << 1$, s is the deflection of the surface boundaries from the arms of the right angle, which is assumed to be small ($A << 1$, $A > 0$ corresponds to compression). It follows from Laplace equation (7.2.38) that δn should satisfy the relationship

$$\delta n = \frac{d\ln a}{d\ln r} \ . \tag{7.2.49}$$

By substituting (7.2.48) and (7.2.49) into the equations. (7.2.40) and (7.2.41), we obtain the set of equations

$$A\frac{\partial a}{\partial t} - \frac{\pi}{8}r\frac{\partial^2 a}{\partial r \partial t} + \frac{a^2}{2} = 0 \ ;$$

$$\frac{\partial A}{\partial t} = a \ . \tag{7.2.50}$$

Thus, whereas for acute angles the problem was reduced to ordinary differential equations, for angles close to $\pi/2$, simplification is also possible, albeit less considerable, such that the 2D problem is reduced to a 1D problem.

Self-Similar Solution for a Right Angle

Let us employ the system (7.2.50) to analyze the motion of the angle $\theta_0 = \pi/2$ at zero initial conditions; i.e., the expansion of (7.2.46) is $\theta_0 = \pi/2$ assumed to hold true at large distances from the angle vertex:

$$\varphi = Cgtr^2\cos 2\theta \ . \tag{7.2.51}$$

Then, it follows from a comparison of (7.2.48) and (7.2.51) that the solution of the equations (7.2.50) should be sought in the following form:

$$a = 2Cgtu(\xi),$$

$$A = Cgt^2 w(\xi),$$

where

$$\xi = -\frac{8C g t^2}{\pi} \ln r$$

is the self-similar variable. Here, the equations (7.2.50) are reduced to a set of ordinary differential equations

$$w(u+2\xi u')+2\xi u'' + 3u' + u2 = 0 ; \qquad (7.2.52)$$

$$w + \xi w' = u$$

with initial conditions $u(0) = w(0) = 1$.

The plots of the functions $u(\xi)$ and $w(\xi)$ are shown in Fig. 7.13. At $\xi >> 1$, $u(\xi)$and $w(\xi)$ become of the order of $\xi^{-2/3}$, which means that the magnitude of the angle is $A \sim t^{2/3}/(-\ln r)$. This means that, at a given distance from the vertex, the angle that initially collapses as $\sim t^2$, closes more slowly at later times, as $\sim t^{2/3}$. Note that at $r \to 0$ $A \to 0$; consequently, the angle remains right, although only with logarithmic accuracy. It should be noted that at later times the angle can be considered acute and nearly independent of r due to the weak logarithmic dependence on radius. Then, for its closing at a given r, one can use equations of motion of an acute angle (7.2.44) that at small A and when $B = 1/A$ also yield the dependence $A \sim t^{2/3}$. Thus, the regions of applicability for the solutions of equations (7.2.44) and (7.2.50) overlap, and the asymptotics of the solution of the equations (7.2.52) can be used as initial conditions for the equations (7.2.44).

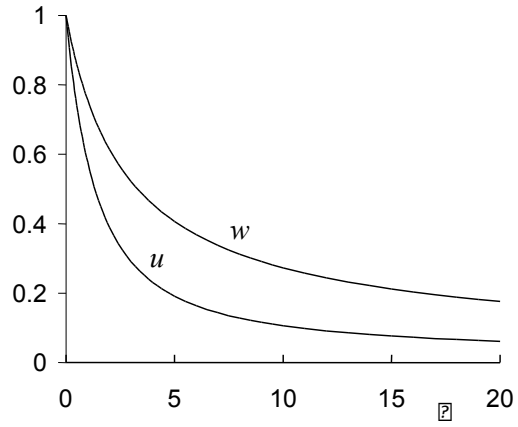

Fig. 7.13. Functions of self-similar variables that determine the growth of right-angle perturbations.

Self-Similar Solution for Angles Slightly Larger than the Right Angle

If the initial angle θ_0 slightly exceeds $\pi/2$, its closure can also be described using the equations (7.2.50). Let the initial angle deflection from the right angle be $A = -A_0$, $A_0 << 1$. Then, in accordance with (7.2.46) and (7.2.47), the solution of the corresponding angle closure problem will be self-similar:

$$a = \frac{2C\,g\,t}{r^{8A_0/\pi}}u(\xi) \ ,$$

$$A = -A_0 w(\xi) \ ,$$

where

$$\xi = \frac{C\,g\,t^2}{A_0 r^{8A_0/\pi}} \ .$$

The equations (7.2.50) in these variables will again transform into a set of ordinary differential equations,

$$2\xi^2 u'' + (5-2w)\xi u' + (1-w)u + \xi u^2 = 0 \ ,$$

$$w' = -u \qquad (7.2.53)$$

with initial conditions $u(0) = w(0) = 1$. The pattern of angle closure determined by the self-similar solution of the equations (7.2.53) is shown in Fig. 7.14 for the case of $\theta_0 = 2\pi/3$, $A_0 = \pi/12$ (we show a half angle, because the problem is symmetrical with respect to the bisector; the coordinates x, y are measured in the units $(C\, gt^2/2A_0)^{\pi/8A_0}$. At $\xi >> 1$ $w \sim -\xi^{1/3}$, i.e., at large times, the angle closes according to the same law $t^{2/3}$ as does the right angle, and similarly to the right-angle case, because of the weak dependence on r, closing of the angle at large times for each r can be described using the formulas (7.2.44).

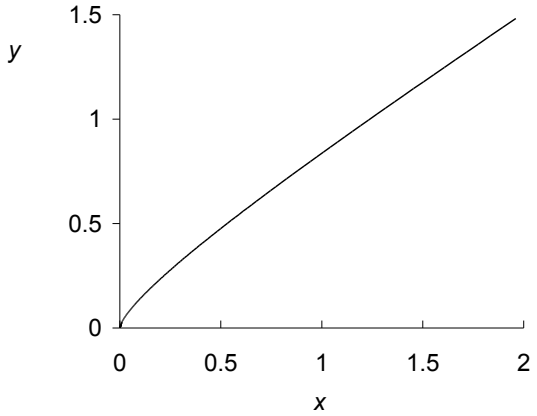

Fig. 7.14. The pattern of self-similar growth of a perturbation in the form of an angle slightly larger than the right angle.

Localized Initial Perturbation

The case of $\theta_0 = \pi$ (localized perturbation) is special, because there is no angle at all in this case, and perturbation evolution does not depend on the geometry of all the fluid. However, let us consider this case in more detail in view of its especial importance, because any perturbation initially occupying a limited region* should, in a sufficiently large time, "forget" its initial shape.

The unperturbed surface of fluid is assumed to be horizontal based on the equilibrium condition [7.8]. For dimensional reasons it follows that

$$\phi = \frac{gt^3}{2}\psi\left(\frac{2x}{gt^2}, \frac{2y}{gt^2}\right).$$

* Note that the evolution of such perturbations is commonly addressed in the analysis of the sausage z-pinch stability [7.33]. As long as the perturbation size remains small by comparison with the pinch radius, this case is reduced to the plane case of the Rayleigh-Taylor instability.

Equations (7.2.38), (7.2.40), and (7.2.41) for the function ψ in the self-similar variables denoted below by the same letters $x = 2x/gt^2$, $y = 2y/gt^2$ are written as

$$\Delta\psi = 0 \ ; \tag{7.2.54}$$

$$3\psi - 2r\nabla\psi + (\nabla\psi)^2 + Y\,|_s = 0 \ ; \tag{7.2.55}$$

$$\frac{dY}{dX} = \frac{Y - \dfrac{\partial\psi}{\partial y}}{X - \dfrac{\partial\psi}{\partial x}}\,|_s \ , \tag{7.2.56}$$

where $Y(X)$ is the free surface equation (note that self-similar equations describing the growth of a localized perturbation in the axially symmetric case coincide with equations (7.2.54–7.2.56) for the polar coordinates r, z, except that the Laplacian is written in the polar coordinates, and y is replaced with z, and x, with r). Since the fluid particles that came to motion in early stages will freely fall at large times, the coordinates of the tip of the spike will be $X = 0$, $Y = -1$. The fluid is at rest at infinity. Then, the surface can be expected to have the shape shown in Fig. 7.15 (we show half of the surface, because the problem is symmetrical with respect to the replacement $x \to -x$). Equations (7.2.55, 7.2.56) suggest that at the top of the bubble and at the tip of the spike

$$\phi_y(0, y_0) = y_0 \ ;$$

$$\phi(0, y_0) = \frac{y_0^2 - y_0}{3} \ . \tag{7.2.57}$$

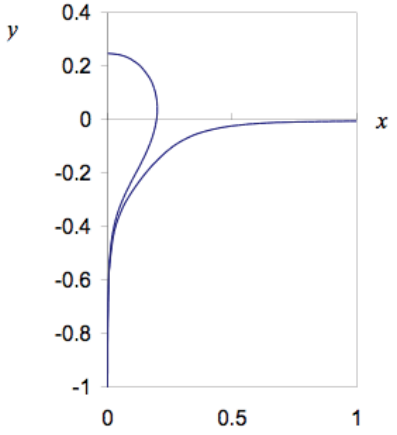

Fig. 7.15. Shape of the surface with self-similarly growth of localized perturbation.

Problem (7.2.54–7.2.56) was solved numerically in the following way. There were several point "charges" Q_i with potentials $-Q_i \ln r_i$ (r_i is the distance from the charge) outside the fluid. Then, equation (7.2.54) is satisfied automatically. It follows from the problem symmetry that the charges should be arranged symmetrically with respect to the axis y. The requirement that the total fluid flux coming from infinity should be zero (locality condition) yields $\sum_i Q_i = 0$. In addition, the charges were subject to condition (7.2.57). For the given arrangement of charges and the given coordinate of the bubble top Y_0, we solved equations (7.2.56) for the surface shape. Then, the charge locations and the bubble top coordinate were varied for the left side of (7.2.55) to be close to zero.

For five pairs of charges, the charge coordinates and values obtained by simulations and corresponding to the minimum mismatch of (7.2.55) are given in Table 7.1 (Q is the total charge of the pair, X is the coordinate of the right charge). The maximum value of the left-hand side in (7.2.55) was 0.022. The shape of the surface is presented in Fig. 7.15. The coordinate of the bubble top is $Y_0 = 0.248$, and its diameter is 0.400. The computed bubble diameter agrees with measurements [7.28], in which it was 0.46. At the same time, the computed depth of bubble penetration into the fluid is considerably smaller than that measured in experiments [7.28]: $Y_0 = 0.4$. The same situation is observed in the case of axisymmetric local perturbation evolution: the bubble diameter obtained numerically by Garanin and Startsev [7.29] agrees with the experiment, while the depth of bubble penetration does not. This is probably attributable to measurement errors, because the height of bubble ascent in the experiment was counted from the surface, which, being unstable, was covered with spikes, and the coordinates of which were difficult to determine for this reason.

Table 7.1. Coordinates and quantity of charges that generate the potential of the self-similar solution in case of localized perturbation**.**

X	Y	Q
0.038	0.101	-0.05674
0.303	-0.673	0.17760
0.520	-0.617	-0.30622
0.255	-1.211	0.83059
0.499	-1.434	-0.64523

Thus, for the self-similar solution we obtain the surface shape shown in Fig. 7.15. However, one can put a question: How can a localized initial perturbation assigned in the shape of a projection, rather than a hole, transform itself into the shape shown in Figure 7.15? One can imagine that the initial projection produces a spike surrounded by bubbles on both sides and that, with time, the spike thickness will increase more slowly (if at all) than the bubble dimensions, and in the growing scale of the problem the role of the spike with time will trend to zero. Such an evolution dynamics is confirmed by experimental data (see, for example, Volchenko *et al.* [7.28]), which show that neighboring bubbles merge into a single bubble.

Opening of the angles $\theta_0 < \pi$ (inner) can be analyzed using the same technique of solving 2D self-similar equations as that described above for $\theta_0 = \pi$, this time, however, taking into account the asymptotics of (7.2.46). The flow pattern may turn out to be similar to that shown in Fig. 7.15, i.e., spikes may form, which will stay at the location of the original angle vertex.

7.3. MHD Turbulence and MHD-Turbulent Plasma-Cooling Mechanisms

7.3.1. Behavior of 2D Magnetohydrodynamic Turbulent Flows Across a Magnetic Field in a Bounded Region.

Two-dimensional magnetohydrodynamic (MHD) flows of plasma across a magnetic field play an important role in many dynamic plasma systems with magnetized plasma, including the MAGO system, in which plasma motion at both stages (formation of hot magnetized plasma, and its compression) occurs in the $r - z$ plane perpendicular to the azimuthal magnetic field.

Plasma heating at the first stage occurs when the plasma is pushed to flow from section 1 to section 2 by the magnetic piston (Fig. 7.16). The initially cold plasma is accelerated in the nozzle region to supersonic velocities (exceeding the Alfven velocity) and is heated during its deceleration in collisionless shockwaves formed at the exit from the nozzle (Chapter 4) and, as a result of anomalous viscous heating, in the near-electrode layers (Chapter 5). In this way, the magnetic energy of the plasma is first transformed into kinetic and then thermal energy. After the passage of the plasma to the second section and leveling out of the total pressure in the first and second sections, there forms relatively quiet plasma in the second section with $\beta \sim 1$ (β is the thermal-to-magnetic pressure ratio) and essentially subsonic velocities.

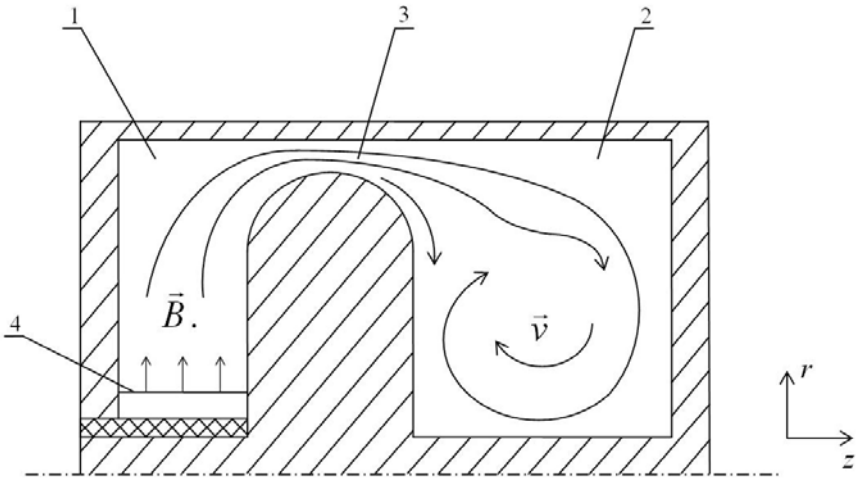

Fig. 7.16. Schematic diagram of the MAGO plasma chamber: B is the magnetic field, 1 and 2 are first and second sections, 3 is the annular nozzle, and 4 is the magnetic piston.

It is this plasma that is intended for compression in a quasi-spherical or cylindrical manner by moving the walls of the second chamber section (e.g., by moving the outer cylindrical chamber wall in Fig. 7.16 inward along the radius). In spite of the comparatively low plasma velocities and low kinetic energy of the plasma by comparison with the magnetic energy, these velocities are still higher than compression velocities, and this plasma motion is important in several aspects. First, this plasma motion can affect the convective plasma cooling, carrying heat from hot plasma regions to the cold walls. Second, while moving, the plasma can get contaminated with impurities washed away from the walls. Such washing-off of the wall material can be especially substantial when the plasma is compressed for thermonuclear ignition, because the wall material in this case is obviously in the plasma state and, as it has no strength, it easily intermixes with the hydrogen plasma. Therefore, for such systems, it is important to know how the hydrodynamic flow will evolve after the plasma heating stage and how long it will be maintained.

Classical transport coefficients of hot magnetized plasma [7.33], such as viscosity and the magnetic diffusion coefficient, are small in the MAGO chamber conditions, which is why those flows are characterized by large Reynolds and magnetic Reynolds numbers and, as is almost always the case with large Reynolds numbers, become turbulent. Since the plasma motion across the magnetic field occurs at small Alfven-Mach numbers M_A, MHD instabilities also develop across the magnetic field (Section 7.1) and the

turbulence that occurs is two-dimensional by nature [7.34]. It is difficult to get answers to fundamental questions concerning 2D flow relaxation in direct 2D MHD simulations (see Section 7.3.4), which are performed in a specific special geometry with specific boundary and initial conditions and which include a wide range of physical effects. The reason for this is that one has to separate the phenomena of interest against the backdrop of other effective factors, as well as that the inclusion of all the factors inevitably reduces computational capabilities concentrated on the study of 2D flow itself and phenomena directly associated with the flow. Therefore, it makes sense to consider the 2D turbulent MHD flow separately without taking into account phenomena insignificant to this flow. Since, in this case, the MHD problem is reduced to the problem of 2D hydrodynamic turbulence, its major features can be analyzed both in the MHD and in the 2D hydrodynamic formulation.

In this section, following Garanin *et al.* [7.35–7.37], we present the results of numerical simulations of flows in a bounded region for large Reynolds numbers in order to determine the parameters of such flows and the rate of kinetic energy dissipation. Possible dissipation mechanisms in our simulations are viscosity∗ and generation of sound with its subsequent nonlinear damping in shock waves.

Generation of Sound by Turbulence in a Bounded Region

Generation of sound and its subsequent shock-wave damping could rank among important kinetic energy dissipation channels for a 2D turbulent flow, because other mechanisms turn out to be weak in such flows as a result of the smallness of transport coefficients (viscosity and magnetic diffusion) and because the energy loss rate due to generation of sound (see Landau and Lifshits [7.8], as well as the results below) should be determined only by Mach numbers M (which are smaller than unity for real flows after the heating stage in the MAGO chamber, but not too small, at about M ~ 0.4). In order to explore the possibility of generation of acoustic waves by turbulence in a bounded volume for small Mach numbers M (the letter M will denote the total Mach number, which in our simulations was virtually equal to M_A), it is sufficient to analyze this possibility in a simplified formulation, for a 1D problem, in which a turbulent motion acts as a driving force producing compressions and rarefactions in the volume.

∗ For a magnetized plasma with $*(\omega\tau)_I >> 11$, viscosity-related energy dissipation is more significant than ohmic dissipation by a factor of m_i/m_e, and for small M_A, the relative contribution of the ohmic dissipation becomes even smaller.

The theory of sound generation by turbulence occupying a finite volume in an unbounded medium was developed by Lighthill [7.8]. This theory is applicable when the medium dimensions are large by comparison with the characteristic acoustic wavelengths excited by a turbulent flow. If the turbulence occupies a volume with a characteristic dimension of ~ L and there is no surrounding immobile medium, and characteristic flow velocities are ~ v, the characteristic wavelengths are ~ $\frac{c}{v}L$ (c is the velocity of sound, $c >> v$), which is much larger than the dimensions of the volume occupied by the turbulent flow. In this case, the Lighthill theory is inapplicable, and the question arises of whether acoustic waves are generated in this case, and if so, what the intensity of these waves is. In other words, will turbulent motion be dissipated along this channel and what will the rate of this dissipation be?

Since the scale of pressure pulsations in a turbulent flow is ~ ρv^2, to clarify this issue, we can consider a 1D flow generated in a region with a dimension ~ L by such pressure pulsations with a characteristic times of ~ L/v. Such pulsations of ~ ρv^2 can be produced if the relative volume variation equals ~ v^2/c^2, which corresponds to matter displacements of ~ $\left(\frac{v}{c}\right)^2 L$ for characteristic spatial dimensions of ~ L. For characteristic times of ~ L/v, these displacements correspond to characteristic velocities of ~ $\left(\frac{v}{c}\right)^2 v$. Therefore, we analyzed the flow in the region bounded by a rigid wall on one side and a piston performing preset oscillations with an amplitude of ~ $\left(\frac{v}{c}\right)^2 L$ and characteristic times of ~ L/v on the other side. We sought the answer to the following question: Will shock waves be excited in the region for small values of ν, and will the piston, on average, perform work? To make the motion of the piston sufficiently smooth at the initial time, its motion was defined in the form of the sum of two sine functions,

$$x = L\left(\frac{v}{c}\right)^2\left(0.55\sin\frac{2\pi t}{1.1T} - 0.45\sin\frac{2\pi t}{0.9T}\right), \qquad (7.3.1)$$

where $T = 2L/n$. To ensure that the simulations are credible, they were performed with a large number of grid cells over a long time span on the order of ~ 200 T.

Fig. 7.17 shows the velocity profiles obtained in computations with Mach numbers M ≡ v/c = 0.5 and M = 0.33 at time t = 1000 L/c. These profiles are representative for both computations and show that shock waves are formed in the region for M = 0.5 and are not formed for M = 0.33. Computations for other Mach numbers M show that shock waves are formed in the region for M ≥ 0.5 and the piston, on average, performs work, while no shock waves are formed for M ≤ 0.33 and the piston, on average, performs no work. Thus, one can conclude that in 2D turbulence, where a small fraction of energy is contained in a small-scale region (in the spectrum of 2D turbulence, the values of $E(k)$ for large wave numbers k decrease faster than k^{-3} [7.36]), this energy dissipation channel does not exist for small Mach numbers.

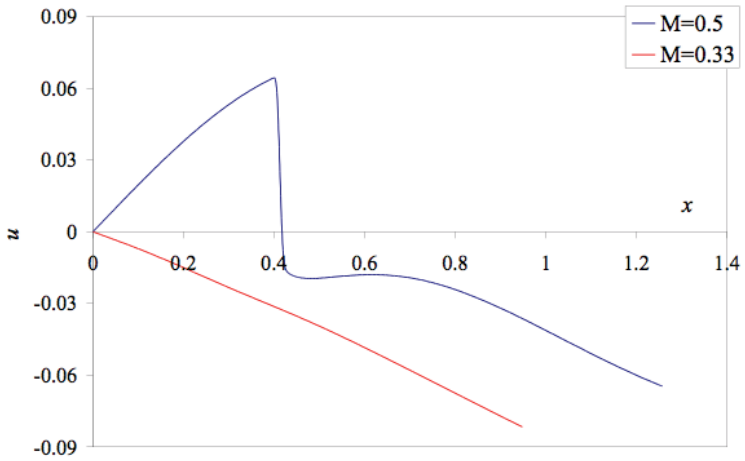

Fig. 7.17. Velocity profiles $u = v/c$ produced by the piston oscillating according to law (7.3.1) for Mach numbers M ≡ v/c = 0.5 and M = 0.33 at time t = 1000 L/c.

For 3D turbulence in a bounded region, however, this dissipation channel still exists because there a noticeable fraction of energy is contained in the short wavelength spectral region, although it is strongly suppressed for small values of M. Indeed, the characteristic frequencies of pulsations in the turbulent flow are ~ kv. Therefore, in the case of 3D turbulence, where $E(k) \sim k^{-5/3}$ for large values of k and, accordingly, the velocities are $v_k \sim v(kL)^{-1/3}$, the frequencies increase with k and the applicability condition $kv_k \sim c/L$ for the Lighthill theory holds for sufficiently large values of k. Since the amount of energy emitted acoustically by a unit of mass of a turbulent medium per unit time is given by

$$\varepsilon_s \sim \frac{v^8}{c^5 L},$$

the same estimate will be valid in the range of theory applicability upon the substitution of $v \to v_k$, $L \to 1/k$, which yields for a bounded volume

$$\varepsilon_s \sim \frac{v^{10.5}}{c^{7.5} L} .$$

Thus, the intensity of sound generation by a 3D turbulent flow is additionally attenuated in a bounded volume by a factor of $(v/c)^{2.5}$, by comparison with that in an unbounded medium.

Two-Dimensional Computations of Relaxation of a Vortex Flow

Garanin *et al.* [7.36] studied the relaxation of a 2D magnetohydrodynamic flow across the magnetic field in a bounded region for the case of a solitary vortex in a square box. The initial density was uniform. The computations demonstrated that, in accordance with expectations for 2D turbulence and as distinct from 3D turbulence, kinetic energy dissipates over the time $\sim L^2/\nu$ (L is the characteristic dimension of the system, ν is kinematic viscosity), which in these computations, where the viscosity was numerical $\nu \sim \nu \cdot \Delta x$ (Δx is the grid size), corresponded to the times $\sim \frac{L}{\Delta x}\frac{L}{v}$. Kinetic energy spectra of the turbulent flow in the bounded region in the inertial range (intermediate range between the energy-carrying and viscous ranges) subside with the growth of wave numbers rather rapidly—more rapidly than by the k^{-3} law. However, the strong nonuniformity of plasma density in the MAGO chamber could affect the processes of turbulence attenuation. The turbulence vorticity rot $\vec{v}$, which is conserved in 2D flows of ideal uniform fluid [7.8], is not conserved in fluid with nonuniform density; consequently, Kraichnan's arguments [7.38], derived for the 2D turbulence, to the effect that the energy cascade is impossible from larger to smaller scales, become invalid. However, although the vorticity is not conserved in a nonuniform fluid, one cannot exclude that the kinetic energy in the 2D turbulence of a nonuniform fluid will nevertheless be conserved at infinitesimal viscosity, and kinetic energy dissipation can turn out to be proportional, for example, to the square root of viscosity, as predicted by Chertkov [7.39] on the basis of Obukhov's heat conduction dissipation scenario [7.8].

In order to study this issue, 2D numerical computations of the same vortex in a square region were performed using the EGAK code [7.40]. The fluid was assumed to be nearly incompressible (small Mach numbers) and to have small viscosity (large Reynolds numbers). Both uniform density and essentially nonuniform density, with a 10-fold initial density difference, were considered. We studied viscosity effects on flow behavior and energy dissipation.

First, we considered a circular vortex flow in a square region for the case of uniform initial density. The region of $-3 < x < 3$, $-3 < y < 3$ was assumed to be initially filled with a substance of constant density $\rho_0 = 1$. The substance was assigned an azimuth velocity dependent on the radius according to the law

$$v_\varphi = \begin{cases} r & \text{at } 0 < r < 1, \\ 2 - r & \text{at } 1 < r < 2, \\ 0 & \text{at } r > 2 \end{cases} \qquad (7.3.2)$$

(the radius r and the azimuthal velocity $v\varphi$ are measured from the region center). The initial velocity distribution is shown in Fig. 7.18. We used an ideal gas equation of state with $\gamma = 2$. The initial velocity of sound was assumed to be constant and equal to $c = 2.5$, such that the initial Mach number in this simulation can be taken as M = 0.4. The turbulent flow in this case can be treated as a flow of incompressible fluid, because the kinetic energy in the entire region equals about 2% of the internal energy.

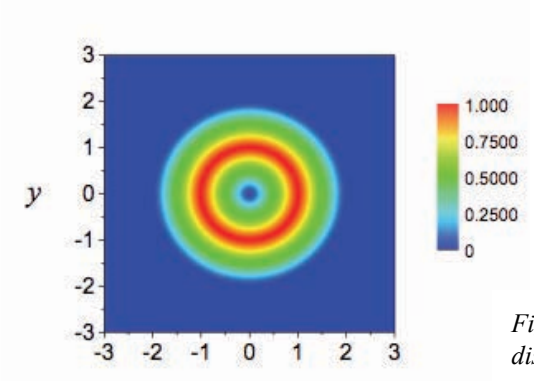

Fig. 7.18. Initial velocity distribution in the computations.

We slightly shifted the vortex over the y coordinate (by a magnitude 0.1) to create as full a set of perturbations as possible. In the calculations we used a rectangular Eulerian (i.e., fixed spatial) grid. The physical viscosity, which varied in different calculations, was the main dissipation process in the calculations.

Figure 7.19 shows the spatial distribution of the velocity absolute value obtained in the calculations with the number of grid cells at 400×400 and a dynamic viscosity of $\eta = 5 \cdot 10^{-5}$ (the effective Reynolds number Re ~10^4) at times $t = 80$, 120 and 500.

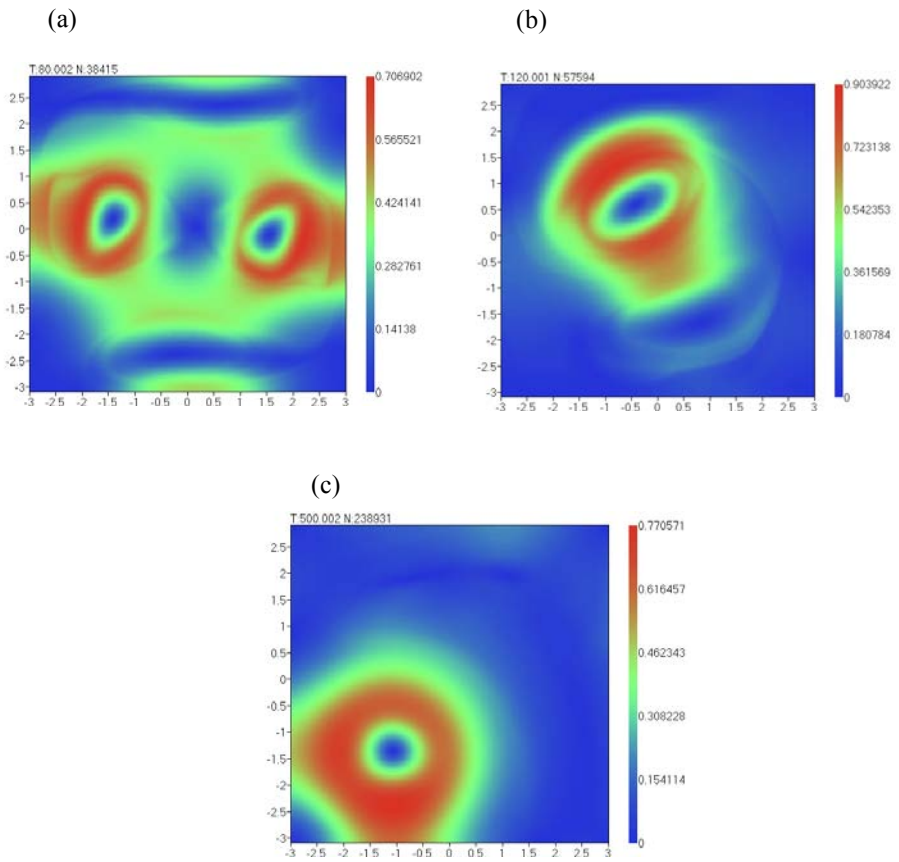

Fig. 7.19. Spatial distribution of the velocity absolute value obtained in the calculation with the viscosity $5 \cdot 10^{-5}$, with uniform initial density, with the grid cell number 400×400, at times a) t = 80, b) t = 120, and c) t = 500.

Figure 7.19 shows that the unstable vortex flow in the 2D case disintegrates as a result of the development of the instability; later in the region, however, in contrast to a chaotic turbulent flow (the kind that would be expected), a quasi-stationary flow is formed with one major vortex (two vortices formed in the region under other conditions and with other computational grids). In this flow, minor small-scale perturbations are present that do not, however, make the vortex disintegrate, and their growth is saturated, apparently as the result of nonlinear effects. In time, the major vortex slowly shifts within the region under consideration.

Figure 7.20 presents the time dependence of the system's kinetic energy in computations with varying viscosities. The figure shows that, as expected, the kinetic energy of the 2D turbulent flow with large Reynolds number decays rather slowly. As one would expect, this decay turned out to be essentially proportional to the viscosity.

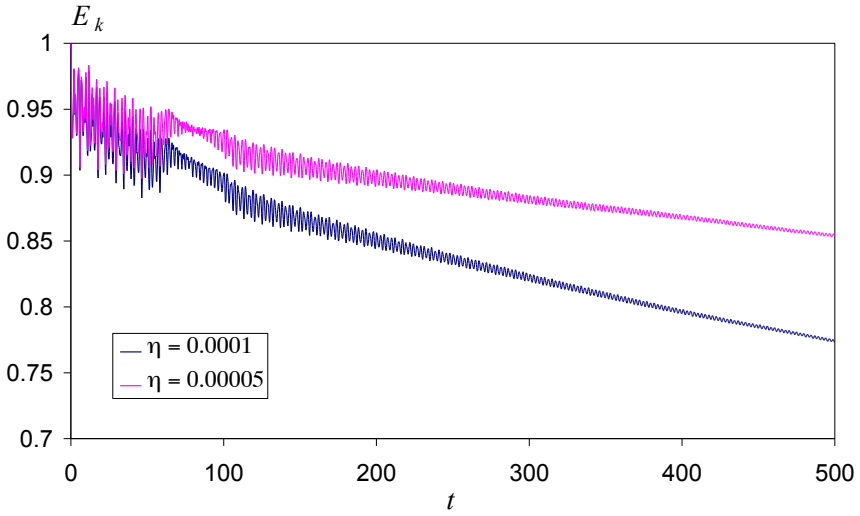

Fig. 7.20. Time dependence of the system's kinetic energy E_k (measured in the units of the initial value) in the computations with uniform initial density, grid cell number 200×200, and varying viscosities.

The following modifications of the initial conditions were introduced into the computations in order to study of the effect of the density heterogeneity on the relaxation of the vortex flow. In the zone $r < 2$, where the initial velocity does not equal zero, the material density ρ_1 was assigned to be one-tenth the density ρ_2 in the rest of the zone. The total mass of the material remained unchanged. The dependence of the velocity on radius (7.3.2) remained the same, but a coefficient 2.62 was introduced into that formula to keep the initial value of the kinetic energy unchanged. The initial pressure in the area was assumed to be constant and equal to the material pressure in the problem with constant density. Thus the Mach numbers were the same as in the problem with constant density.

Figure 7.21 presents the spatial distribution of the velocity absolute value obtained in the computations. The figure shows that in those computations, after the vigorous turbulent phase, the phase of quasi-stationary flow with two slowly changing vortices occurs. These vortices have lower densities inside. The turbulent phase is accompanied by considerable density equalization, and in the quasi-stationary phase the density equalizes rather slowly.

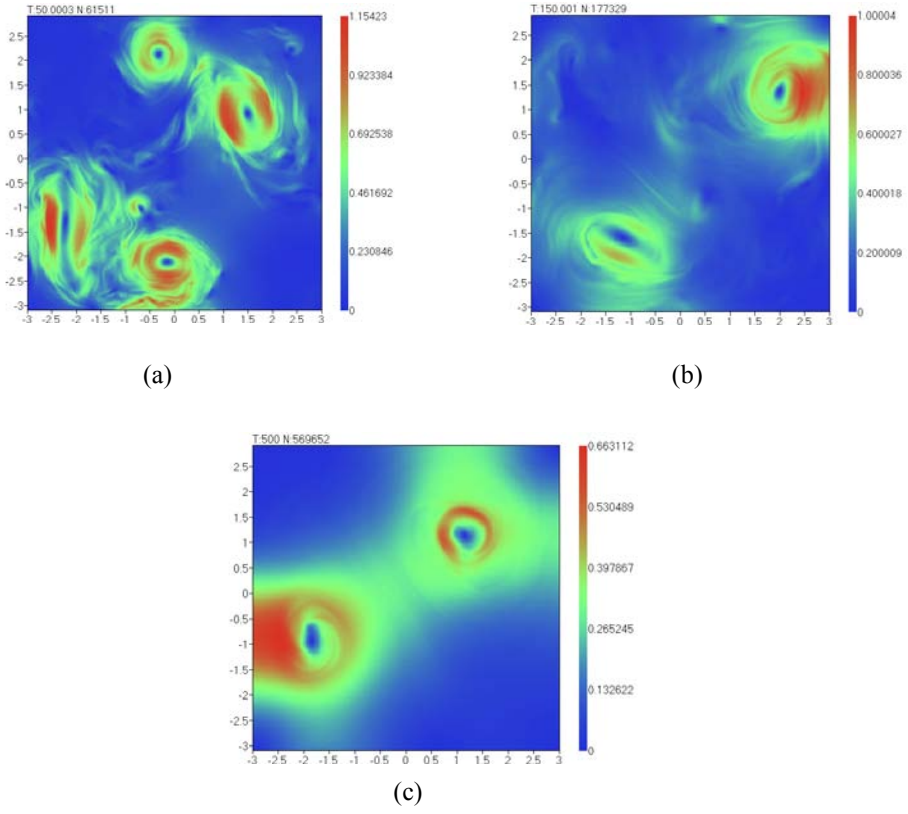

(a) (b)

(c)

Fig. 7.21. Spatial distribution of the velocity absolute value obtained in the calculations with the viscosity $5 \cdot 10^{-5}$, with nonuniform initial density ($\rho_2 = 10\rho_1$), with the grid cell number 400×400, at times a) t = 50, b) t = 150, and c) t = 500.

Figure 7.21 shows that, the circular motion breaks down faster in the case of nonuniform density than in the case of the uniform density in Fig. 7.19. The next phase of vigorous turbulent flow reorganization is more active in the case of nonuniform density and is accompanied by the appearance of

smaller-scale zones in which kinetic energy could dissipate. However, after that is a lengthy quasi-stationary phase similar to that in the case of uniform density. For the vortices formed in this stationary phase, both in the nonuniform case and the uniform case, in a considerable part of the distances r from their centers, the condition of stability [7.8] is fulfilled

$$v_\varphi \frac{d(\rho v_\varphi r)}{dr} > 0, \qquad (7.3.3)$$

where v_φ is the azimuthal velocity relative to the vortex center.

Figure 7.22 shows the time dependence of the system's kinetic energy in the calculations with a nonuniform initial density, a grid cell number 200×200, and varying viscosities. A comparison of Fig. 7.22 and Fig. 7.20 shows that when a nonuniform initial density is assigned, the kinetic energy decay over the times considered is substantially larger than in the case of a uniform initial density; however, this entire difference is accumulated during the turbulent phase of the flow reorganization; in the quasi-stationary phase the decays of kinetic energy in the uniform and nonuniform cases are small and commensurate.

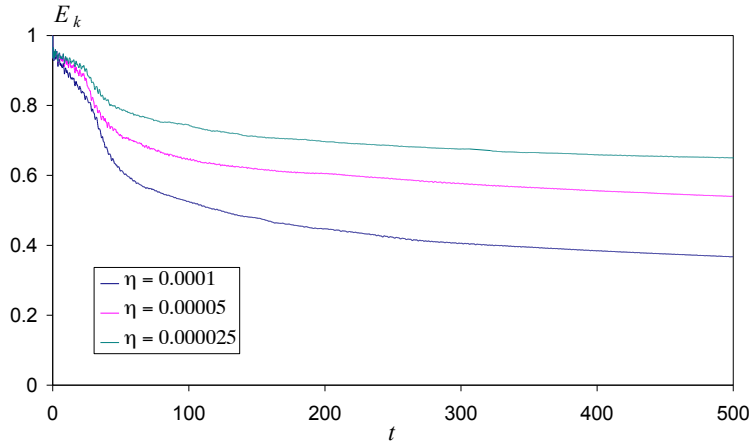

Fig. 7.22. Time dependence of the system's kinetic energy E_k (measured in the units of the initial value) in the calculations with nonuniform initial density, a grid cell number 200×200, and varying viscosity.

Figure 7.22 shows that the viscosity played an important role in the calculations under consideration. We can ask ourselves how the kinetic energy decrease in a 2D turbulent flow of heterogeneous fluid is connected with viscosity. If we suppose that it is connected with the viscosity in the same manner as in the case with 2D turbulence for a homogeneous fluid,

then the kinetic energy decay decrements should be proportional to the viscosity. But if it is qualitatively the same as in the 3D turbulence and is connected with the energy transfer to smaller scales (as in the Kolmogorov-Obukhov scenario), the kinetic energy decay should not depend on the viscosity. In the intermediate case, according to Chertkov's predictions [7.39] the kinetic energy decay decrement can be determined by the heat-conductance dissipation [7.8] for the system with characteristic accelerations that facilitate the mixing in the active turbulence phase $\sim \nu^2/L$ and can be proportional to the square root of the viscosity.

Thus, the selection of scenario is determined by the dependence of the kinetic energy decay decrement λ on the viscosity η

$$l \sim \eta^k,$$

where $k = 1$ corresponds to the scenario of 2D turbulence of a homogeneous fluid, $k = 0$ corresponds the Kolmogorov-Obukhov scenario, while $k = 0.5$ corresponds to Chertkov's prediction. Using Fig. 7.22, we compared the kinetic energy decay decrements for the viscosities differing two-fold from each other. In the most vigorous phase of turbulent flow corresponding to the time interval $20 < t < 100$, the ratio of the decrements turned out to be 1.44, that is, close to $\sqrt{2}$, and thus better corresponding the prediction [7.39]. Then, at a quieter phase of the quasi-stationary vortex corresponding to the time interval $200 < t < 500$, the ratio of the decrements turned out to be 1.71, that is, intermediate between the scenario of the 2D turbulence with a homogeneous fluid and the prediction [7.39].

However, the correlation functions built in the inertial interval for the performed calculations confirmed neither of the mentioned scenarios. For the Kolmogorov-Obukhov scenario, in the inertial interval, the velocity pulsations, as well as the density pulsations, should have been proportional to $r^{1/3}$, where r is the distance between points. For the scenario of Chertkov [7.39] the velocity pulsations δv should have been proportional to $r^{0.6}$, and the density pulsations should have been $\delta\rho \sim r^{0.2}$; while for the 2D turbulence of a homogeneous fluid, there should have been $\delta v \sim \delta\rho \sim r$.

Figure 7.23 shows the velocity correlation function $(\delta v)^2$ obtained in the calculations in the inertial interval for different times. The graph shows also the trend lines $(\delta v_l)^2 \sim r^n$ and indicates the exponent n for the corresponding times. It can be seen from Fig. 7.23 that for only one of the times presented, $t = 30$, can the velocity correlation function correspond to one of the scenarios under consideration—Chertkov's scenario [7.39]. This also corresponds to the square root dependence of the energy dissipation rate on

the viscosity found for this time interval. However, even for this instant of time the density correlation function obtained in this calculation and having the scaling $(\delta\rho)^2 \sim r^{0.96}$ in the inertial interval does not correspond to the scenario [7.39] $\delta\rho \sim r^{0.2}$. The scalings of the density correlation function obtained for other times (see Table 7.2) failed to reveal correspondence with the enumerated turbulence development scenarios or any clear correspondence with the velocity correlation function scalings, as well.

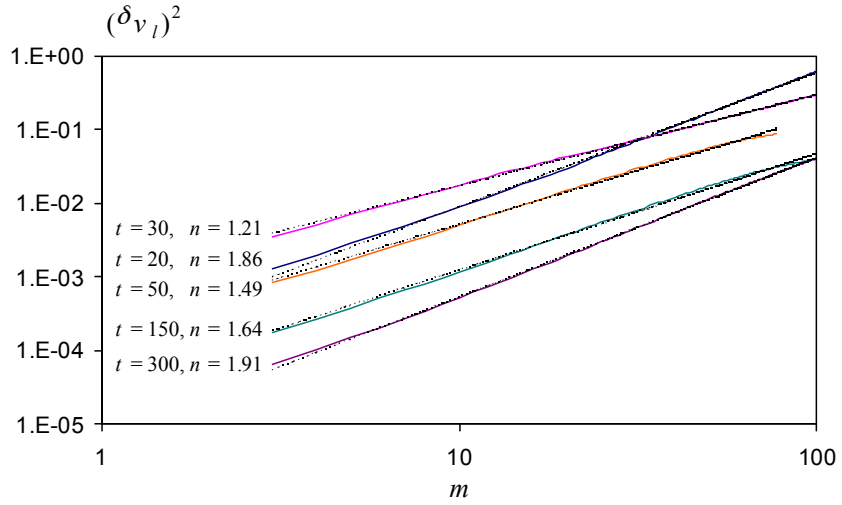

Fig. 7.23. Velocity correlation function in the calculations with nonuniform initial density, a viscosity of 0.00005, and a 400×400 grid at different times; m is the spatial scale measured in the units of numerical-calculation grid cell; n is the trend line exponent describing the correlation function by the power dependence.

Table 7.2. Scalings of the velocity correlation function, $(\delta v)^2$, and the density correlation function, $(\delta\rho)^2$, in the inertial interval.

t	$(\delta v)^2$	$(\delta\rho)^2$
20	1.86	1.23
30	1.21	0.96
50	1.49	0.84
150	1.64	0.96
300	1.91	1.66

CONCLUSION

Thereby, based on the calculations performed, we can draw the following conclusions about the main features of 2D turbulent flows in a bounded region:

In the case of 2D turbulence in a bounded region at low Mach numbers, turbulence causes no sound generation, and, thus, this dissipation channel does not exist for small Mach numbers M.

The calculations showed that in the case of both uniform and nonuniform density, the 2D flow within a bounded region, being unstable, starts to break up with time because of the growth of perturbations and acquires a complex turbulent form. However, the flow then turns into one or two vortices, which, although slightly twisted by the perturbations occurring, retain their shapes on the whole. In such form, the flow is quasi-stationary, gradually losing energy due to viscous dissipations.

In the case of uniform density, the kinetic energy decays with time rather slowly in both phases: in the phase of the flow reorganization, when it has a complex turbulent form, and in the quasi-stationary phase. Here the decay of the kinetic energy is proportional to the viscosity, as it should be in the case of a 2D turbulent homogeneous fluid.

In the case of nonuniform density in the phase of the flow reorganization, when it has a complex turbulent form, there is a relatively large drop in kinetic energy and a relatively rapid equalization of the material density throughout the volume. In the quasi-stationary phase, the density equalizes throughout the volume rather slowly, and the density minimums form in the centers of the vortices. The kinetic energy in this phase also drops slowly, almost as slowly as in the case of a homogeneous fluid.

The preliminary results indicate that in the active phase of the flow reorganization, the kinetic energy decay decrements are proportional to the viscosity square root, i.e., they correspond neither to the 2D turbulence of a homogeneous fluid, where they should be proportional to the viscosity, nor to the Kolmogorov-Obukhov scenario, where they should be independent of the viscosity. The square root dependence on the viscosity corresponds to Chertkov's prediction [7.39], based on the scenario of Obukhov's heat-conductance dissipation [7.8]. In the quasi-stationary phase, the kinetic energy attenuation decrement turned out to be proportional to the viscosity to the power of 0.77, which is an intermediate value between the dependence according to Chertkov [7.39] and the dependence for the 2D turbulence of a homogeneous fluid. However, the correlation functions built in the inertial interval for the calculations performed have confirmed neither of the mentioned scenarios. We should note, however, the preliminary nature of the results obtained.

Because of considerable differences of the properties of 2D and 3D turbulent flows, one should be careful when applying 2D calculations to 3D turbulent flows. In 3D turbulent flows, the attenuation of the kinetic energy, the heat transfer, and the mixing of materials can proceed considerably faster than in 2D calculations. Thus, for the flow in a bounded region, in the 3D case, the kinetic energy attenuation should proceed over times $\sim \alpha L/\nu$, where α is a small factor characterizing the value of turbulent pulsations, whereas in 2D calculations, the kinetic energy attenuation proceeds over times $\sim L^2/\nu$ for uniform densities or $\sim L^{3/2}/\sqrt{\nu}$ in the vigorous phase of the flow reorganization for nonuniform density.

Since the energy dissipation time for 2D turbulence depends on the viscosity, for calculations of plasma flows in a magnetic field, one must properly describe the physical mechanisms leading to the dissipation (the longitudinal physical viscosity [7.33], which, in the case of magnetized plasma, can be determined mainly by the establishment of equilibrium between longitudinal and transverse degrees of freedom of ions, and strongly magnetized shear viscosity [7.33]).

Distribution of plasma impurities and temperature can be more inhomogeneous than in the 3D case, which can turn out to be significant for the description of plasma radiation on the impurities and its cooling. Since the kinetic energy of the turbulent motion in the 2D case decreases more slowly, the impurities can be washed out from the walls over longer times and, thus, can be more dangerous than in the 3D case.

7.3.2. Convective Plasma Cooling During its 2D Turbulent Motion in Magnetic Field

In the MAGO/MTF approach, wall-confined preheated magnetized plasma is brought to thermonuclear temperatures by liner compression. In this approach, the plasma cooling caused by the transfer of heat into the cold walls can be amplified because of the presence of convective turbulent motion; this heat transfer depends essentially on whether the forming turbulent motion is 2D, or 3D. In the MAGO system this flow is 2D and depends on coordinates *r* and *z*, since the azimuthal magnetic field impedes the bending of the magnetic field lines and occurrence of flows that violate azimuthal symmetry. In this section, the processes of convective heat transfer to walls are studied via the use of estimations and 2D MHD calculations [7.41]. Two options to increase the heat transfer are considered:

The turbulent motion in the chamber, which is caused by the initial plasma flow and the plasma flow that maintained over that time, can, in theory, bring the hot plasma from the depth to the wall, thereby increasing the heat transfer. This option will be called the turbulent thermal diffusion.

When the plasma comes in contact with the external wall, its cooling causes a decrease in its pressure and, accordingly from the equilibrium conditions, an increase of the magnetic field. As a result, the conditions are created for the development of the sausage instability, $m = 0$, and the cooled plasma elements descend to smaller radii. Then, the descending cold plasma mixes with the hot plasma at small radii, and the formed turbulent motion intensifies the heat transfer. This option will be called convection.

Turbulent Thermal Diffusion

The processes of turbulent thermal diffusion can be described qualitatively using the notion of the turbulent diffusivity D, which, in the case of 3D turbulence, can be considered to be equal on the order of magnitude (just like the kinematical coefficient of viscosity [7.8])

$$D_t \sim \alpha L v ,$$

where L is the dimension characteristic for the considered flow, v is a characteristic flow velocity, and α is a small dimensionless numerical factor. If we consider the process of heat transfer to the wall by turbulent flow, distance x from the wall should be taken as the characteristic dimension L, and then the turbulent diffusivity will be equal to

$$D_t \sim a x v .$$

In the case of 2D turbulence in a bounded region, since small energy (Section 7.3.1) is contained in a region of small scales (large wave numbers), the relative velocity v of two particles a small distance x apart is determined by large scales of the flow and is proportional to this distance

$$\delta v \sim v \frac{x}{L} . \qquad (7.3.4)$$

In the near-wall region, where, by contrast with the 3D case, the turbulent velocity pulsations will no longer be of the order of the velocity itself, but will be of the order of (7.3.4), the effective diffusivity (and, accordingly, turbulent thermal diffusivity) can be considered to be

$$D_t \sim \alpha x \delta v \sim \alpha \frac{x^2}{L} v , \qquad (7.3.5)$$

that is, decreasing quite intensely with the approach to the wall. The turbulent coefficient of kinematical viscosity of the order of (7.3.5), in agreement with Clercx and van Heijst [7.42], yields the frictional force of the flow against the wall

$$F \sim \alpha u^{3/2} \sqrt{\rho \eta / L}$$

(u is the flow velocity), proportional to the square root of the physical viscosity, η.

Convection

If hot plasma at large radii borders an external conductor, the plasma will be cooled down because of its contact with the cold metal wall. The cooling process should be enhanced with convection. In fact, as a result of cooling, the plasma parameter $\Phi = \frac{p^{1/\gamma} r}{B}$ decreases and, thus, an area is created in which the condition of Kadomtsev [7.9]

$$\frac{\partial \Phi}{\partial r} < 0$$

is fulfilled for convection development. The plasma cooling processes with MHD convection inclusion were numerically simulated by Lindemuth *et al.* [7.43].

Let us consider the process of convective plasma cooling. Assume that at the initial time, plasma with $\beta \sim 1$ is in contact with a cold wall of radius R. If we consider the plasma motion at distances $x \leq R$, then the plasma being cooled will attain the acceleration

$$g \sim c^2/R$$

where c is the sound velocity in the plasma. Initially, for small times, when

$$g t^2 < \sqrt{\kappa t}$$

(κ is the real, not turbulent, plasma thermal diffusivity), the plasma cooling will proceed according to the diffusion law

$$x \sim \sqrt{\kappa t} \ .$$

At $t > \kappa^{1/3}/g^{2/3}$ convection enters the process. Then, at the diffusion layer boundary

$$x_D \sim \kappa^{2/3}/g^{1/3} \ ,$$

temperature of the order of initial temperature T_0 is maintained. The motion of the mixing layer will be determined by the equation

$$\frac{d^2 x}{d t^2} \sim \frac{x}{t^2} \sim 0.1 g \frac{\delta T}{T_0} \ , \qquad (7.3.6)$$

where the multiplier $\delta T/T_0$ (δT is the temperature variation in the layer x) describes the decrease of the gravitational force lowering the cooled plasma to smaller radii. In addition, given that in 2D case bubbles rise at roughly ~ 0.1 gt^2 (Section 7.2.3), we introduce the multiplier 0.1 into the formula (7.3.6). Since the diffusion zone size remains constant and, consequently, the heat flux is also constant, with taking into account formula (7.3.6), we obtain the time dependence of the convection zone width

$$x \sim 0.09\ \kappa^{1/6} g^{2/3} t^{3/2} \tag{7.3.7}$$

and the temperature distribution in the convection zone

$$\delta T / T_0 \sim 0.4 \frac{\kappa^{2/9}}{g^{1/9} x^{1/3}} \ . \tag{7.3.8}$$

In the 2D computations, this convection is taken into account automatically. In the 1D computations, for example, for a cylindrical system in which all quantities (averaged over the turbulent pulsations violating azimuthal symmetry) depend solely on radius r, the convection can be modeled as follows. At each plasma point, short-wave increments of the convective instability γ (7.1.21) are calculated. In the areas that are unstable relative to the convection, the magnetic diffusion and thermal conductivity coefficients are increased using exponential multipliers $\mathrm{ch}(\int \gamma dt) \equiv \mathrm{ch}(G)$. The comparison of the 1D model with 2D computations results and estimations of (7.3.7–7.3.8) has shown that, in many cases, the physical magnetic diffusion and thermal conductivity coefficients turn out to be too high to ensure small coefficients in the formulas of (7.3.7–7.3.8). Therefore, it makes sense to increase these coefficients a little less, but following the law

$$\mathrm{Ch}(G^2/(G + G_0)) \ ,$$

where G_0 is a semi-empirical coefficient determined for typical cases through comparison with 2D calculations and estimations of (7.3.7–7.3.8).

For a qualitative inclusion of 2D turbulence (7.3.5) in the proposed 1D model, we can assume that $G \geq G_{\min}$ for some $G_{\min}$ in a central plasma area.

Cooling of Cylindrical Magnetized Plasma Layer

To determine the role of turbulent thermal diffusion and convection and validate the 1D model for the plasma cooling description, we performed a numerical 2D MHD simulation of cooling of magnetized plasma bounded by cold walls.

The 2D computation set-up was as follows. We assumed that at the initial time, the plasma of density $\rho_0 = 3 \cdot 10^{-6}$ g/cm^3 and temperature $T = 0.2$ keV is in the space between two coaxial cylinders 2 cm long; the radius of the internal cylinder is 0.9 cm, the radius of the external cylinder is 6 cm. The plasma is in an azimuthal magnetic field corresponding to a field of direct current $I = 2.5$ MA. The walls were assumed to be rigid, perfectly conducting, and cold, and the cylinder bases were rigid, perfectly conducting, and thermally isolated. At the initial time, small density perturbations were assigned in the plasma volume. In one calculation run, the initial plasma velocities were assumed to be zero. To determine the role of the turbulent thermal diffusion, another calculation run assigned an initial field of velocities whose order of magnitude coincided with that of the velocities generated as convection developed, while the velocity distribution itself rapidly became chaotic because of instabilities. The level of the initial turbulent kinetic energy in this calculation was ~3 % of the thermal energy.

The 2D calculations showed that the presence of additional velocities had virtually no effect on the plasma cooling, and the developing convection resulted in the thermal energy of the plasma dropping down to 70 % of the initial energy by the time $t = 5$ μs (according to 1D calculation, convection-free thermal conduction had cooled the plasma to 80% of the initial thermal energy by that time).

The 1D model calculations of the convection with $G_0 = 10$ and $G_{\min} = 1$ showed that, by the time $t = 5$ μs, the plasma thermal energy decreased down to 67% of the initial thermal energy, which describes the 2D calculation results. Thus, the parameters $G_0 = 10$ and $G_{\min} = 1$ can be looked upon as reasonable for the description of cooling of infinitely long plasma cylinders with the level of turbulent kinetic energy being ~3 % of the thermal energy.

7.3.3. Plasma-Driven Material Washout from the Walls in the MAGO Chamber

Among the sources of impurities that reduce plasma lifetime in the MAGO chamber are the walls of the chamber. The action of the heat fluxes on the wall material can result in wall material melting or vaporizing at the boundary with the plasma, losing of strength, and easily detaching. The heat fluxes themselves from plasma to the walls are ultimately determined by thermal conductivity, drift heat transport and plasma radiation. However, these fluxes can grow considerably because of the presence of hydrodynamic convective motion that brings hot plasma to the walls or because of the plasma flow friction against the electrode surface (see Section 5.3) or an increase in radiation from the plasma after it is

contaminated by impurities. Plasma contamination imparts a positive feedback to the system: the increased content of impurities results in increased heat fluxes to the wall, which, in turn, increases the impurities' ingress into plasma, and so on.

In this section, following the work of Garanin *et al*. [7.44 and 7.45], we provide estimates of heat fluxes to the walls in the MAGO chamber, consideration of the possible melting or vaporization of the walls, and estimates of the amount of impurities brought by the MHD-turbulence into the plasma.

Heat fluxes from plasma to electrodes and insulator. Melting or vaporization of electrode metal and insulator vaporization

Let us estimate the heat fluxes incident on the walls with using different approaches. The first method of estimating the fluxes involves using the results of 2D MHD computations, where these fluxes are determined by thermal conductivity for magnetized plasma and its radiation. The drawback of these estimates is that many effects evolving at small distances from the surface are not reproduced in the computations, because of the grid size limitations. Moreover, the computations do not take into account some physical phenomena, such as the plasma friction against the surface (which, according to Section 5.3, can be of a kinetic nature, i.e., ions interact with the metal surface at distances smaller than the Larmor radius), the Hall effect, and the Nernst effect.

Another way to obtain such estimates is to use the results of 1D analysis of near-electrode layers in the MAGO chamber (see Section 5.3). This approach takes into account the above-mentioned physical phenomena, as well as models the turbulence caused by large near-electrode plasma velocity gradients. The drawback of these estimates is that they do not take into account flows from heated plasma, since, in this work, the near-electrode layers are considered for cold plasma acceleration. Let us start with these estimations.

According to Section 5.3.1, when plasma with a density of $n_0=6\cdot10^{17}$ cm^{-3} is accelerated in a magnetic field $B \sim 10^5$ G, heat fluxes in the near-cathode and near-anode layers equal approximately $q \sim$ 26-52 J/cm$^2\mu$s at time $t = 0.5$ μs, when the plasma velocity far from the electrodes is 40 cm/μs. By this time, the volume density of heat release in the copper wall is

$$\sim q\sqrt{\frac{t}{\kappa}} \sim 6-12 \text{ kJ/cm}^3$$

($\kappa \sim 10^{-6}$ cm$^2/\mu$s is the coefficient of copper temperature conductivity) or heat release per mass unit is ~ 0.7-1 kJ/g, which may exceed the heat required for melting copper, which is ~ 0.6 kJ/g.

When the residual low-density plasma with the density $n_0 = 1.5 \cdot 10^{16}$ cm^{-3} is accelerated in the vicinity of the nozzle, the near-anode heat fluxes, which on the average are 2400 J/cm$^2\mu$s, are especially significant. Since the flow time of the residual plasma through the nozzle is ~ 0.3 μs, the heat release on the anode per mass unit can be ~ 100 kJ/g, which significantly exceeds the heat of vaporization for copper, which is ~ 6 kJ/g.

The estimates of the heat fluxes onto the walls for a small chamber with a radius of 6 cm, obtained using 2D computations, yield a maximum for the heat flux on the walls of ~30 J/cm^2 and a radiation energy flux of ~ 40 J/cm^2 (under assumption that the level of impurities is ~$5 \cdot 10^{-3}$ Torr of oxygen). The characteristic times are ~2 μs, and the heat release per mass unit is ~ 6 kJ/g, which is on the order of the copper vaporization heat.

According to the 2D computations, radiation fluxes to the insulator are ~ 1 J/cm^2, and their action time is ~ 1 μs. Since, for ceramics, the coefficient of temperature conductivity per mass unit is ~ 0.2–1 g^2/cm^{4}s, the heat release per mass unit, ~ 6 kJ/g, warms up its surface layer higher than 2000° C. Such temperatures can cause the vaporization of ceramics, and in this vapor, breakdowns and the *H*-thrown discharge may occur (Section 6.5).

Instability of Tangential Discontinuity at the Plasma–Electrode Interface

In the MAGO chamber at the plasma–electrode interface, there is a tangential discontinuity: plasma flows along the electrode with velocities of u ~ 10^7 cm/s (near the nozzle the velocities are up to ~ 10^8 cm/s), and the electrode material, which can be in the melted or vaporized state at the surface and whose density is considerably higher than that of the plasma, is at rest. At this interface, a tangential instability [7.8] should develop whose increments

$$\gamma = \mathrm{k}\sqrt{\frac{\rho_\mathrm{p}}{\rho_\mathrm{m}}}\mathrm{u} \qquad (7.3.9)$$

(ρ_p, ρ_m) are plasma and electrode material densities, k is the wave number) are inversely proportional to the square root of the electrode material density. Thus, the development of this instability is most dangerous in the case of plasma contact with the vaporized electrode.

Turbulence Developing at the Plasma–Metal Interface and the Ingress of Impurities into Plasma

Let us consider the distribution of a heavy material in a light one (plasma) in a developing tangential instability. Beginning with the formula (7.3.9) and using, for the characteristic turbulent velocities v, the formulae applicable to 3D turbulence, we can assume that

$$\mathrm{v} \sim \alpha \sqrt{\frac{\rho_\mathrm{p}}{\rho}}\mathrm{u} \ ,$$

where ρ is the local density, α is a small coefficient, characteristic for turbulent pulsations. Since the velocities v transport the material a distance of $x \sim vt$, the density distribution can take the form

$$\rho \sim \rho_\mathrm{p} \left(\frac{\alpha \mathrm{u}\, \mathrm{t}}{\mathrm{x}} \right)^2 .$$

Then the total mass of the heavy material brought into plasma from the unit area per time unit is

$$\frac{\mathrm{dm}}{\mathrm{dt}} \sim \frac{\rho \mathrm{x}}{\mathrm{t}} \sim \alpha^2 \rho_\mathrm{p} \frac{\mathrm{u}^2 \mathrm{t}}{\mathrm{x}} \sim \alpha \rho_\mathrm{p} \mathrm{u} \ . \qquad (7.3.10)$$

The relation (7.3.10) was earlier used in Bakhrakh *et al.* [7.46] for describing experimental data on strong shockwave damping in a tube. Comparison of the calculations and experiments gave the value of the constant $\alpha \cong 0.02$. The 2D numerical computations performed showed that this value is reasonable for describing mixing of a heavy fluid and a light fluid in the 2D case. Nevertheless, we tried to estimate the material washout from the walls in the MAGO chamber at the phase of preliminary heating, using more complicated qualitative models of 2D turbulence with reasonable dependences in different extreme cases. At the phase of the MAGO plasma compression, we used the relation (7.3.10) for estimation of the material washout from the walls.

Plasma-Driven Material Washout from the MAGO Chamber Walls in the Phase of Preliminary Heating

As we have noted already, the turbulent plasma motion in the azimuthal magnetic field in the MAGO systems can be 2D, because the magnetic field impedes the bending of the magnetic-field lines and occurrence of the corresponding flows. Garanin *et al.* [7.47] studied the transport of impurities

from the walls with regard to axisymmetric MHD 2D flows in a bounded region. The process of the mixing of wall material with plasma was described in Garanin *et al.* [7.47] by the 1D diffusion equation

$$\frac{\partial \rho}{\partial t} = \mathrm{div}(D \nabla \rho),$$

where ρ is the concentration of impurities, D is the turbulent diffusion coefficient, consisting of two parts, determined by the turbulent motion set in the chamber volume and the turbulent motion that is caused by the plasma convection development on the boundary with the cold wall: $D = D_t + D_c$. The dependence of the impurities' turbulent diffusion coefficients on the characteristics of those flows was determined for the case of 2D turbulent flows, and numerical factors in the formulas for D were determined in the case of $m = 0$ stable plasma with an azimuthal magnetic field.

Garanin *et al*. [7.47] ascertained that turbulent diffusion is unable to bring the material away from the wall by itself, because the 2D turbulent diffusion coefficients decrease fast as the wall is approached. To determine the material flows from the walls, near-wall processes (molecular diffusion, physical viscosity, heat conduction, heat-driven release of impurities from the wall, heterogeneity of density, etc.) should be included. But if only numerical hydrodynamic calculations are used for the transport of impurities, in a uniform fluid the result will depend on the spatial grid, and the material flows from the walls will decrease with a spatial grid refinement. We can, however, specify two factors that can result in the finite value of flows from the walls. First, it is the finite width of the layers of melted or vaporized wall material. Second, in the vicinity of the walls where the material density gradients can be high, we should assume that the diffusion coefficient D_t is not the same as in the 2D case [7.47], but, qualitatively, the same as in the 3D case. This change also leads to a finite value for the flows of impurities from the walls.

On the basis of the 1D model, with account taken of the two factors resulting in finite values for the flows, we estimated the impurity washout from the MAGO chamber walls. We used the 1D computation results for plasma cooling to take into account specific profiles of the values in the chamber, which required generalization of the model for the case of arbitrary (stable and unstable) plasma profiles. In addition, in the 2D calculations we took into account the time dependences of characteristic turbulent plasma velocities.

The calculations have shown that by the times 0.5–1 μs after heated plasma is generated in the central area of the chamber, the mass of light-element gas impurities is less than 1 % of the plasma mass, which is insufficient to

explain the X-ray diode signals obtained in the experiments. However, a significant gas amount has mixed in with the plasma by the time of a few microseconds, which agrees with the post-experiment values of gas leakage in the chamber training and experiments at the Cascade facility.

It was found that, in the case of vaporization of the surface of copper walls, the amount of copper impurities in the chamber can be 0.2–0.4 % of the plasma mass in 0.5–1 μs, which, given the considerable uncertainties attending the estimates, can explain the diode signals. Thus, mixing in of the copper impurities can be an important and even determining factor that affects the energy losses in the chamber. The estimates obtained agree well with the calculations of the X-ray diode signals of the Dante spectrometer, shown in Section 3.4.4.

Plasma-Driven Material Washout from the MAGO Chamber Walls in the Phase of Plasma Compression

The formula for the mass washout rate (7.3.10) with the specified value of the coefficient $\alpha \cong 0.02$ is used to estimate the mass washout from the MAGO chamber walls during the compression of preheated plasma by a hemispherical chamber wall. We write a set of two equations:

$$\frac{dm}{dt} = \alpha \frac{m}{V} u_t S \ , \tag{7.3.11}$$

$$m u_t R = \text{const} = m_0 u_{t0} R_0 \ . \tag{7.3.12}$$

The first equation is the formula for the washout rate (7.3.10). The second one is the angular momentum conservation law for plasma motion in vortices. This equation takes into account the angular acceleration of the vortices in plasma and their deceleration due to the involvement in this motion of the mass that has been washed out from the walls. In the equations (7.3.11) and (7.3.12)

m is the total plasma mass, including the washed-out mass;

S is the surface area of the walls surrounding the plasma;

V is the plasma volume;

R is the radius of the plasma-compressing hemisphere.

Strictly speaking, the projection of the plasma angular momentum onto the direction perpendicular to r and z that is under consideration is not conserved for the plasma moving in the axisymmetric MAGO chamber. However, we can provide the following in justification of the formula (7.3.12). As follows

from the Thomson theorem [7.8], the quantity proportional to $\mathrm{rot}\,\vec{u}\cdot\overrightarrow{dS}$ is conserved in the ideal fluid flow. In the compression of the 2D region, if $\mathrm{rot}\,\vec{u}$ is assumed to be on the order of u_t/R (the main contribution to the turbulent motion's kinetic energy will not be made by smaller-scale motions) and $dS \sim R^2$, then $u_t R \sim$ const. $u_t R \sim \text{const}$. To obtain (7.3.12) therefrom, we assume that the mixing of the washed-out mass and the plasma proceeds with conservation of momentum rather than energy.

By substituting u_t from (7.3.12) into (7.3.11) and changing the variable t to the variable R($\frac{dR}{dt} = -u_n$), we obtain

$$\frac{dm}{dR} = -\alpha\beta\frac{m_0 u_{t0} R_0}{R^2 u_n}. \qquad (7.3.13)$$

Here, β is the coefficient in the formula $\frac{S}{V} = \frac{\beta}{R}$, $S = 3\pi R^2$, $V = \frac{2}{3}\pi R^3$, $\beta = 45$ and the quantities with the subscript 0 are initial values of mass, tangential velocity, and radius. The solution of equation (7.3.13) can be written as

$$\frac{m}{m_0} = 1 + \alpha\beta\frac{u_{t0}}{u_n}\left(\frac{R_0}{R} - 1\right). \qquad (7.3.14)$$

Here we assumed that the radial compression velocity u_n is time-independent.

We also note that the writing of the initial equations (7.3.11) and (7.3.12) means that, during the entire process of plasma compression (from the very beginning), we assume the presence of vaporized material in a sufficiently large amount (such that it does not have enough time to become washed out completely) over the entire surface area of the chamber walls. The available 2D MHD computations of plasma flow in the chamber suggest that by the initial moment of compression, the walls are vaporized only in some locations (which represent a small portion of the total area). However, according to the estimates, starting from the degree of compression of ~ 2 (by volume), the bremsstrahlung alone of the pure DT plasma yields, on average for the entire surface of the walls, an energy flux of ~ 10^{13} erg/cm^2·s, which is sufficient for the copper vaporization.

With the above provisos taken into account, we can assume that the numerical estimates presented below yield results that are correct in the terms of the order of magnitude, albeit slightly overestimated.

Using the obtained formula (7.3.14), we estimate the washed-out mass for a case in which the plasma velocity in the chamber at the initial time of compression is $u_{t0} \sim 10^7$cm/s (based on the results of the 2D MHD computations) and the velocity of the plasma compression by the hemispherical shell is $u_n \sim 10^6$ cm/s. In this case, for $\frac{R_0}{R} = 2$ (the compression degree is $\delta = 8$), $\frac{m}{m_0} \sim 2$; for $\frac{R_0}{R} = 5$ ($\delta = 125$), $\frac{m}{m_0} \sim 5$.

The result obtained, with account taken of the fact that estimates under discussion are very approximate, can be formulated as follows. The mass washed out from the chamber walls during plasma compression in the MAGO chamber at the compression degrees of interest to us is of the order of magnitude of the DT-gas mass itself. If this is correct, it follows that in the experiments on the DT plasma compression in the MAGO chamber, the chamber walls (or the wall coating) should be made not of copper, but of light materials (e.g., graphite or beryllium), so that the radiation losses of the DT plasma heavily contaminated by the wall material do not cool the plasma too rapidly.

It should be said that the obtained estimates are based on the hypothesis of conservation of angular momentum in plasma compression or, to be more exact, on the hypothesis that, in the plasma compression, the 2D turbulent kinetic energy increases in inverse proportion to the area of the 2D cross-section of the region (not including the mixing, of course). There is a probability that this hypothesis does not hold. It should be also noted that, according to the results of Section 7.3.1, the dissipation of kinetic energy in 2D turbulence is determined by real physical viscosity, and determining the kinetic energy of turbulent motion and, with it, the amount of washed-out mass (7.3.14) in the MAGO experiments requires computations that take into account the physical viscosity of magnetized plasma [7.33].

CONCLUSION

According to the estimates, the value for heat flux at which the copper wall begins to vaporize in the MAGO chamber (with a characteristic duration of heat flux of ~ 10^{-6} s) is ~ $3 \cdot 10^{14}$ erg/cm^{2}s. The same parameter for a ceramic (Al_2O_3) insulator is ~ 10^{13} erg/cm^{2}s. The estimates based on different 1D and 2D computations show that such heat fluxes can occur during plasma-chamber operation.

The estimates of the turbulent washout of impurities from the walls by plasma showed that, at the stage of plasma preheating in the MAGO chamber, by the times 0.5 – 1 μs after heated plasma is generated in the central area of the

chamber, the mass of light-element gas impurities is less than 1% of the plasma mass, which is insufficient to explain the X-ray diode signals obtained in the experiments. However, a considerable amount of gas is mixed in by the time of a few microseconds, which agrees with the values of gas leakage measured post-experimentally in the chamber training and experiments at the Cascade facility.

It was found that in the case of vaporization of the surface of the copper wall, the amount of copper impurities in the chamber by time 0.5–1 μs can be 0.2–0.4% of the plasma mass, which, given the considerable uncertainties of the estimates, could explain the diode signals. Thus, the mixing in of the copper can be an important and even determining factor affecting the energy losses in the chamber.

It was also found that the mass of the material washed out from the MAGO chamber walls during the process of plasma compression by a hemispherical shell can be of the same order as the mass of compressed DT-gas. If the experiments show this to be true, then, in order to prevent the wall impurities from cooling the plasma too rapidly, the MAGO chamber walls and the insulator may be fabricated from light materials (carbon or beryllium for the walls, boron carbide or boron nitride for the insulator) for the experiments on plasma compression.

7.3.4. Simulation of MAGO Plasma Compression by Imploding Liner with Account Taken of Convection

In Section 2.1.2, we have already presented the parameters of the plasma obtained in the MAGO chamber. In a number of experiments in the coaxial cylindrical volume with a height 8 cm, an external radius of R ~ 10 cm, and an internal radius of 1.2 cm, DT plasma was obtained with the following parameters:

mean density $n = 8 \cdot 10^{17} \text{cm}^{-3}$,

mean temperature $T = 250$ eV,

characteristic current in the plasma $I \sim 4$ MA,

characteristic magnetic field in plasma $B \sim 0.15$ MG,

characteristic $\beta \sim 0.6$,

which makes it possible to consider this plasma as suitable for ignition in its quasi-spherical compression. According to the estimates presented in Section 2.1.2, if such plasma lives in MAGO for $\sim 10^{-5}$ s, then the ignition in the MAGO/MTF system can be achieved using an implosion system with a liner energy of ~20 MJ and a velocity of ~1 cm/μs. In the joint VNIIEF/LANL experiment HEL-1 (High Energy Liner), a liner with similar

parameters (energy of ~25 MJ, velocity of ~0.8 cm/μs) has been obtained [7.48]. In the experiment, a portion of the liner remained solid (unmelted), persisting against the Rayleigh-Taylor instability.

This Section, following the work of Buyko *et al.* [7.49], presents the results of 1D quasi-spherical simulations and 2D simulations (with account taken of convection) of MAGO plasma compression by a solid liner, with the parameters characteristic of the HEL-1 experiment. In both simulations, the plasma was assumed to be of pure hydrogen without impurities.

1D Quasi-Spherical Simulation

The 1D quasi-spherical MHD simulation was conducted in the channel approximation (Section 2.1.2). We assumed for the quasi-spherical compression calculation that the channel width changed proportionally to the radius. In the simulation, magnetic diffusion, classic electron and ion thermal conductivities [7.33], and radiation transport along the channel in the "forward-reverse" approximation [7.50] were taken into account. Enhanced thermal conductivity resulting from the development of turbulence in the plasma was not taken into account. Nor was the effect of thermonuclear energy release on the plasma and liner heating.

The entire plasma volume can be regarded as consisting of channel sectors in each of which the width varies in proportion to the spherical radius. The simulation was performed for a sector in-between the equator and the pole, which we considered as most representative. Therefore, in our calculation we assumed that the plasma parameters were those obtained in the MAGO experiments—density $n = 8 \cdot 10^{17}\text{cm}^{-3}$ and temperature $T = 250$ eV—but the magnetic field in the plasma corresponded to a somewhat higher current, $I = 5$ MA. The radius of the central copper rod along which the plasma magnetizing current flowed was also taken to be somewhat larger at $r = 1.6$ cm than the cylindrical radius of the MAGO chamber internal rod at $r = 1.3$ cm. In the simulation, the plasma, initially located within the range $1.6 \text{ cm} < r < 10$ cm, was compressed by an aluminum liner 0.44 cm thick and with the initial velocity of 0.8 cm/μs. If we assume that the height of this liner equaled to its radius, then its energy was 25 MJ, and, thus, the liner had the characteristics obtained in the HEL-1 experiment.

The simulation showed that the maximum internal energy of the DT plasma (all the integral values are given for the spherical segment width equal to the radius), equal to 3.1 MJ, was achieved at the time 8.84 μs. The system total energy, which was about 25 MJ and was initially contained mainly in the liner kinetic energy, at this time was distributed among different components: magnetic energy (plasma β was ~1), liner and internal rod

heating by thermal fluxes from plasma, remainder of liner kinetic energy, etc. The elastic energy tied up in liner compression was chief among these components. Magnetic and thermal pressure reduced the radius of the internal rod down to 1.3 cm, and the plasma was compressed to a layer 0.32 cm thick and achieved a density $3.9 \cdot 10^{20}$ cm^{-3}. The neutron yield, under compression, was $3 \cdot 10^{18}$, and the full width at half-maximum was 0.91 μs. In the simulation, the total thermonuclear energy release was 8.9 MJ, i.e., greater by a factor 2.9 than the maximum internal energy of the DT plasma; this means that the ignition was achieved in this simulation.

Fig. 7.24 shows profiles of density ρ, temperature T, pressure p, and magnetic field B obtained in the simulation at time $t = 9$ μs, close to the time of neutron generation maximum.

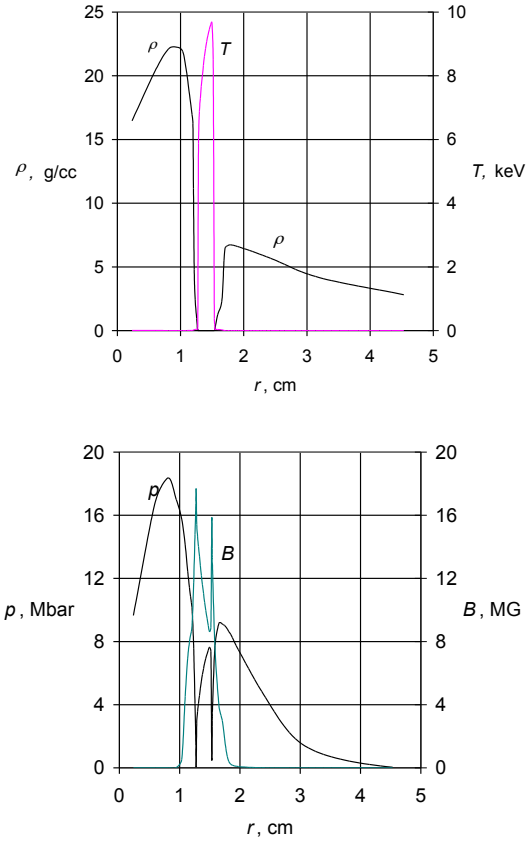

Fig. 7.24. Profiles of density ρ, temperature T, pressure p, and magnetic filed B in the system including internal rod, plasma, and liner at time t = 9 μs.

2D Simulation of Plasma Compression

To assess the effect of 2D convection on the plasma cooling processes associated with plasma compression, we performed a numerical 2D simulation of plasma compression by a liner. It was assumed that the plasma initially occupying a hemispherical volume with the radius of 10 cm and magnetized with current $I = 4$ MA running along a cylindrical rod of $r = 1.3$ cm radius was compressed by an incompressible hemispherical liner with an initial thickness of 0.44 cm, a density of 2.7 g/cm^3, and an initial velocity of 0.8 cm/μs. The 2D effects were considered only for the DT plasma, the liner shape was assumed to be purely spherical, and the internal rod and the hemisphere base were assumed to be absolutely rigid. The initial density and initial temperature of the plasma were assumed to be $n = 8 \cdot 10^{17}$ cm^{-3} and $T = 250$ eV, respectively. All the plasma boundaries (the liner, the internal rod, and the hemisphere base) were assumed to be ideally conductive and cold.

The maximum internal energy of the DT plasma was reached in this simulation at time 8.7 μs and equaled 7.9 MJ, when the liner's internal radius was 1.54 cm. The magnetic energy at that time was 4.7 MJ, such that the characteristic magnetic field was 29 MG. The neutron yield at the compression maximum was $6 \cdot 10^{18}$, and the characteristic width of the neutron pulse was 0.15 μs. The thermonuclear energy value in this simulation also exceeded the maximum internal energy of the DT plasma, i.e., ignition was also achieved in this simulation.

The plasma density and temperature isolines at times $t = 6.4$ μs and $t = 8.4$ μs are shown in Figs. 7.25 and 7.26.

Calculations show that in the experiments with the 0.4-m-diameter DEMG, it is possible to obtain the second neutron peak produced by the MAGO plasma compression with a quasi-spherical liner. The second neutron peak can be higher than the first one obtained during the plasma generation, even with plasma volume compression as low as $\delta \approx 10$ (if one compares neutron generation rates at the moment at which volume compression was 10 against the neutron generation rate from the preheated plasma).

At higher levels of plasma compression, the simulations predict considerably higher neutron generation rates, e.g., at $\delta \approx 100$, the neutron generation rate is $\sim 10^{16}$ μs^{-1}. Such levels of plasma compression are quite feasible with good symmetrization of the liner system, because the values of the typical maximum plasma compression predicted in 1D simulations are much higher ($\delta \sim 1000$).

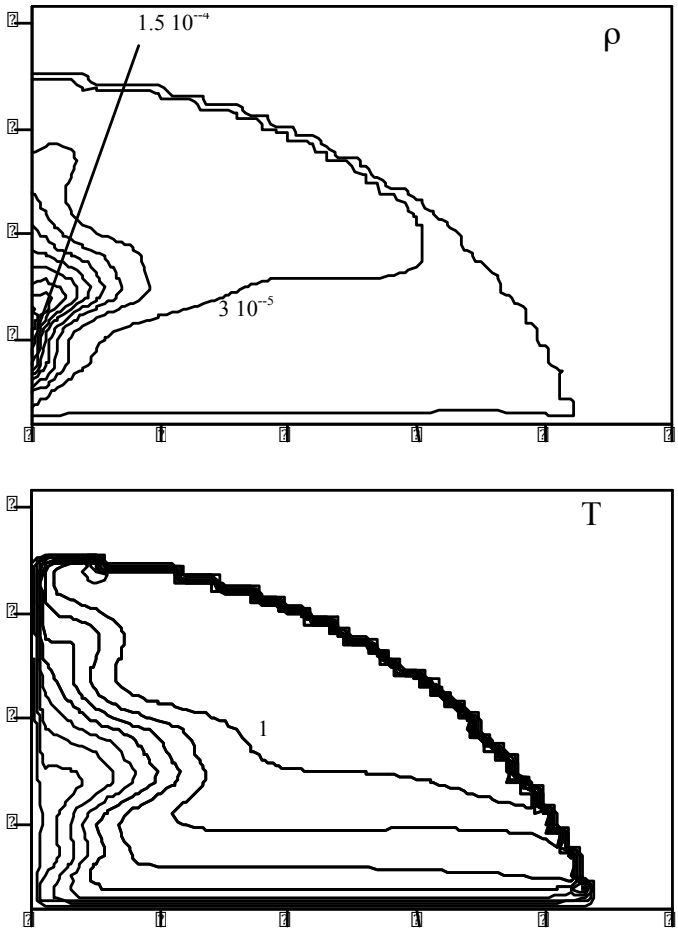

Fig. 7.25. Plasma density and temperature isolines at time t = 6.4 μs.

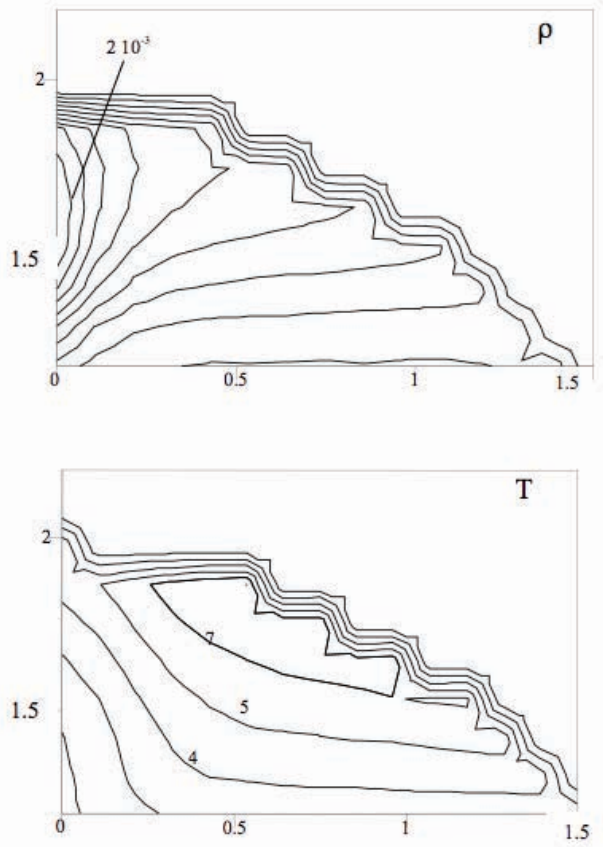

Fig. 7.26. Plasma density and temperature isolines at time t =8.4 μs

CONCLUSION

The presented results of the numerical simulations confirm the feasibility of achieving ignition with MAGO plasma compression by liners with experimentally achieved characteristics. The 1D and 2D simulations took into account the main physical effects and processes; some of them taken into account in 1D simulation, and others, in 2D simulation. Taking convection into account in the 2D calculation does not result in considerable plasma cooling and do not impede the achievement of ignition.

REFERENCES

7.1 L.D. Landau. "On Stability of Tangential Discontinuities in a Compressible Fluid," *DAN SSSR* [Sov. Phys. Dokl.], Vol. 44, p. 151, 1944.

7.2 S.I. Syrovatskiy. "Instability of Tangential Discontinuities in a Compressible Medium," *ZhETF* [J. Exp. Theor. Phys.], Vol. 27, p. 121–124, 1954.

7.3 S.I. Syrovatskiy. "Magnetohydrodynamics," *UFN* [Sov. Phys. Usp.], Vol. 62, p. 247, 1957.

7.4 A.B. Mikhaylovskiy. *Elektromagnitnye Neustoychivosti Neodnorodnoy Plazmy* [Electromagnetic Instabilities of Nonhomogeneous plasma]. Moscow: Energoatomizdat [Publishing House], 1991.

7.5 A.G. Gonzales, J.J. Gratton. "The Kelvin–Helmholtz Instability in a Compressible Plasma: The Role of the Orientation of the Magnetic Field with Respect to the Flow," *Plasma Phys.,* Vol. 51, No. 1, pp. 43–60, 1994.

7.6 S.F. Garanin, S.D. Kuznetsov. "Instability of a Tangential Discontinuity in a Cold Plasma with a Magnetic Field Orthogonal to the Jump in Velocity," *Plasma Phys. Reports*, Vol. 22, No. 8, pp. 674-678; *Fizika Plasmy* [Plasma Phys. Reports], Vol. 22, No. 8. pp. 743–746, 1996.

7.7 B.B. Kadomtsev. *Kollektivnye Yavleniya v Plazme* [Collective Phenomena in Plasma]. Moscow: Nauka [Publishing House], 1988.

7.8 L.D. Landau, E.M. Lifshitz. *Gidrodinamika* [Fluid Mechanics]. Moscow, Nauka [Publishing House], 1986; 2nd ed. Addison-Wesley Publishing Co., Reading, MA, 1987.

7.9 B.B. Kadomtsev. "Hydromagnetic Plasma Stability," *Voprosy Teorii Plazmy: Sb. Statey* (Reviews of Plasma Physics: Collection of Papers). Ed. M.A. Leontovich. Moscow: Atomizdat [Publishing House], No. 2, p. 132–176, 1963.

7.10 N.I. Gerlakh, N.M. Zuyeva, L.S. Solovyev. "On the Development of MHD Instability in Z-Pinch," *Preprint IPM* [IPM preprint], No. 83, Moscow, 1979.

7.11 B.A. Trubnikov. "On the Instability of a Plasma Cylinder," *Fizika Plazmy I Problema Upravlyaemyh Termoyadernyh Reaktsiy* [Plasma Physics and Problems of Controlled Thermonuclear Reactions].

Moscow: Izdatelstvo AN SSSR [Publishing House of USSR Academy of Sciences], Vol. 1, pp. 289–298, 1958.

7.12 M. Kruskal, M. Schwarzschild. "Some Instabilities of a Completely Ionized Plasma," *Proc. Roy. Soc. A.*, Vol. 223, pp. 348–360, 1954.

7.13 V.D. Shafranov. "On the Stability of Cylindrical Gas Conductor in a Magnetic Field," *Atomnaya Energiya* [Atomic Energy], No. 5, p. 38, 1956.

7.14 V.V. Vikhrev, S.I. Braginskii. "Z-Pinch Dynamics," *Voprosy Teorii Plazmy: Sb. Statey* (Reviews of Plasma Physics: Collection of Papers). Ed. M.A. Leontovich. Moscow: Atomizdat [Publishing House], No. 10, pp. 243–318, 1980.

7.15 V.F. Dyachenko, V.S. Imshennik. "Two-Dimensional Magnetohydrodynamic Model of Plasma Focus of Z-Pinch)," *Voprosy Teorii Plazmy: Sb. Statey* (Reviews of Plasma Physics: Collection of Papers). Ed. M.A.Leontovich. Moscow: Atomizdat [Publishing House], No. 8, p. 164–246, 1974.

7.16 D.L. Book, E. Ott, M. Lampe. "Nonlinear Evolution of the Sausage Instability," *Phys. Fluids*, Vol. 19, p. 1982, 1976.

7.17 B.A. Trubnikov, S.K. Zhdanov. "Waist Breaking on Plasma Pinches with Current," *Pisma v ZhETF* [Letters to J. Exp. Theor. Phys.], Vol. 41, p. 292, 1985.

7.18 S.F. Garanin, Yu.D. Chernyshev. "Nonlinear phase of Z-Pinch Instability," *Fizika plazmy* [Plasma Phys. Reports], Vol. 13, No. 8, pp. 974–980, 1987.

7.19 D.J. Lewis. "The Instability of Liquid Surfaces when Accelerated in a Direction Perpendicular to their Planes. II," *Proc. Roy. Soc.*, *A.* Vol. 202, pp. 81–96, 1950.

7.20 P.B. Garabedian, "On Steady-State Bubbles Generated by Taylor Instability," *Proc. Roy. Soc.*, *A.* Vol. 241, pp. 423–431, 1957.

7.21 G.R. Baker, D.I. Meiron, S.A. Orszag. "Vortex Simulations of the Rayleigh–Taylor instability," *Phys. Fluids*, Vol. 23, p. 1485, 1980.

7.22 S.K. Zhdanov, B.A. Trubnikov. "Theory of Acceleration Phenomena Accompanying Breaking of the Plasma Pinch Waist," *ZhETF* [J. Exp. Theor. Phys.], Vol. 90, No. 4, p. 1380–1391, 1986.

7.23 S.F. Garanin, V.I. Mamyshev. "Peripheral Plasma Motion Behind the Z-Pinch Waist," *VANT* [Aspects of Atomic Science and Technology]. Theoretical and Applied Physics Series, No. 1, p. 23–26, 1989.

7.24 G.I. Taylor. “The Instability of Liquid Surfaces when Accelerated in a Direction Perpendicular to their Planes,” *Proc. Roy. Soc. London*, Vol. A 201, No. 1065, pp. 192–196, 1950.

7.25 G. Birkhoff, D. Carter. “Rising Plane Bubbles,” *J. Math. Mech.,* Vol. 6, No. 6, p. 769, 1957.

7.26 C.L. Gardner, J. Glimm, O. McBryan, et al. “The Dynamics of Bubble Growth for Rayleigh-Taylor Unstable Interfaces,” *Phys. Fluids*, Vol. 31, No. 3, pp. 447–465, 1988.

7.27 S.W. Haan, “Onset of Nonlinear Saturation for Rayleigh-Taylor Growth in the Presence of a Full Spectrum of Modes,” *Phys. Rev.*, Vol. A 39, No. 11, pp. 5812–5825, 1989.

7.28 O.I. Volchenko, I.G. Zhidov, E.E. Meshkov, V.G. Rogachev. “Development of Localized Perturbations on the Unstable Boundary of Accelerated Fluid Layer,” *Pisma v ZhTF* [Letters to J. Tech. Phys.], Vol. 15, No. 1, p. 47–51, 1989.

7.29 S.F. Garanin, A.I. Startsev. “Numerical Simulation of Nonlinear Growth of Local Perturbations with Corners for the Rayleigh-Taylor Instability,” *VANT* [Aspects of Atomic Science and Technology]. Theoretical and Applied Physics Series, No. 3, p. 6–9, 1992.

7.30 S.F. Garanin. “Self-Similar Evolution of Rayleigh-Taylor Instability in the Corner-Point Regions,” *Proc. Fifth International Workshop on Compressible Turbulent Mixing.* Eds. R. Young, J. Glimm, and B. Boston, World Scientific: Singapore, New Jersey, London, Hong Kong, pp. 33–39, 1995.

7.31 S.F. Garanin. “Self-Similar Evolution of Rayleigh-Taylor Instability in the Corner-Point Regions.” *VANT* [Aspects of Atomic Science and Technology]. Theoretical and Applied Physics Series, No. 3/1, p. 12–17, 1995.

7.32 V.V. Vikhrev, V.V. Ivanov, G.A. Rozanova. “Development of Waists in the Presence of Short-Wave Perturbations of the Z-Pinch Boundary),” *Fizika Plazmy* [Plasma Phys. Reports], Vol. 15, No. 1, pp. 77–82, 1989.

7.33 S.I. Braginskii. "Transport Processes in a Plasma,” *Voprosy Teorii Plazmy: Sb. Statey.* Ed. M.A. Leontovich. Moscow: Atomizdat [Publishing House], No. 1, pp. 183–272, 1963; Reviews of Plasma Physics. Consultants Bureau, New York, Vol. 1, p. 205, 1965.

7.34 S.D. Danilov, D. Gurariy. “Quasi-Two-Dimensional Turbulence,” *UFN*, Vol. 170, № 9, p. 921-968, 2000 (*Phys. Usp.* Vol. 43, p. 863, 2000).

7.35 S.F. Garanin, O.M. Burenkov, G.G. Ivanova, V.N. Sofronov, V.I. Mamyshev, V.F. Tishkin, N.V. Zmitrenko, “Relaxation of a 2D MHD Flow Transverse to a Magnetic Field in a Bounded Domain,” *Dig. Tech. Papers*, *Pulsed Power Plasma Science – 2001.* Eds. R. Reinovsky and M. Newton, (Las Vegas, Nevada, USA), Vol. 1, pp. 512–515, 2001.

7.36 S.F. Garanin, O.A. Amelicheva, O.M. Burenkov, G.G. Ivanova, V.N. Sofronov, “Relaxation of a 2D MHD Flow Across a Magnetic Field (2D hydrodynamic flow) in a Bounded Region),” *J. Exp. Theor. Phys.* (Translated from ZhETF), Vol. 97, No. 1, pp. 61–69, 2003.

7.37 S.F. Garanin, E.M. Kravets, O.N. Pronina, O.G. Sin’kova, A.L. Stadnik, Yu.V. Yanilkin. “Behavior of a 2D Vortex Flow in a Bounded Region.” Paper presented at XI Khariton Lectures, Extreme States of Matter. Detonation. Shock waves. (Sarov, Nizhniy Novgorod Oblast, Russia), 2009.

7.38 R.H. Kraichnan. “Inertial Ranges in Two-Dimensional Turbulence,” *Phys. Fluids*, Vol. 10, No. 7, pp. 1417–1423, 1967.

7.39 M. Chertkov. “Phenomenology of Rayleigh-Taylor Turbulence,” *Phys. Rev. Lett.*, Vol. 91, N. 11, p. 115001(4), 2003.

7.40 Yu.V. Yanilkin, S.P. Belyaev, A.V. Gorodnichev, et al. “EGAK++ Program Complex for Simulation on Adaptive-Embedded Fractional Computational Grid,” *VANT.* Mathematical Modeling of Physical Processes Series, No. 1, pp. 20–28, 2003.

7.41 S.F. Garanin, G.G. Ivanova, V.I. Mamyshev, V.N. Sofronov. “Convective Cooling of Plasma During its 2D Turbulent Flow in Magnetic field,” *Proc. X Int. Conf. Megagauss Magnetic Field Generation and Related Topics*, 2004. Ed. M. von Ortenberg, Humboldt University, Berlin, Germany–VNIIEF, Sarov, Russia, pp. 380–383, 2005.

7.42 H.J.H. Clercx, G.J.F. van Heijst. “Dissipation of Kinetic Energy in Two-Dimensional Bounded Flows,” *Phys. Rev. E*, Vol. 65, p. 066305(4), 2002.

7.43 I.R. Lindemuth, J.S. Pettibone, J.C. Stevens, R.C. Harding, D.M. Kraybill, L.J. Suter. "Unstable Behavior of Hot, Magnetized Plasma in Contact with a Cold Wall," *Phys. Fluids*, Vol. 21, No. 10, pp. 1723–1734, 1978.

7.44 S.F. Garanin, V.I. Mamyshev, V.B. Yakubov. "Assessment of Effects Resulting in Plasma Pollution with Wall Material in MAGO Chamber," *Proc. IX Int. Conf. Megagauss Magnetic Field Generation and Related Topics.* Moscow–St. Petersburg, 2002. Eds. V.D. Selemir and L.N. Plyashkevich, Sarov, VNIIEF, pp. 684–688, 2004.

7.45 S.F. Garanin, V.I. Mamyshev, E.M. Palagina. "Calculations of Wall-Material Washout by Plasma in MAGO Chamber," *IEEE Trans. Plasma Sci.,* Vol. 34, No. 5, pp. 2268–2273, 2006.

7.46 S.M. Bakhrakh, V.N. Mokhov, A.V. Pevnitskiy, V.P. Sevastyanov, V.I. Tarasov. "Motion of Explosion Products and Cylindrical Channel Walls in a Strong Explosion)," *FGV* [Combustion and Explosion Physics], Vol. 13, No. 2, p. 302–305. 1977.

7.47 S.F. Garanin, V.I. Mamyshev, E.M. Palagina. "Wall Material Washout by Plasma During its 2D Flow in Magnetic Field," *Proc. X Int. Conf. Megagauss Magnetic Field Generation and Related Topics. Berlin.* Ed. M. von Ortenberg, Humboldt University, Berlin, Germany–VNIIEF, Sarov, Russia, pp. 409–412, 2004.

7.48 V.K. Chernyshev, V.N. Mokhov, V.N. Buzin, O.M. Burenkov, A.M. Bujko, V.V. Vakhrushev, S.F. Garanin, B.E. Grinevich, Y.N. Gorbachev, V.A. Demidov, V.I. Dudoladov, V.V. Zmushko, A.I. Kuzyaev, A.I. Kucherov, B.M. Lovyagin, Y.I. Matsev, P.N. Nizovtsev, A.A. Petrukhin, A.I. Pishchurov, S.S. Sokolov, V.P. Solovjov, A.I. Startsev, V.B. Yakubov, B.G. Anderson, C.A. Ekdahl, J.H. Goforth, D. Clark, I.R. Lindemuth, R.E. Reinovsky, R.J. Faehl, S.M. Younger. "Study of High Energy Liner Compression in HEL-1 Experiment," *Dig. Tech. Papers*, *Proc. XI IEEE Int. Pulsed Power Conf.* Eds. G. Cooperstein and I. Vitkovitsky in Cooperation with IEEE Nuclear and Plasma Sciences Society, pp. 566–572, 1997.

7.49 A.M. Buyko, S.F. Garanin, G.G. Ivanova, S.D. Kuznetsov, V.I. Mamyshev, V.N. Sofronov, V.B. Yakubov. "Modeling of MAGO Plasma Compression by Imploding Liner," *Dig. Tech. Papers*, *12-th IEEE Int. Pulsed Power Conf.* Eds. C. Stallings and H. Kirbie in Cooperation with IEEE Nuclear and Plasma Sciences Society, Vol. 2, p. 1052–1055, Monterey, California, USA, 1999.

7.50 Ya.B. Zeldovich, Yu.P. Raizer. *Fizika Udarnykh Voln Vysokotemperaturnykh Gidrodinamicheskikh Yavleniy* [Physics of Shock Waves and High-Temperature Hydrodynamic Phenomena]. Moscow: Nauka [Publishing House], 1966; Vol. 1. Academic Press, New York, 1966.

Los Alamos National Laboratory, an affirmative action/equal opportunity employer, is operated by Los Alamos National Security, LLC, for the National Nuclear Security Administration of the U.S. Department of Energy under contract DE-AC52-06NA25396. A U.S. Department of Energy tvLaboratory Los Alamos National Laboratory, an affirmative action/equal opportunity employer, is operated by Los Alamos National Security, LLC, for the National Nuclear Security Administration of the U.S. Department of Energy under contract DE-AC52-06NA25396. A U.S. Department of Energy Laboratory.

LA-UR-13-29094